Extremum-Seeking Control for Constrained Optimal Formation Flight of Commercial Airliners

by

Izaak van Zyl

Thesis presented in partial fulfilment of the requirements for the degree of
Master of Science in Electrical and Electronic Engineering
at Stellenbosch University

Department of Electrical and Electronic Engineering,
University of Stellenbosch,
Private Bag X1, 7602 Matieland, South Africa.

Supervisor: Dr J.A.A. Engelbrecht

March 2018

UNIVERSITEIT·STELLENBOSCH·UNIVERSITY
jou kennisvennoot • your knowledge partner

Plagiaatverklaring / *Plagiarism Declaration*

1. Plagiaat is die oorneem en gebruik van die idees, materiaal en ander intellektuele eiendom van ander persone asof dit jou eie werk is.
   Plagiarism is the use of ideas, material and other intellectual property of another's work and to present is as my own.

2. Ek erken dat die pleeg van plagiaat 'n strafbare oortreding is aangesien dit 'n vorm van diefstal is.
   I agree that plagiarism is a punishable offence because it constitutes theft.

3. Dienooreenkomstig is alle aanhalings en bydraes vanuit enige bron (ingesluit die internet) volledig verwys (erken). Ek erken dat die woordelikse aanhaal van teks sonder aanhalingstekens (selfs al word die bron volledig erken) plagiaat is.
   Accordingly all quotations and contributions from any source whatsoever (including the internet) have been cited fully. I understand that the reproduction of text without quotation marks (even when the source is cited) is plagiarism.

4. Ek verklaar dat die werk in hierdie skryfstuk vervat, behalwe waar anders aangedui, my eie oorspronklike werk is en dat ek dit nie vantevore in die geheel of gedeeltelik ingehandig het vir bepunting in hierdie module/werkstuk of 'n ander module/werkstuk nie.
   I declare that the work contained in this assignment, except where otherwise stated, is my original work and that I have not previously (in its entirety or in part) submitted it for grading in this module/assignment or another module/assignment.

March 2018

Abstract

Formation flight of commercial airliners has become a topic of interest due to the possibility of significant fuel savings. With air traffic rapidly increasing, the aeronautical industry recognizes the necessity to improve fuel efficiency of long distance flights. Previous studies have shown that extended formation flight of existing commercial aircraft is plausible, but have not dedicated much attention to fully utilising the wingtip generated wakes.

This study presents the design, implementation, and verification of a perturbation-based extremum-seeking controller that enables follower aircraft to locate and maintain optimal formation separations in a practical formation flight scenario. Typically, the trailing vortices of the leader aircraft are displaced due to atmospheric disturbances, such as static winds and turbulence, and models of the vortex positions are not exact. Due to the dangers related to flight deep in the leader's wake, a novel constrained objective function is proposed that prevents the extremum-seeking controller from guiding the follower aircraft too close to the vortex core. In this constrained objective function, the extremum is represented by a constrained extremum *contour* instead of a single point. A novel extremum-seeking state machine is proposed that controls the different modes of operation that the follower aircraft transitions through as it approaches the constrained extremum. The states and the state transition boundaries are defined as functions of the objective function, which allow them to follow the displaced trailing vortex, instead of remaining static relative to the leader aircraft. This also enables the extremum-seeking control to not only track a static trailing vortex, but also a constrained extremum for a dynamic trailing vortex. It is also shown that by approaching the constrained extremum at a constant approach rate, rather than the classical proportional approach rate, the effects of the non-linear wake on the seeking performance may be mitigated.

The extremum-seeking controller was verified in simulation on a formation flight model of two Boeing 747 aircraft in right echelon formation. The formation is subjected to realistic atmospheric disturbances and sensor noise. The simulation results show that the extremum-seeking controller is able to successfully guide the follower to the constrained extremum, even in the presence of varying static wind and light turbulence, and that thrust reductions of up to 23% may be achieved.

Uittreksel

Formasie vlug van kommersiële vliegtuie kry baie belangstelling vanweë die moontlikheid van aansienlike brandstofbesparings. Met lugverkeer wat vinnig aan die toeneem is, erken die lugvaartbedryf die noodsaaklikheid om die brandstofdoeltreffendheid van langafstandvlugte te verbeter. Vorige studies het getoon dat uitgebreide formasie vlug van bestaande kommersiële vliegtuie wel moontlik is, maar het nie veel aandag geskenk om die vlerkpunt-gegenereerde volgstroom van die leier vliegtuig ten volle te benut nie.

Hierdie studie beskryf die ontwerp, implementering en verifikasie van 'n storing-gebaseerde ekstremum-soekende beheerder wat volger vliegtuie in staat stel om die optimale ligging in die formasie op te spoor en te volg in 'n realistiese formasie vlug scenario. Tipies word die volgstroom van die leiervliegtuig verplaas weens atmosferiese steurnisse soos statiese winde en turbulensie. As gevolg van die gevare van te diep vlieg in die leier vliegtuig se volgstroom, word 'n nuwe beperkte doelfunksie voorgestel wat die ekstremum-soekende beheerder verhoed om die volger vliegtuig te naby aan die kern van die leier se draaikolk te laat kom. In hierdie beperkte doelfunksie word die ekstremum verteenwoordig deur 'n beperkte ekstremum *kontoer*, in plaas van 'n enkele punt. 'n Ekstremum-soekende toestandsmasjien word voorgestel wat die verskillende operasie modusse van die volger vliegtuig beheer soos wat dit die beperkte ekstremum nader. Die toestande en oorgangsgrense van die toestandsmasjien word gedefinieer as funksies van die doelfunksie, wat hulle in staat stel om saam met die verplaasde volgstroom te beweeg, in plaas daarvan om staties te bly ten opsigte van die leiervliegtuig. Dit stel ook die ekstremum-soekende beheerder in staat om 'n beperkte ekstremum vir 'n dinamiese volgstroom te volg, en nie net vir 'n statiese volgstroom nie. Dit word ook getoon dat die effek van die nie-lineêre volgstroom op die verrigting van die ekstremum soek beheerder beperk kan word deur die beperkte ekstremum teen 'n konstante spoed te benader, eerder as teen 'n spoed wat proporsioneel is aan die gradient van die doel funksie.

Die ekstremum-soek beheerder is geverifieer in simulasie op 'n formasievlugmodel van twee Boeing 747-vliegtuie in regsgerigte-echelon-formasie. Die formasie word onderwerp aan realistiese atmosferiese steurnisse en sensor ruis. Die simulasie resultate toon dat die ekstremum-soekende beheerder in staat is om die volger na die beperkte ekstremum te lei, selfs in die teenwoordigheid van wisselende statiese wind en ligte turbulensie, en dat enjin stukrag verlagings van tot 23% verkry kan word.

Acknowledgements

I would like to express my sincere gratitude to the following people and organisations for their support and contributions toward the successful compilation of this thesis:

- My supervisor, Dr Japie Engelbrecht, for his excellent guidance and support throughout the two years of my Masters. Always able to explain the most difficult of concepts in the simplest ways. Thank you for your significant contribution to this project, it was a privilege and an honour to have you as my supervisor.
- My initial supervisor, Prof Thomas Jones, who supervised my project for the first six months. Thank you for helping me grasp the basic concept of extremum-seeking and guiding me through the first phase of my project.
- The Airbus company for their financial support and teleconference meetings, during which they provided valuable, practical insights.
- My family, who supported me throughout my years of study. Without you, I would never have been able to achieve what I have. I adore you and appreciate all the hard work and commitment it took to get me where I am.
- My two office buddies, Christiaan Müller and Jannes Engelbrecht, for their support and friendship through all my years of study. Thank you for all the laughs and interesting insights into my project.
- My dear friend, Luca Brits, who always provided an ear (figuratively) to listen to my complaints, be they work related or personal. Thank you for your dear friendship and long conversations about basically everything.
- And finally, my dearest companion, partner, and best friend, Roné Mostert. You have been my pillar and cornerstone for the past five and a half years, and I will never be able to thoroughly express my gratitude to you. Thank you for all the 'coffee breaks', and always listening to me ramble on about my work. You mean everything to me.

Contents

List of Figures

List of Tables

Nomenclature

Abbreviations and Acronyms

6DOF	6-Degrees-of-freedom
AT	Auto-thrust
BPF	Band-pass filter
CG	Centre of Gravity
CPT	Cape Town International Airport
CR	Climb Rate
CT	Cross-track
DXB	Dubai International Airport
DC	Direct Current
ESC	Extremum Seeking Control
ESRL	Earth System Research Laboratory
FBW	Fly-by-wire
FCS	Flight Control System
FF	Formation flight
FPA	Flight Path Angle
GPS	Global Positioning System
INS	Inertial Navigation System
LPF	Low-pass filter
NED	North-East-Down
NOAA	National Oceanic and Atmospheric Administration
UAV	Unmanned Aerial Vehicle

Symbol Conventions and Vector Notation

x	Scalar
$\mathbf{x}$	Vector
$\mathbf{x_y}$	Vector x coordinated in axis system y (coordinate vector)
$\mathbf{X}$	Matrix
$\dot{x}$	First time derivative of x
$\ddot{x}$	Second time derivative of x
$\frac{\partial f}{\partial x}$	Partial derivative of function, f, with respect to x

Constants

g	Gravitational acceleration

Aircraft Parameters

m	Aircraft mass
$\mathbf{I_B}$	Moment of inertia matrix of the aircraft body
I_{xx}, I_{yy}, I_{zz}	Principle moment of inertia of aircraft body x-axis, y-axis, and z-axis
S	Wing surface area
b	Aircraft wingspan
$\mathit{Æ}$	Aspect ratio
$\bar{c}$	Mean aerodynamic chord
a_i, a_o	Inner and outer engine placement dimensions respectively
θ_e, ψ_e	Engine pitch and inboard orientation angles

Aircraft Dynamics

X, Y, Z	Coordinates of force vector in body-axis (axial, lateral, and normal force)
L, M, N	Coordinates of moment vector in body-axis (roll, pitch, and yaw moment)
U, V, W	Coordinates of linear velocity vector in body-axis (axial, lateral, and normal velocity)

P, Q, R	Coordinates of angular velocity vector in body-axis (roll, pitch, and yaw rates)
$\delta_A, \delta_R, \delta_E$	Aileron, rudder, and elevator control surface deflections.
$\overline{V}, \alpha, \beta$	Airspeed magnitude, angle of attack, and sideslip angle
N, E, D	Coordinates of inertial position vector (north, east, and down position)
ϕ, θ, ψ	Euler 3-2-1 attitude parameters of body-axis system with respect to inertial-axis system (roll, pitch, and yaw angle)

Aerodynamic and Atmospheric Model

C_X, C_Y, C_Z	Aerodynamic force coefficients along body x-axis, y-axis, and z-axis
C_l, C_m, C_n	Aerodynamic moment coefficients about body x-axis, y-axis, and z-axis
C_L, C_D	Aerodynamic lift coefficient and drag coefficient in wind axes
ρ	Air density
q	Dynamic pressure

Formation Flight Separation Model

ξ	Geometric axial separation, normalised to wingspan.
η	Geometric lateral separation, normalised to wingspan.
$\eta_{I,eff}$	Instantaneous effective lateral separation, normalised to wingspan.
η_{eff}	Effective lateral separation, normalised to wingspan.
ζ	Geometric vertical separation, normalised to wingspan.
$\zeta_{I,eff}$	Instantaneous effective vertical separation, normalised to wingspan.
ζ_{eff}	Effective vertical separation, normalised to wingspan.
τ_D	Time delay between two aircraft

Wind Model

λ, γ	Longitude and latitude
$\Delta N, \Delta E$	Distance travelled in inertial NE-axis
r	Radius of earth
w_a	Vertical wind disturbance velocity

v_a	Lateral wind disturbance velocity

Extremum Seeking

η_c, ζ_c	Lateral and vertical separation commands
$\hat{\eta}, \hat{\zeta}$	Lateral and vertical separation motion updates
a_η, a_ζ	Lateral and vertical dither amplitudes
a_D	Dither amplitude when lateral and vertical amplitudes are selected equal
T_D	Dither period
$\gamma_\eta, \gamma_\zeta$	Lateral and vertical phase lag components
K_η, K_ζ	Lateral and vertical control gains
C	Constant approach rate
Θ_z	Freestream pitch angle due to vertical motion
$\theta_{\omega_\eta}, \theta_{\omega_\zeta}$	Lateral and vertical demodulation outputs
$\theta_O, \theta_E, \theta_D, \theta_I$	Near approach, near escape, disengage, and critical escape pitch angle logic boundaries

Subscripts

B	Body axis
I	Inertial axis
W	Wind axis
S	Stability axis
c	Command
T	Trim
F	Formation
j	Leader aircraft
k	Follower aircraft

Superscripts

A	Aerodynamic
G	Gravitational

T	Thrust
L	Leader aircraft
F	Follower aircraft
g	Guidance axis

Chapter 1

Introduction

For long distance flights across different time zones, several commercial airliners often tend to fly nearly the same routes at nearly the same time. It is thus viable to consider flying these airliners in extended formation, with trailing aircraft saving fuel through a reduction in induced drag. Large airliners used in many commercial, cargo, and military applications have wakes that persist for long distances in cruise [1], and trailing aircraft flown in the generated upwash can benefit from increased lift to reduce thrust. The problem of flying aircraft in close formation has been studied extensively, but presents an unacceptable high risk of collision for most applications involving larger aircraft. Climate change issues have been shaping scientific discourse worldwide and have increased environmental awareness, demanding a "greener" aerospace industry. This, together with the issues of increasing air traffic and fuel prices, has shifted research focus to the application of extended formation flight of commercial airliners, and recent studies predict fuel savings of up to 25% [2, 3]. To achieve these significant fuel savings, the follower aircraft is required to fly deep inside the wake of the leader, presenting a range of difficulties for the pilot. First of all, the aircraft is difficult to control due to the aerodynamic effects of the wake. This requires stabilising aircraft controllers to maintain the follower in formation without saturating any control surfaces. Secondly, the optimal position in the wake corresponding to minimum fuel consumption is uncertain and possibly time-varying during flight, due the effect of static wind, turbulence, and gusts on the wake profile. Lastly, although not explicitly addressed by this study, several concerns exist with regard to the comfort of passengers on board the follower aircraft as well.

Several previous studies [2, 4, 5] have successfully designed and implemented rudimentary extended formation flight control systems to enable multiple aircraft to fly in formation. One particular study by Van Wyk [2] investigated the use of a complementary filter controller, in addition to the formation flight controllers, to utilise differential thrust across the aircraft's port and starboard engines to counter the strong rolling moments experienced during formation flight. This novel implementation enabled the follower aircraft to retain most of its aileron authority for general flight manoeuvres, and allowed stable flight deep inside the leader wake without fear of saturating any control surfaces. The work by Van Wyk, along with several others [6, 7, 8], also investigated the use of an extremum-seeking control system to locate the optimal location in the wake for minimum fuel consumption. The concept of extremum-seeking control is generally applied over a wide variety of applications to locate the extremum of an unknown objective function [9]. The aforementioned studies show that extremum-seeking control proves effective in locating the optimal location for reduced fuel consumption during formation flight. However there are several aspects regarding the application of extremum-seeking to formation flight that are not explicitly addressed by these studies.

Due to the risks that correspond with flying deep in the leader-generated wake, several studies suggest flying the follower in an outer region at the cost of reduced fuel savings [2, 5, 10]. Locating and maintaining this constrained optimal formation separation pose various difficulties, since extremum-seeking control is classically intended for the seeking of clear, well-defined extrema. Since the bandwidth of the fuel flow rate (and thrust dynamics) are too low for the purpose of extremum-seeking control, these studies propose the use of the follower lift or drag as an optimisation objective. However, lift or drag is difficult to measure directly during flight, and some other variable must be used as a proxy in the optimisation objective for the extremum-seeking controller. Another important aspect of extremum-seeking control that is not addressed in literature is the effect of varying the extremum-seeking control parameters, such as dither frequency, dither amplitude, and controller gains, on the seeking performance in formation flight. There are many combinations of feasible controller parameters that ensure convergence, but most studies do not explicitly motivate the selection of these parameters. Although it is difficult to find an optimal combination of parameters, it is important to at least understand the relative effect each parameter has on performance. Classic control schemes utilise a seek rate proportional to the estimated gradient of the objective, which usually results in faster seeking closer to the extremum. This may be undesirable for formation flight applications, since it may result in irregular motion commands to the follower aircraft which may be experienced as uncomfortable or alarming for the pilot and passengers. Finally, most studies only consider the seeking of a static extremum, where the location of the extremum is not time-varying, but remains static at a constant displacement relative to the leader aircraft. Naturally, these studies are only concerned with locating an unknown static extremum through extremum-seeking control, rather than with tracking a moving extremum to maintain the optimal separation for the duration of the flight. However, formation flight in realistic flight conditions will be subjected to external wind disturbances, that tend to displace the wake from its undisturbed location behind the leader. As the wind conditions change over the course of the flight, the displacement of the wake will vary over time. This introduces the more challenging task of tracking a dynamic extremum to ensure optimal formation separation, which is a topic that has not thoroughly been addressed in literature.

The primary contribution of this thesis lies in the detailed design, implementation, and verification of an extremum-seeking controller that allows for the locating and tracking of a dynamic constrained extremum in realistic flight conditions. A novel constrained objective function is proposed, where the extremum is represented by a constrained extremum contour instead of a single point. Near-optimal drag-reduction and fuel consumption is achieved by ensuring the follower aircraft remains close to a constrained extremum when the wake is displaced by static winds, atmospheric turbulence and gusts. A novel extremum-seeking state machine is proposed that controls the different modes of operation that the follower aircraft transitions through as it approaches the constrained optimum location in the leader's wake. The extremum-seeking states and the extremum-seeking state transition boundaries are defined as functions of the objective function, and not as functions of the geometric separation between the leader aircraft and the follower aircraft (as in a previous study by Van Wyk [2]). A novel extremum seeking approach method is presented that uses a constant approach rate that is independent of the magnitude of the objective function gradient, instead of using an approach rate that is proportional to the magnitude of the wake gradient. Additionally, the effect of the controller and dither parameters on the seeking performance is investigated, and based on the results a systematic procedure for selecting the parameters is proposed.

1.1 Research Goal

The goal of this research project is to design, implement, and verify a constrained extremum-seeking controller for formation flight of passenger airliners that controls the follower aircraft to locate and track the constrained optimal location in the leader aircraft's wake that minimises the follower's fuel consumption, while still maintaining a safe separation distance from the leader's trailing vortex. Since the trailing vortex may be displaced by time-varying external wind disturbances, the extremum-seeking controller must be able to track a moving constrained optimal location.

The extremum-seeking controller must be verified in simulation with two commercial passenger aircraft flying in right echelon formation. The flight control systems that control both aircraft should be representative of the fly-by-wire flight control systems that are typically used on modern commercial passenger aircraft.

1.2 Reseach Objectives

The research objectives of this study are outlined as follows:

1. Gain an understanding of the driving mechanics behind formation flight, commercial fly-by-wire flight control laws, and extremum-seeking control.
2. Develop a full non-linear formation flight simulation model, which includes modelling the aircraft dynamics, designing the flight controllers for both the leader and the follower aircraft, and designing the formation flight controllers for the follower aircraft.
3. Design and implement an extremum-seeking controller capable of seeking a dynamic constrained extremum in formation flight.
4. Investigate the effect of varying the extremum-seeking parameters on the seeking performance, providing insight to guide the selection of the parameters.
5. Evaluate the robustness of the extremum-seeking controller to representative wind disturbances and sensors noise.

1.3 Project Overview and Methodology

The project was executed in four distinct phases.

Phase I – Development of the Isolated Aircraft Model

During the first phase of the project the flight mechanics model of the aircraft in isolated flight was developed and verified in simulation. A literature study was performed on aircraft dynamics and modelling, and on the conventional fly-by-wire flight control architecture used on modern commercial airliners. The aircraft model was created using a six-degrees-of-freedom equations of motion model with force and moment models specific to the aircraft, which include a thrust model, a gravitational model, and an aerodynamic model. A simulation model of the aircraft dynamics was then developed in Matlab Simulink. Once the aircraft model was established, the conventional fly-by-wire flight controllers were designed using a linearised aircraft model, and were verified in simulation using the full non-linear simulation model. In order to ensure that the flight control system is representative of what is expected on modern aircraft, an Airbus A330 fly-by-wire control architecture is used under a research collaboration agreement with the Airbus company.

Phase II – Development of the Extended Formation Flight Aircraft Model

Once the isolated aircraft model had been implemented, a formation flight model was developed that includes the aerodynamic effects caused by a leading aircraft's wake. A literature review was performed on wake effects and the existing conventional flight control system was modified to include formation guidance controllers that control the axial, lateral, and vertical separation between the leader and the follower aircraft. The complementary filter system developed by Van Wyk [2] was integrated into the flight control system and the extended formation flight controllers were verified in a two-aircraft formation flight simulation.

Phase III – Development of the Extremum-Seeking Control System

During the third phase of the project, an extremum-seeking controller was designed and verified in simulation. A literature review was performed on extremum seeking and the application thereof to formation flight. A new extremum-seeking scheme was proposed and the different components of the system were designed in detail. The extremum-seeking controller was implemented in simulation and its ability to locate a static constrained extremum was verified. Simulation experiments were performed to investigate the effects of varying the extremum-seeking controller parameters on the seeking performance. Finally, the extremum-seeking controller was modified to enable tracking of a dynamic constrained extremum, and was verified in simulation.

Phase IV – Robustness of Extremum-Seeking Control to Wind Disturbances and Sensor Noise

During the final phase of the project, the robustness of the extremum-seeking controller to random wind disturbances, such as turbulence and gusts, and to realistic sensor noise was verified. Simulations were performed where the follower was tasked with locating and maintaining the optimal constrained formation separation in changing static wind conditions, with no turbulence, light turbulence, and moderate turbulence. Finally, a simulation was performed to verify the robustness of the extremum-seeking controller to representative sensor noise on the follower aircraft's pitch angle estimate.

1.4 Thesis Outline

The rest of the thesis report is organised as follows:

- Chapter 2 presents the relevant literature on formation flight and extremum-seeking control. The presented literature provides valuable insight into the dynamics of formation flight, as well as the operation of extremum-seeking control and its application to formation flight. (Phase I and II)
- Chapter 3 presents the mathematical models required to describe and develop both the isolated and formation-extended aircraft models. The extended twin-engine model is described as well as the atmospheric effects expected during flight. The linearisation of the isolated aircraft model about a specified trim condition is presented. An analysis of the aircraft's linear dynamics and response to control inputs provide insight on the aircraft's natural modes of motion.(Phase I and II)
- Chapter 4 presents the complete flight control system design for an aircraft in formation, which consists of the conventional flight control for an aircraft in isolated flight, as

well as extended controllers specifically designed for extended formation flight. The controllers are implemented, tested and evaluated on a Matlab Simulink simulation model of a Boeing 747 aircraft, developed in Chapter 3. (Phase I)

- Chapter 5 presents the design, implementation, and verification of an extremum-seeking control system that enables a follower aircraft to locate and maintain the constrained optimal formation separation for reduced fuel consumption. (Phase III)
- Chapter 6 verifies the robustness of the extremum-seeking controller to random wind disturbances, such as turbulence and gusts, and to realistic sensor noise. (Phase IV)
- Chapter 7 presents the conclusions of the research project, and the recommendations for future work.

Chapter 2

Literature Review

The concept of saving on fuel through formation flight of commercial airliners has been extensively researched in previous studies. In order to gain a good understanding of the underlying concepts, an in-depth review of existing literature was performed before attempting to address the objectives set by this study. This chapter presents a brief overview of the most important concepts regarding formation flight and extremum-seeking.

Firstly, the concept of saving fuel through drag reduction in extended formation flight is presented. A follower aircraft can benefit greatly from flying in the wake generated by a leader aircraft, but not without certain challenges. Secondly, the concept of extremum-seeking and its application to optimal formation flight is presented. Lastly, a brief overview is given of the previous formation flight research performed in collaboration by the University of Stellenbosch, the University of Cape Town, and the Airbus company, that naturally led to the work addressed by this study.

2.1 Saving Fuel through Extended Formation Flight

It is well known that by flying in the upwash region of the wake generated by the leading aircraft, the lift experienced by a trailing aircraft can be significantly increased [1, 2, 3, 4, 5, 11]. This corresponds directly to a reduction in induced drag and thus a reduction in the thrust required to maintain a desired airspeed. This reduction in thrust translates to reduced fuel consumption, with reported savings between 20 and 30%. The concept has been extensively studied in literature and only a brief overview of the important concepts required for this project is presented here. This section presents the basic concept of formation flight and defines the optimal location in the wake for maximum drag reduction.

2.1.1 Generation of Wingtip Vortices

A difference in pressure between the bottom and top surfaces of the wing of a fixed-wing aircraft, produces a span-wise flow below the wing, from the fuselage to the wingtip, and above the wing, from the wingtip back to the fuselage. The difference in direction of air flow at the trailing edge of the wing produces a free shear layer, or vortex sheet, that rolls up into two counter-rotating wingtip vortices [12]. The roll-up process is shown in Figure 2.1, and may be considered complete within roughly 10 wingspans downstream of the aircraft.

The wake generated by an aircraft may be divided into three distinct regions, as shown in Figure 2.2. The first region is called the *near-field* wake, and extends from the trailing edge of the aircraft wing to roughly 10 wingspans downstream. It is in this region that the vortex roll-up process occurs. The next region, from 10 to 100 wingspans, is called the *far-field* wake,

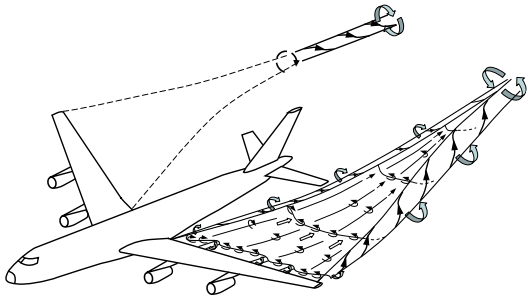

Figure 2.1: Wake vortex roll-up process (reproduced from [12]).

and the wingtip vortices do not undergo much change as they propagate through space. The longevity of the far-field wake, however, is greatly influenced by atmospheric turbulence and stratification[1]. The final region is called the *decay* region, since the vortices rapidly die away once they pass beyond the far-field wake [10, 12].

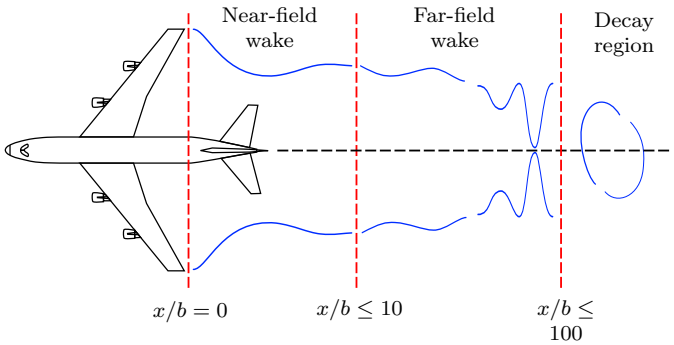

Figure 2.2: Stages of wake vortex lifespan.

Figure 2.3 shows a cross-section of the aircraft wake in the far-field wake. Directly behind the aircraft, a region of downwash is created by the circulating vortices. Similarly two regions of upwash are created on the outer sides of the trailing wake.

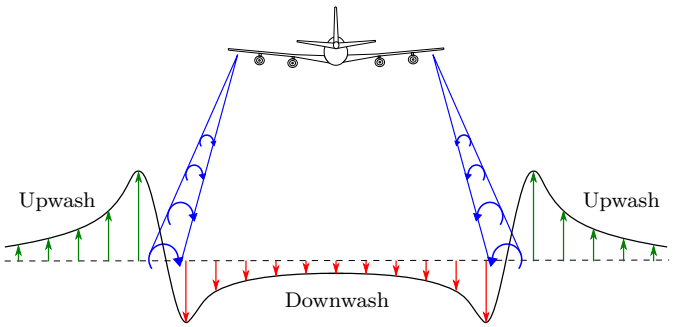

Figure 2.3: Upwash and downwash induced by wingtip vortices (reproduced from [2]).

[1]The earth's atmosphere is composed of a number of layers, and is thus said to be stratified, with each layer known as a *strata*. Atmospheric pressure decreases with altitude, but temperature increases or decreases with altitude depending on the strata and atmospheric conditions.

2.1.2 Drag Reduction of Follower Aircraft

The drag experienced by a follower aircraft may be significantly reduced by flying in the upwash region of the leader aircraft's wake. This reduction in drag is attained through a rotation of the follower's lift vector [3, 13, 14], which is shown in Figure 2.4. When in formation, the freestream lift and drag vectors, denoted by L and D respectively, are rotated through the change in angle of attack $\Delta\alpha$ induced by the upwash effect of the trailing vortices. The rotated lift and drag vectors are represented by L' and D' respectively. The change in drag due to the rotation in lift force is denoted by ΔD, while, similarly, the change in lift due to the rotation in drag is denoted by ΔL. It is assumed that the change in angle of attack is sufficiently small as to allow for accurate small-angle approximations. Since drag tends to be orders of magnitude less than lift, it is influenced significantly more by the rotation effect. A small change in angle of attack will thus result in a substantial reduction in drag, while simultaneously causing an insignificant increase in lift [3].

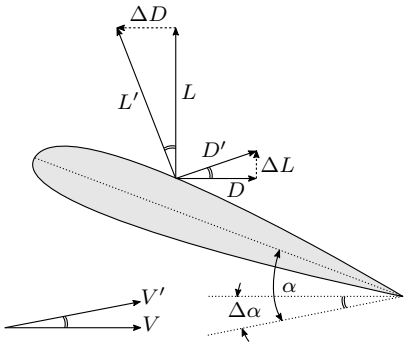

Figure 2.4: Rotation of lift and drag vectors due to wake upwash (reproduced from [3]).

During a practical flight, the pilot will be required to adjust the pitch and thrust of the aircraft in order to maintain steady flight. The reduction in drag means that less thrust is required to maintain a desired airspeed, which introduces the opportunity to lower fuel consumption. The rotation in airspeed velocity vector, from V to V', makes the follower appear to be in a descent with respect to the incoming air, and the reduction in thrust ensures that the desired altitude is maintained. Finally, the increase in lift requires that the nose of the aircraft be pitched forward to maintain the desired flight path.

During extended formation flight, the follower aircraft is positioned downstream from the leader within the far-field wake. The position of the follower aircraft relative to the leader aircraft is described by means of formation separation variables in the longitudinal, vertical and lateral directions. These formation separations are usually normalised to the aircraft wingspan, and the aerodynamic effects of the leader wake on the follower are dependant on the formation separation [13]. Since the decay of the trailing vortices is negligible between ten and forty wingspans [11], the far-field wake is considered to be constant with regards to the longitudinal separation. The same is, however, not true of the lateral and vertical separation, which significant affects the aerodynamic effects induced on the follower.

Figure 2.5 shows the wake-induced drag, ΔC_{D_F}, and wake-induced lift, ΔC_{L_F}, for a Boeing 747 aircraft wake model, which was developed by Bizinos [10]. The wake-induced aerodynamic coefficients are given as functions of the aircraft wingspan, where a separation of $\eta = 0, \zeta = 0$ corresponds to the follower flying directly behind the leader. Changes in lateral and vertical separation both significantly affect the additional lift and drag experienced by the follower, with a clear, global extremum at a lateral separation of approximately $\eta = 0.78$, and

a vertical separation of $\zeta = 0$. Flying at the extremum, the wake induced-drag is minimised, and the follower will experience a maximum reduction in required thrust. Note that if the follower flies too deep into the wake, the induced lift becomes negative, indicating that the follower is in the downwash region of the wake.

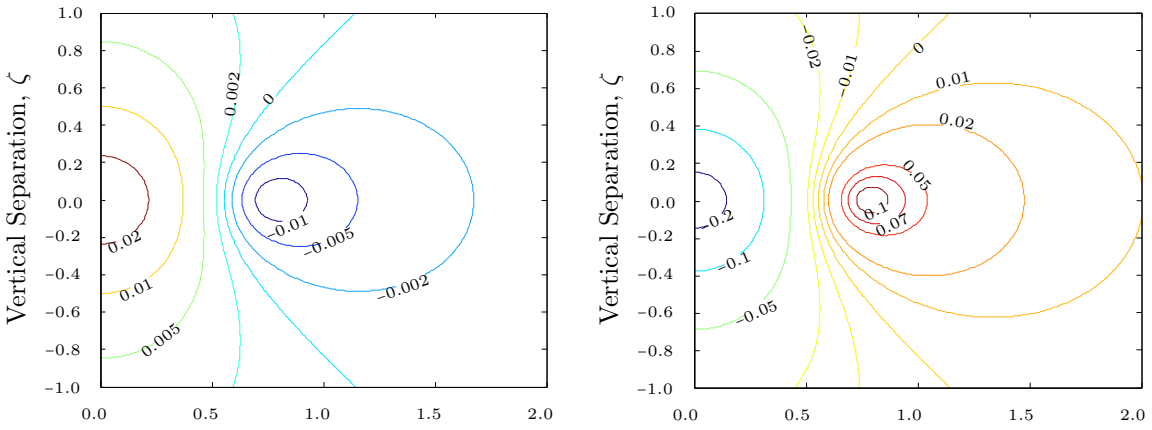

(a) Formation induced drag ΔC_{D_F}. (b) Formation induced lift ΔC_{L_F}.

Figure 2.5: Contours of (a) induced drag and (b) lift on follower due to leader wake.

2.1.3 Challenges of Formation Flight

Besides the wake-induced effects on lift and drag, flying in formation also introduces additional side-force and moments on the follower aircraft. The most challenging of these additional effects is the wake-induced rolling moment, which is caused by the non-linear lift profile on the follower aircraft, as shown in Figure 2.6. The rolling moment, which is opposite to that of the vortex rotation, tends to roll the follower out of the wake to a less beneficial formation separation. In order to maintain station within the leader wake, the follower aircraft requires high aileron deflections to counter this rolling moment. Since the ailerons are also required for general aircraft movement and disturbance rejection, allocating such considerable deflections to station-keeping poses a significant problem. A study by Van Wyk [2] explored the possibility of using differential thrust and rudder deflection, instead of aileron deflection, to produce the necessary counter rolling moment.

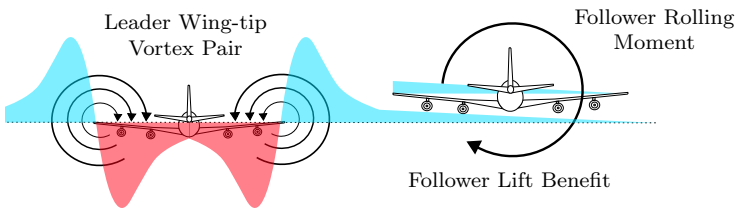

Figure 2.6: Rolling moment induced on follower through formation flight (reproduced from [2]).

A contour plot of the wake-induced rolling moment for the B747 wake model is shown

in Figure 2.7. Two extrema may be identified from the plot: a minimum at a formation separation of approximately $\eta = 0.4$ and $\zeta = 0$, and a maximum at $\eta = 0.78$ and $\zeta = 0$. Since the wake is typically approached from a positive lateral separation, the maximum wake-induced rolling moment is of greater concern than the minimum. Note that the maximum wake-induced rolling moment is located at the same formation separation as the minimum wake-induced drag. This means that, in order for the follower to benefit from maximum reduction in thrust, it will have to counter the maximum wake-induced rolling moment.

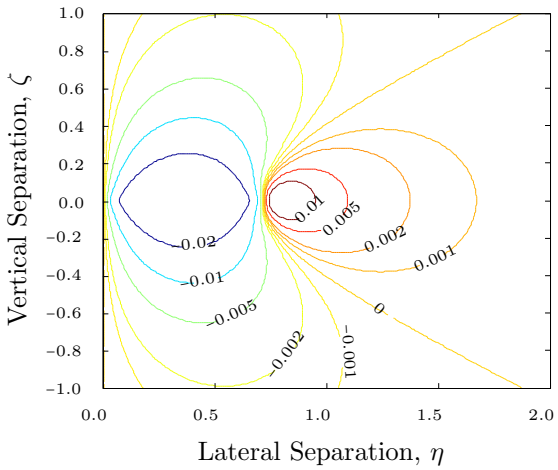

Figure 2.7: Contour of induced rolling moment on follower due to leader wake.

2.2 Optimal Extended Formation Flight

As mentioned in the previous sections, there exists a clear location in the leader's wake where the increase in the follower's lift and reduction in the follower's drag is maximized. If the follower aircraft flies at this "sweet-spot", less thrust is required to maintain equilibrium, and lower fuel consumption is achieved. Although the position of the sweet-spot may easily be determined theoretically, the significant longitudinal separation between aircraft in formation indirectly introduces uncertainty in its exact position relative to the formation. Atmospheric turbulence and static wind shift the relative position of the trailing vortices generated by the leader aircraft, and the wake position cannot not be accurately estimated based on the relative aircraft positions alone. Even by neglecting the effect of these external disturbances, the exact position of the sweet-spot is also determined by the shape and size of the aircraft generating the wake [15].

Many studies have recognised the necessity of optimal formation flight, and, since the location of the sweet-spot is not explicitly known during flight, have investigated and proposed various wake sensing techniques in order to 'estimate' the wake location. These techniques will be discussed in more detail in Section 2.2.1. Most of these techniques are, however, impractical for actual flight, being either too expensive or unable to perform wake-estimation in real-time. Due to the significant aerodynamic interaction between the wake and the follower aircraft, flying at the sweet-spot presents a daunting task for pilots, and it is generally suggested to automate the process of locating the sweet-spot and maintaining station deep within the wake [14]. A method known as extremum seeking has been extensively researched as a method for locating extrema in a wide variety of applications, including formation flight.

This section mainly provides an overview of extremum-seeking control, both in general and as specifically applied to formation flight. Research performed in previous studies are

briefly presented, highlighting some of the important contributions to optimal formation flight, as well as opportunities for future research.

2.2.1 Current Wake Sensing Techniques

In order to fly at the sweet-spot of the generated wake, it is necessary to actually know the location and shape of the wake. The sensing and detection of wake vortices is not a new concept and much research and technology development has focused on detecting wake-hazards in airspace and on airport runways. However, most of these wake-detecting tools utilize heavy, expensive and complex instrumentation, primarily designed for ground use. Methods such as lidar, radar, and sodar (sonic detection and ranging) arrays have all been investigated and configured as a means of aircraft wake-hazard detection, but cannot be implemented physically on-board aircraft [16, 17, 18, 19, 20]. Systems such as airborne lidar, fit for in-flight use, remain impractical for commercial use due to their excessive cost and weight.

Other more practical methods include the characterization of wakes through use of pressure probes distributed about the trailing aircraft [16, 21, 22]. Data assimilated by these sensors are analysed post-flight, and are used to reconstruct the estimated wake. Although the cited studies do not implement this method for wake sensing in real time, they do introduce possible practical instrumentation configurations for real-time wake detection.

An alternative solution to the wake-sensing problem, or more specifically the seeking of the sweet-spot location, is the implementation of extremum or peak-seeking control [14, 23]. This method does not require prior knowledge of the wake, but rather detects the optimal location in the wake based on the minimization of some cost function. The method of peak-seeking is discussed in more detail in the following sections.

2.2.2 Extremum Seeking Control

Extremum-seeking control (ESC), also known as peak-seeking control, is a form of real-time adaptive control that seeks to optimize a steady-state input-output characteristic for dynamic problems where only limited system information is available. The only required knowledge is that the characteristic, usually non-linear, does indeed exist and that it has some optimal value at some set point. This point is considered an extremum of the characteristic and can be either a maximum or minimum. The objective of the extremum-seeking controller is to maintain the output at this extremum value by keeping the system input close to the identified set point [8, 24].

An illustration of the concept is shown in Figure 2.8, where a basic system is described with a well defined steady-state characteristic: for every constant input u there exists a constant output y_p. The addition of system disturbances, denoted by d, is ignored for the moment. The steady-state map, seen on the right hand side of the figure, is expressed as $y_p = f(u, p)$ and exhibits a clear extremum of value $y^*(p) = f(u^*(p), p)$ at set point $u = u^*(p)$. The inclusion of parameter p denotes that the steady state map may be influenced by other parameters besides the input u. An extremum-seeking controller may be implemented to find and maintain the set point $u^*(p)$ so that the output remains at the extremum $y^*(p)$. The critical advantage of the controller is that it can achieve these objectives without requiring any explicit knowledge about the system, its characteristic map f, or the parameter p. The initial value of u is not even required to be near the extremum set point u^*[9].

The concept of extremum-seeking control dates back as far as the 1920's when it appeared as the first method of "adaptive control", and development intensely ensued in the 1940's. In the 1960's, extremum seeking branched into two directions. On the one hand, the emergence

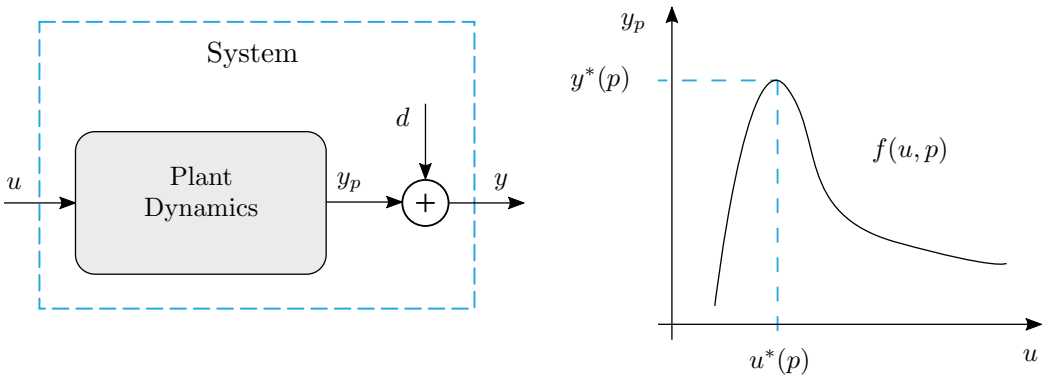

Figure 2.8: System steady-state input-output characteristic with clear extremum.

of computers steered the effort on real-time optimization toward general-purpose algorithms, and on the other, a distinction between stabilization and optimization objectives for adaptive control became clear, that led to model reference adaptive control methods that were more easily tractable to be solved with simpler Lyapunov tools. This resulted in the research on extremum seeking becoming dormant for approximately 30 years. It was not until the late 1990's, when proof of its stability emerged, that an interest in extremum seeking once again resurged [8]. The first rigorous assessment of the stability of a classic extremum seeking feedback scheme was published in 2000 by Wang and Krstic [25, 26], sparking a new interest in its theory and application to modern control problems.

Since extremum seeking is at its core a gradient based optimization method, it inherits all the shortcomings of such methods. In the presence of local extrema, a global extremum will not be found without exploring many different initializations. Modifications dealing with local extrema and passage through local extrema using ideas from simulated annealing have been explored, but much work remains to be done [9].

Several variations on extremum-seeking control exist in both the discrete and analogue domains. The discrete or stochastic methods will not be discussed here since they are not feasible methods for aircraft control. The position of the aircraft cannot be discretely moved to explore the non-linear steady-state map, and thus requires continuous movement corresponding to analogue methods of extremum-seeking control. Several variations are presented in the following section as well as a detailed discussion on the preferred scheme for this study.

Variations on Extremum Seeking Methods

As mentioned above, extremum seeking can be either discrete or continuous. Discrete extremum seeking uses a stochastic sequence of probing inputs that exploit the idea and recipes from numerical optimization methods. Continuous extremum seeking uses a deterministic or continuous excitation input to explore the steady-state map, from which an implicit gradient can be obtained. As mentioned, the discrete methods are not feasible for aircraft control and thus only variations on continuous extremum seeking will be discussed. Continuous extremum seeking control algorithms can be categorized into five groups [27]:

- Sliding mode ESC
- Neural network ESC
- Approximation-based ESC

- Adaptive ESC
- Perturbation-based ESC

In the work of Calli et al. [27], these different methods are compared in terms of their robustness to noise and system dynamics. In the absence of noise and system dynamics, it was found that the performance of the sliding mode, neural network and approximation-based methods were much better than that of the perturbation-based method. The distance travelled by the perturbation method results in significantly larger rise times and settling times. However, when noise and system dynamics are added, the perturbation-based method proves to be the most robust, producing consistent results. Smooth references are created for the plant even under severe noise. Taking into account that the algorithm must be applied in the wake of an aircraft subjected to external disturbances, perturbation-based extremum seeking seems to be the logical choice due to its robustness. The generation of smooth control references are desired for aircraft motion, as well as the extension of the algorithm to a multivariate case, since the objective function will be seen to span over two dimensional space.

Perturbation-Based Extremum-Seeking Control

Perturbation-based extremum seeking involves the induction of a 'slow' periodic dither signal superimposed on the control inputs to the plant. This superposition allows for the exploration of the steady-state map and thus enables the controller to 'sense' the gradient of the optimization objective as the inputs change. The controller then steers the states of the system plant towards the extremum. A basic perturbation based scheme, derived from the work of Krstić by Binetti [6, 28], is shown in Figure 2.9.

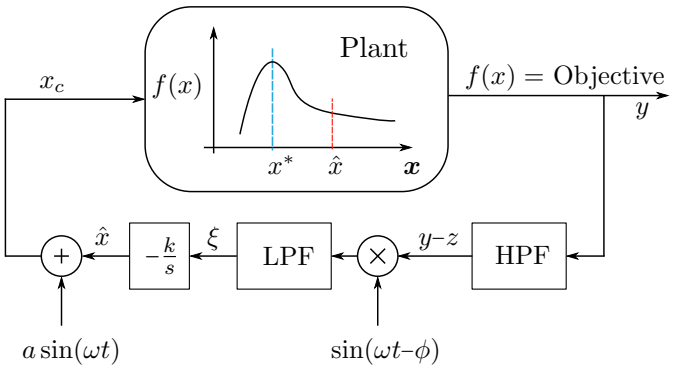

Figure 2.9: Perturbation based ESC scheme as proposed by Krstić [26].

Three time scales can be identified in the suggested scheme: (1) the plant dynamics, (2) the perturbation or dither signal, and (3) the learning dynamics of the integrator in the controller. The integrator dynamics are the slowest, and the dither signal, since it must fall within the system bandwidth, is slower than the plant dynamics but much faster than the integrator dynamics.

A perturbation signal $a\sin(\omega t)$ is superimposed on the current setpoint $\hat{x}$ to produce the new plant input x_c. The extremum-seeking controller then gives the best estimate $f(\hat{x}_c)$ at the setpoint $\hat{x}_c$ of the extremum $f(x^*)$. Since the perturbation frequency is set to be slower than the plant dynamics, the plant behaves as a static map and its dynamics do not affect the operation and performance of the extremum-seeking controller. If a deviation exists between

the estimated setpoint $\hat{x}$ and the optimal setpoint x^*, the periodic result y produced by the plant will either be in phase or out of phase with the dither signal. This phase difference depends on whether the deviation is positive or negative and whether the extremum being sought is a maximum or minimum. The high-pass filter removes the 'DC component' in the output signal, which roughly yields a zero mean sinusoidal response at the dither signal frequency ω with some phase lag ϕ relative to the dither signal. Demodulation with the phase-corrected dither signal produces a signal with a DC component as well as higher frequency components. Passing this signal through a low-pass filter eliminates the higher frequency components and produces a DC signal, either positive or negative, that is used used as the control reference to converge the system states towards the extremum setpoint x^*.

Krstić and Wang [26] state that the above scheme is stable under the following three assumptions:

1. The gradient map of the plant is continuous for the specified range of inputs.
2. The plant is stable and converges for the entire range of control inputs.
3. There exists an extremum $f(x^*)$ at some optimal setpoint x^* that persists and remains stable under minor dynamic perturbations.

and posit the plant $f(x)$ to be of the form:

$$f(x) = f^* + \frac{f''}{2}(x - x^*)^2 \tag{2.1}$$

where f'' is either greater or smaller than zero for all x. If $f'' > 0 \ \forall x$, $f(x)$ is convex with a global minima, and if $f'' < 0 \ \forall x$, $f(x)$ is convex with a global maxima. The function $f(x)$ is considered to only possess a global extremum, though work has been done on finding global extrema in the presence of local extrema [29, 30]. The setpoint error dynamics is then derived by Krstić (full derivation can be found in [8]) as,

$$\dot{\tilde{x}} \approx -\frac{kaf''}{2}\tilde{x} \tag{2.2}$$

where the setpoint error $\tilde{x}$ is defined as,

$$\tilde{x} = x^* - \hat{x} \tag{2.3}$$

Equation 2.2 represents the control law of the extremum-seeking controller, adjusting the setpoint proportional to the error. Two cases of extremum seeking exist: (1) the convergence to a maxima and (2) the convergence to a minima. For convergence, and thus stability, it is required that $kf'' > 0 \ \forall x$. If $f'' < 0$, and thus convergence to a maxima is desired, the control gain k is required to be negative in order to steer $\hat{x}$ towards the maxima. On the other hand, if $f'' > 0$, and thus convergence to a minima is desired, the control gain k is required to be positive in order to steer $\hat{x}$ towards the minima.

Multi-dimensional Extremum Seeking

The extremum-seeking scheme presented in Figure 2.9 may be extended to objective functions with multiple dimensions [31], which requires dithering in each respective dimension. Since

only one output is available for the estimation of multiple gradients, a separation of the dither signals is necessary, either by frequency or by phase.

When separating the dither signals by frequency, the overall speed of convergence of the algorithm is lowered. Only one of the dither signal loops will be able to operate at the maximum frequency, which is determined by the slowest dynamics of the plant. The other dither signals are required to have lower frequencies, and the speed of the algorithm will be determined by the lowest among them [32]. Additionally, separating dither signals by frequency requires very accurate filters to differentiate between the effects in the objective function caused by each dither signal. If the filtering is inaccurate, the objective output corresponding to one dither signal will contain changes induced by one or several other dither signals.

Dither signals may also be separated by phase while operating at the same frequency. This allows the convergence speed of the system to be determined by the maximum possible frequency, contrary to the case of separation by frequency. However, separating dither signals by phase limits extremum-seeking to only two dimensions, since only two signals can ever be separated by phase. Apart from 90°, no other phase exists that allows for an explicit separation. On the contrary, separation by frequency allows for extremum-seeking in unlimited dimensions. Separating dither signals by phase has the disadvantage of being very sensitive to the dynamics of the plant, which typically introduce phase lag between plant inputs and outputs. Any phase lag in the objective function relative to the dither input signals will result in inaccurate gradient estimation.

2.2.3 Research on the Application of ESC to Formation Flight

The concept of formation flight of large transport aircraft has been a topic of interest since the early 1900's, stemming from the observations of natural formations of migratory birds [33]. The prospect of significant fuel savings over transatlantic flights have spurred many scientists and engineers to characterise and model the possible drag reduction follower aircraft might benefit from during formation flight. Even though it has long been accepted that some optimal formation configuration exists, it was only in the late 1990's that the application of extremum-seeking control to optimal formation flight received much attention in literature.

Hummel, who dedicated much research to the concept of formation flight as applied to birds [33, 34], was one of the first to recognise the use of extremum-seeking as a means to locate and maintain the optimal formation separation relating to maximum reduction in drag [14]. Hummel stated that by dithering at the optimal, the follower experiences a loss in power reduction, compared to the theoretical stationary flight typically considered. Two separate cost criterion were used to evaluate the reduction in thrust attained through changes in vertical and lateral formation separations. The reduction in thrust due to vertical position was determined by the upwash measured in the symmetry plane of the trailing airliner, while changes due to lateral position was evaluated through aileron deflection. Hummel found that the extremum-seeking controller successfully enabled the follower aircraft to locate the optimal formation separation, with power reductions of up to 10%.

In the work of Chicka et al. [23, 35], the extremum-seeking controller implemented by Hummel is augmented by replacing the classical filter combination with a modified Kalman filter. The filter is used in combination with an estimator to estimate the slope of the wake-induced lift experienced by the trailing aircraft. These gradient estimates are then used in conjunction with the sign of the gradient, to steer the follower aircraft to the optimal separation. Chicka et al. argue that by using the Kalman filter for gradient estimation, the controller should be more robust to system noise. It is important to note that the work done by Chicka et al. applies to a simplified, linear aircraft model, including only the dominant

non-linear terms caused by the wake interaction. Furthermore, the wake-induced lift is used as the function to be optimised, a parameter that is very difficult to physically measure.

A study by Binetti et al. [6] addresses some of the shortcomings identified in the work of Hummel and Chicka, by supplying a general design procedure with an easily measurable objective for extremum-seeking control. Binetti proceeds to use the wake-induced pitch angle of the follower aircraft as a proxy for the reduction in thrust attained through formation flight, modelling the freestream pitch angle of the follower through a simple linear model. The design procedure is applied to a formation of Lockheed C-5 aircraft in close formation flight, and is the first study to attain stable extremum seeking for a plant with non-linear feedback.

Similar to the work of Chicka et al., a study by Brodecki et al. implements an extended Kalman filter for gradient estimation in turbulent conditions [7]. Determining the position of the follower in the kinematic reference frame of the leader was found to be communicationally intensive, and an alternative formation setup was investigated that required only the inertial velocity of leader to be transmitted to the follower. Simulations of two F-16 aircraft in formation have shown the algorithm to be robust to errors induced by turbulence, and the controller was consistently able to locate the sweet-spot in the wake.

In the work of Xie et al. [36], a hierarchical control system is presented that allows a team of UAVs to navigate in a close formation simulation. While the lower-layer consists of off-the-shelf autopilots, at the higher-layer, two non-linear robust formation control algorithms are developed and integrated with an extremum-seeking controller. The first controller requires knowledge of the leader's velocity and acceleration, while the second controller does not. The control system allows a team of UAVs with limited inter-vehicle communication to perform complex navigation tasks at maximum energy efficiency.

2.3 Previous Formation Flight Research at Stellenbosch University

The research conducted on formation flight at the University of Stellenbosch forms part of a research collaboration with the University of Cape Town and the Airbus company. The formation flight of commercial airliners has been the topic of research for several previous studies performed under this collaboration, and this section aims to provide a brief overview of the research conducted thus far. The first study was performed at the University of Cape Town, while the following three were performed at the University of Stellenbosch.

A study by Bizinos et al. [10] investigated the passenger comfort levels experienced on board a follower aircraft during formation flight within atmospheric turbulence. One of the major contributions was the development of a simple aerodynamic wake-interaction model for a Boeing 747 aircraft, that is used to calculate the forces and moments induced on a follower flying in the wake of a leader. Bizinos found that passengers would experience only a slight increase in discomfort when flying at a lateral separation of one wingspan, as opposed to the significant increase in discomfort experienced when flying at the optimal lateral separation. Additionally, simulations showed that seating at the back of the follower aircraft tends to be more comfortable than seating at the front, which is the opposite of what is expected in the trend for typical isolated flight.

In the work of Büchner [5], the stability and performance of formation flight was investigated using the wake-interaction model developed by Bizinos. A trim analysis revealed two feasible trim regions for the follower aircraft: a potentially dangerous region which is sandwiched between two untrimmable regions with respect to maximum aileron deflection, and a less risky outer region which offers less fuel savings. A state-space representation was constructed and a linear analysis showed that the flight dynamics are more sensitive to changes

in vertical separation than to changes in lateral separation. Finally, Büchner developed an automatic flight control system for formation flight based on the results of the trim and linear analyses.

Extending the work of Bizinos and Büchner, a study by Trollip [4] investigated the ride comfort during formation flight using conventional flight controllers. Trollip performed full non-linear simulations with realistic turbulence to verify the correct operation of the extended flight controllers, and found that formation-hold performance degrades very quickly with increasing levels of turbulence. Regarding ride comfort, it was found, contrary to the results of Bizinos, that seating in the front of the follower aircraft would be more comfortable. Additionally, seating locations with vertically higher displacements and on the leader aircraft side of the follower aircraft, were found to be most comfortable. A clear increase in discomfort was found when moving from light to moderate turbulence, but levels remained within the *not uncomfortable* region as defined in the ISO 2631-1 standard.

Lastly, a simultaneous study by van Wyk [2] investigated means to increase the flight efficiency of aircraft flying in formation. A higher-order engine model with non-linearities was developed for a Boeing 747 aircraft in order to more accurately model the fuel savings attained through formation flight. A novel complimentary filter control system was designed to reduce aileron demand by inducing sideslip on the follower aircraft to counter the wake-induced rolling moment. It was shown that by applying small rudder or differential thrust settings, the aileron demand could be significantly reduced while effectively regulating formation-hold deep within the wake. Van Wyk also experimented with extremum-seeking control to locate the point of maximum drag reduction. A simple extremum-seeking scheme was developed based on the work of Binetti et al. [6]. In simulation, a mean thrust reduction of 25% was obtained in light turbulence, with the follower at a lateral separation of one wingspan, and a vertical separation of zero.

Chapter 3

Flight Mechanics Modelling

This chapter details the modelling of the aircraft in isolated flight, as well as in extended formation flight. The flight mechanics modelling of the aircraft in isolated flight follows the same approach as Peddle [37, 38, 39] and is reproduced here for clarity and for the convenience of the reader. First the axis systems, aircraft notation and conventions to model an aircraft in isolated flight are established. Next, the six-degrees-of-freedom equations of motion that describe the general translational and rotational motion of a body, and the force and moment models that are specific to an aircraft are developed. The forces and moments acting on the aircraft originate from aerodynamic, engine thrust, and gravity. Next, the linearisation of the aircraft model about an equilibrium point is presented. An analysis of the linear dynamics provides valuable insight on the natural modes of motion of the aircraft. The effects of formation flight are then added to the aircraft models. First, the position of the follower aircraft relative to the leader aircraft is defined as the geometric separation, and the location of the follower aircraft relative to the trailing vortex is defined as the effective separation. The geometric separation is used to maintain the formation, while the effective separation is used to model the aerodynamic effects of the leader's wake on the follower aircraft. The aerodynamic model of the follower aircraft in isolated flight is then augmented to include the wake-induced forces and moments to produce the model of the aircraft in extended formation flight. The external wind disturbances that act on both aircraft and also displace the trailing vortex are also modelled. The static wind model was developed using a dataset of global wind data provided by the Earth System Research Laboratory (ESRL) of the National Oceanic and Atmospheric Administration (NOAA). The atmospheric turbulence model implemented using the standard Von Karman turbulence model. To simplify modelling, aircraft are considered to be rigid bodies and sensors are assumed to be ideal.

3.1 Axis Systems

In order to formulate the aircraft equations of motion and to model the external forces and moments, four axis systems, commonly referred to as the inertial, body, stability and wind axis, are required.

Inertial Axes

The inertial axes is used to describe the aircraft's motion relative to the physical world, which is assumed to be flat and non-rotating. Over the relatively short distances that the aircraft motion is typically observed, the Earth can be approximated as flat. The angular rotation of the Earth is considered to be negligible in comparison to that of the aircraft.

The standard North-East-Down (NED) axis system, common to most aerospace problems, is used and shown in Figure 3.1. The axis system is right-handed, and the origin is selected to coincide with any arbitrary fixed point on the Earth's surface. where the positive Z_I-axis is aligned with the positive Down axis. The positive X_I-axis is directed North and the positive Y_I-axis is directed East.

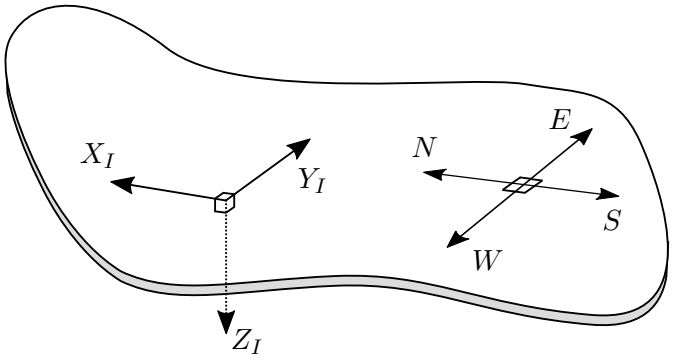

Figure 3.1: Inertial axis system.

Body Axes

The body axes, with origin at the aircraft's center of mass, are orthogonal and fixed to the aircraft as shown in Figure 3.2. The x-axis points along the zero-angle-of-attack line, the y-axis lies perpendicular to the plane of symmetry and points in the direction of the starboard wing, and the z-axis points downwards relative to the fuselage.

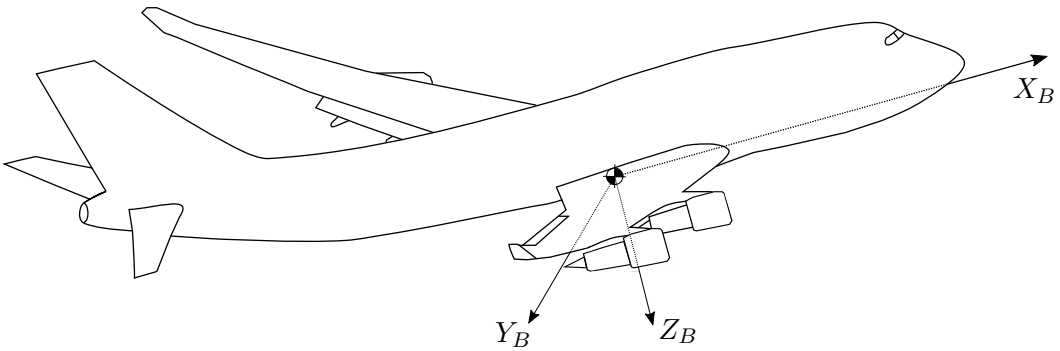

Figure 3.2: Body axis system.

Wind and Stability Axes

The wind axis system describes the orientation of the incoming freestream air relative to the aircraft body. Similar to the body axis system, the origin of the wind axis system coincides with the center of mass of the aircraft, and the wind axis system therefore also moves with the aircraft. However, the x-axis X_W of the wind-axis system points in the direction of the aircraft's airspeed velocity vector (and not in the direction of the aircraft's nose). The z-axis Z_W of the wind axis system lies in the aircraft's plane of symmetry and points downward relative to the fuselage. The y-axis Y_W completes the right hand axis system and points approximately in the direction of the starboard wing. The orientation of the wind axis system relative to the body axis system is defined by two angles, namely the angle of attack α and the sideslip angle β. From the body axis system, the wind axis system is obtained

by first rotating about the y-axis through the angle of attack, and then rotating about the z-axis through the sideslip angle. The stability axis system is a supporting axis system that is obtained by only rotating the body axis system about the y-axis through the angle of attack (and not also rotating about the z-axis through the sideslip angle). The axes orientations are indicated in Figure 3.3.

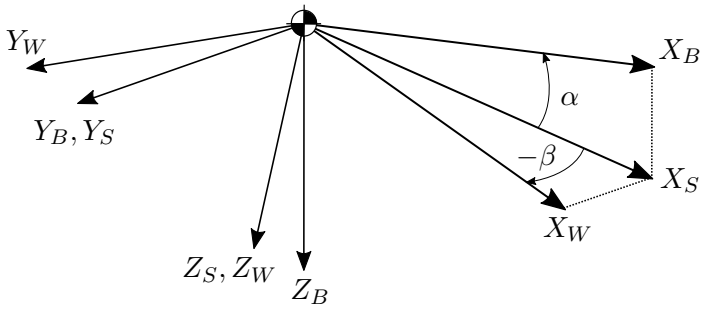

Figure 3.3: Wind and stability axis systems.

3.2 Aircraft Notation

Figure 3.4 illustrates the primary notation and sign conventions used for the Boeing 747-100 aircraft model. The symbols and there definitions are described in Table 3.1. It is important to note that the definition for positive aileron deflection is different to standard convention. For the rudder and elevator, *positive* deflections produce *negative* moments, while for a *positive* aileron deflection, a *positive* moment is produced. This deviation from standard notation is a result of how the aircraft simulation data is presented in sourced literature. The roll Φ, pitch Θ, and yaw Ψ angles represent the orientation of the aircraft body relative to the inertial axes.

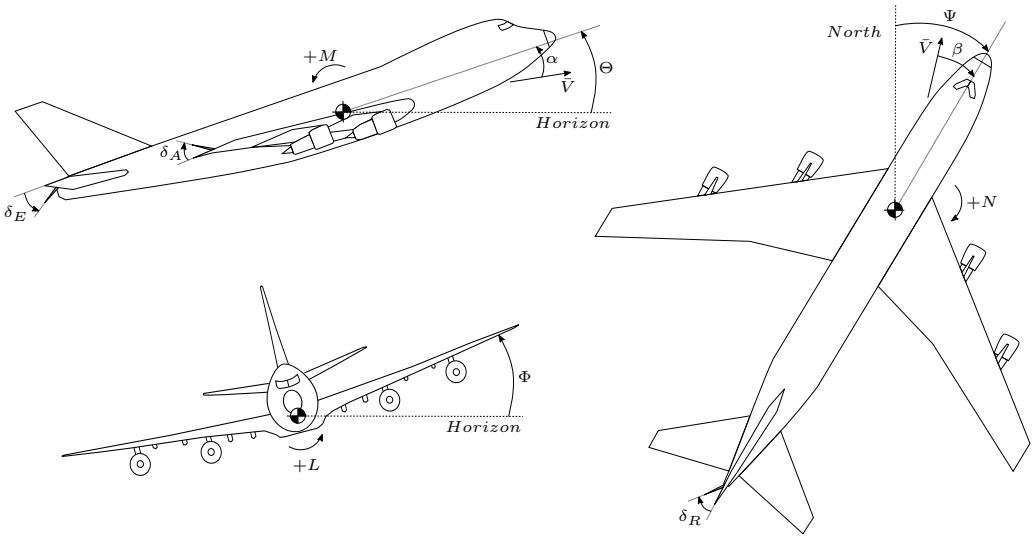

Figure 3.4: Wind and stability axis systems.

Table 3.1: Notation for B747-100.

Symbol	Definition
Inertial Axes	
N, E, D	Coordinates of position vector
Φ, Θ, Ψ	Euler 3-2-1 attitude parameters (roll, pitch, and yaw angle)
Body Axes	
X, Y, Z	Coordinates of the force vector (axial, lateral, and normal force)
L, M, N	Coordinates of the moment vector (roll, pitch, and yaw moment)
U, V, W	Coordinates of the linear velocity vector (axial, lateral, and normal velocity)
P, Q, R	Coordinates of the angular velocity vector (roll, pitch, and yaw rate)
$\delta_A, \delta_R, \delta_E$	Aileron, rudder, and elevator deflections.

The airspeed magnitude $\overline{V}$, angle of attack α, and sideslip angle β are fundamental when calculating the aerodynamic forces and moments acting on the aircraft, and are related to the airspeed velocity vector in the body axes through,

$$\overline{V} = \sqrt{U^2 + V^2 + W^2} \tag{3.1a}$$

$$\alpha = \arctan\left(\frac{W}{U}\right) \tag{3.1b}$$

$$\beta = \arcsin\left(\frac{V}{\overline{V}}\right) \tag{3.1c}$$

with the inverse relationships being,

$$U = \overline{V}\cos\alpha\cos\beta \tag{3.2a}$$

$$V = \overline{V}\sin\beta \tag{3.2b}$$

$$W = \overline{V}\sin\alpha\cos\beta \tag{3.2c}$$

3.3 Six Degrees of Freedom Equations of Motion

The aircraft is modelled as a rigid body with six degrees of freedom, which consist of three translational and three rotational degrees of freedom. Modelling the airframe as a rigid body implies that the position of each mass element on the airframe remains fixed relative to the body axes. The structural flexibility of large aircraft are typically disregarded during the modelling process, since the resulting modes of motion are most often outside the bandwidth conventional aircraft controllers [37]. The equations that describe the aircraft motion is divided into kinetic and kinematic equations, with the relationship as shown in Figure 3.5.

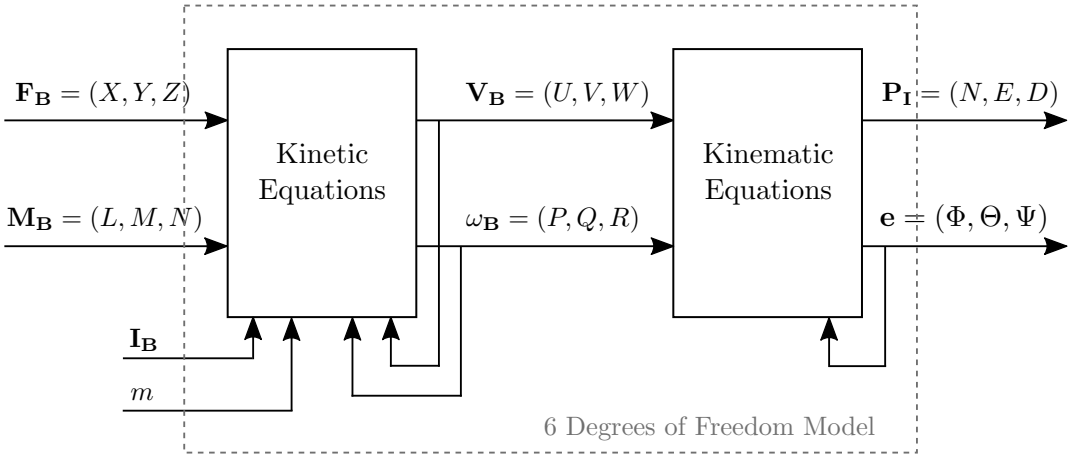

Figure 3.5: Six-degrees-of-freedom equations of motion model (adapted from [37]).

3.3.1 Kinetics

The forces and moments acting on the aircraft are related to the kinematic state of the aircraft, namely its position, velocity and acceleration, through the set of kinetic equations, coordinated in the body axes, given by,

$$\boldsymbol{F} = m\dot{\boldsymbol{V}} + \boldsymbol{\omega} \times m\boldsymbol{V} \tag{3.3a}$$

$$\boldsymbol{M} = \mathbf{I_B}\dot{\boldsymbol{\omega}} + \boldsymbol{\omega} \times \mathbf{I_B}\boldsymbol{\omega} \tag{3.3b}$$

where $\boldsymbol{V}$ and $\boldsymbol{\omega}$ are the aircraft velocity and angular rate vectors, $\mathbf{I_B}$ and m are the moment of inertia matrix and aircraft mass, and $\boldsymbol{F}$ and $\boldsymbol{M}$ are the force and moment vectors acting on the aircraft. The cross-product terms are a result of coordinating the vectors in the body axes and not in the inertial axes. The six differential equations that describe the motion of the aircraft are given by,

$$X = m(\dot{U} - VR + WQ) \tag{3.4a}$$
$$Y = m(\dot{V} - UR + WP) \tag{3.4b}$$
$$Z = m(\dot{W} - UQ + VP) \tag{3.4c}$$
$$L = \dot{P}I_{xx} + QR(I_{zz} - I_{yy}) \tag{3.4d}$$
$$M = \dot{Q}I_{yy} + PR(I_{xx} - I_{zz}) \tag{3.4e}$$
$$N = \dot{R}I_{zz} + PQ(I_{yy} - I_{xx}) \tag{3.4f}$$

where it is assumed that,

- The aircraft is symmetrical about its X_BZ_B-plane. The cross products of inertia I_{xy} and I_{yz} are thus zero, which is a accurate assumption for conventional aircraft [37].
- The mass of the aircraft remains constant. Although there is a considerable difference in the mass of an aircraft with and without fuel, the amount of fuel consumed during the period of the dynamic analysis may be safely neglected [40].

3.3.2 Kinematics

The motion variables of the aircraft, such as position, attitude, linear velocity, and angular rate, are related to one another through the kinematic equations of motion. The position and attitude of the aircraft are given relative to the inertial axis system, as illustrated in Figure 3.1. The position is represented as a vector with north, east, and down coordinates and the attitude by the Euler 3-2-1 parameters Φ, Θ, and Ψ as shown in Figure 3.1.

Attitude Representation

The Euler 3-2-1 attitude parameters represent the yaw, pitch and roll angles of the aircraft and describes the rotation between the body and inertial axes in a predefined order. The transformation starts with the body and inertial axis systems aligned and then rotates the body axis system with the following sequence:

1. A rotation about the Z_B-axis through heading angle Ψ
2. A rotation about the Y_B-axis through pitch angle Θ
3. A rotation about the X_B-axis through roll angle Φ

This transformation can be used to transform vectors in the inertial axis system to the body axis system, and vice versa, using the direction cosine matrix (DCM) as follows,

$$\begin{bmatrix} x_B \\ y_B \\ z_B \end{bmatrix} = \begin{bmatrix} C_\Psi C_\Theta & S_\Psi C_\Theta & -S_\Theta \\ C_\Psi S_\Theta S_\Phi - S_\Psi C_\Phi & S_\Psi S_\Theta S_\Phi + C_\Psi C_\Phi & C_\Theta S_\Phi \\ C_\Psi S_\Theta C_\Phi + S_\Psi S_\Phi & S_\Psi S_\Theta C_\Phi - C_\Psi S_\Phi & C_\Theta C_\Phi \end{bmatrix} \begin{bmatrix} x_I \\ y_I \\ z_I \end{bmatrix} \tag{3.5}$$

where $S_{(\,)} = \sin(\,)$ and $C_{(\,)} = \cos(\,)$. Transforming from the body axis system to the inertial axis system requires the inverse DCM. Since the DCM is an orthogonal matrix, its inverse is simply its transpose.

Position Kinematics

The coordinates of the aircraft velocity in the body axis system may be transformed to velocity coordinates in the inertial axis system through use of the inverse DCM,

$$\begin{bmatrix} \dot{N} \\ \dot{E} \\ \dot{D} \end{bmatrix} = \Big[DCM\Big]^{-1} = \Big[DCM\Big]^{\mathsf{T}} \begin{bmatrix} U \\ V \\ W \end{bmatrix} \tag{3.6}$$

Attitude Kinematics

The roll, pitch, and yaw rates can be related to the time rate of change of the Euler angles through,

$$\begin{bmatrix} \dot{\Phi} \\ \dot{\Theta} \\ \dot{\Psi} \end{bmatrix} = \begin{bmatrix} 1 & \sin\Phi\tan\Theta & \cos\Phi\tan\Theta \\ 0 & \cos\Phi & -\sin\Phi \\ 0 & \sin\Phi\sec\Theta & \cos\Phi\sec\Theta \end{bmatrix} \begin{bmatrix} P \\ Q \\ R \end{bmatrix} \qquad |\Theta| \neq \frac{\pi}{2} \tag{3.7}$$

The singularity that occurs at $\Theta = \pm 90°$ can safely be ignored, since the pitch angle of a commercial airliner should never reach $\pm 90°$ during normal cruise conditions.

3.4 Forces and Moments Model

The most significant forces and moments that act on an aircraft comprise aerodynamic, thrust generated, and gravitational forces and moments. Figure 3.6 illustrates the forces and moments model, where the total forces $\boldsymbol{F}$ and moments $\boldsymbol{M}$ experienced by the aircraft are expressed as the sum of the three sources. The superscripts A, T, and G denote the aerodynamic, thrust, and gravitational components respectively. The modeling of each component will be discussed in more detail in the sections to follow.

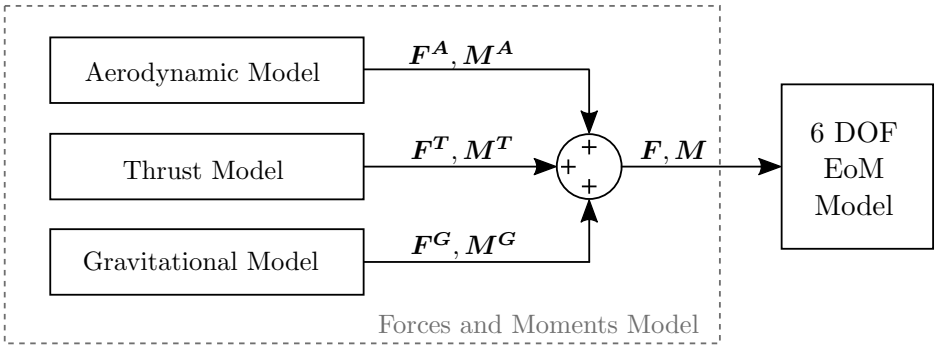

Figure 3.6: Forces and Moments Model.

3.4.1 Aerodynamic Forces and Moments

The aerodynamic characteristics of the aircraft are incorporated into the aerodynamic forces and moments model in the form of non-dimensional aerodynamic coefficients. These coefficients are specific to the aircraft and describe the aerodynamic properties of the airframe in the form of stability and control derivatives.

The aerodynamic forces and moments that act upon the aircraft in the body axis system are given by,

$$X^A = \bar{q}SC_X \tag{3.8a}$$

$$Y^A = \bar{q}SC_Y \tag{3.8b}$$

$$Z^A = \bar{q}SC_Z \tag{3.8c}$$

$$L^A = \bar{q}SbC_l \tag{3.8d}$$

$$M^A = \bar{q}S\bar{c}C_m \tag{3.8e}$$

$$N^A = \bar{q}SbC_n \tag{3.8f}$$

where S is the area of the wing, b is the wingspan, $\bar{c}$ is the mean aerodynamic chord, $\bar{q}$ is the dynamic pressure, and $C_{()}$ are the non-dimensional aerodynamic coefficients. These aerodynamic coefficients are in turn functions of the angle of attack α, the sideslip angle β, the angular rates of the aircraft relative to inertial space (P, Q, R), the airspeed magnitude $\overline{V}$, and the deflections of elevator, ailerons, and rudder $(\delta_E, \delta_A, \delta_R)$, expressed mathematically as,

$$C_{(\,)} = f(\alpha, \beta, P, Q, R, \overline{V}, \delta_E, \delta_A, \delta_R) \tag{3.9}$$

The data for the Boeing 747-100 aircraft used in this study was extracted from Heffley and Jewel [41], which provides the stability and control derivatives as coefficients in the stability axes linearised about a specified flight condition. This linear approximation is deemed accurate as long as the aircraft operates close to this equilibrium point, and thus removes the necessity for a more complex non-linear aerodynamic model as found in [42].

A summation and transformation of these coefficients from the stability axis system to the body axis system result in the form as given in Equations 3.8a to 3.8f. Details regarding the control and stability derivatives as well as their transformation are provided in Appendix A.

3.4.2 Thrust Forces and Moments

In the work of Van Wyk [2], a higher-order thrust model was developed for the Boeing 747-100 aircraft which included the thrust actuation of the four engines present on the aircraft as well as the engine dynamics. For this study, only the thrust distribution model will be used, which allows for the use of differential thrust by applying an unequal thrust distribution across the four engines.

Thrust Dynamic Model

The dynamics of the thrust actuation are modelled as a first-order lag system described as,

$$\dot{T} = -\frac{1}{\tau}T + \frac{1}{\tau}T_c \tag{3.10}$$

where T is the thrust magnitude, T_c is the thrust command, and τ is the engine lag time constant. This simplified thrust model is deemed sufficient since a conventional aircraft is assumed to fly close to its equilibrium conditions.

Thrust Distribution Model

The thrust distribution model splits the thrust command T_c evenly among the four engines of the aircraft. Application of differential thrust δ_{Tc} increases the thrust on the one side of the aircraft while decreasing it on the other side. This imbalance in thrust between the starboard and port side engines induces a yawing moment on the aircraft. The differential thrust is defined so that a positive command produces a negative moment. The thrust distribution is given by,

$$T_{soc} = T_{sic} = \frac{T_c + \delta_{Tc}}{4} \tag{3.11a}$$

$$T_{poc} = T_{pic} = \frac{T_c - \delta_{Tc}}{4} \tag{3.11b}$$

where T_{soc} and T_{sic} represent the starboard outer and inner thrust respectively, and T_{poc} and T_{pic} the port side outer and inner thrust respectively. Note that the thrust produced by the two starboard engines are always equal, as well as the thrust produced by the two port side engines. The position and orientation of the four Boeing 747 engines were obtained from modelling data provided by Hanke and Nordwall [42], and are illustrated in Figure 3.7.

The forces and moments produced by the distributed thrust model is given by,

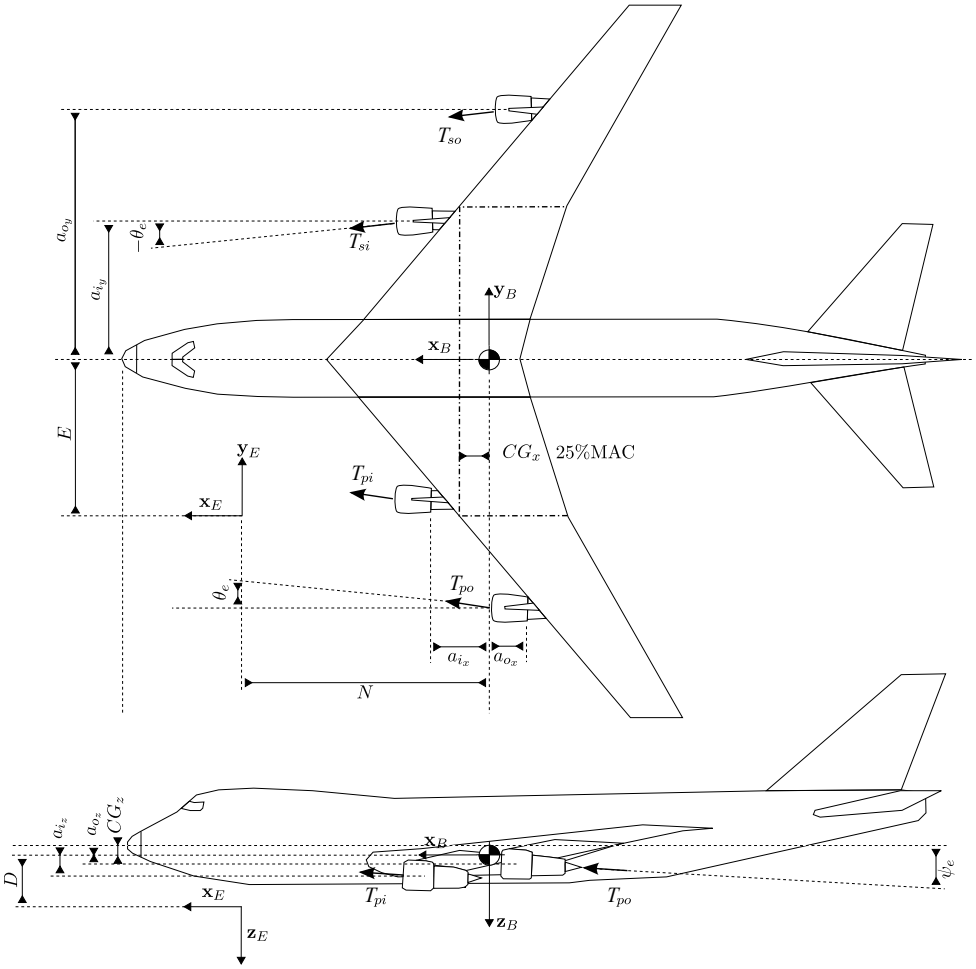

Figure 3.7: Dimensions for thrust distribution model (reproduced from [2]).

$$X^T = T\cos\theta_e\cos\psi_e \tag{3.12a}$$

$$Y^T = \delta_T\sin\psi_e \tag{3.12b}$$

$$Z^T = -T\sin\theta_e \tag{3.12c}$$

$$L^T = \frac{\delta_T}{2}(\sin\psi_e(a_{iz}+a_{oz}) - \sin\theta_e(a_{iy}+a_{oy})) \tag{3.12d}$$

$$M^T = \frac{T}{2}(\sin\theta_e(a_{ix}-a_{ox}) + \cos\theta_e\cos\psi_e(a_{iz}+a_{oz})) \tag{3.12e}$$

$$N^T = -\frac{\delta_T}{2}(\sin\psi_e(a_{ix}-a_{ox}) + \cos\theta_e\cos\psi_e(a_{iy}+a_{oy})) \tag{3.12f}$$

where ψ_e and θ_e are the engine inboard and pitch orientation angles. The engine positions relative to the aircraft CG are denoted by $a_{(\,)}$ where the subscripts i and o denote inboard and outboard engines respectively and x, y, and z indicate the orientation of the dimension in the aircraft body axes. The values for the relevant dimensions are provided in Appendix A.

3.4.3 Gravitational Forces and Moments

Assuming a constant gravitational acceleration that does not vary with latitude or altitude, the gravitational force acting on the aircraft can be modelled as a downward force in the inertial axis system, or,

$$\mathbf{F_I^G} = \begin{bmatrix} 0 \\ 0 \\ mg \end{bmatrix} \tag{3.13}$$

Transforming to the body axis system using the DCM yields,

$$\begin{bmatrix} X^G \\ Y^G \\ Z^G \end{bmatrix} = \begin{bmatrix} -\sin\Theta \\ \cos\Theta\sin\Phi \\ \cos\Theta\cos\Phi \end{bmatrix} mg \tag{3.14}$$

Since the gravitational force acts through the centre of mass of the aircraft, and since the gravity gradient moment acting on the aircraft is negligible, the gravitational moments are assumed to be zero,

$$L^G = M^G = N^G = 0 \tag{3.15}$$

3.5 Linearisation of Aircraft Dynamics

To facilitate the design of the flight control laws using linear systems theory, the nonlinear dynamic equations of the aircraft must first be linearised about a nominal equilibrium condition, or trim condition. This section presents the calculation of the trim state and trim inputs for a desired straight and level flight condition, and the linearisation of the aircraft model about the calculated trim point. Subsequently, the linearised aircraft dynamics are analysed to provide insight into the stability and dynamic response of the aircraft's natural modes of motion. The trim calculation and the derivation of the linearised model follows the example of previous studies and course notes [37, 38] and is reproduced here for clarity and for the convenience of the reader.

3.5.1 Definition and Calculation of Trim Condition

When an aircraft is flying at a specified trim condition, all forces and moments acting on the aircraft are in equilibrium. An aircraft initialised in this trim state will remain so until disturbed by pilot commands or external disturbances such as wind.

For this study, the chosen trim condition is that of straight and level flight, where the variables at this trim condition are denoted by the subscript T. This requires that all the lateral motion and control variables are zero, or in vector form,

$$\begin{bmatrix} V & P & R & \Phi & \delta_A & \delta_R & \delta_T \end{bmatrix}_T = \mathbf{0} \tag{3.16}$$

where V is the lateral velocity of the aircraft in the body axes, P and R are the roll and yaw rates respectively, Φ is the roll angle, δ_A and δ_R are the aileron and rudder deflections,

and δ_T is the differential thrust. Only the longitudinal states and control settings must now be solved,

$$\begin{bmatrix} \overline{V} & \alpha & Q & \Theta & \delta_E & T \end{bmatrix}_T \tag{3.17}$$

where $\overline{V}$ is the airspeed magnitude of the aircraft, α is the angle of attack, Q and Θ are the pitch rate and angle respectively, δ_E is the elevator deflection, and T is the forward thrust. The trim airspeed and altitude are chosen according to a typical cruise condition. For straight and level flight the pitch rate is zero and the pitch angle equals the angle of attack, or,

$$\begin{aligned} Q_T &= 0 \\ \Theta_T &= \alpha_T \end{aligned} \tag{3.18}$$

This leaves only three variables to be solved for trim, namely the angle of attack, elevator deflection and thrust setting,

$$\begin{bmatrix} \alpha & \delta_E & T \end{bmatrix}_T \tag{3.19}$$

Matlabs's Symbolic Toolbox was used to solve for these variables simultaneously and the results are shown in Table 3.2. The flight data is selected based on a NASA Contractor report Heffley and Jewell [41] for a Boeing 747 cruising at an altitude of 40 000 ft and at a Mach number of 0.8 M.

Table 3.2: Calculated trim values for straight and level flight.

Selected Variables	Calculated Variables
$\overline{V}_T = 236 m/s$	$\alpha_T = 4.43°$
$\Theta_T = \alpha_T$	$\delta_{E_T} = 0.473°$
$(V, P, Q, R, \Phi, \delta_A, \delta_R, \delta_T) = \mathbf{0}$	$T_T = 175.8\,kN$

3.5.2 Linearisation About Trim

The dynamics of the aircraft are derived as a set of non-linear differential equations described in non-linear state space form as,

$$\dot{\mathbf{x}} = \mathbf{f}(\mathbf{x}, \mathbf{u}) \tag{3.20}$$

where

$$\begin{aligned} \mathbf{x} &= \begin{bmatrix} U & V & W & P & Q & R & \Phi & \Theta \end{bmatrix}^\mathsf{T} \\ \mathbf{u} &= \begin{bmatrix} \delta_E & \delta_A & \delta_R & \delta_T & T \end{bmatrix}^\mathsf{T} \end{aligned} \tag{3.21}$$

and $\mathbf{f}$ is the non-linear vector function describing the aircraft dynamic equations. Through use of small disturbance theory, each state vector and control input vector can be written as the sum of a trim value and a perturbation about this trim condition,

$$\mathbf{x} = \mathbf{x}_T + \Delta\mathbf{x} \tag{3.22}$$

$$\mathbf{u} = \mathbf{u}_T + \Delta\mathbf{u} \tag{3.23}$$

where the perturbation state and control inputs are given by,

$$\begin{aligned}\Delta\mathbf{x} &= \begin{bmatrix} u & v & w & p & q & r & \phi & \theta \end{bmatrix}^{\mathsf{T}} \\ \Delta\mathbf{u} &= \begin{bmatrix} \delta_e & \delta_a & \delta_r & \delta_t & \Delta T \end{bmatrix}^{\mathsf{T}}\end{aligned} \tag{3.24}$$

The non-linear vector function in Equation 3.20 can be expanded as a Taylor series about the trim condition, and yields,

$$\dot{\mathbf{x}}_T + \Delta\dot{\mathbf{x}} = \mathbf{f}(\mathbf{x}_T + \Delta\mathbf{x}, \mathbf{u}_T + \Delta\mathbf{u}) = \mathbf{f}(\mathbf{x}, \mathbf{u}) + \left.\frac{\partial \mathbf{f}}{\partial \mathbf{x}}\right|_T \Delta\mathbf{x} + \left.\frac{\partial \mathbf{f}}{\partial \mathbf{u}}\right|_T \Delta\mathbf{u} + \mathcal{O} \tag{3.25}$$

where $\mathcal{O}$ represents the higher order terms. Assuming that the deviations from trim are small, the higher order terms can be disregarded. At equilibrium the time rate of change of the states and controls are zero,

$$\dot{\mathbf{x}}_T = \mathbf{f}(\mathbf{x}_T, \mathbf{u}_T) = 0 \tag{3.26}$$

and the dynamics can be approximated by the linearised deviations about trim,

$$\Delta\dot{\mathbf{x}} \approx \mathbf{A}_T \Delta\mathbf{x} + \mathbf{B}_T \Delta\mathbf{u} \tag{3.27}$$

where,

$$\begin{aligned}\mathbf{A}_T &= \left.\frac{\partial \mathbf{f}}{\partial \mathbf{x}}\right|_T \Delta\mathbf{x} \\ \mathbf{B}_T &= \left.\frac{\partial \mathbf{f}}{\partial \mathbf{x}}\right|_T \Delta\mathbf{x}\end{aligned} \tag{3.28}$$

To obtain the linearised model, the vector partial derivatives of the state space matrices in Equation 3.28 must be calculated. These matrices can however be decoupled into the longitudinal and lateral dynamics by making the proper assumptions.

Decoupling of Longitudinal and Lateral Dynamics

The perturbation state and control input vectors can be written as,

$$\begin{aligned}\Delta\mathbf{x} &= \begin{bmatrix} \Delta\mathbf{x}_{long} & \Delta\mathbf{x}_{lat} \end{bmatrix}^{\mathsf{T}} \\ \Delta\mathbf{u} &= \begin{bmatrix} \Delta\mathbf{u}_{long} & \Delta\mathbf{u}_{lat} \end{bmatrix}^{\mathsf{T}}\end{aligned} \tag{3.29}$$

where,

$$\begin{aligned}\Delta\mathbf{x}_{long} &= \begin{bmatrix} u & w & q & \theta \end{bmatrix}^{\mathsf{T}} & \Delta\mathbf{x}_{lat} &= \begin{bmatrix} v & p & r & \phi \end{bmatrix}^{\mathsf{T}} \\ \Delta\mathbf{u}_{long} &= \begin{bmatrix} \delta_e & \Delta T \end{bmatrix}^{\mathsf{T}} & \Delta\mathbf{u}_{lat} &= \begin{bmatrix} \delta_a & \delta_r & \delta_t \end{bmatrix}^{\mathsf{T}}\end{aligned} \tag{3.30}$$

Equation 3.27 can written in terms of its longitudinal and lateral components,

$$\begin{bmatrix} \Delta\dot{\mathbf{x}}_{long} \\ \Delta\dot{\mathbf{x}}_{lat} \end{bmatrix} = \begin{bmatrix} \mathbf{A}_{T_{11}} & \mathbf{A}_{T_{12}} \\ \mathbf{A}_{T_{21}} & \mathbf{A}_{T_{22}} \end{bmatrix} \begin{bmatrix} \Delta\mathbf{x}_{long} \\ \Delta\mathbf{x}_{lat} \end{bmatrix} + \begin{bmatrix} \mathbf{B}_{T_{11}} & \mathbf{B}_{T_{12}} \\ \mathbf{B}_{T_{21}} & \mathbf{B}_{T_{22}} \end{bmatrix} \begin{bmatrix} \Delta\mathbf{u}_{long} \\ \Delta\mathbf{u}_{lat} \end{bmatrix} \tag{3.31}$$

Assuming that an aircraft is in straight and level trim flight, a deflection in elevator will only cause a pitching moment about the body y-axis Y_B and will eventually cause changes in the forces F_{X_B} and F_{Z_B}. Due to aircraft symmetry about its XY-plane, this deflection does not cause a rolling or yawing moment or any change in the side force F_{Y_B}. Through this assumption,

$$\begin{aligned} \mathbf{A}_{T_{21}} &= \mathbf{0} \\ \mathbf{B}_{T_{21}} &= \mathbf{0} \end{aligned} \tag{3.32}$$

Due to small disturbance theory and the assumption of small perturbations, changes in V, P or R are assumed to have negligible effect on the longitudinal dynamics. Through this assumption,

$$\begin{aligned} \mathbf{A}_{T_{12}} &\approx \mathbf{0} \\ \mathbf{B}_{T_{12}} &\approx \mathbf{0} \end{aligned} \tag{3.33}$$

With these assumptions in place, Equation 3.5.2 can be divided into its longitudinal and lateral dynamic components,

$$\begin{aligned} \Delta\dot{\mathbf{x}}_{long} &= \mathbf{A}_{T_{11}}\Delta\mathbf{x}_{long} + mvA_{long}\Delta\mathbf{u}_{long} \\ \Delta\dot{\mathbf{x}}_{lat} &= \mathbf{A}_{T_{22}}\Delta\mathbf{x}_{lat} + \mathbf{B}_{T_{22}}\Delta\mathbf{u}_{lat} \end{aligned} \tag{3.34}$$

where,

$$\mathbf{A}_{long} = \mathbf{A}_{T_{11}} \tag{3.35}$$
$$\mathbf{B}_{long} = \mathbf{B}_{T_{11}} \tag{3.36}$$
$$\mathbf{A}_{lat} = \mathbf{A}_{T_{22}} \tag{3.37}$$
$$\mathbf{B}_{lat} = \mathbf{B}_{T_{22}} \tag{3.38}$$

Determining the linear state space model requires calculation of the decoupled state space matrices.

Linearised Longitudinal Model

The longitudinal dynamics in Equation 3.34 can be expanded to obtain the linearised longitudinal model,

$$\begin{bmatrix} \dot{u} \\ \dot{w} \\ \dot{q} \\ \dot{\theta} \end{bmatrix} = \begin{bmatrix} \frac{\partial\dot{U}}{\partial U} & \frac{\partial\dot{U}}{\partial W} & \frac{\partial\dot{U}}{\partial Q} & \frac{\partial\dot{U}}{\partial\Theta} \\ \frac{\partial\dot{W}}{\partial U} & \frac{\partial\dot{W}}{\partial W} & \frac{\partial\dot{W}}{\partial Q} & \frac{\partial\dot{W}}{\partial\Theta} \\ \frac{\partial\dot{Q}}{\partial U} & \frac{\partial\dot{Q}}{\partial W} & \frac{\partial\dot{Q}}{\partial Q} & \frac{\partial\dot{Q}}{\partial\Theta} \\ \frac{\partial\dot{\Theta}}{\partial U} & \frac{\partial\dot{\Theta}}{\partial W} & \frac{\partial\dot{\Theta}}{\partial Q} & \frac{\partial\dot{\Theta}}{\partial\Theta} \end{bmatrix} \begin{bmatrix} u \\ w \\ q \\ \theta \end{bmatrix} + \begin{bmatrix} \frac{\partial\dot{U}}{\partial\delta_E} & \frac{\partial\dot{U}}{\partial T} \\ \frac{\partial\dot{W}}{\partial\delta_E} & \frac{\partial\dot{W}}{\partial T} \\ \frac{\partial\dot{Q}}{\partial\delta_E} & \frac{\partial\dot{Q}}{\partial T} \\ \frac{\partial\dot{\Theta}}{\partial\delta_E} & \frac{\partial\dot{\Theta}}{\partial T} \end{bmatrix} \begin{bmatrix} \delta_e \\ \Delta T \end{bmatrix} \tag{3.39}$$

In flight dynamics, it is most common to work with the velocity magnitude and angle of attack perturbations in the state vector rather than the body velocity magnitude perturbations u and w. For small perturbations, the angle of attack α is linearly related to the normal velocity perturbation w through,

$$\alpha \approx \frac{\Delta w}{U_T} \tag{3.40}$$

where U_T is the axial component of the velocity vector at trim. Since the angle of attack is typically small in straight and level trim flight, the axial component U_T of the trim airspeed velocity vector is approximately equal to the trim airspeed magnitude $\overline{V}_T$. The following substitutions can therefore be made:

$$\begin{aligned} \dot{u} &\approx \dot{\bar{v}} \\ \dot{w} &\approx \dot{\alpha}\overline{V}_T \end{aligned} \tag{3.41}$$

The linearised state space model for the longitudinal dynamics, with airspeed magnitude and angle of attack as state variables, is therefore obtained as,

$$\begin{bmatrix} \dot{\bar{v}} \\ \dot{\alpha} \\ \dot{q} \\ \dot{\theta} \end{bmatrix} = \begin{bmatrix} \frac{\partial \dot{U}}{\partial U} & \overline{V}_T \frac{\partial \dot{U}}{\partial W} & \frac{\partial \dot{U}}{\partial Q} & \frac{\partial \dot{U}}{\partial \Theta} \\ \frac{1}{\overline{V}_T}\frac{\partial \dot{W}}{\partial U} & \frac{\partial \dot{W}}{\partial W} & \frac{1}{\overline{V}_T}\frac{\partial \dot{W}}{\partial Q} & \frac{1}{\overline{V}_T}\frac{\partial \dot{W}}{\partial \Theta} \\ \frac{\partial \dot{Q}}{\partial U} & \overline{V}_T \frac{\partial \dot{Q}}{\partial W} & \frac{\partial \dot{Q}}{\partial Q} & \frac{\partial \dot{Q}}{\partial \Theta} \\ \frac{\partial \dot{\Theta}}{\partial U} & \overline{V}_T \frac{\partial \dot{\Theta}}{\partial W} & \frac{\partial \dot{\Theta}}{\partial Q} & \frac{\partial \dot{\Theta}}{\partial \Theta} \end{bmatrix} \begin{bmatrix} \bar{v} \\ \alpha \\ q \\ \theta \end{bmatrix} + \begin{bmatrix} \frac{\partial \dot{U}}{\partial \delta_E} & \frac{\partial \dot{U}}{\partial T} \\ \frac{1}{\overline{V}_T}\frac{\partial \dot{W}}{\partial \delta_E} & \frac{1}{\overline{V}_T}\frac{\partial \dot{W}}{\partial T} \\ \frac{\partial \dot{Q}}{\partial \delta_E} & \frac{\partial \dot{Q}}{\partial T} \\ \frac{\partial \dot{\Theta}}{\partial \delta_E} & \frac{\partial \dot{\Theta}}{\partial T} \end{bmatrix} \begin{bmatrix} \delta_e \\ \Delta T \end{bmatrix} \tag{3.42}$$

and the derivatives were calculated in Matlab by using the Symbolic Toolbox.

Linearised Lateral Model

The lateral dynamics in Equation 3.34 can be expanded to obtain the linearised lateral dynamics model,

$$\begin{bmatrix} \dot{v} \\ \dot{p} \\ \dot{r} \\ \dot{\phi} \end{bmatrix} = \begin{bmatrix} \frac{\partial \dot{V}}{\partial V} & \frac{\partial \dot{V}}{\partial P} & \frac{\partial \dot{V}}{\partial R} & \frac{\partial \dot{V}}{\partial \phi} \\ \frac{\partial \dot{P}}{\partial V} & \frac{\partial \dot{P}}{\partial P} & \frac{\partial \dot{P}}{\partial R} & \frac{\partial \dot{P}}{\partial \phi} \\ \frac{\partial \dot{R}}{\partial V} & \frac{\partial \dot{R}}{\partial P} & \frac{\partial \dot{R}}{\partial R} & \frac{\partial \dot{R}}{\partial \phi} \\ \frac{\partial \dot{\phi}}{\partial V} & \frac{\partial \dot{\phi}}{\partial P} & \frac{\partial \dot{\phi}}{\partial R} & \frac{\partial \dot{\phi}}{\partial \phi} \end{bmatrix} \begin{bmatrix} v \\ p \\ r \\ \phi \end{bmatrix} + \begin{bmatrix} \frac{\partial \dot{V}}{\partial \delta_A} & \frac{\partial \dot{V}}{\partial \delta_R} & \frac{\partial \dot{V}}{\partial \delta_T} \\ \frac{\partial \dot{P}}{\partial \delta_A} & \frac{\partial \dot{P}}{\partial \delta_R} & \frac{\partial \dot{P}}{\partial \delta_T} \\ \frac{\partial \dot{R}}{\partial \delta_A} & \frac{\partial \dot{R}}{\partial \delta_R} & \frac{\partial \dot{R}}{\partial \delta_T} \\ \frac{\partial \dot{\phi}}{\partial \delta_A} & \frac{\partial \dot{\phi}}{\partial \delta_R} & \frac{\partial \dot{\phi}}{\partial \delta_T} \end{bmatrix} \begin{bmatrix} \delta_a \\ \delta_r \\ \delta_t \end{bmatrix} \tag{3.43}$$

In flight dynamics, it is most common to work with the sideslip angle perturbations in the state vector rather than the lateral velocity perturbation v. For small perturbations the sideslip angle β is approximately linearly related to the lateral velocity perturbation v through,

$$\beta \approx \frac{v}{U_T} \tag{3.44}$$

The trim axial component U_T of the velocity vector is again approximately equal to the trim airspeed magnitude $\overline{V}_T$, and the following substitution can therefore be made:

$$\dot{v} \approx \overline{V}_T \dot{\beta} \tag{3.45}$$

The linearised state space model for the lateral dynamics, with sideslip angle as a state variable, is therefore obtained as,

$$\begin{bmatrix} \dot{\beta} \\ \dot{p} \\ \dot{r} \\ \dot{\phi} \end{bmatrix} = \begin{bmatrix} \frac{\partial \dot{V}}{\partial V} & \frac{1}{\overline{V}_T}\frac{\partial \dot{V}}{\partial P} & \frac{1}{\overline{V}_T}\frac{\partial \dot{V}}{\partial R} & \frac{1}{\overline{V}_T}\frac{\partial \dot{V}}{\partial \phi} \\ \overline{V}_T\frac{\partial \dot{P}}{\partial V} & \frac{\partial \dot{P}}{\partial P} & \frac{\partial \dot{P}}{\partial R} & \frac{\partial \dot{P}}{\partial \phi} \\ \overline{V}_T\frac{\partial \dot{R}}{\partial V} & \frac{\partial \dot{R}}{\partial P} & \frac{\partial \dot{R}}{\partial R} & \frac{\partial \dot{R}}{\partial \phi} \\ \overline{V}_T\frac{\partial \dot{\phi}}{\partial V} & \frac{\partial \dot{\phi}}{\partial P} & \frac{\partial \dot{\phi}}{\partial R} & \frac{\partial \dot{\phi}}{\partial \phi} \end{bmatrix} \begin{bmatrix} \beta \\ p \\ r \\ \phi \end{bmatrix} + \begin{bmatrix} \frac{1}{\overline{V}_T}\frac{\partial \dot{V}}{\partial \delta_A} & \frac{1}{\overline{V}_T}\frac{\partial \dot{V}}{\partial \delta_R} & \frac{1}{\overline{V}_T}\frac{\partial \dot{V}}{\partial \delta_T} \\ \frac{\partial \dot{P}}{\partial \delta_A} & \frac{\partial \dot{P}}{\partial \delta_R} & \frac{\partial \dot{P}}{\partial \delta_T} \\ \frac{\partial \dot{R}}{\partial \delta_A} & \frac{\partial \dot{R}}{\partial \delta_R} & \frac{\partial \dot{R}}{\partial \delta_T} \\ \frac{\partial \dot{\phi}}{\partial \delta_A} & \frac{\partial \dot{\phi}}{\partial \delta_R} & \frac{\partial \dot{\phi}}{\partial \delta_T} \end{bmatrix} \begin{bmatrix} \delta_a \\ \delta_r \\ \delta_t \end{bmatrix} \tag{3.46}$$

and the derivatives were calculated in Matlab by using the Symbolic Toolbox. Now that the conventional non-linear aircraft model has been linearised about a straight and level flight equilibrium condition, the next section focuses on analysing the dynamics to gain insight into the aircraft's natural modes of motion and responses to control inputs.

3.5.3 Linear Dynamics Analysis

The dynamics of a linear system are governed by the locations of its poles – the eigenvalues of the state space matrix **A**. The poles for the longitudinal and lateral linear dynamics are depicted in Figure 3.8. The values correspond very well to those obtained in previous studies that also used the Boeing 747 aircraft data provided by Heffley and Jewel – the flight condition being at approximately 40000 ft and at a Mach number of 0.8. The locations of the open-loop poles that represent the aircraft's natural dynamics show that the conventional aircraft in isolated flight is naturally stable when flying straight and level. The exact locations of the poles are summarised in Table 3.3.

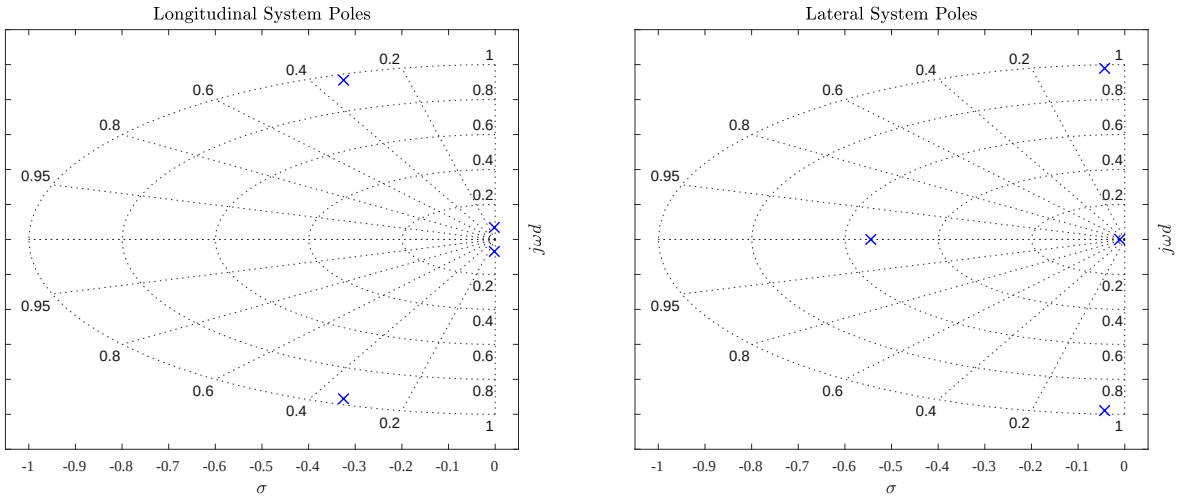

(a) Longitudinal poles in s-plane.

(b) Lateral poles in s-plane.

Figure 3.8: Linear System Poles.

Modes of Motion

The poles summarised in Table 3.3 correspond to the five modes of motion associated with a fixed-wing aircraft. Two of these modes describe longitudinal dynamics. The lower-frequency pole pair represents the phugoid mode: a kinematic mode that describes the exchange between

Table 3.3: Summary of linear system poles.

Linear Modes	ω_n (rad/s)	ζ	Pole Location
Longitudinal			
Phugoid	0.069	0.026	$-0.0018 \pm 0.0688i$
Short Period	0.967	0.336	$-0.3251 \pm 0.9111i$
Lateral			
Dutch Roll	0.98	0.044	$-0.0432 \pm 0.9785i$
Roll	0.544	1	-0.5444
Spiral	0.0106	1	-0.0106

kinetic and potential energy of the aircraft when it is disturbed longitudinally from trim flight. The higher-frequency pole pair represents the short period mode, which describes the aircraft's tendency to realign itself with the velocity vector when disturbed.

The other three modes describe the lateral dynamics of the aircraft. The high-frequency real pole represents the roll mode, which describes the roll dynamics of the aircraft. The complex pole pair describes the Dutch roll mode, a lateral equivalent to the short period mode in that it describes the aircraft's tendency to realign itself with the velocity vector when disturbed laterally. Lastly, the low-frequency real pole represents the spiral mode. This mode of motion, if stable, describes the aircraft's tendency to restore itself to wings-level flight when disturbed. If the mode is unstable, it describes the tendency to diverge from wings level flight.

Response to Controls

Now that the linearised aircraft model has been obtained, it is important to compare the dynamic responses of the linearised model to the dynamic responses of the original non-linear model. This will verify whether the derived uncoupled linear model is a sufficiently accurate representation of the full non-linear model.

Separate steps in elevator deflection and thrust are used to evaluate the longitudinal response to the respective control inputs. The longitudinal state responses to a 1° elevator step and a 50 kN thrust step are shown in Figures 3.9 and 3.10 respectively. It can be seen that the linear and non-linear responses match very well during the initial part of each response, but eventually diverge since the linear model is uncoupled and the non-linear model is not. The brief short-period mode motion is clearly visible during the first 20 seconds of the simulation as higher frequency oscillations. During the rest of the simulation the slow oscillatory phugoid dynamics are dominant. From the responses it is seen that a positive elevator deflection will cause the aircraft to pitch down which result in negative pitch rate and pitch angle responses. A positive step in thrust causes the aircraft to increase speed and pitch up.

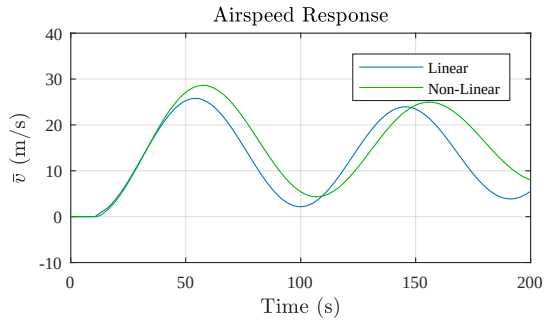

(a) Airspeed response.

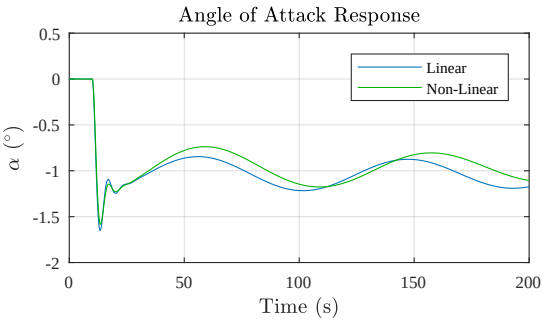

(b) Angle of attack response.

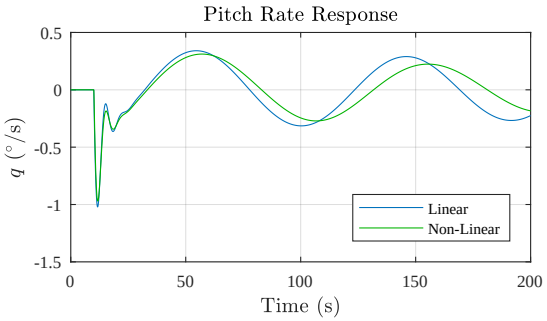

(c) Pitch rate response.

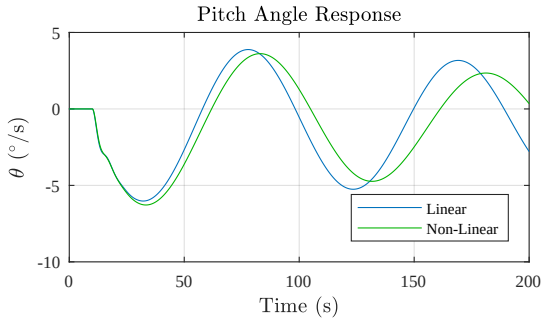

(d) Pitch angle response.

Figure 3.9: Longitudinal state responses to a 1° step in elevator control input.

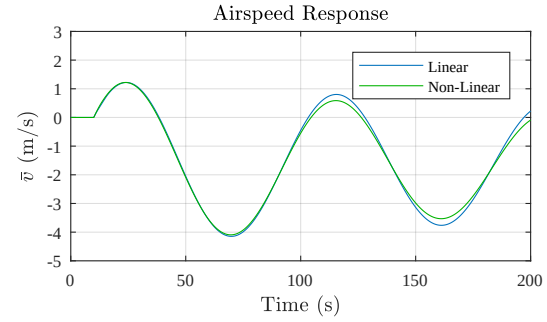

(a) Airspeed response.

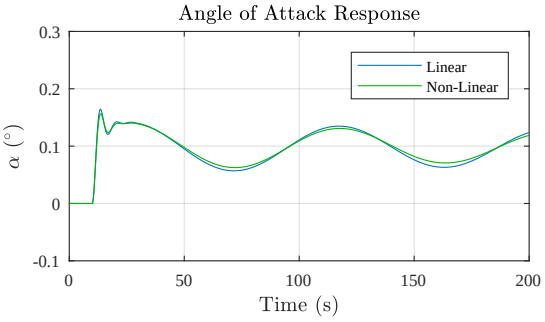

(b) Angle of attack response.

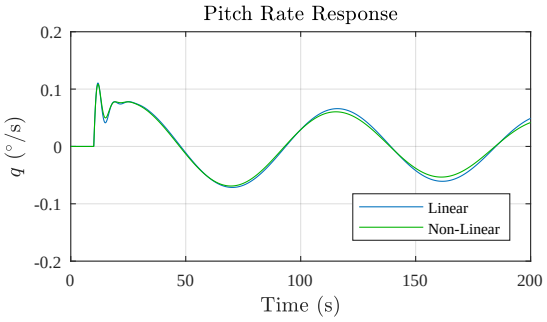

(c) Pitch rate response.

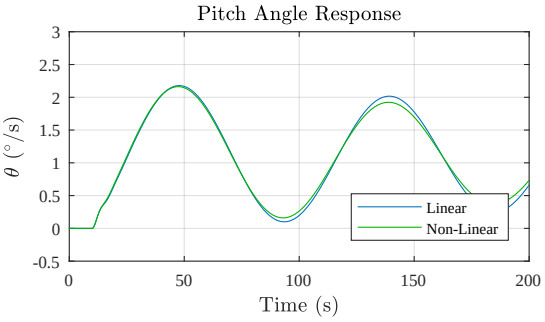

(d) Pitch angle response.

Figure 3.10: Longitudinal state responses to a 50 kN step in thrust input.

Separate steps in aileron, rudder, and differential thrust are used to evaluate the lateral response to the respective control inputs. The lateral state responses to a 5° aileron step, a 1° rudder step, and a 5 kN differential thrust step are shown in Figures 3.11, 3.12, and 3.13 respectively. It can be seen that the linear and non-linear responses match very well during the initial part of each response but, as with the elevator response, the responses eventually diverge due to the non-linear longitudinal model that couples into the lateral dynamics. The Dutch role mode is clearly visible as the slow oscillatory behaviour that dominates both dynamic responses. However, the aircraft may be considered stable since all the responses are asymptotically convergent. A positive aileron command induces a positive rolling moment, which is opposite to normal convention, while a positive step in rudder produces a negative yawing moment. Finally, it is seen that a positive differential thrust command produces a negative yawing moment, as per the convention selected in Section 3.4.2.

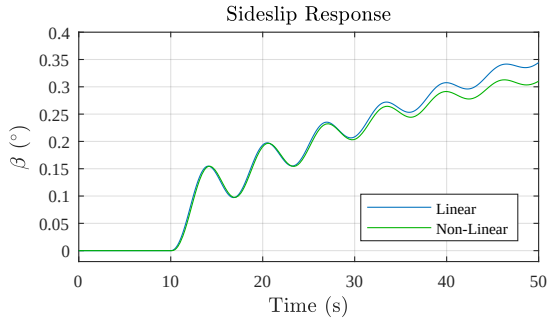

(a) Sideslip response.

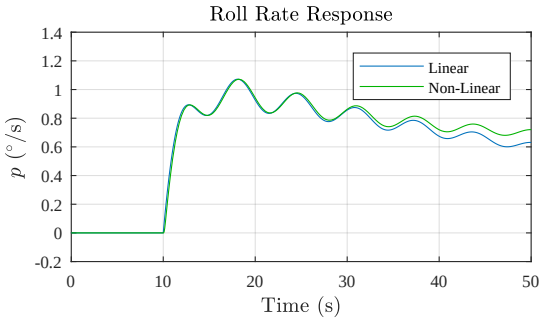

(b) Roll rate response.

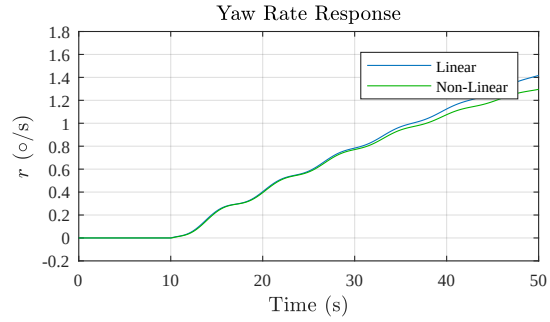

(c) Yaw rate response.

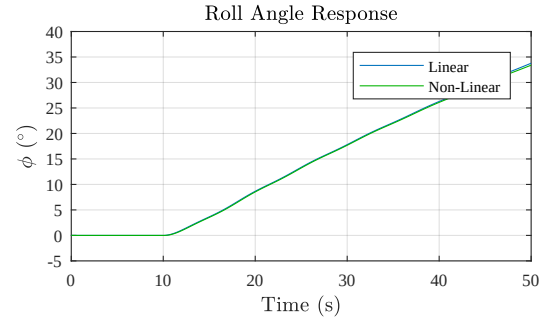

(d) Roll angle response.

Figure 3.11: Lateral state responses to a 5° step in aileron control input.

Some non-minimum phase behaviour is visible in Figure 3.12b during the roll rate response to a rudder input. The roll rate exhibits a sign reversal also known as *adverse roll* in response to rudder. When a positive rudder deflection is applied, a side force is generated on the aircraft's tail fin which in turn generates a negative yawing moment. This negative yawing moment causes a negative rolling moment as well, resulting in the aircraft rolling to the left. However, the side force on tail fin acts at a distance above the roll axis which causes a rolling moment in the opposite direction. Since the aircraft responds quicker to roll than to yaw, the aircraft initially rolls in the wrong direction. Once the yawing moment is established, the rolling moment due to yaw overcomes the adverse rolling moment and the aircraft rolls to the right. A similar characteristic, known as *adverse yaw*, is present, albeit insignificantly small, in the yaw response of the aircraft to a step in aileron deflection, where differential drag effects due to aileron deflections cause a yawing motion in the wrong direction.

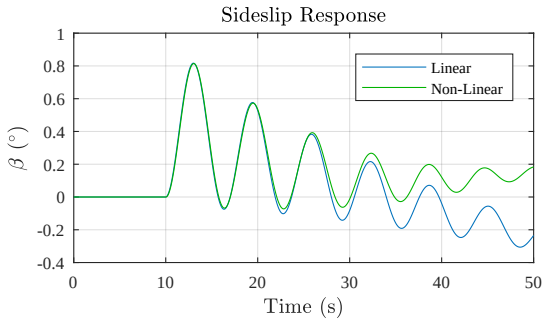

(a) Sideslip response.

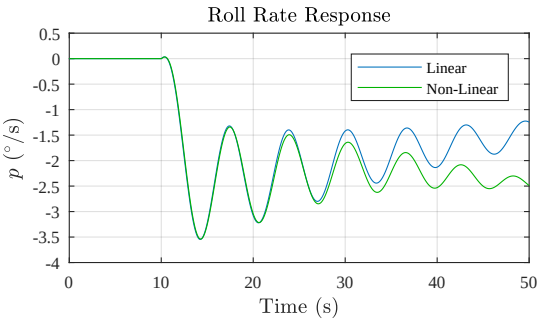

(b) Roll rate response.

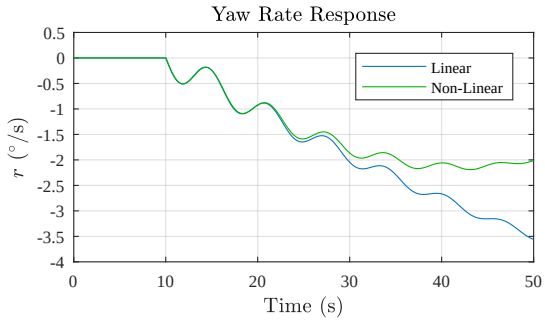

(c) Yaw rate response.

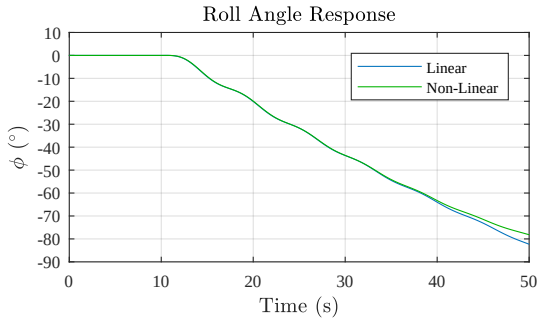

(d) Roll angle response.

Figure 3.12: Lateral state responses to a 1° step in rudder control input.

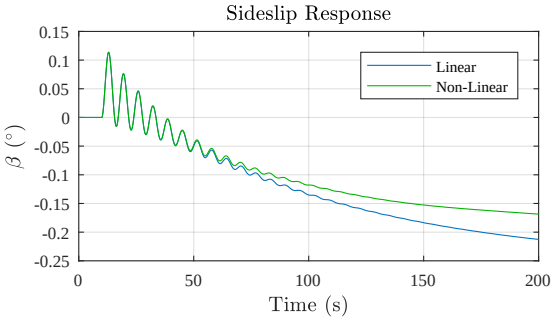

(a) Sideslip response.

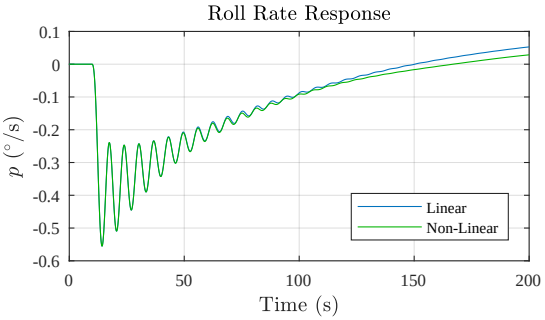

(b) Roll rate response.

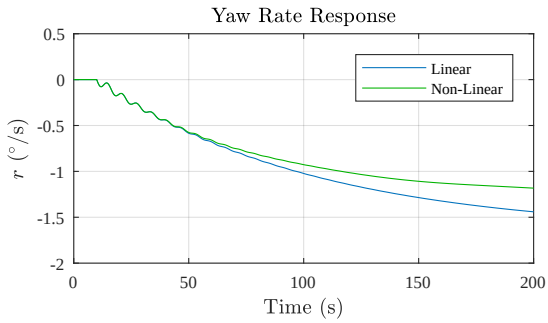

(c) Yaw rate response.

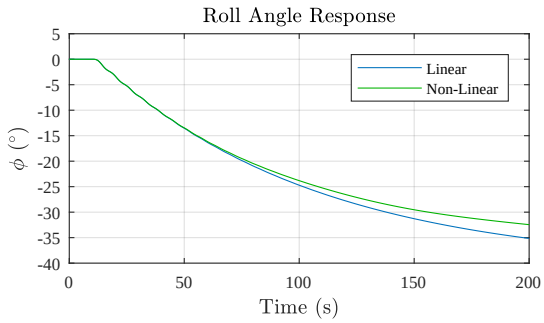

(d) Roll angle response.

Figure 3.13: Lateral state responses to a 5 kN step in differential thrust input.

3.5.4 Summary of Linearisation of Aircraft Dynamics

In this section, the linearised aircraft model was derived and verified to be representative of the full non-linear aircraft model. The selected trim condition of straight and level flight was presented and the aircraft trim states were calculated using small disturbance theory. The conventional aircraft in isolated flight was linearised about this trim condition, decoupled into separate longitudinal and lateral models, and presented in state space form. A linear dynamic analysis was performed to verify whether the derived decoupled linear model is indeed representative of the uncoupled full non-linear model. Both models were simulated in Matlab Simulink and the aircraft responses to steps in elevator, thrust, aileron, rudder, and differential thrust were compared. Results showed that the linear and non-linear responses matched well during the transient part of the simulation, but eventually diverged since the linear model in decoupled while the non-linear model is not. The linear model therefore sufficiently represents the transient dynamics of the aircraft, which is required for the design of a flight control system.

3.6 Formation Flight Model

Simulating a formation flight scenario requires additional modelling of the relative positioning among aircraft as well as the wake-induced forces and moments experienced by the follower. The relative positioning is divided into two parts: the geometrical separation between aircraft, which is required by the formation guidance system to maintain the relative aircraft positions, and the effective separation, which models the position of the follower relative to the trailing vortex generated by the leader. The additional wake-induced forces and moments are calculated through a wake-interaction model. The model uses the effective aircraft separation to determine the aerodynamic effects of the wake on the follower. The following sections present more detail on the formation flight model.

3.6.1 Formation Guidance Axis System

A formation guidance axis system was defined to determine the relative separations and separation rates between aircraft, and is shown in Figure 3.14. The formation guidance axis system is denoted by the superscript g and has orthogonal basis vectors $\boldsymbol{i^g}$, $\boldsymbol{j^g}$, and $\boldsymbol{k^g}$ that originate from the leader's centre of mass. The basis vector $\boldsymbol{i^g}$ is selected to coincide with the airspeed velocity vector of the leader aircraft projected in the inertial $X_I Y_I$-plane. This is to ensure that the formation guidance axis system is insensitive to instantaneous changes in the orientation of the body of the leader aircraft. If the formation separations were defined in the body axis system of the leader, instantaneous changes in the orientation of the leader's body would result in instantaneous changes in the formation separation. Due to the large axial distance between aircraft, a small change in leader body orientation would result in a large change in formation separation. Furthermore, the direction in which the trailing vortices propagate behind the leader is opposite to the direction of flight, and does not necessarily align with the leader's X_B-axis. The selection of the formation guidance base vector $\boldsymbol{i^g}$ in the inertial $X_I Y_I$-plane simplifies the calculation of the formation separations, since the formation guidance base vector $\boldsymbol{k^g}$ aligns with the inertial down axis Z_I. It is assumed that the leader aircraft does not execute large changes in altitude once engaged in formation flight, and that changes in the propagation direction of the trailing vortices due to small perturbations in the flight path angle of the leader are negligible.

Coordinating the axis system in the inertial axes yields,

$$\boldsymbol{i^g} = \left(\frac{\mathbf{V_I^L}}{|\mathbf{V_I^L}|} \cdot \boldsymbol{i}\right)\boldsymbol{i} + \left(\frac{\mathbf{V_I^L}}{|\mathbf{V_I^L}|} \cdot \boldsymbol{j}\right)\boldsymbol{j} + 0\boldsymbol{k} \tag{3.47}$$

where $\mathbf{V_I^L}$ is the velocity vector of the leader aircraft in the inertial axis. Writing $\boldsymbol{i^g}$ as a coordinate vector yields,

$$\mathbf{i_I^g} = \begin{bmatrix} \frac{\mathbf{V_I^L}}{|\mathbf{V_I^L}|} \cdot \boldsymbol{i} \\ \frac{\mathbf{V_I^L}}{|\mathbf{V_I^L}|} \cdot \boldsymbol{j} \\ 0 \end{bmatrix} \tag{3.48}$$

The unit basis vector $\boldsymbol{k^g}$ aligns with the inertial down-axis $\boldsymbol{k}$, and the orthogonal axis system is completed by defining $\boldsymbol{j^g}$ as,

$$\boldsymbol{j^g} = \boldsymbol{k^g} \times \boldsymbol{i^g} \tag{3.49}$$

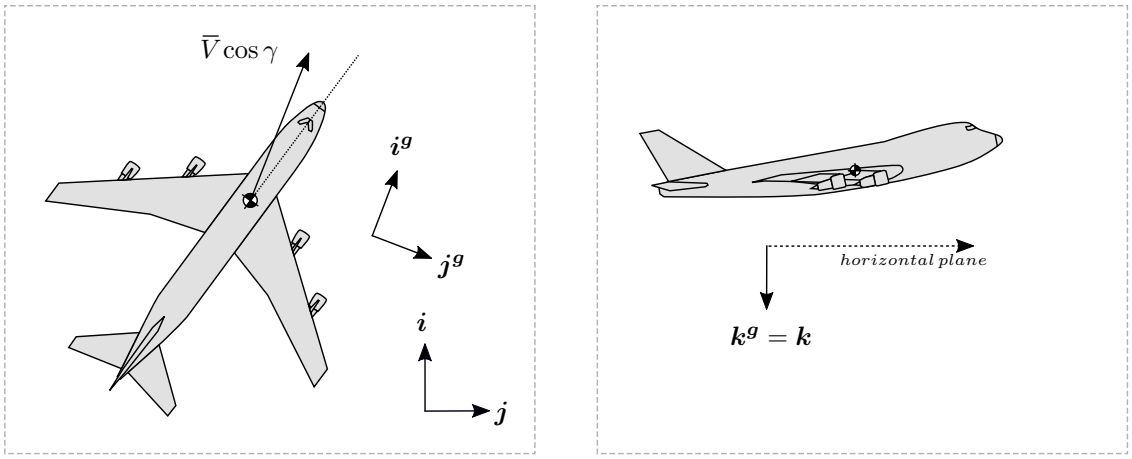

(a) Top view. (b) Side view.

Figure 3.14: Formation guidance axis system.

3.6.2 Geometrical and Effective Aircraft Separation

In the section that follows, the inertial positions of the leader and follower aircraft are used to calculate the relative position, or separation, of the follower aircraft with respect to the leader aircraft. This approach assumes that, in a real-world implementation, the aircraft in formation would communicate their positions, obtained from blending GPS and INS measurements, to one another through an air-to-air telemetry link [43]. For this study, it is assumed that the inertial position of leader is known to the follower exactly and without delay, since the typical measurement noise and signal propagation delay is expected to be negligibly small.

Geometrical Aircraft Separation

The geometrical aircraft separations, normalized to wingspan, are defined in the formation guidance axis system as shown in Figure 3.15. The axial separation ξ is the component in $\boldsymbol{i^g}$,

the lateral separation η is the component $\boldsymbol{j^g}$, and the vertical separation ζ is the component $\boldsymbol{k^g}$. Note that Figure 3.15a also shows the lateral separation rate $\dot{\eta}$, which is used by the formation flight control system.

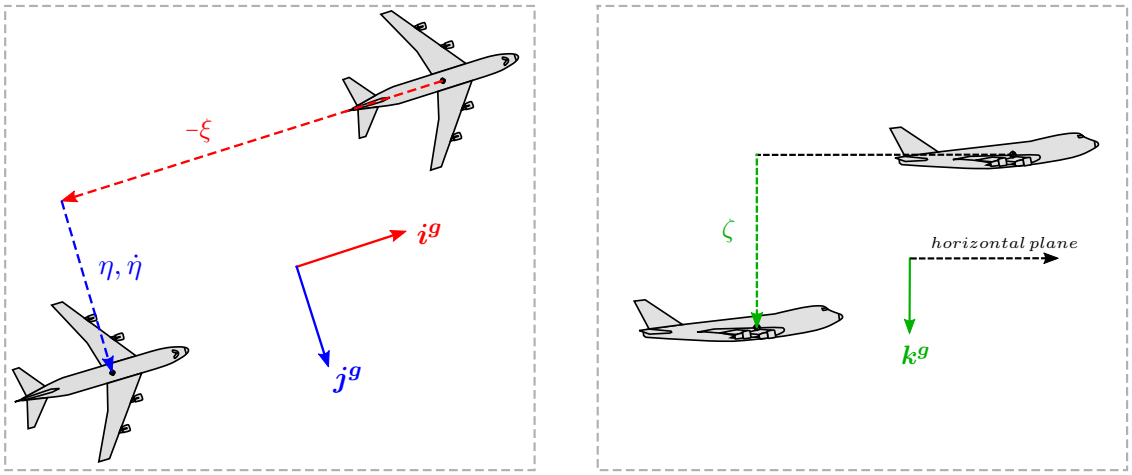

(a) Top view. (b) Side view.

Figure 3.15: Formation geometrical separations.

The geometric separations may be calculated through,

$$\xi = \frac{1}{b}\left(\mathbf{P_I^L} - \mathbf{P_I^F}\right) \cdot \mathbf{i_I^g} \tag{3.50a}$$

$$\eta = \frac{1}{b}\left(\mathbf{P_I^L} - \mathbf{P_I^F}\right) \cdot \mathbf{j_I^g} \tag{3.50b}$$

$$\zeta = \frac{1}{b}\left(\mathbf{P_I^L} - \mathbf{P_I^F}\right) \cdot \mathbf{k_I^g} = \frac{1}{b}\left(D^F - D^L\right) \tag{3.50c}$$

where b is the aircraft wingspan, and $\mathbf{P_I^L}$ and $\mathbf{P_I^F}$ are the inertial position coordinate vectors of the leader and follower respectively. Since the guidance basis vector $\boldsymbol{k^g}$ coincides with the inertial vector $\boldsymbol{k}$, the vertical separation reduces to the difference in the follower and leader down positions. The lateral separation rate $\dot{\eta}$ is calculated by taking the time derivative of Equation 3.50b,

$$\dot{\eta} = \frac{d}{dt}\left[\frac{1}{b}\left(\mathbf{P_I^L} - \mathbf{P_I^F}\right)\right] \cdot \mathbf{j_I^g} + \left(\mathbf{P_I^L} - \frac{1}{b}\mathbf{P_I^F}\right) \cdot \frac{d}{dt}\mathbf{j_I^g} \tag{3.51}$$

The first term in Equation 3.51 describes the rate at which η varies due to the rate at which the leader and follower positions change. The second term describes the rate at which η varies due to the rate at which the formation guidance axis system orientation changes relative to the follower. During conventional formation flight, the leader follows a track which changes very slowly during transit. Changes in the direction of the leader's velocity vector, and the rate at which the formation guidance axis will rotate, is thus assumed to be negligible. The second term of Equation 3.51 is regarded insignificant, and the lateral separation rate may be simplified to,

$$\dot{\eta} = \frac{d}{dt}\left(\mathbf{P}_\mathbf{I}^\mathbf{L} - \mathbf{P}_\mathbf{I}^\mathbf{F}\right) \cdot \mathbf{j}_\mathbf{I}^\mathbf{g} \tag{3.52}$$

Effective Aircraft Separation

In a real-world formation flight scenario, the trailing vortices generated by the leader are displaced due to external disturbances such as static wind, gusts and turbulence. Since the follower can only maintain a commanded geometrical separation, its position relative to the wake will change if the wake is displaced. Besides the displacement of the wake, there is also a time delay between the leader and the follower aircraft. This means that the wake effects that the follower experiences do not immediately change as the geometrical separation changes. The distance between the follower and the displaced wake, with the time delay taken into account, is defined as the effective separation.

Figure 3.16 shows the trailing vortices disturbed laterally and vertically by atmospheric velocities v_a and w_a respectively. It is assumed that the wake is not disturbed longitudinally, and that the effective axial separation is equal to the geometrical axial separation. Two intermediate separations are defined that only capture the displacement of the wake: the instantaneous lateral separation $\eta_{I,eff}$, and instantaneous vertical separation $\zeta_{I,eff}$. These separations are calculated though,

$$\eta_{I,eff} = \sqrt{\xi^2 + \eta^2}\sin(\psi^g - \psi_a) \tag{3.53a}$$

$$\zeta_{I,eff} = \sqrt{\xi^2 + \zeta^2}\sin(\theta^g - \theta_a) \tag{3.53b}$$

where the ψ^g and θ^g are the geometrical lateral and vertical angles between the leader and follower as shown in Figure 3.16, and where ψ_a and θ_a represent the angles by which the wake is disturbed laterally and vertically. These angles may be calculated through,

$$\psi_a = \arctan\left(\frac{v_a}{-\overline{V}\cos\gamma}\right) \tag{3.54a}$$

$$\theta_a = \arctan\left(\frac{w_a}{-\overline{V}\cos\gamma}\right) \tag{3.54b}$$

where v_a and w_a are the lateral and vertical atmospheric disturbance magnitudes, and $\overline{V}$ and γ are the airspeed magnitude and flight path angle of the leader respectively.

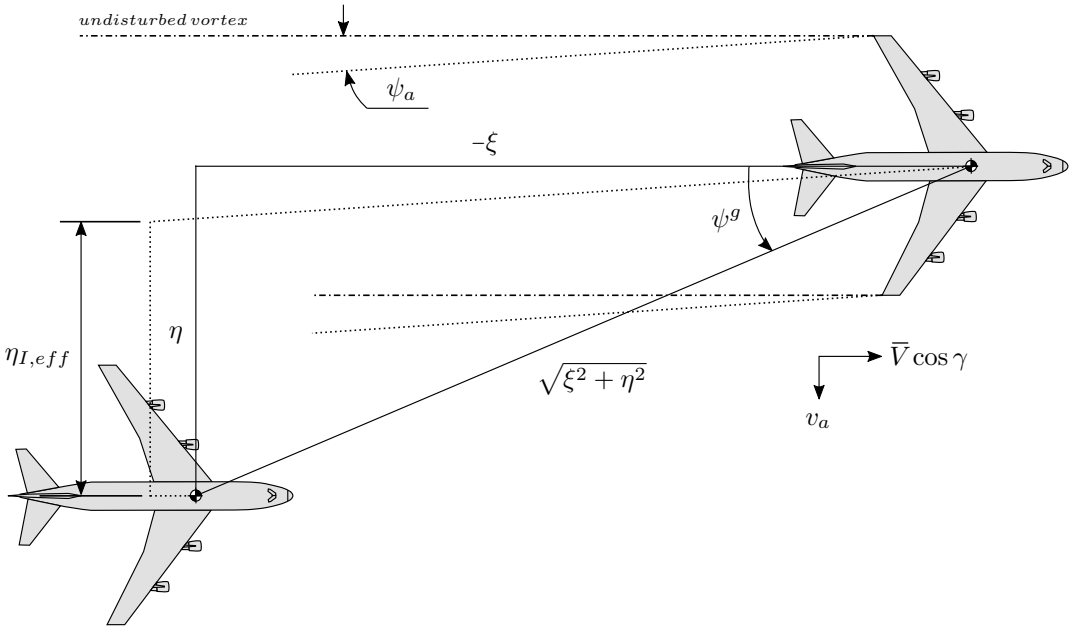

(a) Top view.

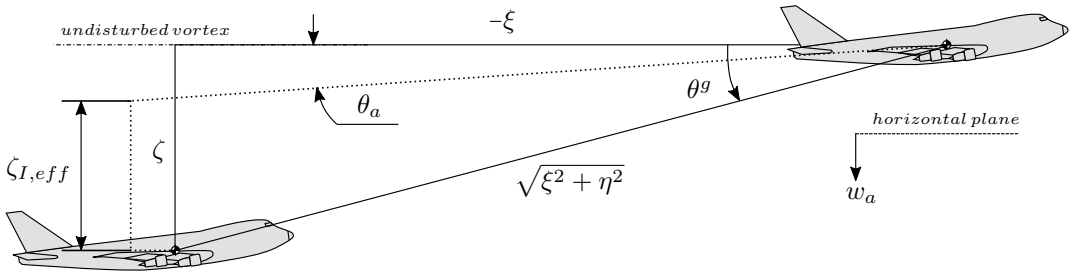

(b) Side view.

Figure 3.16: Effective aircraft separation.

Finally, the instantaneous separations $\eta_{I,eff}$ and $\zeta_{I,eff}$ are delayed by τ_d to obtain the effective separations η_{eff} and ζ_{eff} as follows,

$$\eta_{eff} = \eta_{I,eff}(t - \tau_d) \tag{3.55a}$$

$$\zeta_{eff} = \zeta_{I,eff}(t - \tau_d) \tag{3.55b}$$

The time delay τ_d is calculated by dividing the distance between the leader and follower aircraft by the average airspeed magnitude of the formation. This may be expressed mathematically as,

$$\tau_d = \frac{|\xi b|}{\overline{V}^F} \tag{3.56}$$

where $|\xi b|$ is the axial distance between aircraft, and $\overline{V}^F$ is the average airspeed magnitude of the formation.

3.6.3 Wake Interaction Model

Flying in the wake of a leader aircraft introduces additional aerodynamic forces and moments on the follower aircraft. These formation-induced effects may be modelled as incremental changes to the conventional aerodynamic coefficients as functions of the formation separation. In other words, the wake interaction changes the aerodynamic coefficient functions, and adds the separation variables as additional input variables to the aerodynamic coefficient functions. Figure 3.17 shows the formation-extended forces and moments model, which now includes the incremental wake-induced aerodynamic effects.

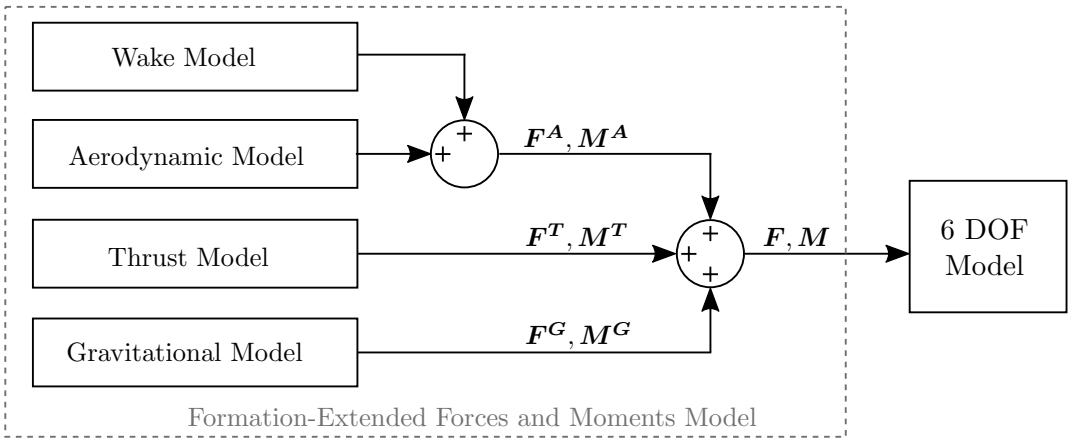

Figure 3.17: Formation-Extended Forces and Moments Model.

This study implements an aerodynamic interaction model developed by Bizinos et al.[10] which approximates the two counter-rotating wing-tip vortices through a single horseshoe vortex model. Two identical aircraft are considered in right echelon formation and the aerodynamic loads acting on the follower wing, tailfin, and tailplane are approximated by determining the downwash or sidewash at a particular point along the bound vortex. Integration along the bound vortex span produces induced load expressions for the incremental lift, drag, side force, rolling moment, and yawing moment. The incremental pitching moment is estimated by considering the change in downwash at the tailplane due to the wake-induced downwash at the wing. These loads are then converted to incremental wake-induced aerodynamic coefficients which are only dependant on lateral and vertical separation. Since the trailing vortices retain their shape and strength for several wingspans downstream, the effect of longitudinal separation is assumed to be negligible as long as the follower remains within the far-field wake [5].

The complete formation flight aerodynamic coefficients may be calculated through,

$$\boldsymbol{C}_{()_{S_k}} = \boldsymbol{C}_{()_S} + \boldsymbol{C}_{()_F} < \eta_{eff}, \zeta_{eff} > \tag{3.57}$$

where the vector $\boldsymbol{C}_{()_S}$ represents the conventional coefficients, and $\boldsymbol{C}_{()_F}$ the incremental formation coefficients as functions of the effective lateral separation η_{eff} and effective vertical separation ζ_{eff}. Details regarding the additional formation coefficients are presented in Appendix B.

3.7 Atmospheric Model

In a real world scenario, flying aircraft will be subjected to a variety of atmospheric phenomena, which include static winds, gusts, and atmospheric turbulence among others. In order to develop a comprehensive formation flight model, it is important to include the effect of these disturbances on the aircraft in formation. Static winds will greatly influence the position of the wake relative to the follower aircraft, which in turn has a significant effect on the reduction in drag. Atmospheric turbulence and gusts subject the formation to external disturbances that reduce the performance of the formation-hold controllers.

Figure 3.18 shows how the atmospheric model is implemented in the flight mechanics model, where $\mathbf{V_B}$ and $\boldsymbol{\omega_B}$ denote velocity and angular rate coordinate vectors in the body axes. The superscripts t and sw denote turbulence and static wind components respectively, while the superscript a denotes the total atmospheric component. The static wind and atmospheric turbulence are modelled separately and the velocity vectors obtained from each model are added together to produce the total velocity of the air around the aircraft. Note that the static wind model has no angular rate component. It is assumed that the contribution of the static wind to the angular rate of the air is negligible relative to the angular rate component contributed by turbulence over the size of the aircraft.

The atmospheric disturbances affect both the motion of the aircraft in formation and the trailing wake of the leader, which changes the effective formation separation as discussed in Section 3.6. The velocity and angular rate of the air are superimposed on the aircraft velocity and angular rate states in the body axes, which are then used to calculate the resulting aerodynamic forces and moments acting on the aircraft. The atmospheric disturbances thus indirectly affect the aircraft motion through the forces-and-moments model. Furthermore, the atmospheric velocity, coordinated in the formation guidance axis system, is used to calculate the effective formation separations.

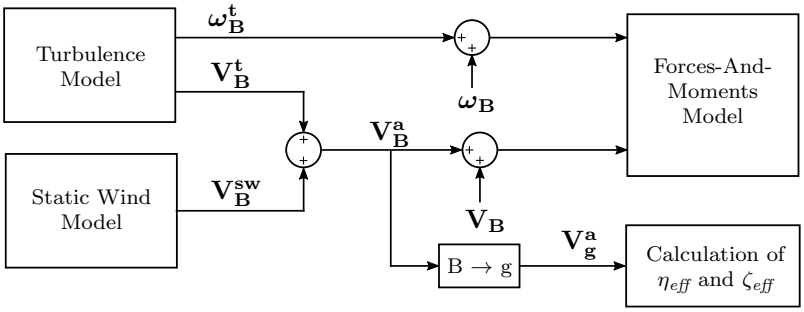

Figure 3.18: Implementation of atmospheric model.

In order to obtain the atmospheric velocity coordinate vector $\mathbf{V_g^a}$ in the formation guidance axis system, the coordinate vector $\mathbf{V_B^a}$ is converted to $\mathbf{V_I^a}$ in the inertial axis system through,

$$\mathbf{V_I^a} = \left[DCM\right]^\mathsf{T} \mathbf{V_B^a} \tag{3.58}$$

The velocity vector $\mathbf{V_g^a}$ is then obtained by projecting $\mathbf{V_I^a}$ in the formation guidance axis through,

$$\mathbf{V_g^a} = \begin{bmatrix} u_a \\ v_a \\ w_a \end{bmatrix} = \begin{bmatrix} \mathbf{V_I^a} \cdot \mathbf{i_I^g} \\ \mathbf{V_I^d} \cdot \mathbf{j_I^g} \\ \mathbf{V_I^a} \cdot \mathbf{k_I^g} \end{bmatrix} \tag{3.59}$$

of which the lateral component v_a and vertical component w_a are atmospheric velocities used to calculate the effective formation separations η_{eff} and ζ_{eff} respectively, as discussed in Section 3.6. The following sections present the modelling of the atmospheric turbulence and static wind.

3.7.1 Static Wind Model

A static wind model was developed using wind data obtained from a dataset containing real world measurements. The Earth System Research Laboratory (ESRL), which forms part of the U.S. Department of Commerce's National Oceanic and Atmospheric Administration (NOAA), provides global wind data in the inertial axes for various altitudes at evenly spaced latitude and longitude coordinates [44], as shown in Figure 3.19. The wind data used for this study was based on measurements for the year 2015.

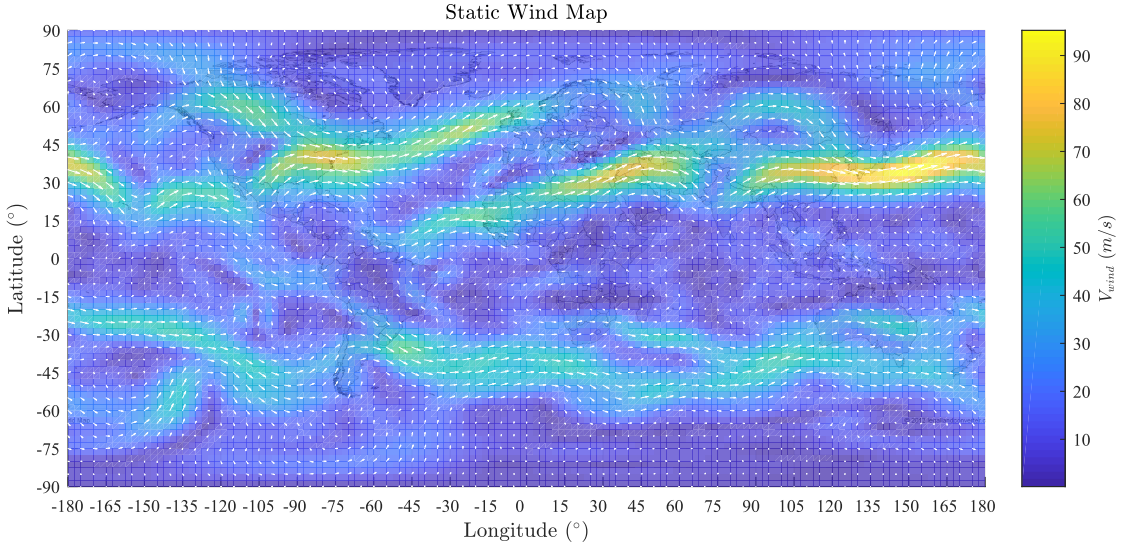

Figure 3.19: Static wind map.

The model converts the inertial position of the aircraft to latitude and longitude coordinates, extracts the appropriate wind values in the inertial axis from lookup tables, and finally outputs the wind values in the body axes. Figure 3.20 illustrates the operation of the model, where ΔN and ΔE represent the displacement of the aircraft in the inertial axes, λ represents the latitude and γ the longitude, and $\mathbf{V_I^{sw}}$ and $\mathbf{V_B^{sw}}$ represent the wind velocity coordinate vectors in the inertial and body axis systems respectively.

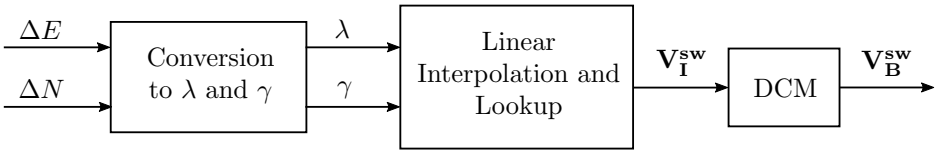

Figure 3.20: Operation of static wind model.

The latitude and longitude is calculated through,

$$\lambda = \frac{\Delta N}{r} \tag{3.60a}$$

$$\gamma = \frac{\Delta E}{r'} \quad where \quad r' = r\cos\lambda \tag{3.60b}$$

where r is the radius of the earth. The conversion is visually illustrated in Figure 3.21, where d represents the physical trajectory travelled on the earth's surface.

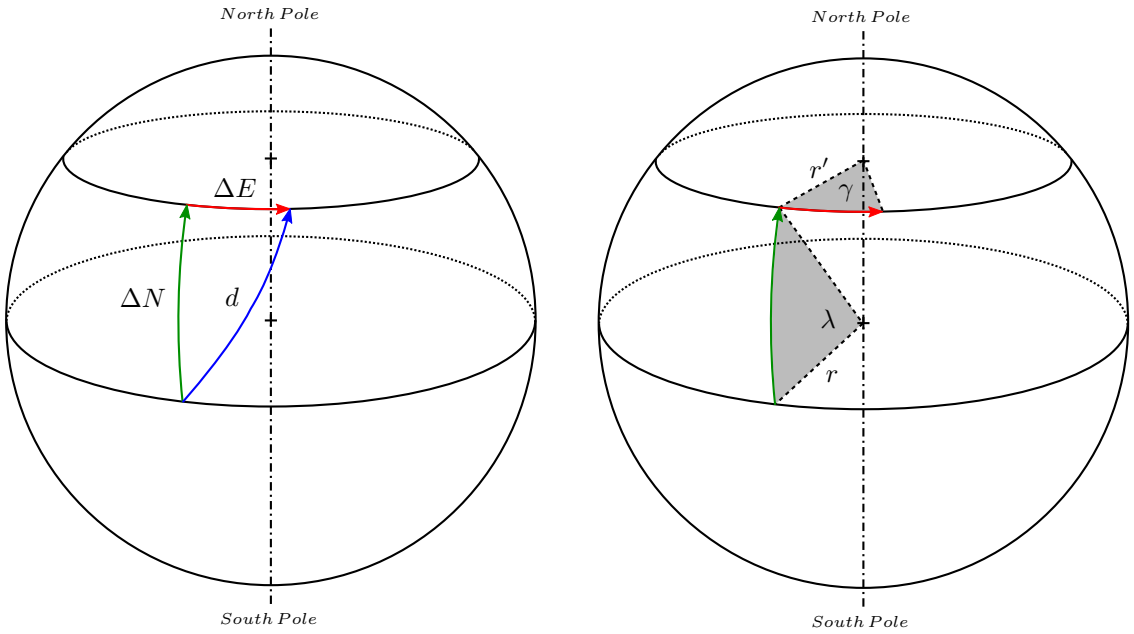

Figure 3.21: Conversion from inertial movement to latitude and longitude.

3.7.2 Atmospheric Turbulence Model

Atmospheric turbulence is commonly encountered during long range flights and may be classified into several pre-defined levels of intensity. These levels are determined by the nature of the turbulence source as well as the degree of stability of the air [45], and are generally defined as follows:

- **Light turbulence** is generally encountered in clean air and may be the result of several natural phenomena e.g. wind shear, jet streams, wind over and between mountains, which usually induce slight erratic changes in altitude and/or attitude. Severe levels of the natural phenomena listed above might increase the intensity of the turbulence.

- **Moderate turbulence** usually occurs when flying through or near Cumulus clouds, and is more intense than light turbulence with larger variations in altitude, attitude and/or airspeed. Control over the aircraft is maintained.
- **Severe turbulence** causes very large and abrupt changes in altitude and/or attitude and, usually, large variations in indicated airspeed. Severe turbulence is generally associated with thunderstorms and can be extremely hazardous, having the potential to cause structural damage or even loss of control.

Atmospheric turbulence is generally modelled as a stationary, isotropic, homogeneous Gaussian process, and is realised by passing band-limited white noise through forming filters that approximate one of two widely used power-spectra: the von Kármán spectrum or the Dryden spectrum. For this study, the von Kármán turbulence model is used rather than the Dryden, since it better matches observed data and is considered the standard for design use [46]. It is also the preferred model of the US Department of Defence in most aircraft design and simulation applications [47]. The von Kármán turbulence model is obtained from Matlab Simulink's Aerospace blockset [48], which determines the turbulence intensities from a lookup table.

The same generated turbulence field is applied to the leader and follower aircraft, considering that the lateral and vertical separations are negligible relative to the scale length of the turbulence field. Since the follower lags the leader, the turbulence experienced by the follower is simply delayed by the axial time separation between the aircraft.

A Note On Gusts

Atmospheric gusts can be classified as having either a continuous or 'discrete' profile [46]. Generally, when a gust profile is continuous, the gust structure is referred to as turbulence. When the gust structure consists of more or less isolated pulses, as shown in Figure 3.22, each pulse is referred to as a gust. Typically, however, gust profiles tend to be continuous and irregular [46, 49], as illustrated in Figure 3.23.

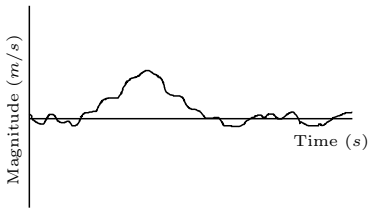

Figure 3.22: Isolated gust profile.

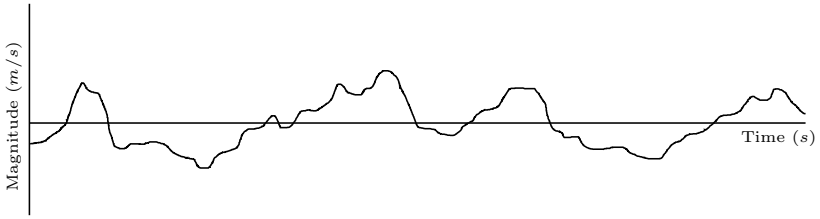

Figure 3.23: Typical continuous gust profile.

In the work of Hoblit [46], it is stated that a continuous turbulence profile can be thought

of as consisting of a series of individual gusts. This concept is illustrated in Figure 3.24. The intensities and time scales associated with gust measurements found in literature are relatively close to that of turbulence [49, 50], considering that those associated with static wind are orders of magnitude larger. Initially, it was intended to have separate static wind, turbulence, and gust models, but after inspection of the turbulence data generated by the Matlab von Kármán model, it was found that the model already generates gust pulses. Figure 3.25 presents lateral turbulence data generated by the von Kármán model as discussed above. Individual gust pulses can clearly be identified, and are approximated, for visual convenience, by the black dotted curves. The effect of gusts are thus already included in the turbulence model provided by Matlab, and it is therefore not necessary to explicitly model external gusts. The wind velocities and angular rates generated by the model is deemed representative of typical gusts encountered during flight.

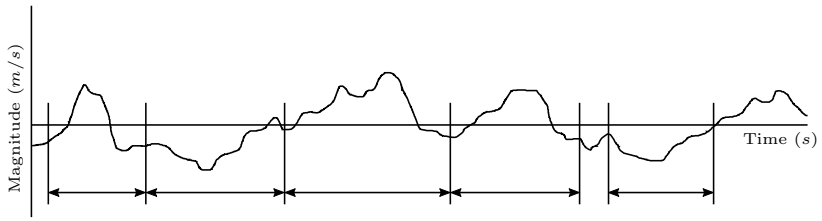

Figure 3.24: Turbulence comprising a series of individual gusts.

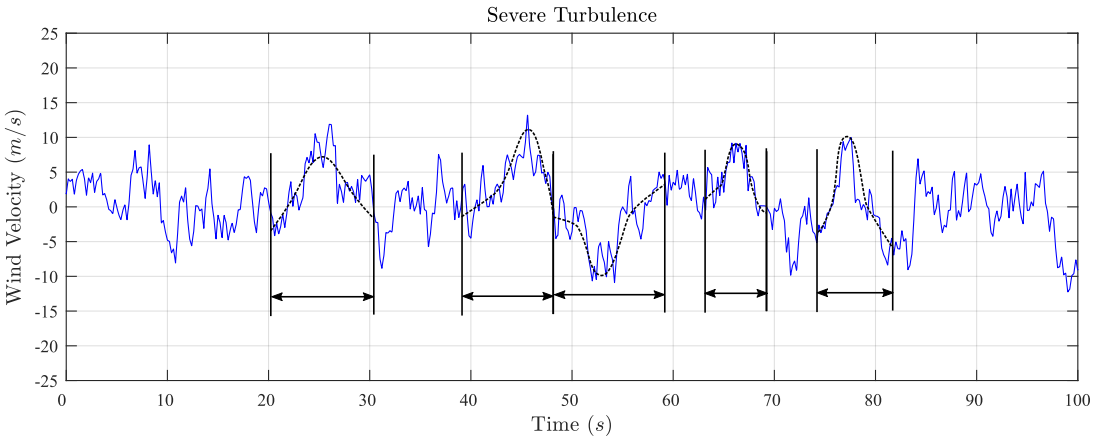

Figure 3.25: Turbulence generated by MATLAB model.

Chapter 4

Fly-by-wire Flight Control System Design

This chapter presents the design of a complete flight control system for multiple aircraft in extended formation flight. Similar to the work done by the previous studies, the architecture of the flight control system is inspired by that of a typical Airbus, and includes the complementary filter control designed by van Wyk [2].

In order to maintain a specific flight condition and trajectory, modern commercial airliners are equipped with a fly-by-wire flight control system that determines the required actuation of each control surface when commands are provided by the pilot. In addition, the control system also aids in stabilizing the aircraft without the explicit knowledge of the pilot. For the purpose of flying multiple aircraft in formation, additional flight controllers are necessary to maintain the desired formation separation. Previous studies at Stellenbosch University have addressed the design of an extended flight control system, based on the flight controller architecture of an Airbus A320/330 [2, 4]. The specifications for the control laws were selected to ensure that the closed-loop responses of the Boeing 747 are representative of what is expected of a typical Airbus aircraft.

The design of both the conventional and formation flight control systems are presented as follows: first, a brief background is provided on the general fly-by-wire architecture used on the Airbus aircraft, which includes an overview of the longitudinal and lateral controller structures. Next, the control architecture and design of the conventional flight control system is presented. Since the linear dynamic models were decoupled, the longitudinal and lateral controllers are designed independently. The closed-loop step responses are simulated for both the derived linear and full non-linear Boeing 747 aircraft models. Finally, the architecture and design of the extended formation flight controllers are presented, following a similar procedure as for the conventional flight control system. In addition, the complementary filter control, which allows for utilisation of differential thrust, is presented and discussed.

4.1 Fly-by-wire Control Architecture for Commercial Aircraft

The implementation of fly-by-wire (FBW) flight control systems on commercial airliners is a relatively modern concept, in which the classical manual flight controls are replaced with an electronic interface. Instead of the pilot directly controlling the actuators of the aircraft through the centre stick, rudder pedals, and throttle control, an on-board flight control system is interposed between the pilot and the control actuators. Physical pilot commands are converted to electrical signals and transmitted to the flight control system, which is then responsible for calculating and commanding the required control surface actuation. In

addition, automatic fly-by-wire flight control systems may also autonomously aid the pilot in stabilising the aircraft.

Figure 4.1 illustrates the general fly-by-wire architecture employed by Airbus. The fly-by-wire control system receives control inputs from the pilot, as well as feedback of the relevant anemometric and inertial measurements, and provides the required control surface commands. Flight control laws are designed to control the longitudinal and lateral behaviour of the aircraft in accordance with the desired specifications, which are usually selected to improve the natural responses and flying qualities of the aircraft [51]. A typical fly-by-wire control system consists of several flight controllers, which are usually divided into inner-loop, middle-loop, and outer-loop controllers. Inner-loop controllers typically control the fastest dynamics (acceleration) of the aircraft, and are responsible for providing the control surface commands. The middle-loop controllers are used to control velocity related dynamics of the aircraft, such as the airspeed and climb rate, and supply acceleration references to the inner-loop controllers. Finally, the outer-loop controllers control the slowest dynamics of the aircraft, such as changes in inertial position, and supply references to the middle-loop controllers. With a full flight control system implemented, the workload of the pilot is reduced to only providing control commands to the aircraft.

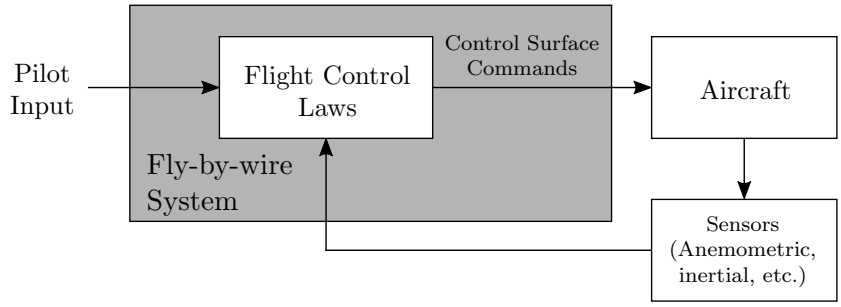

Figure 4.1: General fly-by-wire control architecture (adapted from [51]).

Three different flight control law configurations are implemented in the typical Airbus FBW system. In the first configuration, namely the Normal mode, the pilot controls the aircraft indirectly through the flight control system, and additional stability and handling quality augmentation functions and flight envelope protection systems are active to aid the pilot. In the second configuration, called the Alternative mode, these additional protection functions are disabled. Finally, the third configuration, called the Direct mode, is reserved only for cases where severe failures occur, and these cases require direct control of the control surfaces of the aircraft. This study will focus only on operation in the Normal mode.

The following two sections present the two Normal mode inner-loop control laws unique to the flight control system implemented by Airbus. The first is a longitudinal control law that is responsible for controlling the vertical load factor of the aircraft, while the second is a lateral control law responsible for controlling roll rate and sideslip angles of the aircraft.

Longitudinal Control Law

Figure 4.2 illustrates the Normal mode controller architecture of the longitudinal law. The controller receives a vertical load factor command from the pilot and uses feedback of the load factor and pitch rate of the aircraft to provide the required elevator (and/or horizontal stabilizer) deflection command. The controller comprises a combination of state feedback and integral control, with additional feed-forward of the load factor command to the elevator

deflection command. The integral control of the load factor is to ensure minimal error tracking of the load factor command, while the feed-forward of the load factor command allows for faster responses in load factor. Typically, it is desirable to increase the damping of the short period mode of the aircraft, which is performed through the state feedback control of load factor and pitch rate [51].

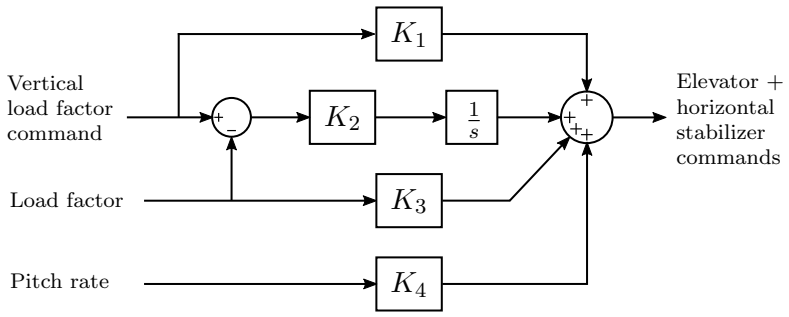

Figure 4.2: Longitudinal control law architecture (adapted from [51]).

Lateral Control Law

Figure 4.3 illustrates the Normal mode controller architecture of the lateral law, which is responsible for controlling the roll angle and sideslip angle of the aircraft. The controller receives roll rate and sideslip angle commands from the pilot and uses full lateral state feedback to provide the required aileron and rudder commands. The roll rate commanded by the pilot is integrated to produce a roll angle command, while feed-forward of the roll rate command is used to decrease the roll response time. The rudder pedal inputs provided by the pilot translate to a combination of both sideslip and roll angle commands, resembling the natural response expected by a pilot when flying a mechanically actuated aircraft. During the natural response of an aircraft, a positive sideslip angle induces a negative rolling moment. This response is reproduced by the control law through the subtraction of the sideslip command from commanded roll angle. A mixing gain matrix K_p is included to command the correct amount of aileron and rudder deflection required to counter the adverse yaw and rolling effects when commanding non-zero bank and sideslip angles, and reduces the workload of the pilot. Typically, the damping of the Dutch roll mode is increased by feeding back the lateral states of the aircraft through the gain matrix K_{ret}, which leaves the roll mode unchanged and increases the stability of the spiral mode [51].

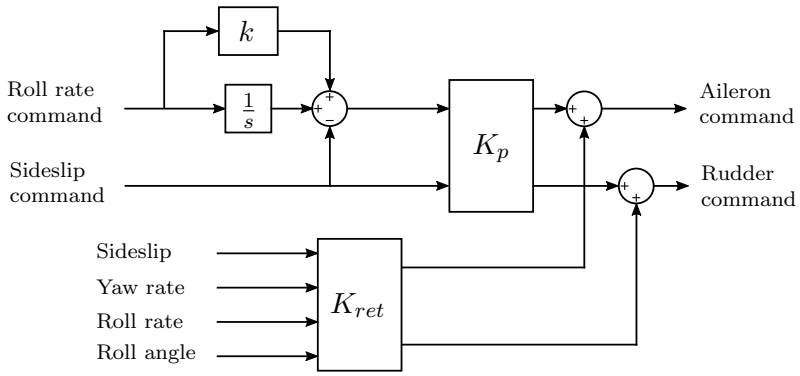

Figure 4.3: Lateral control law architecture (adapted from [51]).

A Note on Conventional Controller Specifications

The controller specifications for both the longitudinal and lateral conventional controllers were selected based on the typical responses of an Airbus A330 aircraft. In the work of Trollip [4], the desired responses of the various controllers were obtained from the simulation results of an Airbus A330 Simulink model. In order for the conventional control system to have similar performance, Trollip formulated the specifications of each controller based on its respective A330 response. Since this study follows a similar controller design procedure and architecture, all control specifications were obtained from the work of Trollip, unless other wise stated.

4.2 Conventional Longitudinal Control System Design

The architecture of the conventional longitudinal control system implemented on the Boeing 747 simulation model, is illustrated in Figure 4.4, and comprises two inner-loop and two guidance-loop controllers. The inner-loop controllers directly command the aircraft actuators based on their respective reference inputs received from the guidance-loop controllers or pilot.

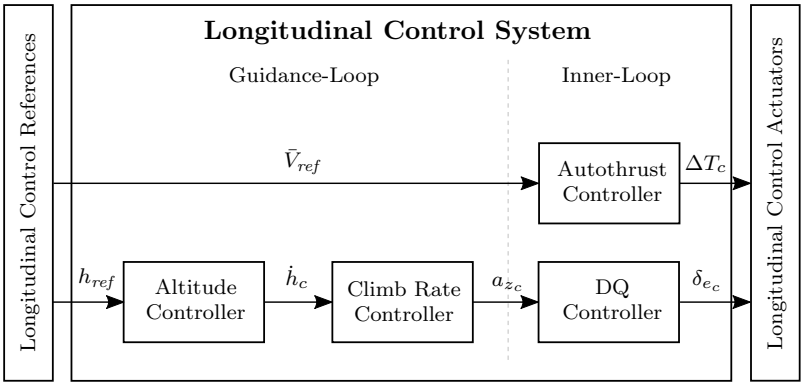

Figure 4.4: Longitudinal controller architecture.

The DQ controller, which originates from the Airbus Normal mode control architecture, increases pitch rate damping and controls the normal acceleration of the aircraft. Since the load factor of the aircraft may be calculated by dividing normal acceleration by the gravity constant, the DQ controller is in essence similar to the vertical load factor controller used in the Airbus architecture. A normal acceleration reference is provided by the first middle-loop controller, namely the climb rate controller. Next, a reference altitude is maintained through use of the second outer-loop controller, an altitude controller, that provides a climb rate reference to the climb rate controller. During take-off and landing, typical flight control systems employ a flight path angle controller, rather than climb rate controller, for altitude-hold control. Climb rate control is generally reserved for nominal cruising conditions, and is for this reason considered in this study rather than a flight path angle controller. Finally. an autothrust controller regulates the desired airspeed by commanding engine thrust.

This section presents the design and verification of the conventional longitudinal control system. The design of the longitudinal control system follows a successive loop closure approach. The inner-loop DQ controller and autothrust controllers are designed using the natural aircraft dynamics as the plant model. The middle-loop climb rate controller is designed next using the closed-loop dynamics after closing the inner loops as the plant model. (The aircraft model is augmented with the autothrust controller before adding the climb rate

controller, since effective climb rate control can only be achieved once the airspeed is successfully regulated.) The outer-loop altitude-hold controller is designed last using the closed-loop dynamics of the middle-loop climb rate controller as the plant model. The aircraft model is augmented with the autothrust control before adding the climb rate controller, since effective climb rate control can only be achieved once the aircraft airspeed is successfully regulated. First the design of the DQ controller is presented, followed by the climb rate controller. Next, the autothrust controller is discussed, and finally, the altitude-hold controller.

4.2.1 DQ Law: A Normal Acceleration Controller

The DQ controller is the first in a consecutive loop of controllers that aim to control the altitude of the aircraft, and the controller architecture is shown in Figure 4.5. The total normal acceleration in the body-axis of the aircraft is regulated through command of elevator deflection to change the angle of attack. Pitch rate feedback is used to increase the damping of the short period mode. The controller utilises state feedback as well as integral control, and is designed by means of a reduced order model which closely corresponds to the work of Trollip [4].

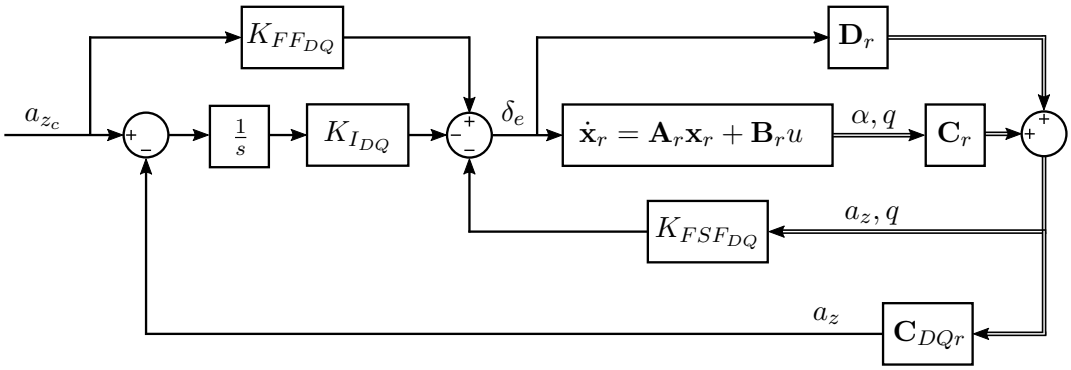

Figure 4.5: DQ controller architecture.

Reduced-Order Model

The DQ controller is designed using a reduced-order model of the linearised longitudinal dynamics, since the short period mode of the aircraft can accurately be described by only two states: the angle of attack α and pitch rate q. The airspeed of the aircraft is considered to vary very slowly relative to the angle of attack and pitch rate, and is therefore assumed to be constant in the model. The pitch angle does not couple back strongly into either the angle of attack or the pitch rate, and can therefore be omitted from the reduced-order model. By having only angle of attack and pitch rate as states, a full state feedback design method may be used to calculate the feedback gains. The state space model of the reduced-order model is given by,

$$\dot{\boldsymbol{x}}_r = \boldsymbol{A}_r\boldsymbol{x}_r + \boldsymbol{B}_r\delta_{e_c}$$

$$\begin{bmatrix}\dot{\alpha}\\ \dot{q}\end{bmatrix} = \begin{bmatrix}\frac{\partial\dot{\alpha}}{\partial\alpha} & \frac{\partial\dot{\alpha}}{\partial Q}\\ \frac{\partial\dot{Q}}{\partial\alpha} & \frac{\partial\dot{Q}}{\partial Q}\end{bmatrix}\begin{bmatrix}\alpha\\ q\end{bmatrix} + \begin{bmatrix}\frac{\partial\dot{\alpha}}{\partial\delta_e}\\ \frac{\partial\dot{q}}{\partial\delta_e}\end{bmatrix}\delta_{e_c} \tag{4.1}$$

where the state vector of the model consists of the angle of attack and pitch rate states. Figure 4.6 shows the angle of attack and pitch rate responses of the full-order and reduced-order models to a unit step in elevator deflection command. A comparison of the responses indicate that the reduced-order model adequately describes the full-order model over the time scales of the short period mode of the aircraft.

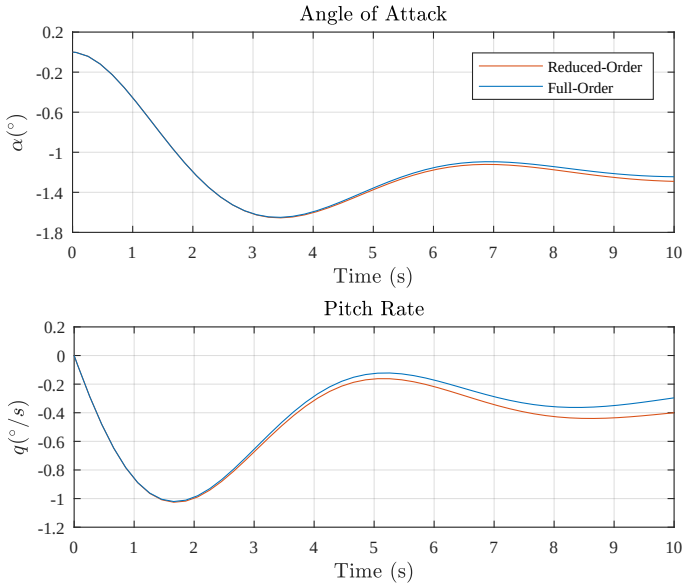

Figure 4.6: Comparison of reduced and full-order linear models.

Since the DQ controller requires feedback of the total normal acceleration, the total normal acceleration must be linearised and expressed as a function of the two reduced-order aircraft states. The total normal acceleration a_z of the aircraft is the sum of the specific normal acceleration, which excludes normal acceleration due to gravity, and the normal component of the gravitational acceleration. It is assumed that acceleration measurements from the aircraft sensors have been adapted to take into account the effect of gravity, thus providing the total normal acceleration a_z, as opposed to only the normal specific acceleration as typically provided by accelerometers. The total normal acceleration in the body axis is described by the following non-linear equation,

$$a_z = \frac{-qSC_L}{m} + g\cos\Theta \tag{4.2}$$

where it is assumed that the aircraft is flying straight and level at a small angle of attack, and that the drag force experienced by the aircraft is an order of magnitude smaller than the lift. The first term in Equation 4.2 describes the aerodynamic contribution to the total normal acceleration, while the second term describes the component due to gravitational acceleration. Since the angle of the engines with respect to the X-axis is very small, the contribution of the thrust to the force in the Z-axis is assumed to be negligibly small. The normal acceleration is linearised about the trim condition to yield,

$$a_z = a_{z_T} + \Delta a_z \tag{4.3}$$

While flying at trim, the aircraft is in equilibrium, and $a_{z_T} = 0$. The linearised normal acceleration may be expressed in state space form as,

$$\Delta a_z = \mathbf{C}_{a_z} \Delta \mathbf{x} + D_{a_z} \Delta u \tag{4.4}$$

where the output matrix $\mathbf{C}_{a_z}$ and feed-forward gain D_{a_z} are given by,

$$\mathbf{C}_{a_z} = \left[\frac{\partial a_z}{\partial \bar{V}} \quad \frac{\partial a_z}{\partial \alpha} \quad \frac{\partial a_z}{\partial Q} \quad \frac{\partial a_z}{\partial \Theta} \right]_T \tag{4.5a}$$

$$D_{a_z} = \left. \frac{\partial \alpha_z}{\partial \delta_e} \right|_T \tag{4.5b}$$

The reduced-order model described in Equation 4.1 is augmented to have the normal acceleration, as derived above, and pitch rate as states. This augmented model serves as the plant for the design of the DQ controller, and is expressed in state space form as,

$$\begin{aligned} \dot{\mathbf{x}}_{DQr} &= \mathbf{A}_{DQr} \mathbf{x}_{DQr} + \mathbf{B}_{DQr} \delta_e \\ a_z &= \mathbf{C}_{DQr} \mathbf{x}_{DQr} \end{aligned} \tag{4.6}$$

where the state vector $\mathbf{x}_{DQr}$ now consists of the states normal acceleration a_z and pitch rate q. The state matrix $\mathbf{A}_{DQr}$ is obtained after modifying the original reduced-order state matrix $\mathbf{A}_r$ to have the normal acceleration as a state instead of angle of attack, and is expressed mathematically as,

$$\mathbf{A}_{DQr} = \mathbf{C}_r \mathbf{A}_r \mathbf{C}_r^{-1} \tag{4.7}$$

where

$$\mathbf{C}_r = \begin{bmatrix} \frac{\partial a_z}{\partial \alpha} & \frac{\partial a_z}{\partial Q} \\ 0 & 1 \end{bmatrix} \tag{4.8}$$

Similarly, the input matrix $\mathbf{B}_{DQr}$ is obtained after modifying the original reduced-order input matrix $\mathbf{B}_r$,

$$\mathbf{B}_{DQr} = \mathbf{C}_r \mathbf{B}_r \tag{4.9}$$

Finally, the normal acceleration is extracted from the state vector $\mathbf{x}_{DQr}$ using the output matrix $\mathbf{C}_{DQr} = \begin{bmatrix} 1 & 0 \end{bmatrix}$. Note that the normal acceleration is not written as a function of the elevator deflection. The feed-forward from elevator deflection to normal acceleration is omitted from the design as it introduces an undesired non-minimum phase response which complicates the design process. Typically, the elevator does not significantly contribute to the normal acceleration output of the aircraft directly. Compared to the contribution of the states of the aircraft, the direct contribution of the elevator is negligible. The term $\mathbf{D}_r = \begin{bmatrix} D_{a_z} & 0 \end{bmatrix}$ is included in the architecture in Figure 4.5 for completeness only.

DQ Controller Design Using Reduced-Order Model

A full-state feedback controller with added integral control is designed with the reduced-order plant as described above. Although the integral control removes steady-state error in normal acceleration output, it introduces undesired integrator dynamics which slows down the system response resulting in a longer settling time. This effect is mitigated through use of a pole-zero cancellation technique to introduce a feed-forward term $K_{FF_{DQ}}$ from the normal acceleration command to the elevator deflection command. The integrator dynamics are described mathematically by,

$$\begin{aligned} \dot{x}_{I_{DQ}} &= a_{z_c} - a_z \\ &= a_{z_c} - (\mathbf{C}_{DQr}\mathbf{x}_{DQr}) \end{aligned} \tag{4.10}$$

$$x_{I_{DQ}} = \int_0^t (a_{z_c} - a_z)dt \tag{4.11}$$

and added to the reduced-order state space model to give,

$$\begin{bmatrix} \dot{\mathbf{x}}_{DQr} \\ \dot{x}_{I_{DQ}} \end{bmatrix} = \begin{bmatrix} \mathbf{A}_{DQr} & \mathbf{0}_{2\times 1} \\ -\mathbf{C}_{DQr} & 0 \end{bmatrix} \begin{bmatrix} \mathbf{x}_{DQr} \\ x_{I_{DQ}} \end{bmatrix} + \begin{bmatrix} \mathbf{B}_{DQr} \\ 0 \end{bmatrix} \delta_e + \begin{bmatrix} \mathbf{0}_{2\times 1} \\ 1 \end{bmatrix} a_{z_c} \tag{4.12}$$

The full-state feedback control law is given by,

$$\delta_e = -\mathbf{K}_{DQr} \begin{bmatrix} \mathbf{x}_{DQr} \\ x_{I_{DQ}} \end{bmatrix} + K_{FF_{DQ}} a_{z_c} \tag{4.13}$$

where $\mathbf{K}_{DQr} = \begin{bmatrix} \mathbf{K}_{FSF_{DQ}} & K_{I_{DQ}} \end{bmatrix}$. The first term in $\mathbf{K}_{DQr}$ is the normal acceleration and pitch rate state feedback gain matrix $\mathbf{K}_{FSF_{DQ}}$, and the second term $K_{I_{DQ}}$ is the integrator gain. The gain vector $\mathbf{K}_{DQr}$ is calculated using a pole placement design technique. Since the integrator gain $K_{I_{DQ}}$ and integrator pole location p_i is known after the pole placement design is performed, the feed-forward gain may be calculated through,

$$K_{FF_{DQ}} = \frac{K_{I_{DQ}}}{p_i} \tag{4.14}$$

Specifications

The natural short-period mode of the Boeing 747 is lightly damped with a damping ratio of $\zeta_{sp} = 0.336$, which results in an oscillatory transient response when the longitudinal dynamics are excited, as shown in Figure 3.9. Through use of a pole placement design, the damping of the short-period dynamics of the aircraft can be increased, while maintaining the same natural frequency. This ensures that the aircraft behaves naturally as expected by the pilot. In accordance with the requirements for Category A flight phases of the military standard MIL-STD-1797A, the desired damping ratio is chosen to be,

$$\zeta_{sp} = 0.9 \tag{4.15}$$

The natural frequency of the open-loop short-period mode is found to be,

$$\omega_{n_{sp}} = 0.9673 \tag{4.16}$$

and the desired natural frequency for the DQ controller closed-loop dynamics is therefore chosen to be $\omega_{n_{DQ}} = 1\,rad/s$. Finally, the closed-loop pole that corresponds to the open-loop integrator pole is placed close to the origin but sufficiently far from the phugoid mode poles. The DQ controller design choices is summarized in Table 4.1.

Table 4.1: Summary of DQ controller design specifications.

Longitudinal System	Mode	Poles	$\omega_{n_{sp}}$	ζ_{sp}
Open-Loop	Short-period	$-0.325 \pm 0.911i$	0.967	0.336
Desired DQ Closed-Loop	Short-period	$-0.900 \pm 0.436i$	1	0.9
DQ Integrator Placement		-0.22		

Figure 4.7 shows the open-loop and desired closed-loop poles in the s-plane.

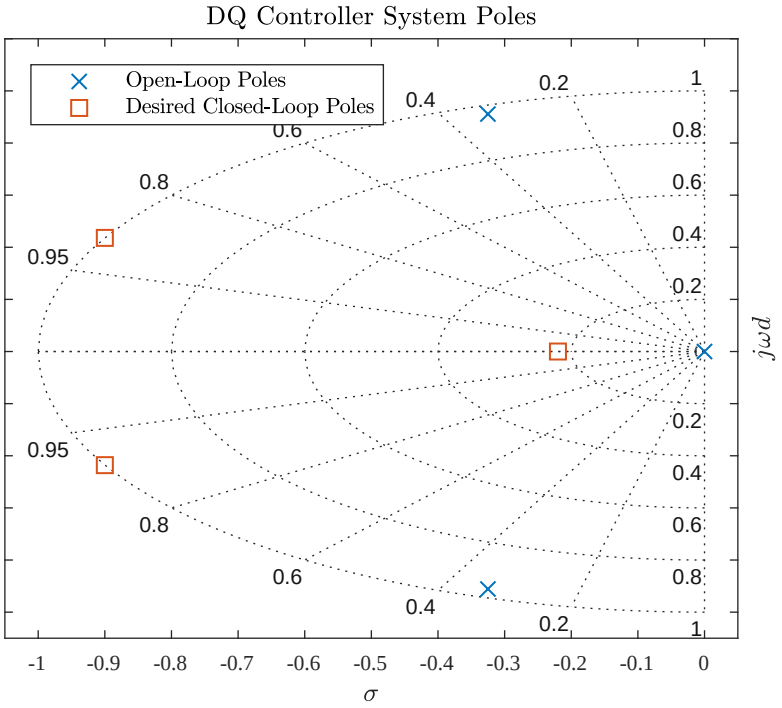

Figure 4.7: Comparison of open-loop and desired closed-loop DQ controller poles.

Simulation Results

Figure 4.8 shows the linear and non-linear closed-loop step responses of the DQ controller. In Figure 4.8a the reduced-order responses are shown for simulations with and without the feed-forward gain. Without the feed-forward gain, the response is fairly slow but the integrator ensures zero steady-state error. When the feed-forward gain is included, the speed of the response is significantly improved with a final settling time of approximately 5 seconds.

Figure 4.8b shows a comparison between the step responses of the full-order linear and non-linear aircraft models. The results show that the linear model approximates the non-linear model well. The observed steady-state error is expected since the aircraft has no means by which to control its airspeed and climb rate. As the aircraft attempts to increase its normal acceleration, it goes into a steep dive, which results in an increase in airspeed. As the aircraft's airspeed increases, the lift force in the positive body z-axis increases, which tends to pitch the aircraft up and decrease the normal acceleration. In order to increase and maintain the commanded normal acceleration, a larger force is required in the negative body z-axis to counter the increasing lift force. Since the normal component of the gravitational force decreases as the aircraft pitches down, a positive elevator deflection is commanded in an attempt to prevent the decrease in total normal acceleration, as shown in Figure 4.9. However, the airspeed continually decreases and the controller is unable to track the commanded normal acceleration. The addition of the autothrust controller in the following section keeps the airspeed constant, while a climb rate controller prevents the aircraft from entering a steep climb or a steep dive, which would disturb the airspeed. At the start of the step response shown in Figure 4.8b, a slight "dip" is observed in the response. This is due to the non-minimum phase dynamics introduced by the feed-forward gain D_{a_z} included in the full-order linear model.

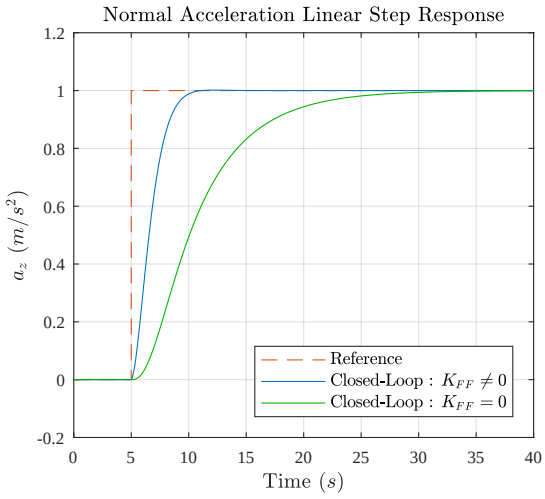

(a) Closed-Loop step response of the reduced-order linear model.

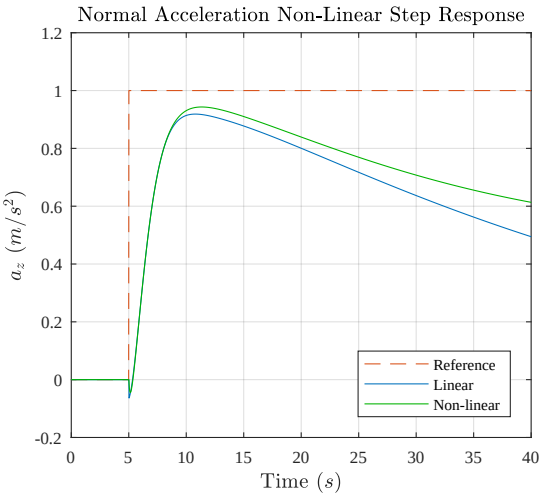

(b) Full-order linear versus the non-linear response.

Figure 4.8: DQ controller step response results.

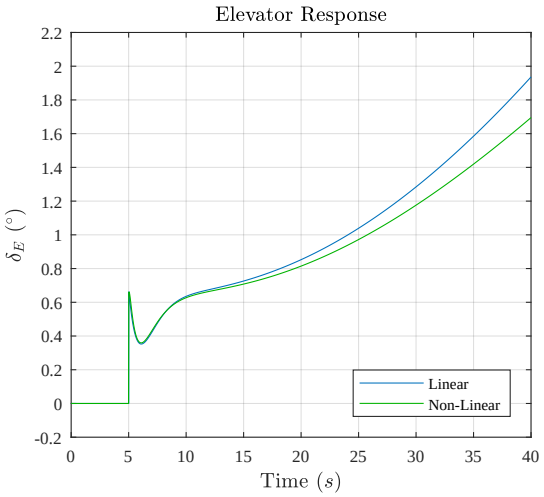

Figure 4.9: Elevator response to a step in the normal acceleration command.

Closed-Loop Model

The closed-loop model that includes the dynamics of the longitudinal model and DQ controller will serve as the open-loop plant for the next controller. The state-space of this closed-loop model can be derived as,

$$\dot{\mathbf{x}}_{DQ} = \mathbf{A}_{DQ}\mathbf{x}_{DQ} + \mathbf{B}_{DQ}\mathbf{u}_{DQ} \tag{4.17}$$

$$\begin{aligned}\begin{bmatrix}\dot{\mathbf{x}}_{long}\\ \dot{x}_{I_{DQ}}\end{bmatrix} &= \begin{bmatrix}\mathbf{A}_{long} - \mathbf{B}_{\delta_e}N\mathbf{K}_{DQ}\mathbf{C}_{DQ} & -NK_{I_{DQ}}\mathbf{B}_{\delta_e}\\ -\mathbf{C}_{a_z} + N\mathbf{K}_{DQ}\mathbf{C}_{DQ}D_{a_z} & NK_{FF_{DQ}}D_{a_z}\end{bmatrix}\begin{bmatrix}\mathbf{x}_{long}\\ x_{I_{DQ}}\end{bmatrix}\\ &+ \begin{bmatrix}NK_{FF_{DQ}}\mathbf{B}_{\delta_e} & \mathbf{B}_{\Delta T}\\ 1 - NK_{FF_{DQ}}D_{a_z} & 0\end{bmatrix}\begin{bmatrix}a_{z_c}\\ \Delta T\end{bmatrix}\end{aligned} \tag{4.18}$$

where the output matrix $\mathbf{C}_{DQ}$ and feed-forward vector $\mathbf{D}_{DQ}$ are given by,

$$\mathbf{C}_{DQ} = \begin{bmatrix}1 & 0 & 0 & 0\\ \multicolumn{4}{c}{\mathbf{C}_{a_z}}\\ 0 & 0 & 1 & 0\\ 0 & 0 & 0 & 1\end{bmatrix}, \qquad \mathbf{D}_{DQ} = \begin{bmatrix}0 & D_{a_z} & 0 & 0\end{bmatrix} \tag{4.19}$$

The full state gain vector $\mathbf{K}_{DQ}$ is given by,

$$\mathbf{K}_{DQ} = \begin{bmatrix}0 & k_{a_z} & k_q & 0\end{bmatrix} \tag{4.20}$$

where K_{a_z} and K_q are the feedback gains of normal acceleration and pitch rate respectively. The auxiliary variable N, of which the derivation may be found in Appendix C, may be expanded to,

$$N = \frac{1}{1 + \mathbf{K}_{DQ}\mathbf{D}_{DQ}} \tag{4.21}$$

Figure 4.10 shows the location of the new closed-loop system poles of the full longitudinal aircraft model, which now includes the phugoid mode poles omitted in the reduced-order model. The effect of the elevator feed-forward term is also shown as a slight shift in the closed-loop poles from their designed positions. The choice to leave out this term during the design process is therefore validated, since it had little effect on the system dynamics. Note, however, that the addition of the DQ controller has changed the dynamics of the phugoid mode from a stable second order response to an unstable first order response. The DQ controller, however, is only tasked with controlling the normal acceleration of the aircraft, and is not responsible for controlling the phugoid dynamics. The middle-loop controllers, designed in the following two sections, will stabilise the phugoid dynamics.

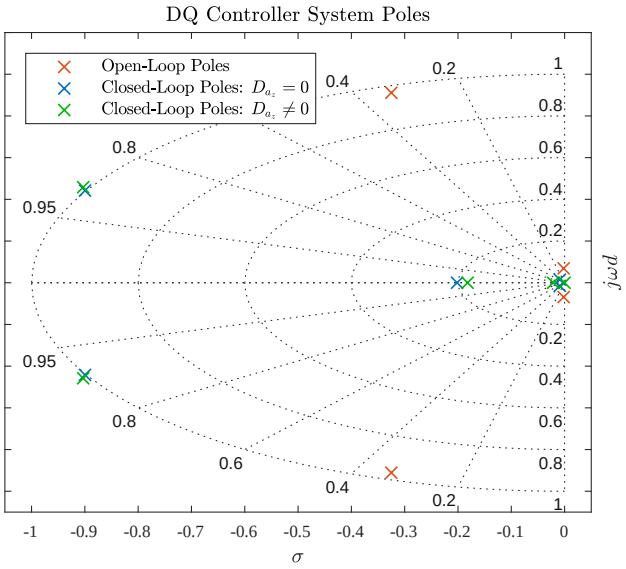

Figure 4.10: Closed-loop poles after addtion of DQ controller.

4.2.2 Climb Rate Controller

The next controller is the climb rate controller. The climb rate controller is a middle-loop controller that uses the DQ controller as an inner-loop controller to control the aircraft to follow a given climb rate command. The feedback control architecture of the climb rate controller is shown in Figure 4.11.

The climb rate controller is a proportional controller that uses feedback from a climb rate sensor and supplies a normal acceleration reference to the DQ controller. The controller is designed using the longitudinal dynamics of the aircraft, with the DQ controller added, as the plant. The airspeed is treated as a constant parameter based on the assumption that an airspeed controller will operate in parallel to the climb rate controller. A flight path angle controller could be designed with the same design process using the fact that flight path angle and climb rate are related through airspeed.

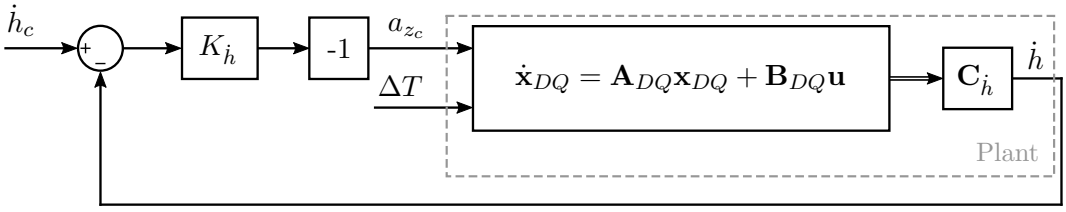

Figure 4.11: CR controller architecture.

Design

The climb rate of the aircraft may be calculated through,

$$\dot{h} = \overline{V}_T \sin(\theta - \alpha) \tag{4.22}$$

where $\overline{V}_T$ is the airspeed of the aircraft in trim. Assuming that the difference between the angle of attack and pitch angle is small, the climb rate may be approximated by,

$$\dot{h} \approx \overline{V}_T(\theta - \alpha) \tag{4.23}$$

and may be extracted from the state vector though an output matrix given by,

$$\mathbf{C}_{\dot{h}} = \begin{bmatrix} 0 & -\overline{V}_T & 0 & \overline{V}_T & 0 \end{bmatrix} \tag{4.24}$$

The climb rate controller is designed as a classic proportional controller that generates the normal acceleration command proportional to the climb rate error. The unstable phugoid mode poles encountered during the DQ law design introduce difficulties when designing for dominant climb rate response. A reduced-order model design is used where it is assumed that the phugoid-mode is controlled to be stable through addition of an airspeed controller. The vertical acceleration of the aircraft is related to the normal acceleration though,

$$\ddot{h} = -a_z \cos\theta \tag{4.25}$$

Once again assuming that the pitch angle is small, this simplifies to,

$$\ddot{h} = -a_z \tag{4.26}$$

The climb rate is then simply found through natural integration of the vertical acceleration. The reduced-order plant architecture is shown in Figure 4.12 and consists of the second-order closed-loop DQ controller dynamics and an integrator. The gain $K_{\dot{h}}$ is determined through a root locus design with the transfer function from the normal acceleration command a_{z_c} to the climb rate $\dot{h}$ as the open-loop transfer function.

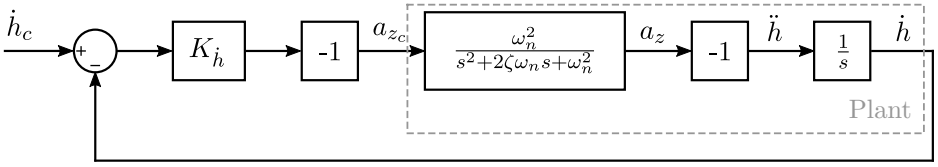

Figure 4.12: Reduced climb rate controller architecture.

Specifications

The specifications for the climb rate controller were selected using the A330 response as a guideline. The overshoot was selected to be as close to 5% as possible, and the 2% settling time approximately 15 s.

Simulation Results

Figure 4.13 shows the closed-loop step response for the reduced order climb rate controller as well as the corresponding root locus used for the design. The gain $K_{\dot{h}}$ was selected to move the poles until the desired specifications was reasonably satisfied. An overshoot of 6% was achieved along with a 2% settling time of just under 13 s. Although the actual overshoot is slightly more than what was specified, the response resembles the climb rate response of the Airbus A330 sufficiently well. The response exhibits a zero steady-state error, and the results are summarised in Table 4.2.

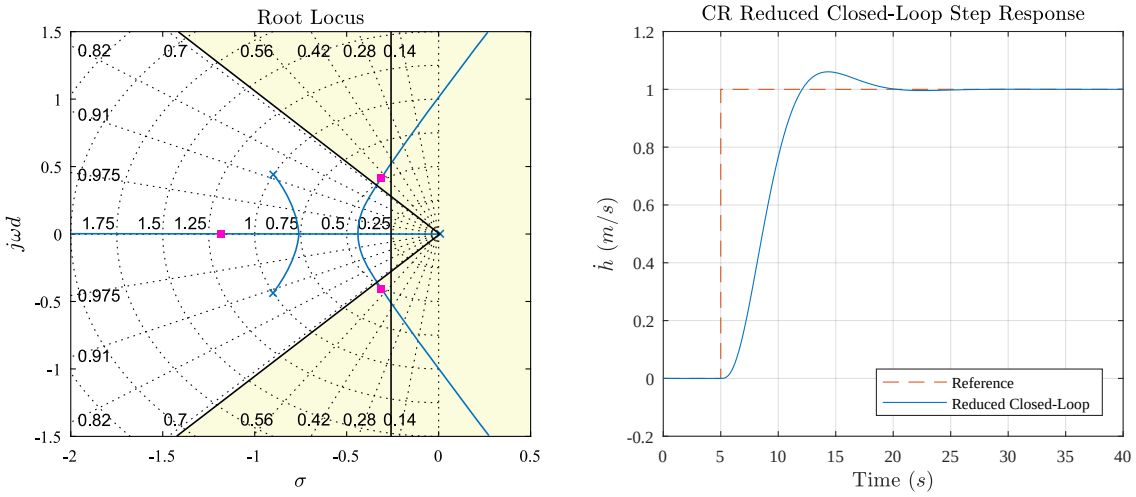

(a) Poles after proportional feedback.

(b) Closed-loop step response.

Figure 4.13: Root locus of reduced order climb rate controller and unit step response.

Table 4.2: Summary of climb rate controller results.

Longitudinal System	Overshoot	2% Settling Time
Desired	5%	15s
Reduced-Order Linear	6%	12.9s

The climb rate responses when using the full-order model and non-linear model will be presented and discussed after the design and addition of the autothrust controller in the following section. The autothrust controller is required to regulate the airspeed of the aircraft.

Closed-Loop Model

The closed-loop model that includes the dynamics of the DQ law and climb rate controller will serve as the open-loop plant for the next controller. The state-space of this closed-loop model is described by,

$$\dot{\mathbf{x}}_{CR} = \mathbf{A}_{CR}\mathbf{x}_{CR} + \mathbf{B}_{CR}\mathbf{u}_{CR} \tag{4.27}$$

$$\dot{\mathbf{x}}_{CR} = \left[\mathbf{A}_{DQ} - \mathbf{B}_{a_z} K_{\dot{h}} \mathbf{C}_{\dot{h}}\right] \mathbf{x}_{CR} + \left[\mathbf{B}_{a_z} K_{\dot{h}} \quad \mathbf{B}_{\Delta T}\right] \begin{bmatrix} \dot{h}_c \\ \Delta T \end{bmatrix} \tag{4.28}$$

Figure 4.14 shows the closed-loop system poles after implementation of the climb rate controller. Note that there is still an unstable real pole, which will be moved to the stable left half-plane by the autothrust controller.

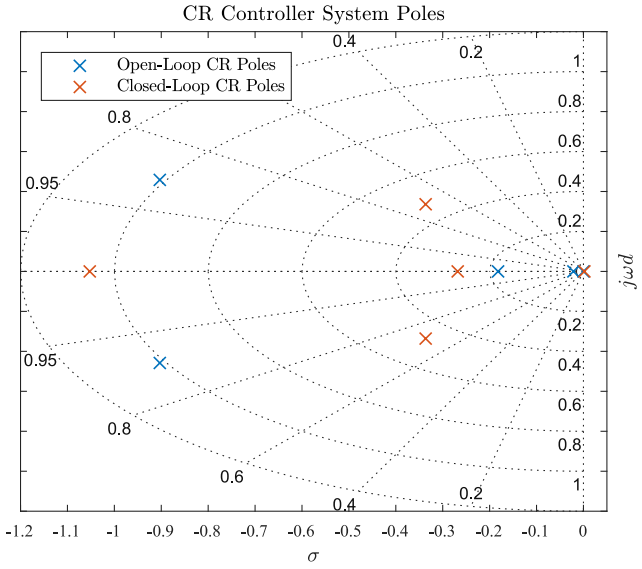

Figure 4.14: Closed-loop poles after addition of climb rate controller.

4.2.3 Auto-Thrust: An Airspeed Controller

In this section, an autothrust (AT) controller is designed that commands the thrust output of the aircraft to maintain a reference airspeed during a manoeuvre. The autothrust controller operates in parallel with the climb rate controller. The feedback control architecture of the autothrust controller is illustrated in Figure 4.15.

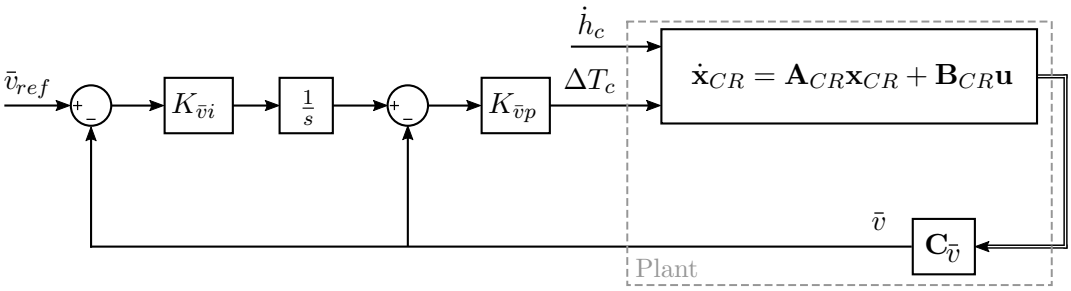

Figure 4.15: AT controller architecture.

The autothrust controller uses feedback from an airspeed sensor, and implements proportional control in series with integral control to actuate the thrust of the aircraft. The

controller is designed using the longitudinal dynamics of the aircraft, with the climb rate controller added, as the plant.

Design

Before introducing the controller integrator pole, the unstable real open-loop pole is shifted to the left half-plane by first closing the proportional control loop. The airspeed is extracted from the state vector using the output matrix,

$$\mathbf{C}_{\bar{v}} = \begin{bmatrix} 1 & 0 & 0 & 0 & 0 \end{bmatrix} \tag{4.29}$$

After the proportional loop is closed, the integral control loop is closed to ensure zero steady-state tracking.

Specifications

The specifications for the autothrust controller are selected using the A330 response as a guideline. The airspeed response is selected to resemble a second order system with a 2% settling time of 80 s and a damping ratio of 0.9 for a 5 m/s step input.

Root Locus and Simulation Results

Figure 4.16a shows the root locus used for the design of the proportional part of the autothrust controller, while Figure 4.16b shows the resulting airspeed response for a 5 m/s step in the airspeed command. The gain $K_{\bar{v}p}$ is increased until the unstable real pole is shifted sufficiently far into the left half-plane to ensure a quick response. In Figure 4.16b it is seen that the response exhibits some small steady-state error, which motivates the need for integral control.

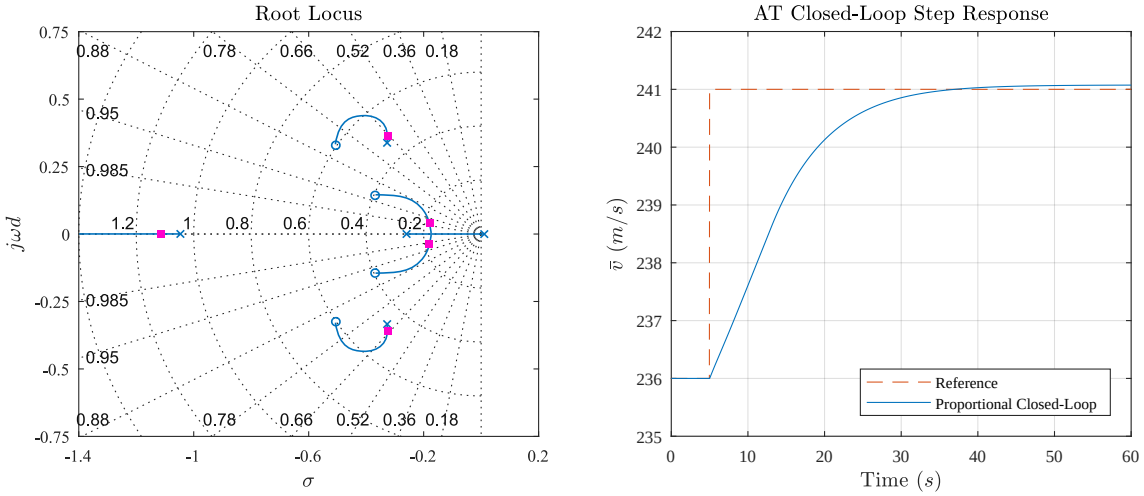

(a) Poles after proportional feedback.

(b) Proportional-loop step response.

Figure 4.16: Proportional autothrust controller design.

After the proportional control loop is closed, a free integrator is added to the plant and the gain $K_{\bar{v}i}$ is adjusted until the specifications are satisfied. Figure 4.17 shows the airspeed response after the addition of the integral control loop. The response exhibits a settling time of approximately 70 seconds and zero steady-state error.

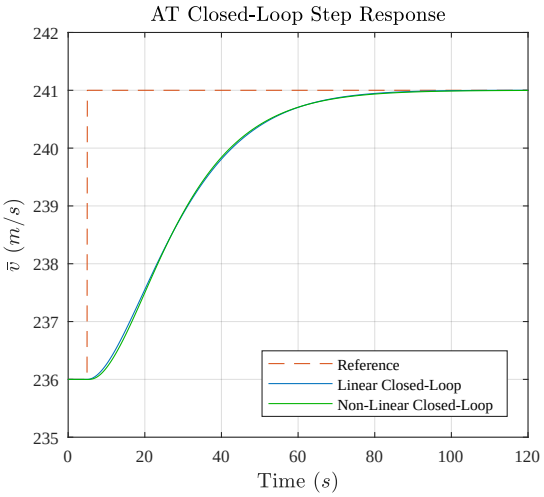

Figure 4.17: Closed-loop autothrust step response after the addition of integral control.

Figure 4.18 shows the thrust command and elevator response for a commanded step in airspeed. Notice that the thrust settles at a lower value once the desired airspeed is achieved, while the elevator deflection settles at a higher value. The increase in airspeed results in an increase in lift, and the aircraft tends to pitch up and climb. In order to regulate the climb rate of the aircraft to zero, the climb rate controller commands an increase in the elevator deflection to reduce the angle of attack. Since a constant altitude is maintained while flying at an increased airspeed, the aircraft can produce the same lift at a lower angle of attack. Since the angle of attack decreases, the pitch angle also decreases, and a larger component of the thrust force points in the direction of the velocity vector. This means that slightly less thrust is required to maintain the desired airspeed.

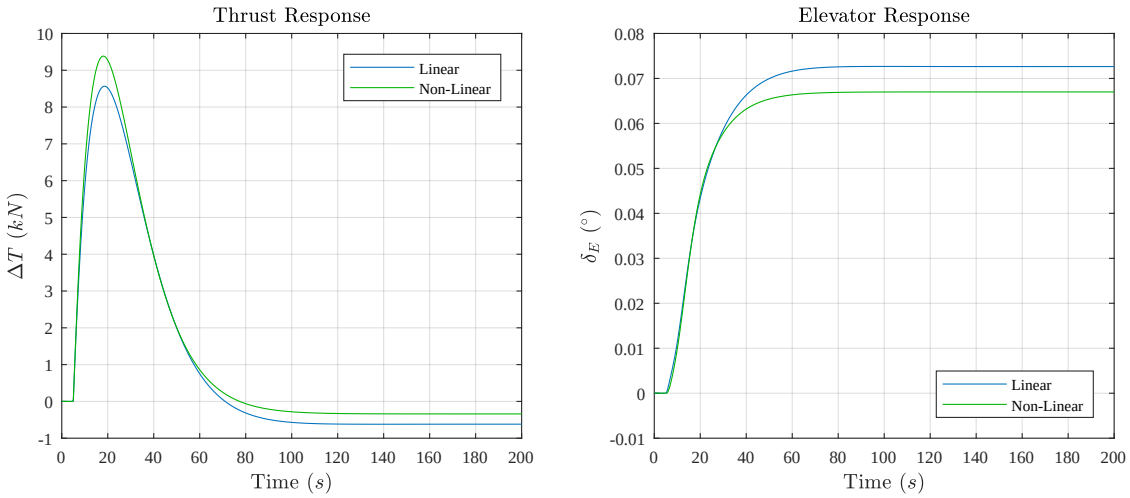

(a) Thrust response.

(b) Elevator response.

Figure 4.18: Thrust and elevator responses for a commanded step in airspeed.

Since the thrust output is physically limited to be between 0 and 100%, large thrust commands might saturate the control input and cause operation in the non-linear region. Figure 4.19 shows the airspeed and thrust response for a 20m/s step command in airspeed.

The airspeed is seen to exhibit unexpected overshoot, which results in a longer settling time. The thrust command well exceeds the physical limits of the possible thrust output of the aircraft, which saturates at 100%. This results in the control input no longer having any effect on the output, and is known as integrator "windup". The integrator continues integrating the error in airspeed even though the thrust output has no effect, which causes the large overshoot seen in the airspeed response. It is thus necessary to prevent the integrator from "winding up" through implementation of a technique known as anti-windup. Once the control is saturated, anti-windup ensures that the error signal is no longer integrated. Figures 4.19c and 4.19d show the airspeed and thrust response after implementation of anti-windup. The large overshoot in airspeed is removed and the response exhibits a 2% settling time of approximately 85s.

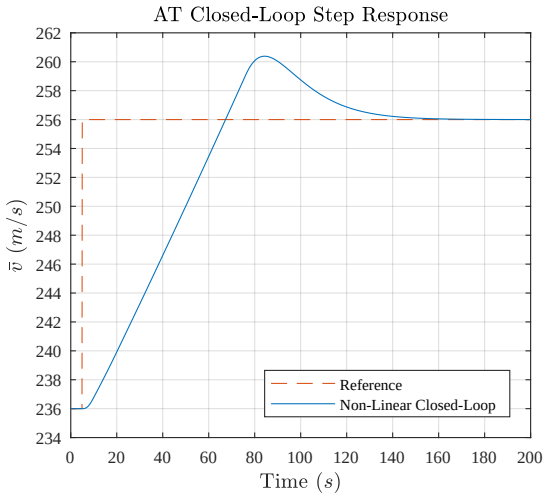

(a) Closed-loop autothrust step response without anti-windup implemented.

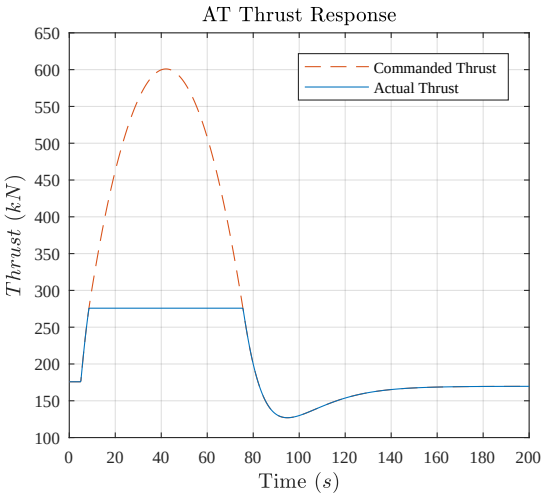

(b) Thrust command without anti-windup implemented.

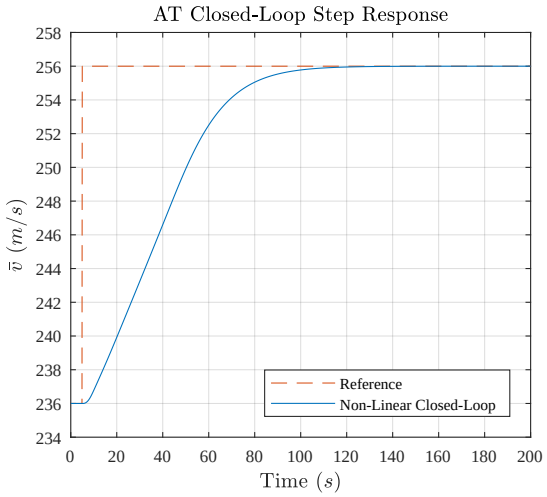

(c) Closed-loop autothrust step response with anti-windup implemented.

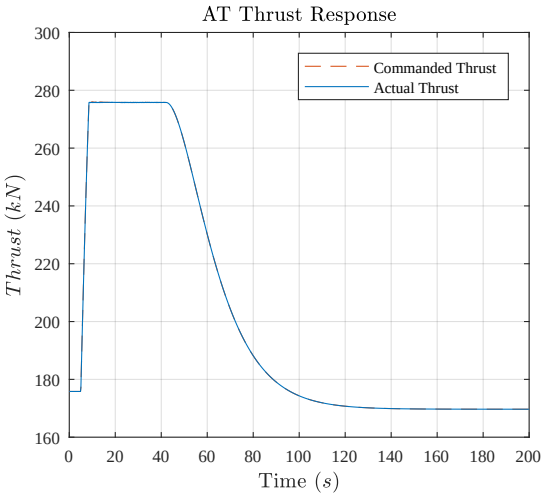

(d) Thrust command with anti-windup implemented.

Figure 4.19: Closed-loop step response of 20m/s airspeed step command, before and after addition of anti-windup.

Climb Rate Controller: Full-order Model and Non-Linear Responses

The reduced-order climb rate response was verified with the full-order and non-linear models after the implementation of the autothrust controller. The results are shown in Figure 4.20 and summarized in Table 4.2. From Figure 4.20a it is seen that the response of the full-order linear model exhibits slightly larger overshoot and a longer settling time than the response of the reduced-order model. The increased settling time is due to the slow airspeed dynamics, that is not present when using the reduced-order model. It Figure 4.20b it is seen that the non-linear response matches the full-order linear response very well.

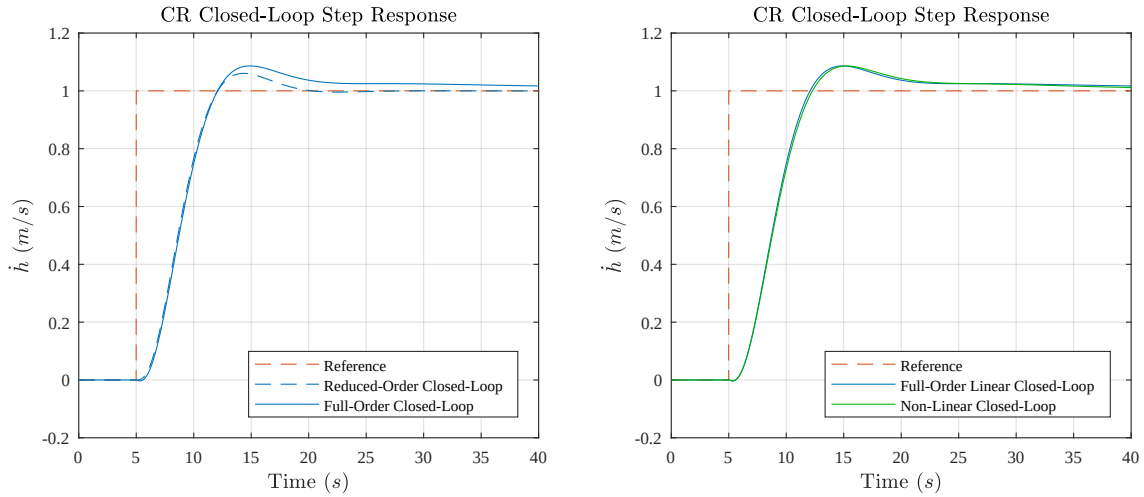

(a) Reduced and full-order climb rate responses.

(b) Full-order and non-linear climb rate responses.

Figure 4.20: Comparison of reduced, full-order, and non-linear climb rate controller unit step responses after implementation of autothrust controller.

Table 4.3: Summary of climb rate controller results.

Longitudinal System	Overshoot	2% Settling Time
Desired	5%	15s
Reduced-Order Linear	6%	12.9s
Full-Order Linear	8.5%	27s
Non-Linear	8.6%	27s

Figure 4.21 shows the normal acceleration response and the elevator response when a unit step in climb rate is commanded. Once the desired climb rate has been reached, the total normal acceleration settles at zero again. Note that the elevator deflection settles at a value higher than the original trim condition for the constant climb rate. While the aircraft is climbing, it maintains a constant flight path angle but quickly loses airspeed. In order to maintain a constant climb rate at a fixed flight path angle, the airspeed must be kept constant. The autothrust controller, which is assumed to operate in parallel with the climb rate controller, commands an increase in thrust to regulate the airspeed. The climb rate controller commands a positive elevator deflection from trim in order for the aircraft to fly at a lower angle of attack. If the same airspeed is maintained, flying at a lower angle of

attack decreases the lift of the aircraft, which is necessary to remain in equilibrium with the decreased component of gravity normal to the airspeed vector.

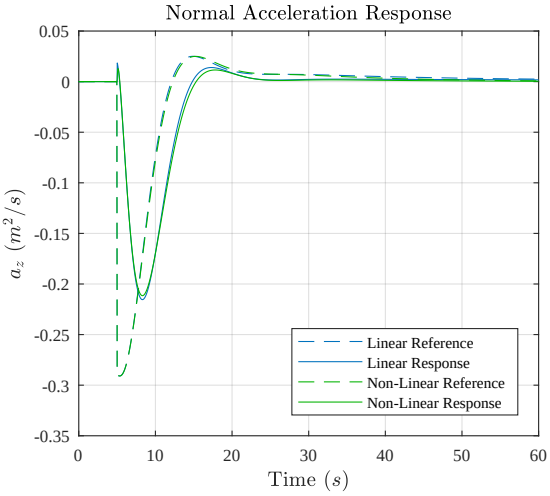

(a) Normal acceleration response for a unit step in climb rate.

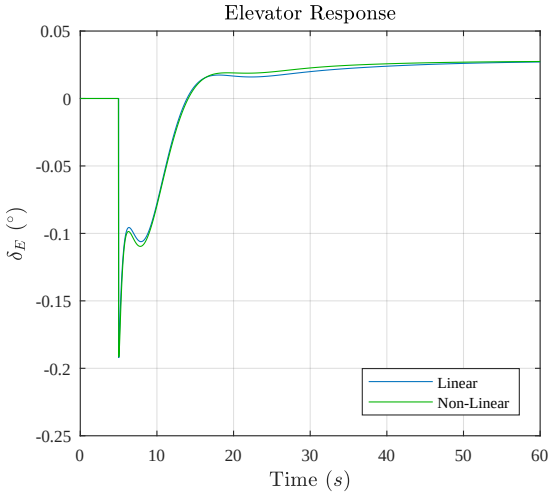

(b) Elevator response for a unit step in climb rate.

Figure 4.21: Normal acceleration and elevator responses induced by climb rate controller.

Closed-Loop Model

The closed-loop model that includes the dynamics of the DQ law and climb rate controller will serve as the plant for the next controller. The closed-loop state space model after closing the proportional loop is described by,

$$\begin{aligned}\dot{\mathbf{x}}_{ATP} &= \mathbf{A}_{ATP}\mathbf{x}_{ATP} + \mathbf{B}_{ATP}\mathbf{u}_{ATP} \\ \dot{\mathbf{x}}_{ATP} &= \left[\mathbf{A}_{CR} - \mathbf{B}_{\Delta T}K_{\bar{v}p}\mathbf{C}_{\bar{v}}\right]\mathbf{x}_{ATP} + \begin{bmatrix}\mathbf{B}_{\dot{h}} & \mathbf{B}_{\Delta T}K_{\bar{v}p}\end{bmatrix}\begin{bmatrix}\dot{h}_c \\ \bar{v}_{ref}\end{bmatrix}\end{aligned} \tag{4.30}$$

where $K_{\bar{v}p}$ is the proportional controller gain. The state space after closing the integral loop is given by,

$$\begin{aligned}\dot{\mathbf{x}}_{AT} &= \mathbf{A}_{AT}\mathbf{x}_{ATP} + \mathbf{B}_{AT}\mathbf{u}_{AT} \\ \begin{bmatrix}\dot{\mathbf{x}}_{ATP} \\ \dot{x}_{\bar{v}i}\end{bmatrix} &= \begin{bmatrix}\mathbf{A}_{ATP} & \mathbf{B}_P K_{\bar{v}i} \\ -\mathbf{C}_{\bar{v}} & 0\end{bmatrix}\begin{bmatrix}\mathbf{x}_{AT} \\ x_{\bar{v}i}\end{bmatrix} + \begin{bmatrix}\mathbf{B}_{\dot{h}} & \mathbf{B}_P \\ 0 & 1\end{bmatrix}\begin{bmatrix}\dot{h}_c \\ \bar{v}_{ref}\end{bmatrix}\end{aligned} \tag{4.31}$$

where $\mathbf{B}_P$ is the second column of $\mathbf{B}_{ATP}$. Figure 4.22 shows the system poles after the model is augmented with the AT controller.

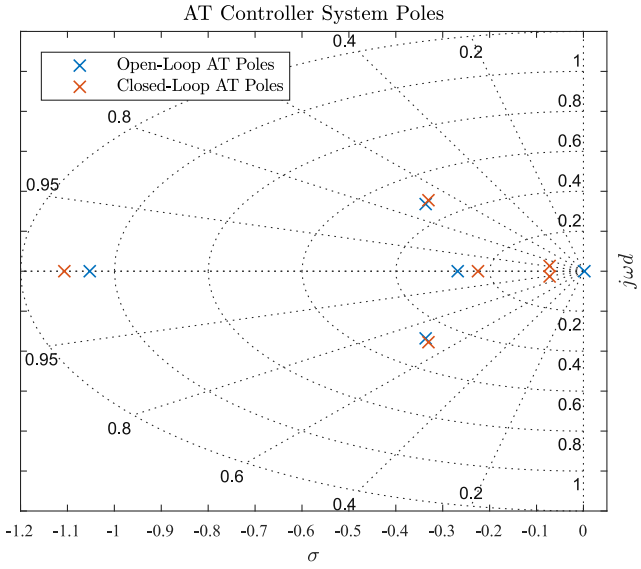

Figure 4.22: Closed-loop poles after addition of AT controller.

4.2.4 Altitude Controller

The final controller required for longitudinal control is an altitude controller, which enables the aircraft to maintain a reference altitude. Figure 4.23 shows the feedback control architecture of the altitude controller.

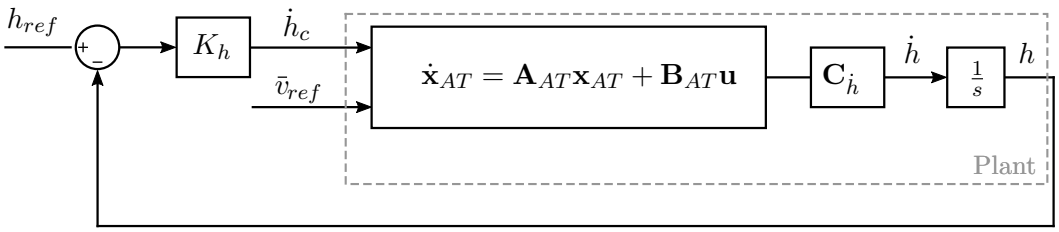

Figure 4.23: Altitude controller architecture.

The altitude controller is a proportional controller that uses feedback from an altitude sensor and supplies a climb rate reference to the climb rate controller. The controller is designed using the longitudinal dynamics of the aircraft, with all the inner-loop and middle-loop longitudinal controllers (DQ controller, climb rate controller, and autothrust controller) added, as the plant.

Design

The controller follows a classic proportional control strategy that commands a climb rate proportional to the error in altitude. The altitude of the aircraft is the result of the natural integration of climb rate, as illustrated by the free integrator in the plant model.

Specifications

The specifications for the altitude controller were selected using the A330 response as a guideline. The altitude response is selected to exhibit 5-10% overshoot and a 2% settling time of 20 s.

Simulation Results

Figure 4.24a shows the closed-loop step response of the altitude controller. The response exhibits zero steady-state error, as expected, since the plant has a natural free integrator and the climb rate sensor is assumed to be ideal. Furthermore, an overshoot of approximately 5% was achieved along with a 2% settling time of 22 s. The altitude controller results are summarized in Table 4.4. In Figure 4.24b it is seen that the climb rate settles at zero again once the desired altitude is reached. Figure 4.25 shows the thrust and elevator responses for a commanded step in altitude. As expected, both the thrust and elevator return to zero once the desired altitude is achieved. Note that the non-linear thrust response peaks at a higher value than the linear thrust response. This is due to the thrust lag dynamics which are not modelled in by the linear aircraft model.

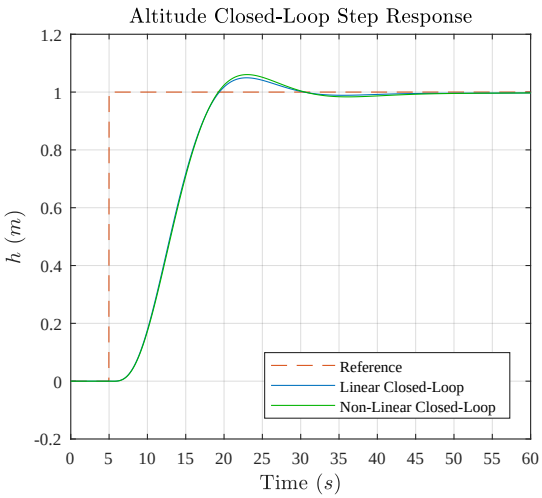

(a) Closed-loop altitude step response.

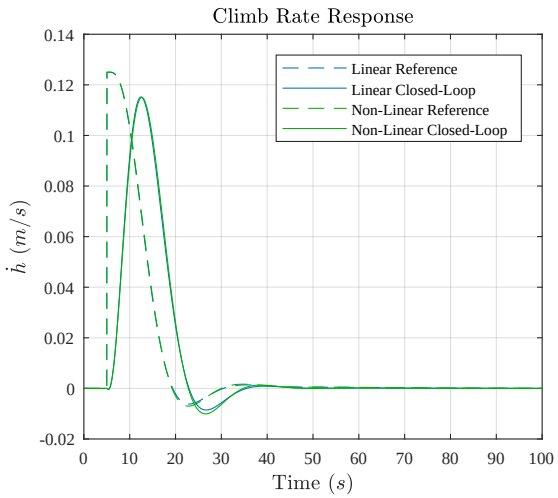

(b) Climb rate response.

Figure 4.24: Altitude and climb rate responses for a unit step in altitude.

Table 4.4: Summary of altitude controller results.

Longitudinal System	Overshoot	2% Settling Time
Desired	5-10%	20s
Linear	5%	22.5s
Non-Linear	6%	23.2s

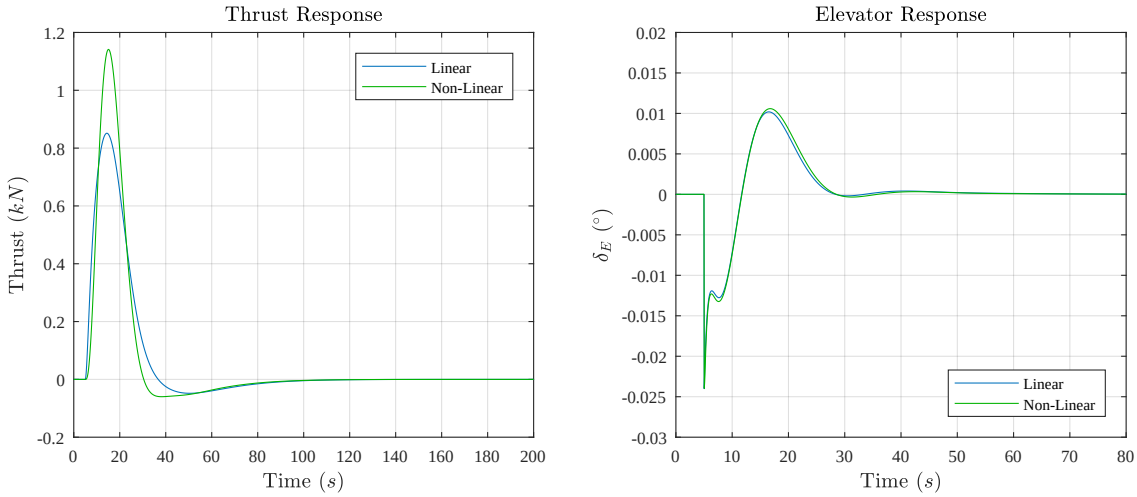

(a) Thrust response.

(b) Elevator response.

Figure 4.25: Thrust and elevator responses for a commanded step in altitude.

Closed-Loop Model

The closed-loop model that describes the longitudinal dynamics of after all the longitudinal controllers are added is given by,

$$\dot{\mathbf{x}}_{ALT} = \mathbf{A}_{ALT}\mathbf{x}_{ALT} + \mathbf{B}_{ALT}\mathbf{u}_{ALT}$$

$$\begin{bmatrix} \dot{\mathbf{x}}_{AT} \\ \dot{h} \end{bmatrix} = \begin{bmatrix} \mathbf{A}_{AT} & -\mathbf{B}_H K_h \\ \mathbf{C}_{\dot{h}} & 0 \end{bmatrix} \begin{bmatrix} \mathbf{x}_{AT} \\ h \end{bmatrix} + \begin{bmatrix} \mathbf{B}_H K_h & \mathbf{B}_{\bar{v}_{ref}} \\ 0 & 0 \end{bmatrix} \begin{bmatrix} h_{ref} \\ \bar{v}_{ref} \end{bmatrix} \tag{4.32}$$

where $\mathbf{B}_H$ represents the first column of $\mathbf{B}_{AT}$. Figure 4.26 shows the system poles after the implementation of the altitude controller.

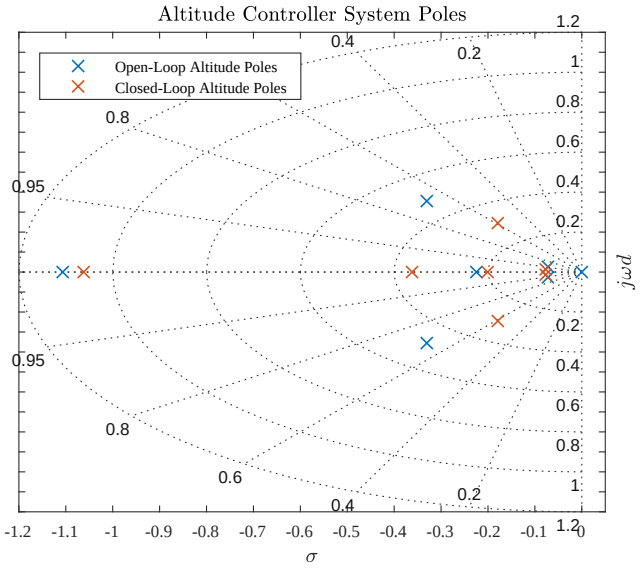

Figure 4.26: Closed-loop poles after addition of altitude controller.

4.3 Conventional Lateral Control System Design

The architecture of the conventional lateral controllers is shown in Figure 4.27, and comprises two controllers: an inner-loop controller called the DPDR law, and a guidance-loop cross-track controller. Similar to the longitudinal control system, the later controller architecture was modelled after the structure employed by Airbus.

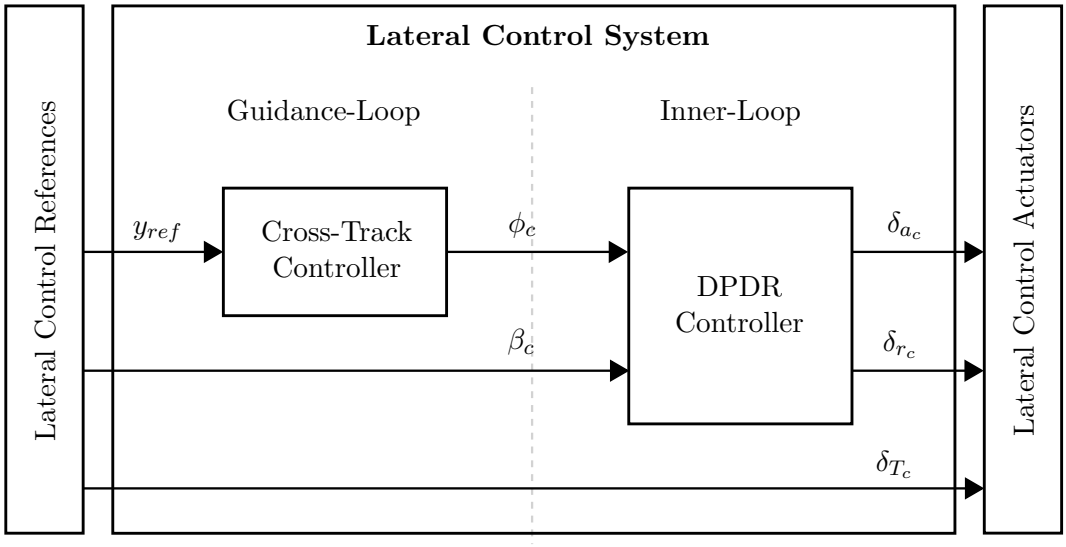

Figure 4.27: Lateral controller architecture.

The DPDR controller, which originates from the Airbus Normal mode control architecture, serves as a bank angle and sideslip controller. A bank angle command is received from the guidance-loop, while sideslip commands are provided directly. The controller utilises full state feedback and commands the ailerons and rudder control surfaces. The bank angle reference is provided by the cross-track controller, which is responsible for navigating the aircraft along a desired flight path.

This section presents the design and verification of the conventional lateral control system. First, the inner-loop DPDR controller is presented and a closed-loop dynamic model is obtained. This model then serves as the open-loop plant for the design of the cross-track controller, which is presented second.

4.3.1 DP and DR Law: A Roll and Sideslip Controller

The DP and DR Law (or DPDR controller) is designed to control the roll and sideslip angles of the aircraft. Figure 4.28 shows the feedback control architecture. The lightly damped Dutch roll mode is artificially damped to stop the elliptical motion of the wingtips [37] when a disturbance in sideslip angle is experienced. The sideslip control is designed to have a natural roll angle response for a commanded sideslip angle, and closely follows the work of Trollip [4].

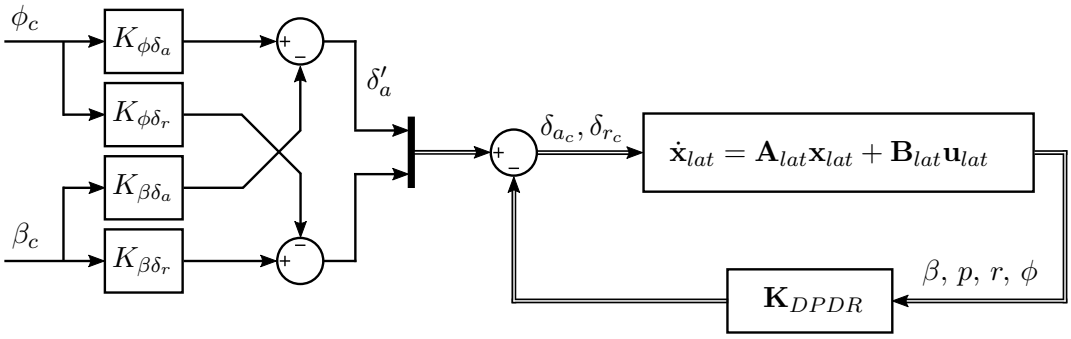

Figure 4.28: DPDR controller architecture.

The controller implements full-state feedback and actuates the aircraft ailerons and rudder to induce rolling and yawing moments. When a positive sideslip angle is induced, the angle of attack of the starboard wing increases. This produces increased lift on the starboard side of the aircraft, which induces an additional rolling moment. Similarly, when a non-zero bank angle is induced, the natural dynamics of the aircraft result in a undesired tendency to sideslip, which requires the correct amount of rudder deflection to push the nose of the aircraft back into the bank. If too large a natural sideslip is induced by the banking manoeuvre, the aircraft will transition into a skidding motion, which results in a loss of airspeed. Additional input mixing gains are included to command the correct amount of aileron and rudder deflection required to counter the adverse yaw and rolling effects when commanding non-zero bank and sideslip angles, ensuring coordinated turning.

Design

The controller consists of two parts: pole placement through use of the full-state feedback gain $\mathbf{K}_{DPDR}$, and a set of mixing gains that ensure turn coordination and natural roll response. The full-state feedback control law is given by,

$$\mathbf{u}_{lat} = \begin{bmatrix} \delta'_a \\ \delta'_r \end{bmatrix} - \mathbf{K}_{DPDR}\mathbf{x}_{lat} \tag{4.33}$$

where δ'_a and δ'_r represent aileron and rudder inputs that may be commanded by the next control loop, or (in this case) by the set of mixing gains. The feedback gain is calculated using an LQR design that minimizes the cost function,

$$J = \int_0^\infty (\mathbf{x}_{lat}^\mathsf{T}\mathbf{Q}\mathbf{x}_{lat} + \mathbf{u}_{lat}^\mathsf{T}\mathbf{R}\mathbf{u}_{lat})\, dt \tag{4.34}$$

The initial values of the state weighting matrix $\mathbf{Q}$ and control weighting matrix $\mathbf{R}$ are selected as diagonal matrices using Bryson's rule,

$$\mathbf{Q}_{ii} = \frac{1}{(\text{max acceptable value of } \mathbf{x}_i)^2} \quad , \quad i \in (1,\ 2,\ 3,\ 4) \tag{4.35}$$

$$\mathbf{R}_{jj} = \frac{1}{(\text{max acceptable value of } \mathbf{u}_j)^2} \quad , \quad j \in (1,\ 2) \tag{4.36}$$

After the initial values of the weighting matrices have been chosen, they are iteratively modified until an acceptable trade-off between performance and control effort is achieved. Once the full-state feedback is implemented, the input mixing gains are added and the control law is augmented to be,

$$\mathbf{u}_{lat} = \begin{bmatrix} K_{\phi\delta_a} & -K_{\beta\delta_a} \\ -K_{\phi\delta_r} & K_{\beta\delta_r} \end{bmatrix} \begin{bmatrix} \phi_c \\ \beta_c \end{bmatrix} - \mathbf{K}_{DPDR}\mathbf{x}_{lat} \tag{4.37}$$

where the direct-coupling gains $K_{\phi\delta_a}$ and $K_{\beta\delta_r}$ are used to govern the responses from input commands for roll and sideslip to their respective outputs. The cross-coupling gains $K_{\phi\delta_r}$ and $K_{\beta\delta_a}$ are used for turn coordination and natural roll response for commands in sideslip.

Turn Coordination

As an aircraft banks to initiate a turn, it experiences unwanted lateral acceleration due to an adverse yaw effect in the form of induced sideslip. A coordinated turn is defined as one during which the centre of gravity of the aircraft experiences zero lateral acceleration while regulating sideslip angle close to zero [40]. This is desirable for passenger comfort and maximises aerodynamic efficiency [52]. The cross gain $K_{\phi\delta_r}$ is used to apply enough rudder to minimise the adverse yaw effect and thus minimise the sideslip angle.

Specifications

The specifications for the DPDR controller are selected using the A330 response as a guideline. The roll responses are selected to exhibit peak times of less than 10 s and the overshoot is limited to 5% for passenger comfort. Zero steady-state error is not required and the sideslip must be reduced as much as possible. The sideslip response is required to peak before 10 seconds and should exhibit an overshoot of less than 20%. In accordance with the response of a A330 aircraft, the sideslip angle should have a steady-state value of roughly half of the commanded sideslip angle. Finally, for natural roll response when sideslip is commanded, the steady-state ratio for bank-angle induced by the sideslip angle is selected to be,

$$\frac{\phi_{ss}}{\beta_{ss}} = -5 \tag{4.38}$$

Pole Placement and Simulation Results

Figure 4.29 shows the system poles after implementation of the full-state feedback using LQR optimization. The dominant pole was placed with time constant,

$$\tau = 0.982 \text{ s} \tag{4.39}$$

which results in a 2% settling time of approximately,

$$t_{s_{2\%}} = 3.9\tau \approx 3.83 \text{ s} \tag{4.40}$$

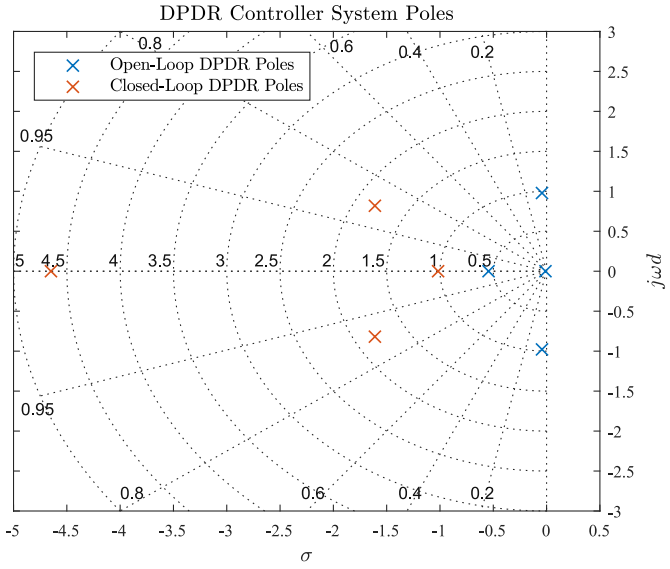

Figure 4.29: DPDR system poles after full-state feedback.

Figures 4.30a and 4.30b show the roll angle and sideslip angle responses for 1° commands in roll angle and sideslip angle respectively. For a step command in roll angle, it is seen that the roll angle response exhibits no overshoot and has a small steady-state error. The sideslip angle is roughly regulated to zero in steady-state. For a step command in sideslip angle, it is seen that the non-linear sideslip angle response exhibits an overshoot of approximately 18%. The roll angle settles at about –2 degrees, slightly less than desired. Both responses achieved 2% settling times of less than 10 s.

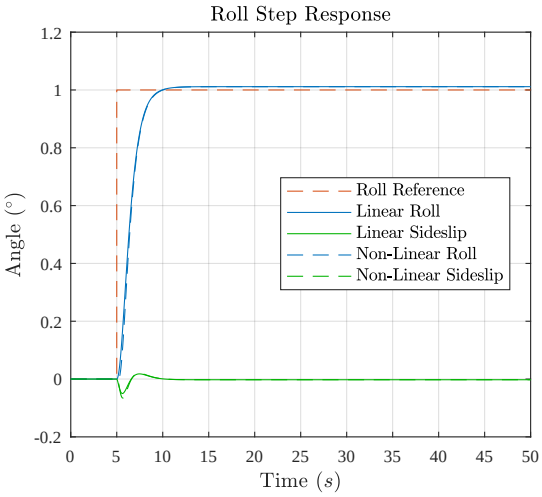

(a) Roll and sideslip response for roll command.

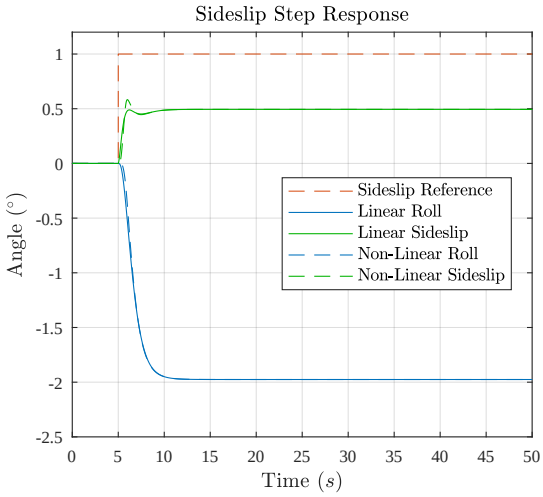

(b) Roll and sideslip response for sideslip command.

Figure 4.30: Roll angle and sidelsip angle responses after implementation of DPDR controller.

The aileron and rudder responses are shown in Figure 4.31 for unit steps in both roll and

sideslip commands. For a roll command, the ailerons are deflected to produce a quick rolling moment while the rudder is applied to damp the adverse yaw. For a sideslip angle command, the rudder is deflected to produce a yawing moment while the ailerons ensure a natural roll response of the aircraft.

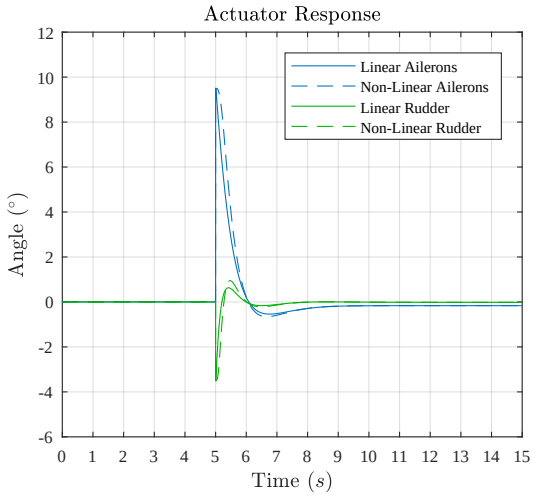

(a) Actuator response for roll command.

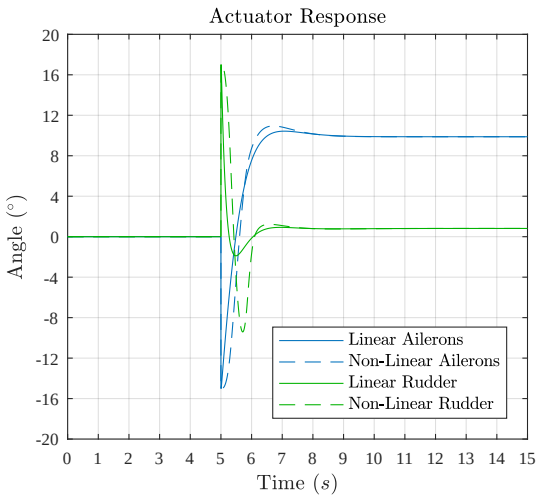

(b) Actuator response for sideslip command.

Figure 4.31: Aileron and rudder response for a) a unit step in roll command, and b) a unit step in sideslip command.

Closed-Loop Model

The closed-loop model that includes the dynamics of the lateral plant and DPDR controller will serve as the plant for the next controller. The state space model that describe the closed-loop dynamics can be derived as,

$$\dot{\mathbf{x}}_{DPDR} = \mathbf{A}_{DPDR}\mathbf{x}_{DPDR} + \mathbf{B}_{DPDR}\mathbf{u}_{DPDR} \tag{4.41}$$

$$\begin{aligned}\dot{\mathbf{x}}_{DPDR} = &\left[\mathbf{A}_{lat} - \mathbf{B}_{lat}\mathbf{K}_{DPDR}\right]\mathbf{x}_{DPDR} \\ &+ \begin{bmatrix}\mathbf{B}_{\delta_a}K_{\phi\delta_a} - \mathbf{B}_{\delta_r}K_{\phi\delta_r} & \mathbf{B}_{\delta_r}K_{\beta\delta_r} - \mathbf{B}_{\delta_a}K_{\beta\delta_a}\end{bmatrix}\begin{bmatrix}\phi_c \\ \beta_c\end{bmatrix}\end{aligned} \tag{4.42}$$

$$\mathbf{x}_{DPDR} = \mathbf{x}_{lat} \tag{4.43}$$

4.3.2 Cross-Track Controller

The final controller required for conventional lateral control is a cross-track (CT) controller, which enables the aircraft to follow a desired ground track. Figure 4.32 shows the feedback control architecture.

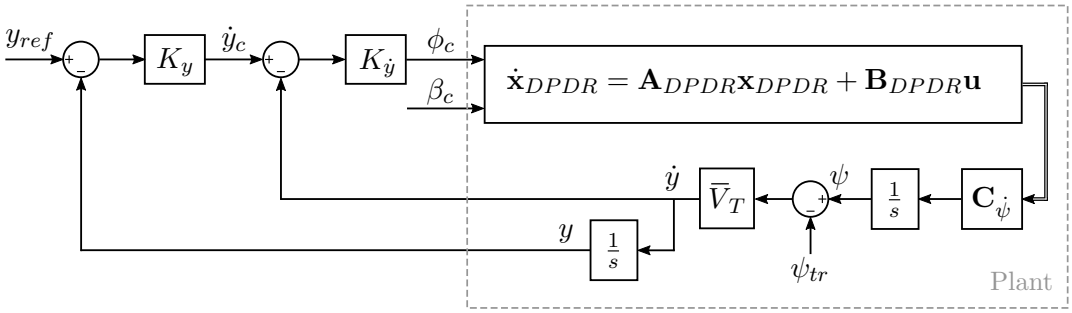

Figure 4.32: CT controller architecture.

The cross-track controller receives a cross-track reference and provides the DPDR controller with a bank angle command. The controller is designed using the lateral dynamics of the aircraft, with the DPDR controller added, as the plant. The aircraft is assumed to fly straight and level at the trim airspeed.

Navigation Guidance Axis System

Figure 4.33 shows a simplified guidance axis system used for waypoint navigation, where ψ_{tr} represents the heading of the ground track and y is the cross-track distance, or the perpendicular distance from the ground track to the aircraft. The origin of the guidance axis system is selected to coincide with the source waypoint, while the z-axis coincides with the inertial down axis. The x-axis is parallel to the ground track, and points from the source waypoint to the destination waypoint. The y-axis completes the right-handed orthogonal axis system and is perpendicular to the ground track.

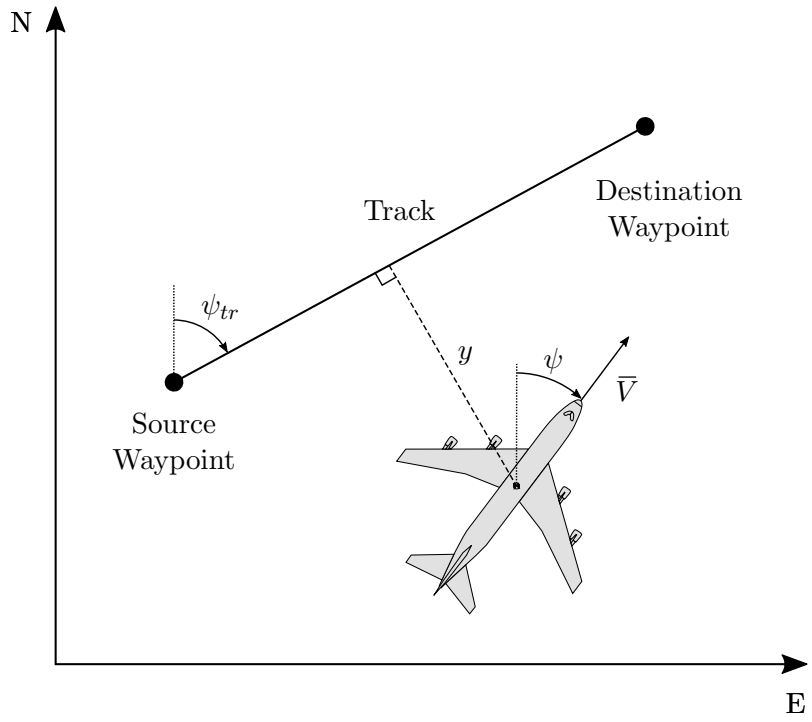

Figure 4.33: Guidance axis system.

Design

The controller consists of two proportional controllers closed consecutively: the first using cross-track rate as feedback, and the second using the cross-track distance as feedback. The controller obtains the cross-track distance by coordinating the aircraft's inertial position into the guidance axis system, and taking the y-axis component. The cross-track rate is obtained by either numerically differentiating the cross track distance, or by coordinating its velocity vector into the guidance axis system. In order to design the controller using the linearised lateral model, however, the cross-track dynamics are modelled as follows: the heading angle rate is extracted from the lateral state vector through $\mathbf{C}_{\dot{\psi}}$, which is then integrated to obtain the heading angle. The track heading angle is subtracted from the aircraft heading angle to obtain the heading angle error, which is then multiplied with the trim airspeed to obtain the cross-track rate. Finally, integrating the cross-track rate yields the cross-track distance. The centripetal acceleration the aircraft experiences during a turn can be modelled as,

$$a_L = g \tan\phi = \overline{V}_T \dot{\psi} \tag{4.44}$$

where g is the gravitational acceleration, ϕ is the bank angle, $\overline{V}_T$ is the trim airspeed, and $\dot{\psi}$ is the heading rate of the aircraft. For small bank angles, $\tan\phi \approx \phi$, and Equation 4.44 can be rearranged to obtain,

$$\dot{\psi} = \frac{g}{\overline{V}_T}\phi \tag{4.45}$$

The heading rate can thus be extracted from the state vector through,

$$\mathbf{C}_{\dot{\psi}} = \begin{bmatrix} 0 & 0 & 0 & \dfrac{g}{\overline{V}_T} \end{bmatrix} \tag{4.46}$$

The heading angle can be obtained through integration of the heading rate, and the cross-track rate through,

$$\dot{y} = \overline{V}_T \sin(\psi - \psi_{tr}) \tag{4.47}$$

For small differences in track and actual heading angle, Equation 4.48 reduces to,

$$\dot{y} = \overline{V}_T (\psi - \psi_{tr}) \tag{4.48}$$

The cross-track distance is then obtained through natural integration of the cross-track rate. The proportional controller gains are determined through root locus design, where the root locus for the cross-track distance loop consists of the closed-loop dynamics of the cross-track rate loop.

Specifications

The specifications for the cross-track controller were selected by using the A330 response as a guideline. The final response is selected to exhibit an overshoot of no more than 5%, an 80% rise time of less than 30 s, and a 2% settling time of less than 60 s. The control gain of the cross-track rate loop $K_{\dot{y}}$ is chosen such that the final closed-loop cross-track response can be achieved through means of only the proportional gain K_y.

Simulation Results

Figure 4.34 shows the closed-loop step responses of the cross-track controller. Figure 4.34a shows the cross-track rate response for a unity step in commanded cross-track rate, while

Figure 4.34b shows the cross-track response for a unity step in cross-track command. The final cross-track response exhibits zero steady-state error, as expected, since the plant has a natural free integrator and the cross-track rate sensor is assumed to be ideal. Furthermore an overshoot of approximately less than 5% was achieved along with a 2% settling time of 26 s. The cross-track controller results are summarized in Table 4.5.

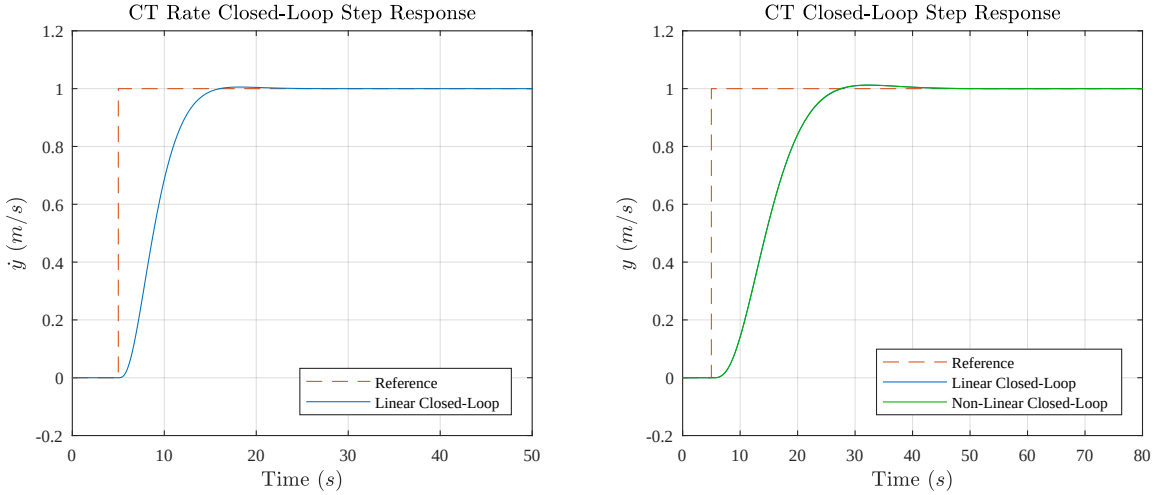

(a) Cross-track rate response for unit step.

(b) Cross-track response for unit step.

Figure 4.34: Cross-track controller responses for unit step commands.

Table 4.5: Summary of cross-track controller results.

Cross-Track System	Overshoot	2% Settling Time
Desired	$< 5\%$	< 60s
Linear	1%	20.5s
Non-Linear	8%	43s

Figure 4.35 shows the responses of bank angle, aileron and rudder to a unit step command in cross-track. The bank angle, shown in Figure 4.35a, is commanded to quickly make the aircraft roll in the desired direction. As the aircraft approaches the desired cross-track distance, the bank angle gradually commands the aircraft to bank in the opposite direction, essentially slowing down lateral movement. The corresponding aileron and rudder responses are shown in Figure 4.35b. The ailerons are deflected to induce a bank angle and the rudder is applied to minimise the sideslip angle. Once the desired cross-track distance is achieved, the actuator deflections return to zero.

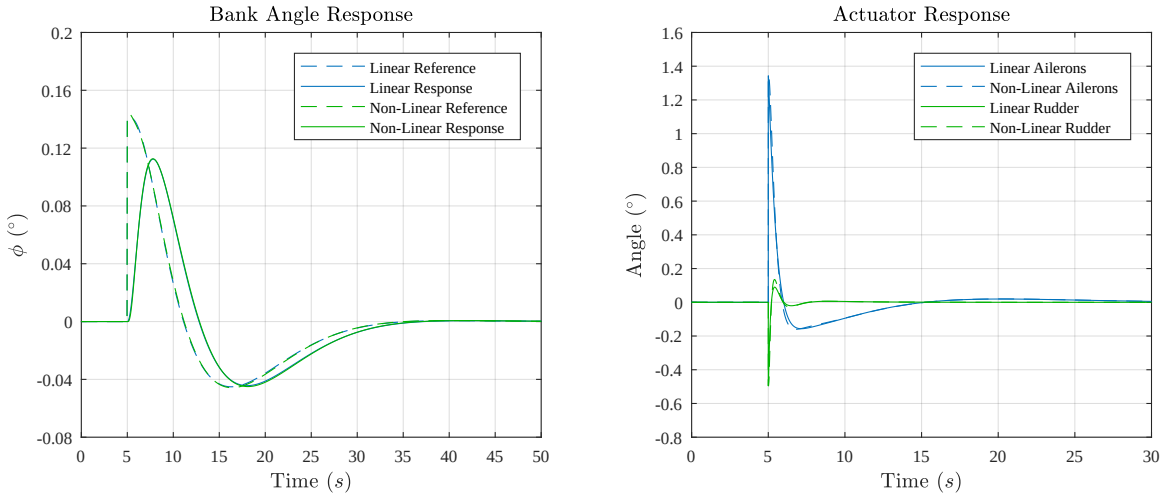

(a) Bank angle response.

(b) Actuator response.

Figure 4.35: Bank angle, aileron, and rudder responses for a unit step command in cross-track distance.

Closed-Loop Model

The closed-loop model that includes the dynamics of both lateral controllers will serve as the plant for the formation flight controllers designed in the next chapter. The closed-loop state space model that describes the lateral dynamics after closing the cross-track rate loop, is given by,

$$\dot{\mathbf{x}}_{CTR} = \mathbf{A}_{CTR}\mathbf{x}_{CTR} + \mathbf{B}_{CTR}\mathbf{u}_{CTR} + N_{CTR}\psi_{tr} \tag{4.49}$$

$$\begin{aligned}\begin{bmatrix}\mathbf{x}_{DPDR}\\ \dot{\psi}\end{bmatrix} &= \begin{bmatrix}\mathbf{A}_{DPDR} & -\mathbf{B}_{\phi}K_{\dot{y}}\overline{V}_T\\ \mathbf{C}_{\dot{\psi}} & 0\end{bmatrix}\begin{bmatrix}\mathbf{x}_{DPDR}\\ \psi\end{bmatrix}\\ &+ \begin{bmatrix}\mathbf{B}_{\phi}K_{\dot{y}} & \mathbf{B}_{\beta}\\ 0 & 0\end{bmatrix}\begin{bmatrix}\dot{y}_c\\ \beta_c\end{bmatrix} + \begin{bmatrix}\mathbf{B}_{\phi}K_{\dot{y}}\overline{V}_T\\ 0\end{bmatrix}\psi_{tr}\end{aligned} \tag{4.50}$$

The cross-track rate closed-loop state space serves model as the plant for the cross-track loop, for which the closed-loop state space model can be derived as,

$$\dot{\mathbf{x}}_{CT} = \mathbf{A}_{CT}\mathbf{x}_{CT} + \mathbf{B}_{CT}\mathbf{u}_{CT} + N_{CT}\psi_{tr} \tag{4.51}$$

$$\begin{bmatrix}\mathbf{x}_{CTR}\\ \dot{y}\end{bmatrix} = \begin{bmatrix}\mathbf{A}_{CTR} & -\mathbf{B}_{\dot{y}}K_y\\ \mathbf{C}_{\psi}\overline{V}_T & 0\end{bmatrix}\begin{bmatrix}\mathbf{x}_{CTR}\\ y\end{bmatrix} + \begin{bmatrix}\mathbf{B}_{\dot{y}}K_y & \mathbf{B}_{CTR_{\beta}}\\ 0 & 0\end{bmatrix}\begin{bmatrix}\dot{y}_c\\ \beta_c\end{bmatrix} + \begin{bmatrix}N_{CTR}\\ -\overline{V}_T\end{bmatrix}\psi_{tr} \tag{4.52}$$

$$\mathbf{C}_{\psi} = \begin{bmatrix}0 & 0 & 0 & 0 & 1\end{bmatrix} \tag{4.53}$$

4.4 Summary of Conventional Flight Control System

In the previous two sections, conventional fly-by-wire flight controllers were developed for a Boeing 747 aircraft. The controllers were designed and simulated in an integrated simulation. Longitudinal control is provided by: a DQ law which controls normal acceleration, an autothrust controller to regulate airspeed, and finally, climb rate and altitude controllers to regulate the altitude. Lateral control is provided by: a DPDR controller which controls the aircraft's roll and sideslip angles through actuation of the rudder and ailerons, and a cross-track controller that commands the aircraft's bank angle to regulate the aircraft's cross-track distance from a reference ground track. Most specifications were chosen in accordance with previous work done, where the responses of a Airbus A330 were used as a guideline. Specifications were reasonably achieved with good correlation between the responses of the linear and non-linear models.

The next section focuses on the design and integration of formation flight controllers which allow a follower aircraft to fly in formation behind a leader aircraft. Previous work has shown that the inner-loop conventional controllers require no modification to enable formation flight, and that the outer guidance-loop controllers only require minor changes to achieve formation flight.

4.5 Extended Formation Flight Control Design

Figure 4.36 illustrates the controller architecture for the extended formation flight control system. The inner-loop controllers are the unmodified conventional controllers designed in the previous sections, with the addition of a complementary filter controller. A set of extended formation flight guidance controllers are designed in this section in order maintain the required formation separations between different aircraft.

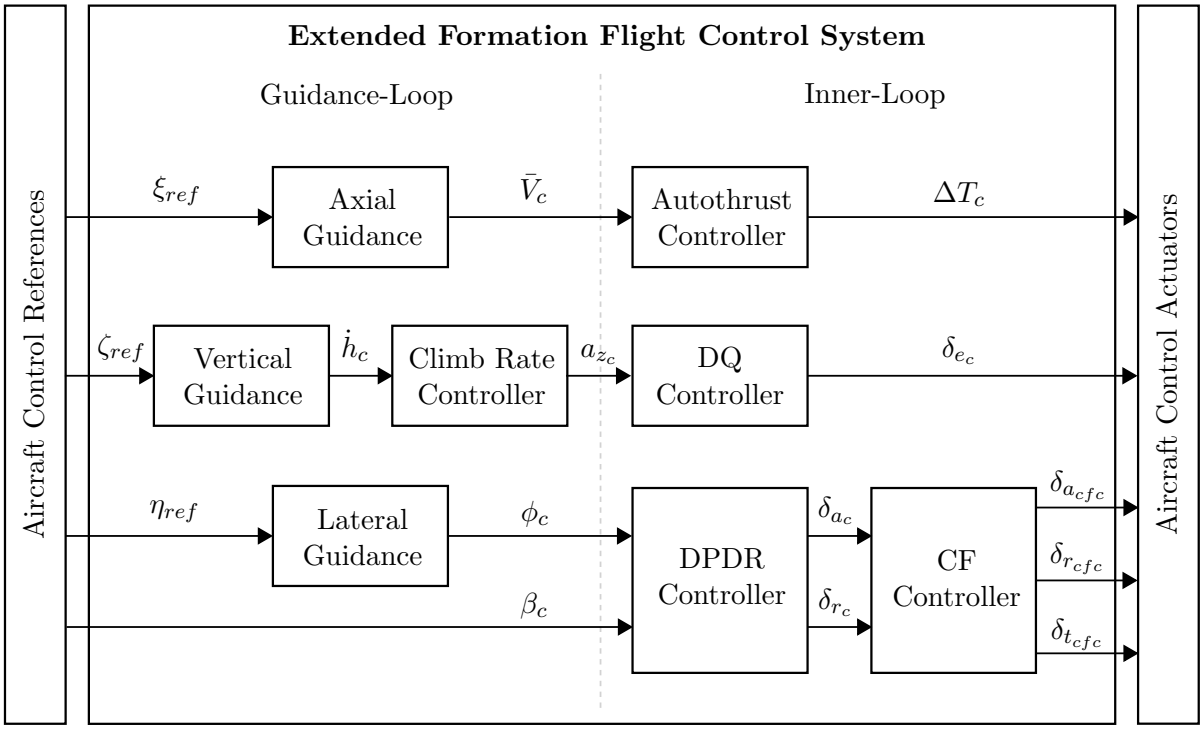

Figure 4.36: Extended formation flight controller architecture.

First, the vertical guidance controller is presented, which replaces the conventional altitude controller and ensures that the follower aircraft in formation are able to maintain their relative altitudes. Next, an axial separation controller is used to maintain a desired in-track distance between aircraft. The controller receives an axial separation reference and provides the autothrust controller with an airspeed command. Finally, a lateral guidance controller is presented that augments the cross-track controller to ensure that follower aircraft are able to maintain the desired later separations while flying in the wake of the leader.

4.5.1 Vertical Guidance Controller

A vertical guidance controller is designed in this section to allow the follower aircraft in the formation to maintain their respective differences in altitude with regards to other aircraft. Figure 4.37 shows the feedback control architecture, which is similar to that of the altitude controller.

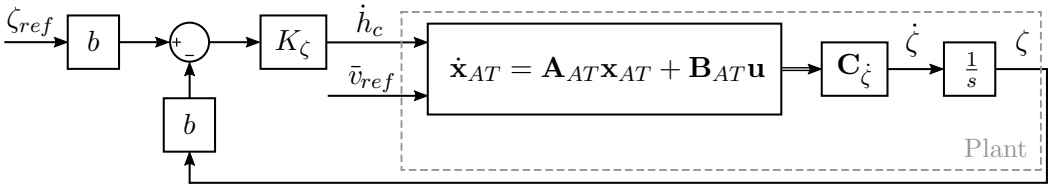

Figure 4.37: Vertical separation controller architecture.

The vertical guidance controller is a proportional controller that receives a separation reference and provides a climb rate command to the climb rate controller. The controller is designed using the longitudinal dynamics, with the autothrust controller added, as the plant. The multiplication by wingspan b converts the command and feedback from wingspans to meters.

Design

The design of the vertical guidance controller is similar to the design of the altitude controller and uses the closed-loop dynamics with all inner-loop and middle-loop controllers implemented as the plant. The vertical separation rate can be modelled as,

$$\dot{\zeta} = \frac{\overline{V}_T}{b}\sin(\theta - \alpha) \tag{4.54}$$

where $\overline{V}_T$ is the airspeed of the aircraft in trim, b is the wingspan, and θ and α are the deviations of pitch angle and angle of attack respectively from trim. Assuming that the difference between the pitch angle and angle of attack is small, the vertical separation rate can be written as,

$$\dot{\zeta} = \frac{\overline{V}_T}{b}(\theta - \alpha) \tag{4.55}$$

and is extracted from the longitudinal state vector through,

$$\mathbf{C}_{\dot{\zeta}} = \begin{bmatrix} 0 & -\overline{V}_T/b & 0 & \overline{V}_T/b & 0 \end{bmatrix} \tag{4.56}$$

Specifications

In accordance with the work of Trollip, the specifications for the vertical separation controller are selected to be similar to that of the altitude controller: an overshoot of 5-10% and a 2%

settling time of 20 s.

Results

Since the vertical separation controller is in essence identical to the altitude controller, the controller gain K_ζ was chosen to be the same as the altitude controller gain K_h. This results in the vertical separation response shown in Figure 4.38a, which is identical to that of the altitude response. The airspeed, shown in Figure 4.38b, "dips" slightly when the aircraft pitches up and the autothrust controller increases the thrust command, as seen in Figure 4.38e, to regulate the airspeed back to its trim value. The vertical separation response exhibits zero steady-state error, as expected, since the plant has a natural free integrator and the climb rate sensor is assumed to be ideal. Furthermore an overshoot of approximately 5% was achieved along with a 2% settling time of 22 s. The controller results are summarized in Table 4.6.

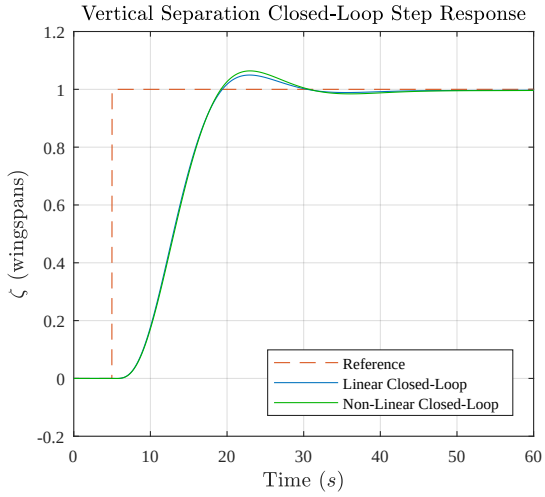

(a) Vertical separation response.

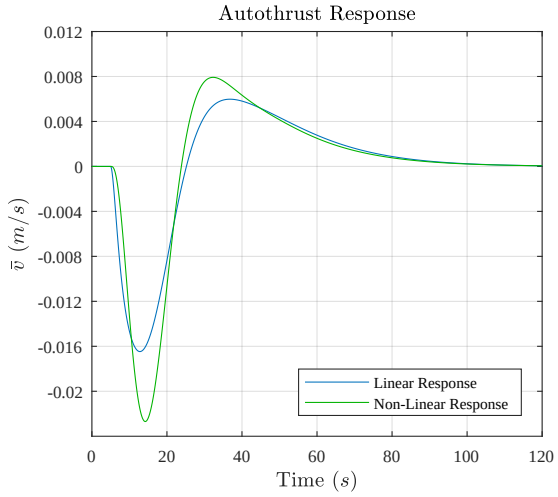

(b) Airspeed response

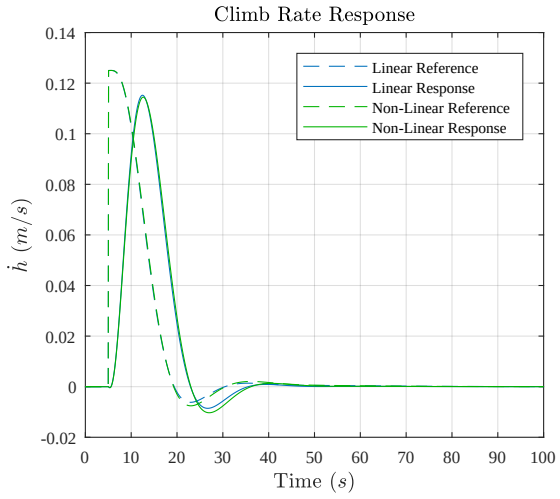

(c) Climb rate response

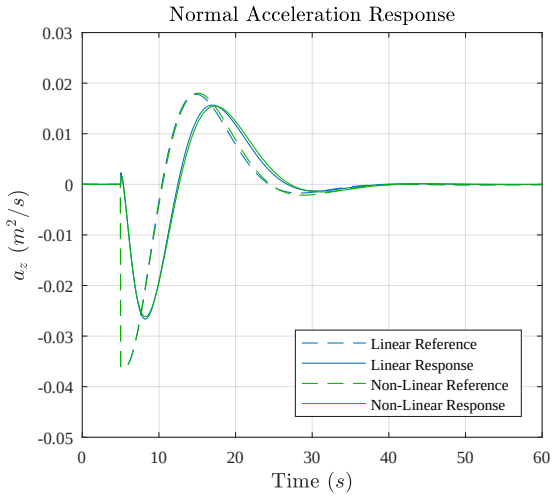

(d) Normal acceleration response.

Figure 4.38: Vertical separation and aircraft state and actuator responses for a commanded step in vertical separation.

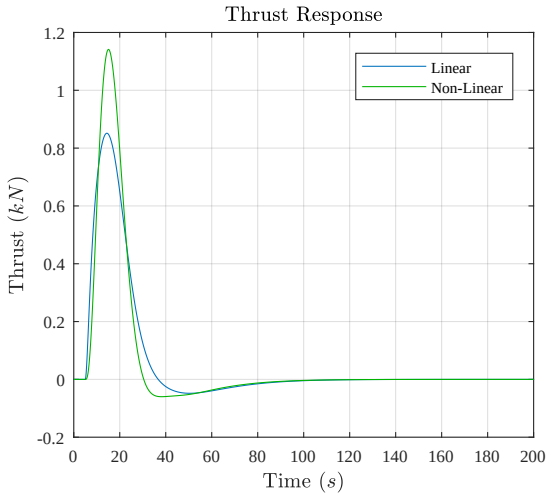

(e) Thrust response

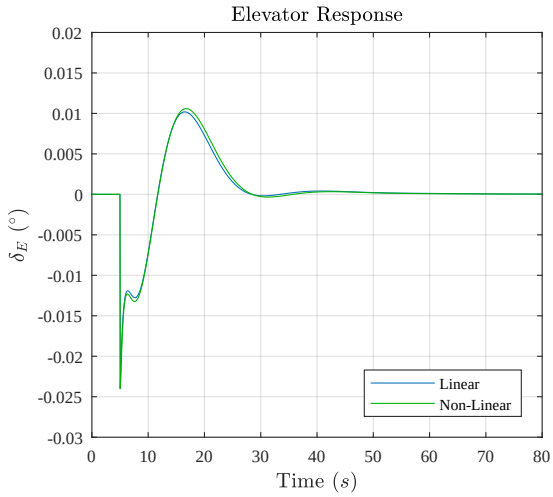

(f) Elevator response.

Figure 4.38: Vertical separation and aircraft state and actuator responses for a commanded step in vertical separation (cont.).

Table 4.6: Summary of altitude controller results.

Longitudinal System	Overshoot	2% Settling Time
Desired	10%	20s
Linear	5%	22.5s
Non-Linear	6%	23.2s

Closed-Loop Model

The closed-loop model that now includes the dynamics of the vertical separation controller will serve as the plant for the axial guidance controller. The state-space model that describes the close-loop dynamics is given by,

$$\dot{\mathbf{x}}_{VS} = \mathbf{A}_{VS}\mathbf{x}_{VS} + \mathbf{B}_{VS}\mathbf{u}_{VS} \tag{4.57}$$

$$\begin{bmatrix} \dot{\mathbf{x}}_{AT} \\ \dot{\zeta} \end{bmatrix} = \begin{bmatrix} \mathbf{A}_{AT} & -\mathbf{B}_H K_\zeta \\ \mathbf{C}_{\dot{\zeta}} & 0 \end{bmatrix} \begin{bmatrix} \mathbf{x}_{AT} \\ \zeta \end{bmatrix} + \begin{bmatrix} \mathbf{B}_H K_\zeta & \mathbf{B}_{\bar{v}_{ref}} \\ 0 & 0 \end{bmatrix} \begin{bmatrix} \zeta_{ref} \\ \bar{v}_{ref} \end{bmatrix} \tag{4.58}$$

Figure 4.39 shows the system poles after the implementation of the vertical separation controller.

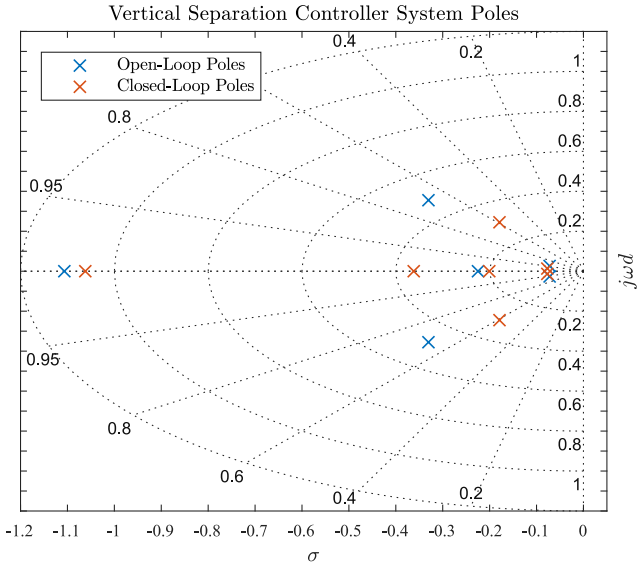

Figure 4.39: Closed-loop poles after addtion of vertical separation controller.

4.5.2 Axial Guidance Controller

An axial guidance controller is designed in this section to allow the follower aircraft in the formation to maintain their respective in-track distances from other aircraft. Figure 4.40 shows the feedback control architecture.

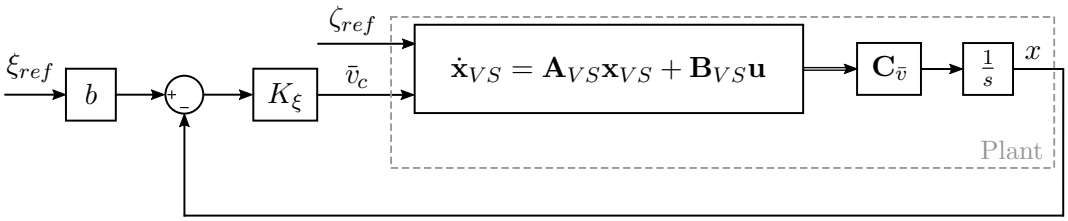

Figure 4.40: Axial separation controller architecture.

The axial separation controller is a proportional controller that receives an axial separation reference and supplies the autothrust controller with an airspeed reference. The controller is designed using the longitudinal dynamics of the aircraft, with the vertical guidance controller added, as the plant.

Design

The axial guidance controller implements proportional control to command an airspeed proportional to the error in in-track distance. The in-track distance rate between aircraft is described by,

$$\dot{x} = \overline{V}^F \cos\left(\psi_w^F - \psi_w^L\right) - \overline{V}^L \tag{4.59}$$

where $\overline{V}^F$ is the airspeed magnitude of the follower, $\overline{V}^L$ is the airspeed magnitude of the leader, and ψ_w^F and ψ_w^L are the heading angles of the follower and leader velocity vectors

respectively. Assuming that the difference between the leader and follower flight heading angles are small, and considering small disturbance theory, Equation 4.59 reduces to,

$$\dot{x} = \left(\overline{V}^F - \overline{V}^L\right) = \Delta\overline{V} \tag{4.60}$$

Assuming that the leader flies at trim, and that the follower and leader aircraft are trimmed at the same airspeed $\overline{V}_T$, $\Delta\overline{V}$ may be expressed as,

$$\Delta\overline{V} = \bar{v}^F \tag{4.61}$$

which is extracted from the longitudinal state vector through,

$$\mathbf{C}_{\bar{v}} = \begin{bmatrix} 1 & 0 & 0 & 0 & 0 & 0 & 0 \end{bmatrix} \tag{4.62}$$

Assuming that the flight heading difference between the leader and follower aircraft is indeed zero, natural integration from airspeed to in-track distance means the system will thus be able to follow a step reference with zero steady-state error.

Specifications

The specifications for the axial separation controller are chosen as follows: minimal overshoot of less than 10% and zero steady-state error. The settling time is not constrained since the wake profile does not change much with regards to axial separation when flying in extended formation flight. Therefore fast convergence in the axial direction is not necessary.

Simulation Results

Figure 4.41a shows the step response of the axial separation controller. The response exhibits an overshoot of roughly 5%, a 2% settling time of approximately 130 s and has zero steady-state error. The vertical separation response is shown in Figure 4.41b. As the airspeed increases in order to decrease the axial separation, the vertical separation momentarily increases as well until it is regulated to its trim condition by the vertical separation controller. The commanded thrust, shown in Figure 4.41d, increases in order to increase the airspeed, and decreases again to slow down the aircraft it approaches the desired axial separation.

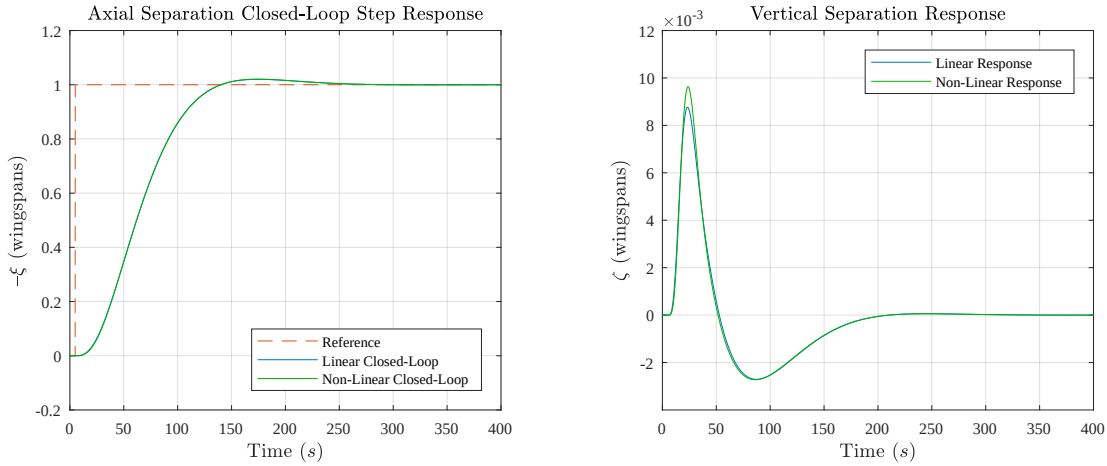

(a) Axial separation response.

(b) Vertical separation response

Figure 4.41: Axial separation and aircraft state and actuator responses for a commanded step in axial separation.

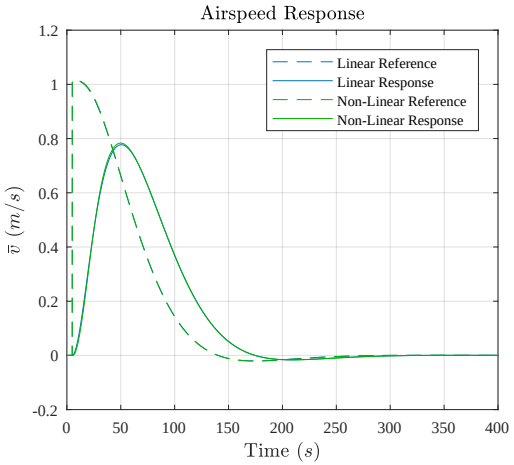

(c) Airspeed response

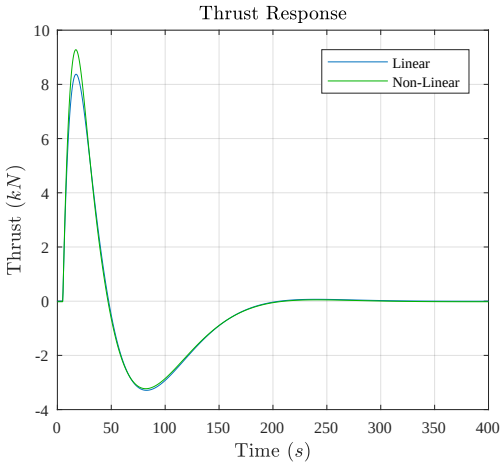

(d) Thrust response.

Figure 4.41: Axial separation and aircraft state and actuator responses for a commanded step in axial separation (cont.).

4.5.3 Lateral Guidance Controller

A lateral guidance controller is designed in this section to allow the follower aircraft in the formation to maintain their respective differences in cross-track distance with regards to other aircraft. Figure 4.42 shows the feedback control architecture.

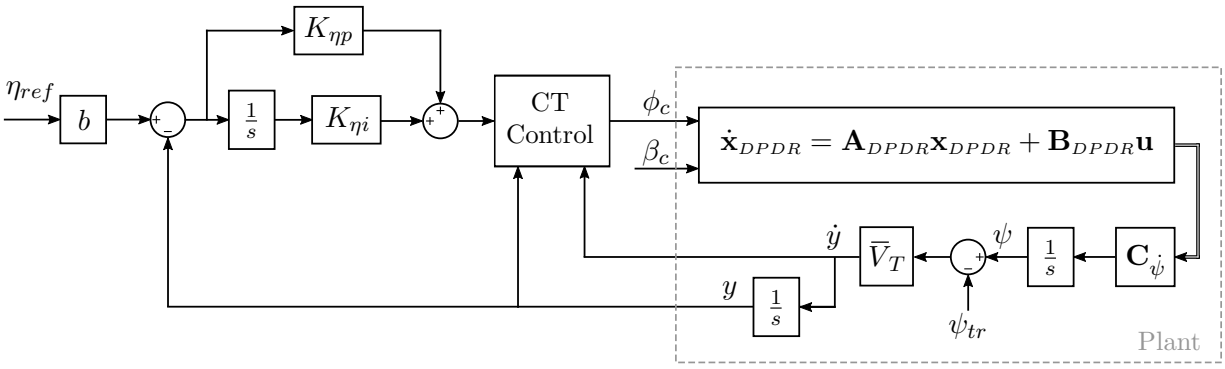

Figure 4.42: Lateral separation controller architecture.

Design

The controller consists of the cross-track controller designed in the previous chapter augmented with a classic PI controller. For the design of the cross-track controller for an aircraft in isolated flight, it was assumed that there are no net aerodynamic forces in the body y-axis. During formation flight this assumption no longer holds, since additional aerodynamic forces are induced on the follower aircraft by the wake of the leader. In order to approach the design with linear control design theory, the wake-induced forces are treated as disturbances, and the controller is augmented with a PI controller to ensure zero error steady-state tracking. Disturbance rejection is thus improved for the lateral formation-hold control. In the work of Trollip, the zero error steady-state tracking was achieved though addition of a limited integrator in parallel with the cross-track proportional gain. This however results in a very long settling time, which is undesired for the purpose of extremum-seeking control.

Specifications

The specifications for the lateral separation controller are chosen as follows: minimal overshoot of less than 10% and a 2% settling time of close to 30 s. The natural integration of cross-track distance and the addition of the control integrator ensures that the response will have zero steady-state error when following a step in input.

Root Locus and Simulation Results

Figure 4.43 shows the step response of the lateral separation controller as well as the root locus used for the controller design. The response exhibits an overshoot of roughly 2% and 2% settling time of approximately 32 s. The PI controller is of the form,

$$D_{PI}(s) = \frac{K(s+z)}{s} = \frac{0.329(s+0.222)}{s} \tag{4.63}$$

where the zero is located at $\sigma = -0.222$.

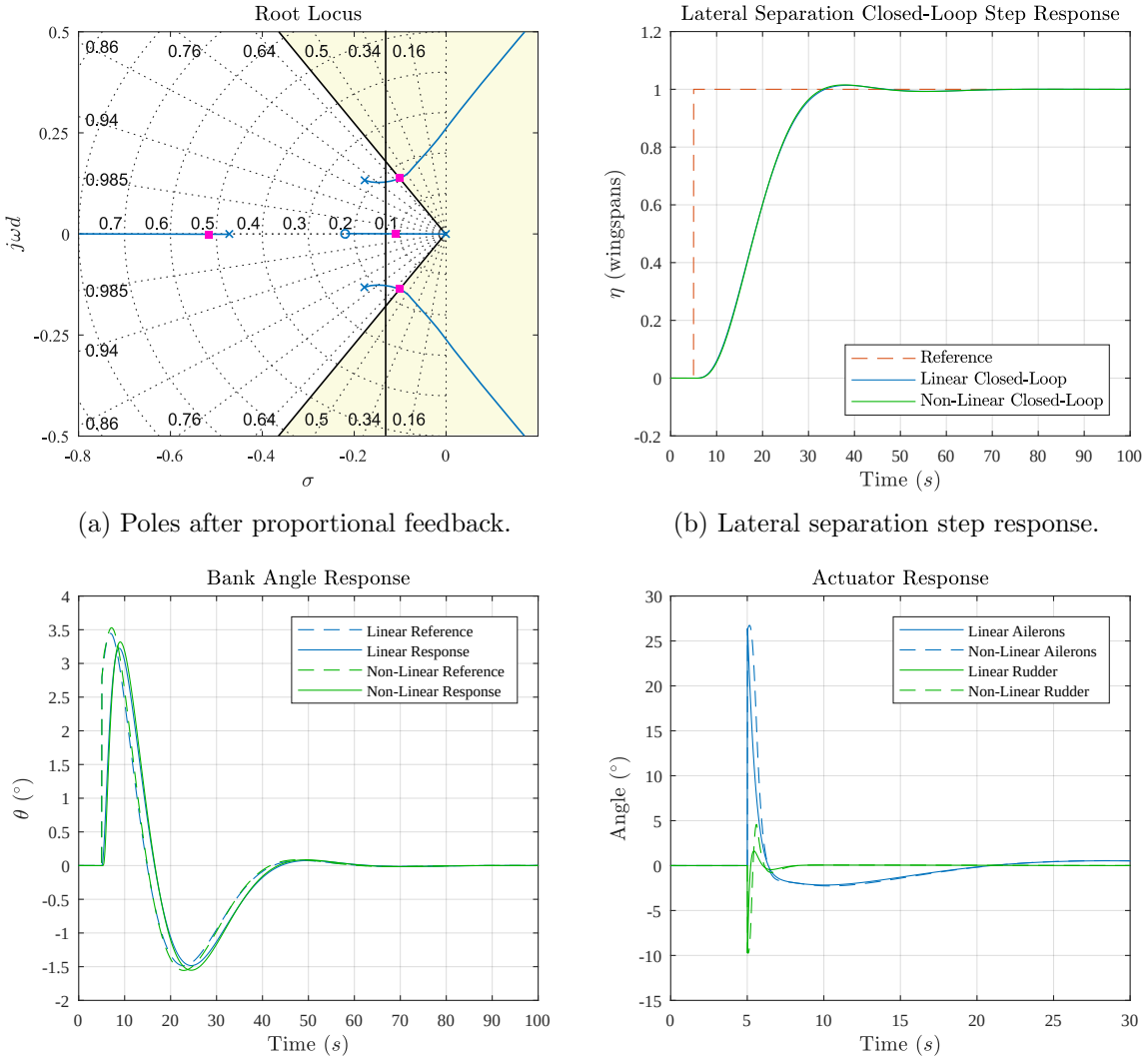

(a) Poles after proportional feedback.

(b) Lateral separation step response.

(c) Airspeed response

(d) Thrust response.

Figure 4.43: Lateral separation and aircraft state and actuator responses for a commanded step in lateral separation.

From Figure 4.43d it can be seen that the aileron demand is higher than the maximum available deflection of 22°. This means that the ailerons will briefly saturate during the manoeuvre. By limiting the speed at which the follower can approach the leader laterally, the aileron deflection command and response overshoot can be reduced. Figure 4.44 shows the lateral separation response, as well as the bank and actuator responses, for a 1 m/s rate limited lateral separation step command. The aileron and rudder demand is significantly reduced and the lateral separation response exhibits a 2% settling time of roughly 75 seconds. It is important to note that the rate limiter only affects large input step commands, and that the response of small input step commands will be similar to the response without rate limitation. For these small input step commands, however, the actuator demand is much less and does not exceed the available control authority.

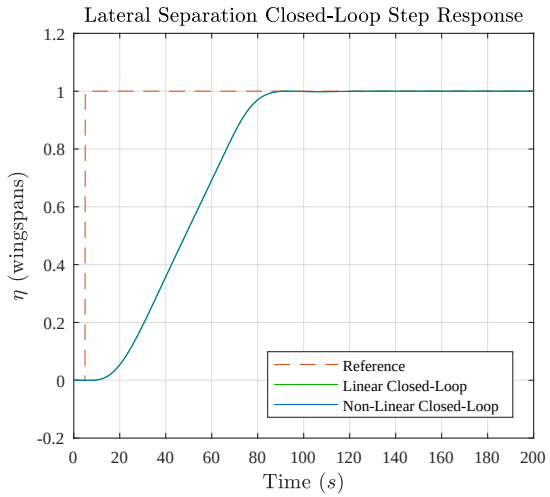

(a) Lateral separation response.

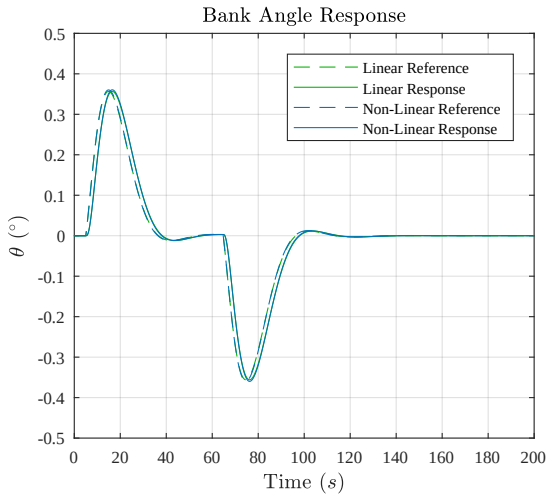

(b) Bank angle response

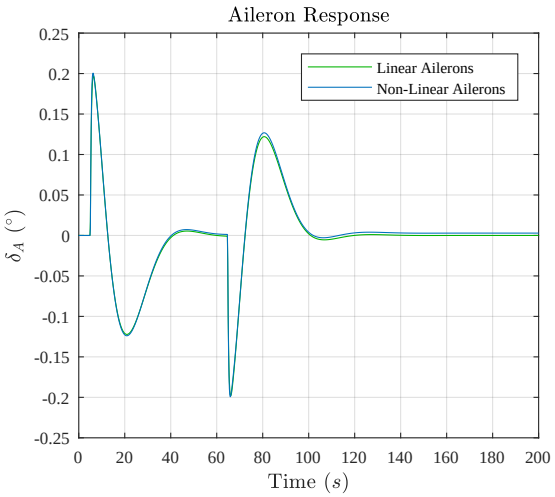

(c) Aileron response.

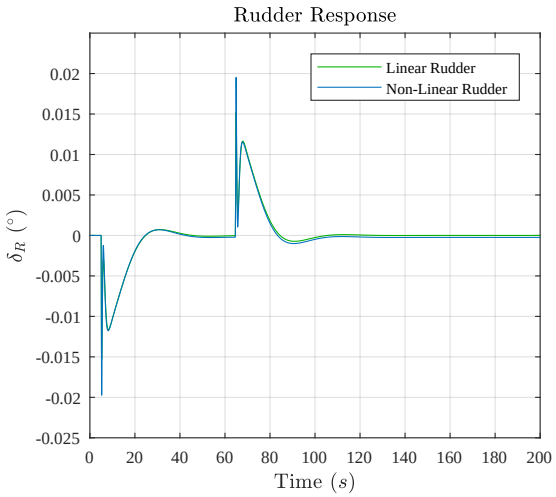

(d) Rudder response.

Figure 4.44: Lateral separation and aircraft state and actuator responses for a rate limited commanded step in lateral separation.

4.5.4 Complementary Filter Controller

In a study by FG van Wyk [2], the formation-hold control authority problem was addressed – stable flight deep in the wake of the leader aircraft requires large aileron deflections to counter the wake-induced rolling moment. The addition of a complementary filter was proposed, which allows the follower to use other control surfaces – rudder and differential thrust – to provide the necessary counter rolling moment to achieve equilibrium in the leader's wake. Rudder can be applied to produce some sideslip which causes a rolling moment. This however requires increasing rudder authority the deeper the follower enters the leader's wake. The principle of rather utilising differential thrust is shown in Figure 4.45, where a yawing moment is induced on the follower causing sideslip and a rolling moment.

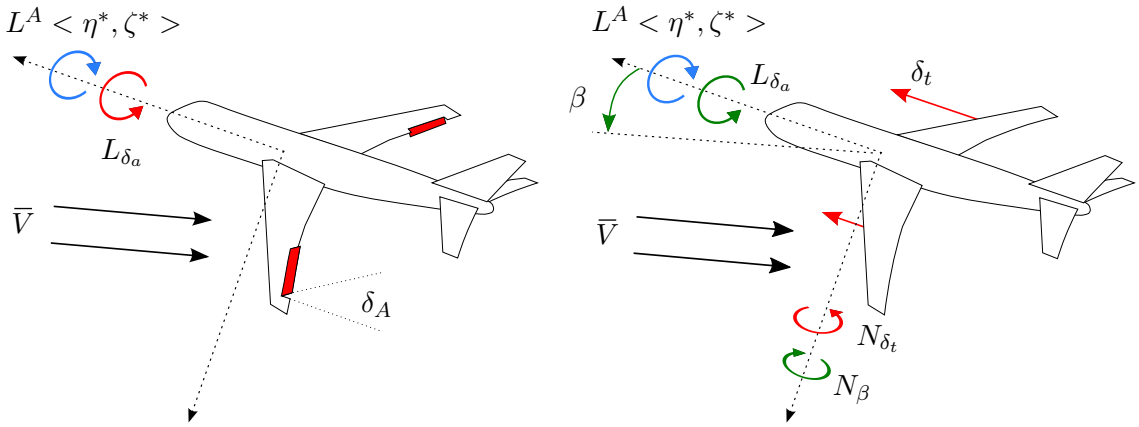

(a) Aileron application.

(b) Differential thrust application.

Figure 4.45: Countering wake-induced rolling moment through application of a) ailerons or b) differential thrust.

The architecture of the complementary filter system is shown in Figure 4.46. The filter system receives the aileron and rudder commands from the DPDR controller and distributes the low frequency components of these commands to differential thrust. If differential thrust is saturated, the controller applies additional rudder to produce the same effect, and if the rudder actuator is saturated, additional aileron deflection is applied. This principle allows the aircraft to retain most of its actuator authority for manoeuvring. The gains of the controller are determined by calculating the gearing ratios between the different actuators. Details regarding the system can be found in [2].

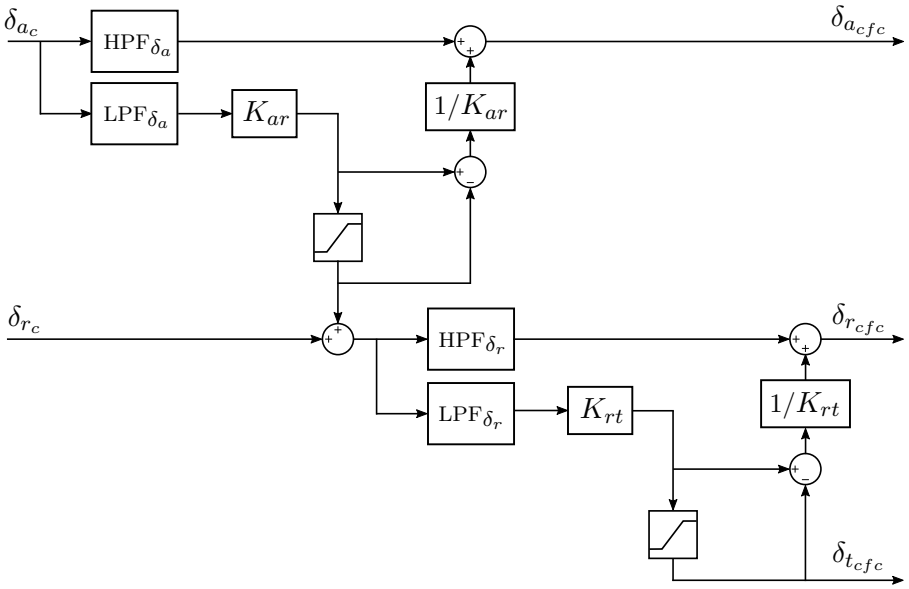

Figure 4.46: Complementary filter controller architecture.

4.6 Summary of Extended Formation Flight Control Systems

In the previous section, controllers were developed that enable aircraft to fly in extended formation flight. The formation flight controller architecture builds upon the conventional flight controllers developed in earlier sections, and which are left unchanged. Three formation flight guidance controllers were added to the guidance loop: a vertical guidance controller maintains a desired geometric vertical separation between aircraft and replaces the altitude controller; an axial guidance controller maintains the desired geometric longitudinal separation by providing an airspeed reference to the autothrust controller; and, lastly, a lateral guidance controller that maintains a desired geometric lateral separation between aircraft was added as an additional loop outside the cross-track controller.

A complementary filter system, as suggested by FG van Wyk, was also added as an inner-loop controller – enabling a follower aircraft to utilise differential thrust in order to counter the wake-induced rolling moment, rather than the conventional aileron deflection. This ensures enough aileron authority for general movement.

In the next chapter, the concept of extremum seeking will be discussed and explored as a feasible method of reducing follower thrust demand during formation flight. The decrease in thrust demand directly corresponds to reduced fuel consumption.

Chapter 5

Extremum-Seeking Control

In order to fly the follower aircraft at the optimal location in the leader's wake, the follower aircraft must locate the trailing vortex and fly at the optimal location relative to the time-delayed vortex core. In an ideal formation flight scenario where there are no external wind disturbances present, the location of the vortex relative to the leader aircraft can be modelled quite accurately, and the follower aircraft could just control its geometric separation relative to the leader aircraft. However, in a realistic formation flight scenario with external wind disturbances, the vortex will be disturbed, and the time-delayed location of the vortex relative to the leader aircraft will not be well modelled. The follower aircraft therefore requires a robust method to find the vortex and to guide itself to the optimal location relative to the vortex. The problem is complicated by the fact that the follower aircraft must seek the optimal location relative to the vortex while still maintaining a minimum safe distance from the vortex core.

In this chapter, an extremum-seeking control (ESC) algorithm is investigated as a means to "sense" the leader aircraft's trailing vortex and to guide the follower aircraft to the optimal location relative to the time-delayed vortex core. The extremum-seeking control does not require any explicit knowledge of the wake, and thus removes the need of additional wake-sensing technologies on board the follower. The research presented in this chapter builds on a previous study by Van Wyk [2] that also investigated extremum-seeking control for formation flight of passenger airliners. However, where Van Wyk's first iteration served to prove the concept, this study aims to design and analyse the extremum-seeking controller more thoroughly and contributes several improvements to the ESC algorithm. The key contributions of this study include:

- The correction of the dither signals with regards to amplitude and phase.
- A novel constrained objective function that uses the wake-induced pitch angle.
- An in-depth analysis of the freestream pitch angle model.
- Novel logic control that enables the follower aircraft to track a dynamic vortex while maintaining a minimum safe distance from its core.
- The implementation of a novel constant rate approach method.
- An analysis of the effects of the ESC parameters on the extremum seeking performance.
- A proposed systematic procedure for selecting the ESC parameters.
- The design and verification of a modified logic controller to track a constrained and dynamic extremum.

The chapter starts with a conceptual overview of the extremum-seeking controller, presenting a breakdown of its different components and operation. Next, detail discussions follow on the design of each component as well as the important considerations taken into account during the design process. The next sections focus on testing the controller in a formation flight simulation. The case of seeking a *stationary* extremum is first investigated, which includes the basic simulation results for different approach methods, as well as an analysis on the choice of different controller parameters. Based on the results of the analysis, a procedure is suggested for selecting the controller parameters. Lastly, the case of seeking a *dynamic* extremum is investigated. As mentioned above, wind disturbances will constantly displace the extremum, shifting it either closer to or further from the follower aircraft.

5.1 Extremum-Seeking Controller Overview

The architecture of the proposed extremum-seeking controller is shown in Figure 5.1.

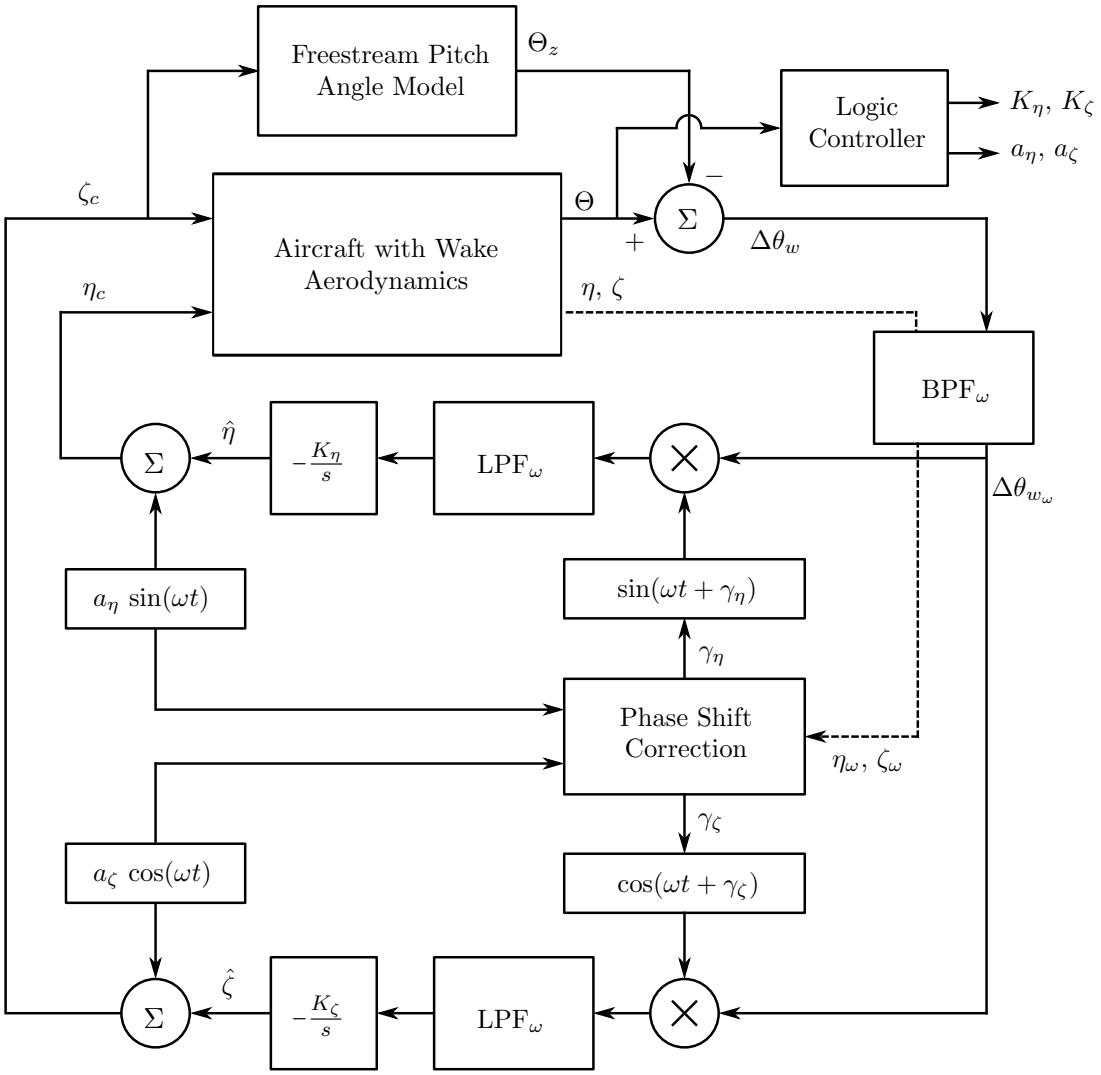

Figure 5.1: Proposed extremum-seeking control architecture.

The control scheme is similar to that used by Van Wyk [2], implementing a band-pass

filter instead of the classical high-pass filter [6, 8, 28]. The controller further consists of several key components: the dither signals, the observer, the objective function, the low- and band-pass filters, the demodulation and phase synchronization stage, and, finally, the logic controller.

General Operation

As discussed in Chapter 2, the purpose of flying aircraft in formation is to reduce the drag force experienced by the follower aircraft through means of the additional lift force present in the upwash region of the leader's wake. An extremum-seeking algorithm may be used to autonomously guide the follower aircraft to the position in the leader's wake where the wake-induced lift force is a maximum. This location also corresponds to the maximum drag reduction and thus the minimum possible fuel consumption of the follower aircraft. The extremum-seeking algorithm achieves this by maximising or minimising an objective, such as the wake-induced drag force, that relates the fuel savings of the follower to its position in the wake. The objective function itself, however, is an unknown function of the lateral and vertical separation. The extremum-seeking algorithm obtains information on the objective function, and indirectly the wake profile, by commanding the follower aircraft to perform small circular dithering motions, at a predefined frequency, better known as conical scanning. The extremum-seeking controller then uses the resulting objective function values, which vary as the follower dithers, and the actual motion of the aircraft to determine the gradient of the objective function. The gradient information is then used to command the lateral and vertical separation rates of the follower aircraft in the direction that maximises or minimises (based on the chosen objective) the objective function. If, for example, the objective of the extremum-seeking controller is selected as maximising the lift of the follower aircraft in the wake, the controller will use the gradient information of the lift, obtained through dithering, to command lateral and vertical separation rates to move the follower to a location of increased lift. As the aircraft moves through the wake, the gradient of the lift objective is calculated continuously, and the lateral and vertical separations rates of the follower are updated until the lift is maximised (the objective of the ESC is completed).

We now consider the controller architecture shown in Figure 5.1. Two orthogonal dither signals, $a_\eta \sin(\omega t)$ and $a_\zeta \cos(\omega t)$, are superimposed on the lateral separation command η_c and vertical separation command ζ_c respectively to serve as inputs to the formation-hold controllers. Since the two dither signals are orthogonal and at equal frequencies, the aircraft is commanded to explore the wake in circular motions. The relative amplitudes of the dither signals determine the shape of the dithering motions, but the amplitudes are generally selected to be equal so that the aircraft performs circular motions. (If the amplitudes are not equal, then the aircraft performs elliptical motions.).

In the work of Binetti et al., two different frequencies are used for the vertical and lateral dither signals, which results in the aircraft performing non-circular motions. This, however, requires very accurate filters to differentiate between the effects in the objective function caused by lateral or vertical movements. If the filters are not accurate, changes in the band-passed objective function of one directional dither will include effects induced by the other directional dither. Using multiple frequencies does, however, allow for extremum seeking over multiple dimensions. Since locating the extremum of a leader-generated wake only requires seeking in two dimensions, using orthogonal dithers is sufficient.

Ideally, the wake-induced lift or thrust demand would serve as adequate objectives for the extremum-seeking controller to optimise, since both relate directly to the reduction in drag of the follower aircraft. However, the lift of an aircraft is difficult to measure, and the bandwidth of the thrust dynamics is too low for the purpose of extremum seeking (slow thrust

dynamics would require very slow dither frequencies, resulting in long convergence times). In the architecture illustrated above, the wake-induced pitch angle variation $\Delta\theta_w$ is selected as the objective, since it is easy to measure and relates to the lift of the aircraft. As the wake-induced lift increases, the follower aircraft must decrease its own generated lift to remain in equilibrium, which is achieved by flying at a lower angle of attack. The follower aircraft thus decreases its pitch angle to pitch the nose of the aircraft down and lower the angle of attack. An increase in the wake-induced lift thus corresponds to a decrease in the pitch angle of the aircraft. However, the pitch angle of the aircraft also changes due to the aircraft's own movement, and not just due to changes in the wake-induced lift. For example, when an aircraft in isolated flight climbs, its pitch angle increases. Similarly, when an aircraft in isolated flight descends, its pitch angle decreases. Performing the commanded dither motions thus also induce changes in the pitch angle. The freestream pitch angle model removes the variation in pitch angle due to the aircraft's own movement Θ_z, and the result is called the wake-induced pitch angle $\Delta\theta_w$. The wake-induced pitch angle is then filtered by a band-pass filter, BPF_ω, to pass only the influence of the wake on the pitch angle in the frequency range of the dither signals.

The effect of each dither signal command on the wake-induced pitch angle is extracted through demodulation and passed through a low-pass filter, LPF_ω, which removes undesired high-frequency information. The low-frequency information output of the low-pass filter describes the mean change in objective as the aircraft moves through the wake, and is used to update the control law which in turn moves the aircraft in the optimal direction. With each iteration of the control loop, the follower can loosely be thought of as flying at a more efficient separation.

Due to the dynamics of the lateral separation controller and the vertical separation controller, a phase lag exists in the objective signal with respect to each of the two dither input commands. The purpose of the phase lag correction stage is to detect and compensate for this phase lag by shifting each respective demodulating dither with the necessary phase before demodulation. The lateral demodulating dither is phase shifted by γ_η and the vertical demodulating dither by γ_ζ. Finally, an extremum-seeking state machine (logic controller) is implemented to vary the ESC gains, K_η and K_ζ, as well as the dither amplitudes, a_η and a_ζ, as the follower aircraft approaches the extremum. By varying the gains and dither amplitudes, the approach rate of the follower aircraft can be varied, a topic that will be discussed in more detail in Section 5.3.3. In addition, changing of the gains and dither amplitude also plays a vital role in keeping the follower aircraft at a minimum safe separation from the vortex core.

Criteria of Stability

The controller scheme as presented above has been proven to be stable by Krstić and Wang [26] under the following three assumptions:

1. The plant gradient map is continuous for the specified range of plant input commands.
2. The plant is robust and thus converges for the entire range of input commands.
3. The optimization objective has a maximum or minimum for a specific input command.

The second assumption is satisfied since the formation-hold controllers designed in Chapter 4 stabilizes the aircraft for all control inputs, given that the follower is not too deep in the wake. It will be shown in Section 5.2.2 that the first and second assumptions are also satisfied based on the choice of objective function.

5.2 Extremum-Seeking Controller Design

This section aims to elaborate on the design process of the extremum-seeking controller described in the previous section. The design of each key component is discussed in more detail, highlighting some of the important considerations taken into account that have not been addressed thoroughly in literature. The layout of the section is shown in Figure 5.2.

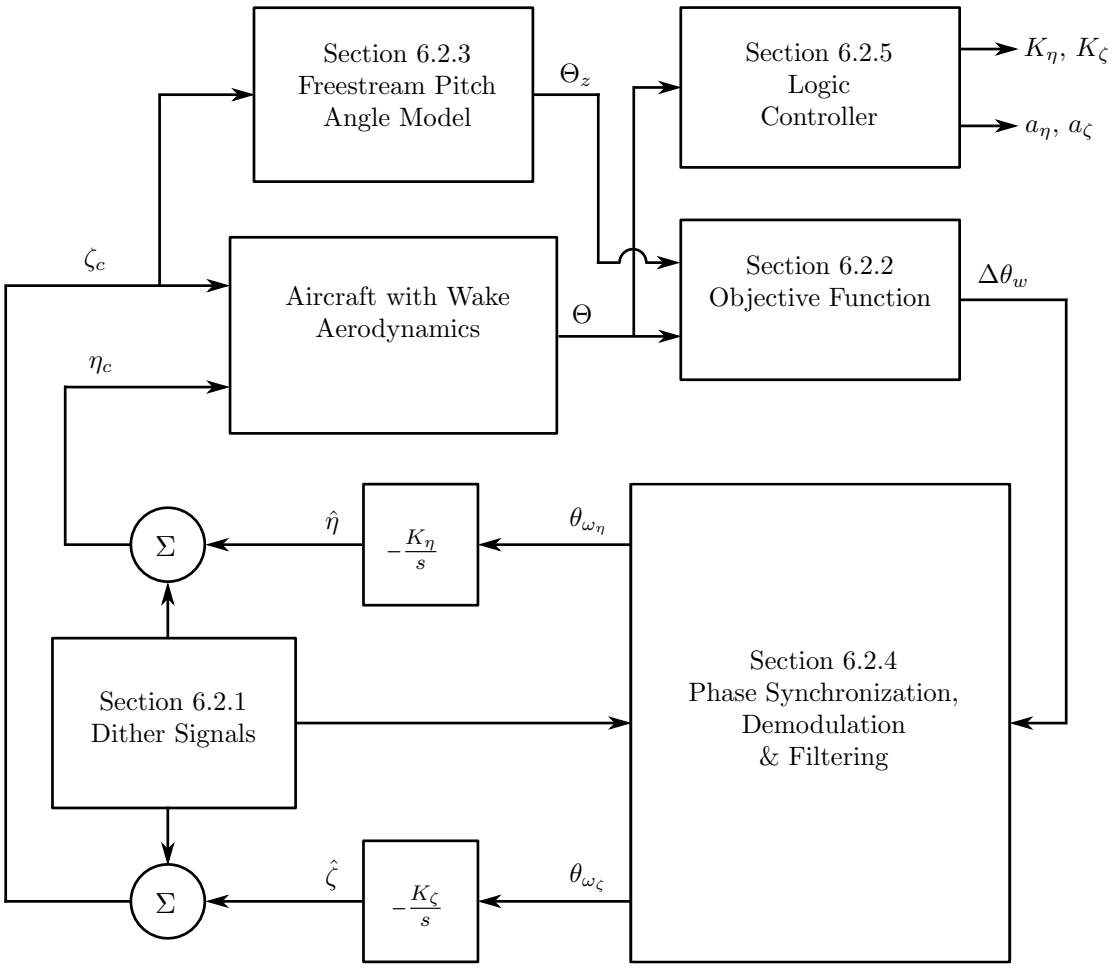

Figure 5.2: Proposed extremum-seeking control scheme.

5.2.1 Dither Signals

As mentioned in the previous section, the vertical and lateral dither signals are used to command the follower aircraft to explore the leader wake. For this study, a method called conical scanning is implemented, which requires that the dither signals are orthogonal and of equal amplitude and frequency. This would result in the follower aircraft executing perfect circular motions at the dither frequency whilst moving through the wake. However, the dynamics of the aircraft's flight control system, specifically the vertical and lateral separation controllers, introduce phase lag and amplitude attenuation in the vertical and lateral motion actually executed by the aircraft, which adversely affects the operation of the extremum-seeking controller. This section briefly presents the corrections that are necessary with regards to dither amplitude and phase for the vertical and lateral separation references, to compensate for the error in the executed vertical and lateral dither motion.

Dither Phase Correction

Since the vertical and lateral separation controllers of the aircraft have different time constants, simply providing vertical and lateral separation commands with dither signals that are separated by 90° is not sufficient to guarantee that the aircraft will execute circular motions. The difference in time constants results in the aircraft responding faster in one axis of movement than in the other, distorting the expected motion, as illustrated by Figure 5.3. Since the lateral and vertical motions are not separated by 90°, inaccurate wake information is relayed to the controller.

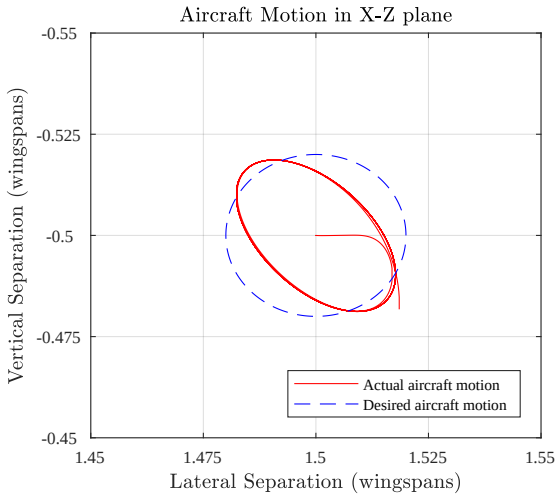

Figure 5.3: Aircraft motion without dither phase correction.

This distortion can, however, be corrected by adjusting the phase of one of the dither signals so that the executed dither motion is circular. The proposed scheme for calculating the required phase shift value is shown in Figure 5.4, where η_ω and ζ_ω are the band-passed follower aircraft separation variables, $\Delta\gamma_\omega$ is the calculated phase difference, and, finally, $\Delta\gamma_D$ is the required phase shift and Δt_D its equivalent time delay.

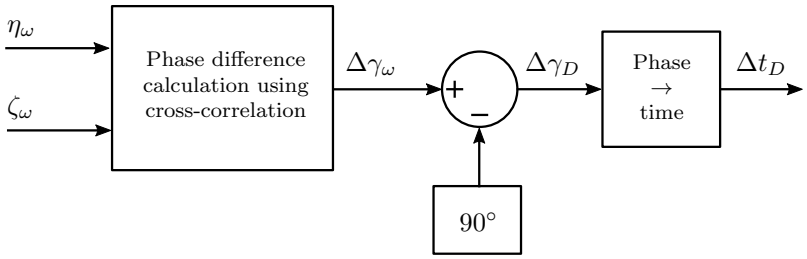

Figure 5.4: Proposed dither phase correction scheme.

The current phase difference between the aircraft's vertical and lateral motions is determined by calculating the cross-correlation of two recordings of the vertical and lateral motions respectively. The phase at which the cross-correlation is a maximum is taken as the current phase difference $\Delta\gamma_\omega$. Next, the required phase change, $\Delta\gamma_D$, is determined by subtracting the desired phase difference of 90 degrees from the calculated phase difference. Finally, the calculated phase is converted to a time shift by which the appropriate dither is then delayed.

Implementing the scheme as presented above yields the result shown in Figure 5.5, where, after a few dither periods, the dither commands are adjusted and the aircraft performs an elliptical motion with its axes aligned with the vertical and lateral directions. The aircraft dither motion will be made circular after compensating for the amplitude attenuation.

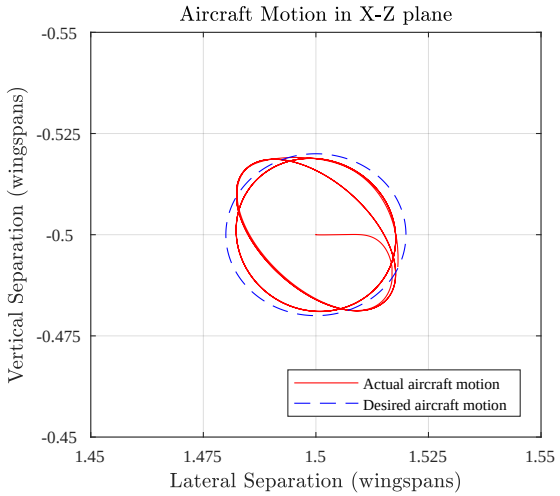

Figure 5.5: Aircraft motion with dither phase correction.

Dither Amplitude Correction

Due to the dynamics of the aircraft's vertical and lateral separation controllers, attenuation occurs from the commanded dither signals to the actual dither motions executed by the aircraft. For accurate gradient estimation through demodulation, the amplitude of the actual lateral and vertical dither motions executed by the aircraft should be equal to the amplitude of the respective demodulating dither signals.

An on-line amplitude correction scheme is implemented that requires recordings of the actual lateral and vertical dither motions executed by the aircraft. After a few dither periods, which are selected to match the amount of periods chosen for phase correction, the recordings of the actual lateral and vertical dither motions executed by the aircraft are compared to the known dither signal commands. The difference in amplitude between the actual lateral and vertical dither motions and the respective dither signal commands, are used to calculate the attenuation in each direction of movement, and the amplitudes of the dither signal commands are adjusted as necessary to compensate for the calculated attenuation. In other words, the amplitudes of the dither commands are adjusted accordingly so that the actual executed lateral and vertical dither motions of the follower are circular. Figure 5.6 shows the resulting dither motion of the follower aircraft after the amplitudes of the lateral and vertical dither signal commands are adjusted to compensate for the attenuation. The actual aircraft motion nearly matches the commanded reference motion. The slight deviation is due to the filter transients that occur in simulation, which affect the recordings of the mean dither amplitudes during the first few periods after the extremum-seeking controller is activated.

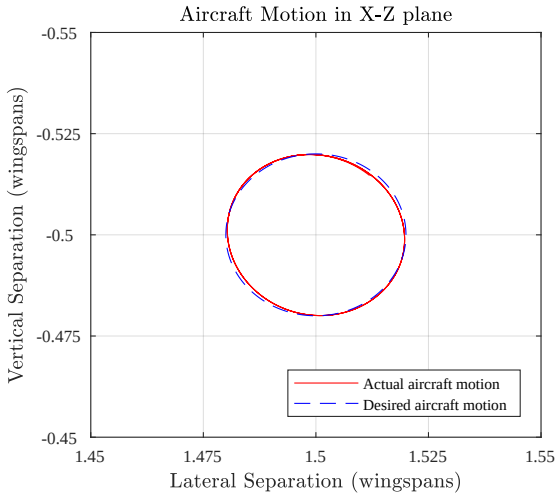

Figure 5.6: Aircraft motion with dither amplitude correction.

5.2.2 Objective Function

As mentioned in Chapter 2, the extremum in the wake corresponds to the location where the drag experienced by the follower aircraft is a minimum. The wake-induced drag cannot be directly measured which means that an alternative objective, related to the drag, is required to locate the extremum. As discussed in Section 5.1, the wake-induced lift or thrust demand of the follower aircraft would be ideal objectives for the extremum seeking algorithm, since they relate directly to the wake-induced drag. The lift of the follower aircraft is related to the drag through the angle of attack of the aircraft, as explained in Section **??**, while a reduction in drag directly translates to a reduction in the required thrust. However, the lift of an aircraft is difficult to measure, and the low bandwidth of the thrust dynamics would require very slow dither signal frequencies, resulting in long convergence times. One of the most popular suggestions is the use of the pitch angle of the follower aircraft as the objective, since it is very easy to measure and is used as a proxy for the wake-induced lift through its relation to angle of attack. Figure 5.7a illustrates the required follower trim pitch angle to fly at different formation separations within the leader's wake. It is clear that the required pitch angle is a minimum at a vertical separation of zero wingspans and a lateral separation of approximately 0.78 wingspans, and increases as the follower moves further away from the leader. This closely corresponds to the wake-induced lift as seen in Figure 5.7b.

The pitch angle, however, does not only change due to wake-induced lift, but also due to normal aircraft movement such as changes in altitude and airspeed. The ESC dither signal commands also result in changes in the altitude of the aircraft. In order to "sense" only the wake-induced changes in pitch angle as the objective function, Binetti [6, 28] suggests the use of an "observer" to remove the changes in pitch angle due to the aircraft's own motion. The freestream pitch angle model, shown in Figure 5.1, models the pitch angle response of the aircraft to vertical separation commands as if it were in isolated flight, and the modelled pitch angle output is then subtracted from the measured pitch angle output of the actual aircraft to yield only the pitch angle deviation due to the wake. The wake-induced pitch angle deviation is calculated by,

$$\Delta\theta_w = \Theta - \Theta_z \tag{5.1}$$

where Θ is the measured pitch angle of the follower, and Θ_z is the modelled pitch angle of the follower if it were in isolated flight. Figure 5.8 shows a plot of the wake-induced pitch

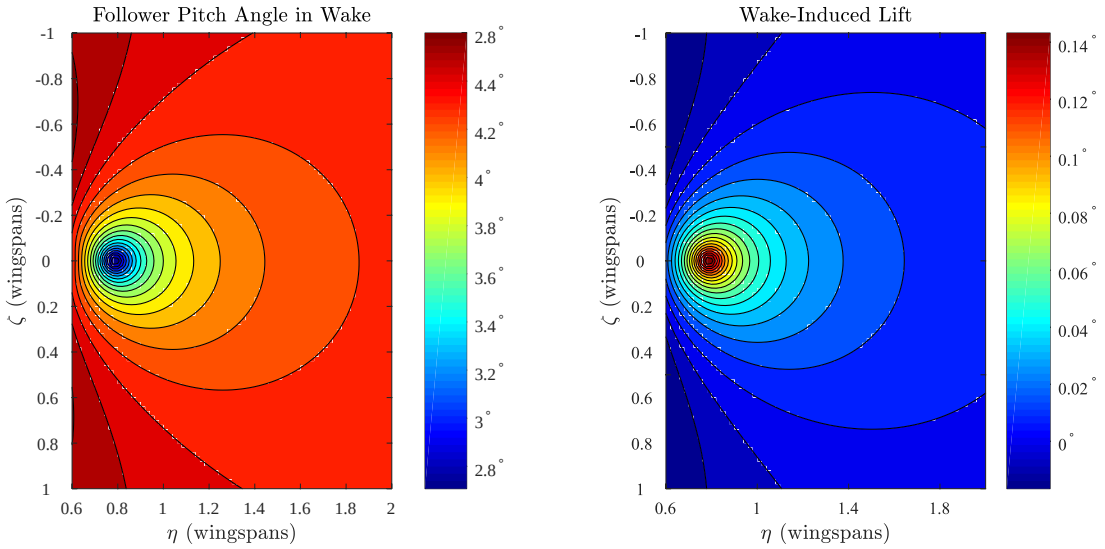

(a) Follower trim pitch angle in wake.

(b) Follower wake-induced lift.

Figure 5.7: Trim pitch angle and wake-induced lift.

angle variation $\Delta\theta_w$ as a function of vertical separation ζ and horizontal separation η (at an axial separation of 10 wingspans). The freestream pitch angle model will be discussed in more detail in the next section.

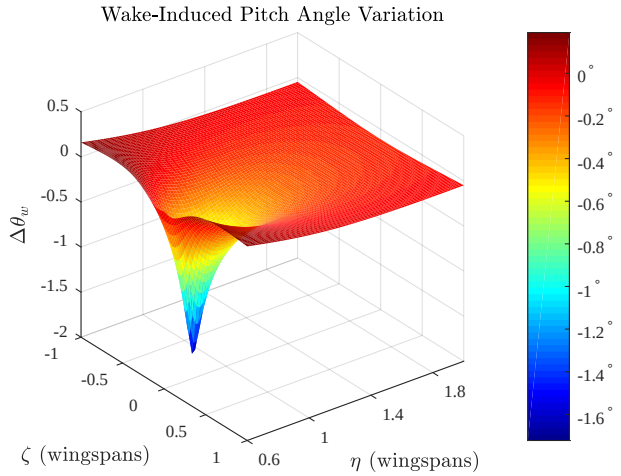

Figure 5.8: Contour plot of follower trim pitch angle variation in wake.

Because of wake model inaccuracies and the high risk of experiencing a large wake-induced rolling moment near the extremum [10], Van Wyk suggests designing the ESC to only command the aircraft to a minimum geometric lateral separation of one wingspan. This is a feasible approach if the wake is not disturbed by external wind disturbances, since the effective separation between the follower and the vortex would then equal the geometric separation between the follower and the leader. However, in the presence of external wind disturbances, the effective separation between the follower and the vortex would differ from the geometric separation between the follower and the leader, and the follower aircraft may therefore be closer to the vortex than the geometric separation would indicate. A minimum *geometric*

separation of one wingspan from the leader aircraft would therefore not guarantee a minimum safe *effective separation* from the vortex. It is important to note that extremum-seeking control is generally used to locate the extremum of an objective function *without* constraints on the inputs variables. Since the follower aircraft must be prevented from flying too deep into the wake of the leader aircraft, the extremum-seeking control must be modified to find the location in the wake with the minimum drag, but with constraints on the minimum allowable effective lateral and vertical separations between the follower aircraft and the trailing vortex of the leader aircraft. One of the main contributions of this study is the development of a novel constrained extremum-seeking control algorithm that allows the follower aircraft to locate a minimum drag location in the wake, and track it as its moves under the influence of external wind disturbances, while obeying the constraints of maintaining a safe effective separation from the trailing vortex.

Constrained Objective Function

In order to locate and track a moving minimum drag location while maintaining a safe effective separation from the trailing vortex, this study proposes that the objective function shown in Figure 5.8 be constrained as a function of the minimum allowable wake-induced follower pitch angle deviation, instead of as a function of the instantaneous geometric separation between the leader aircraft and the follower aircraft (as proposed by Van Wyk [2]). The constrained objective function is shown in Figure 5.9a, where the filled white circle represents the area within the wake where the follower aircraft is not allowed to fly. The boundary of the circle represent the locations where the wake-induced follower pitch angle deviation is at its minimum allowable value. The follower aircraft will experience the same wake-induced drag benefit at any location along the boundary of the circle. The extremum of the constrained objective function is therefore a contour instead of a point.

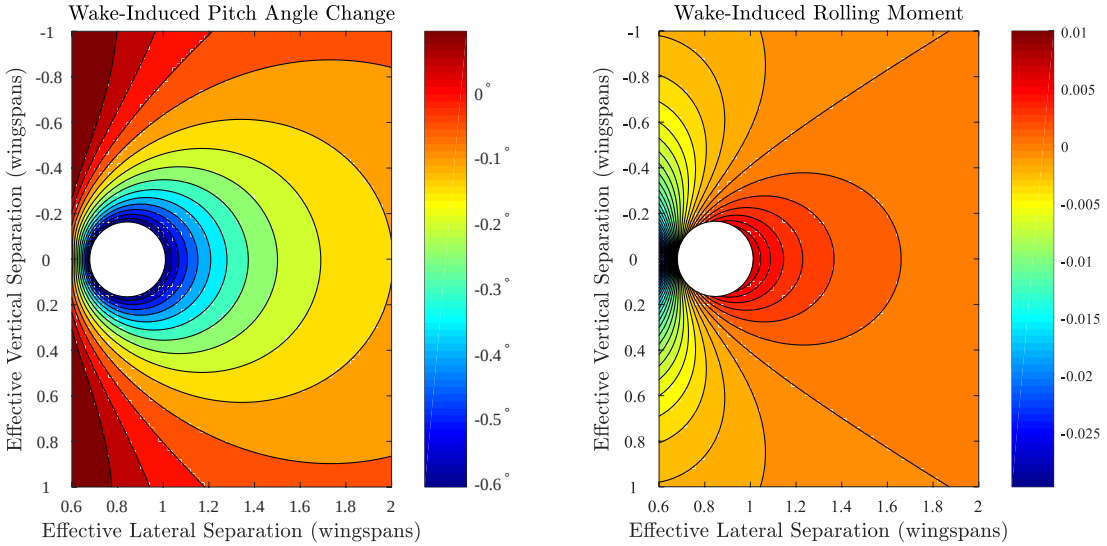

(a) Constrained objective function (wake-induced pitch angle change)

(b) Wake-induced rolling moment.

Figure 5.9: Contour plots of the constrained objective function (wake-induced pitch angle deviation) and the corresponding wake-induced rolling moment.

It is interesting to note that the follower aircraft will experience the same wake-induced

drag benefit at any point along the contour, but not the same wake-induced rolling moment, as illustrated by Figure 5.9b. Moving from right to left along the contour (along either the upper boundary or the lower boundary), the rolling moment changes from a relatively *positive* rolling moment to a large *negative* rolling moment, which will roll the follower into the downwash behind the leader if not countered. Fortunately, this region of dangerous wake-induced negative rolling moment can be avoided by approaching the extremum from the right.

There exists an interesting trade-off between the variation in wake-induced drag and the rolling moment disturbance along the constrained minimum drag contour. Consider the magnitude of the wake-induced lift gradient and rolling moment along the extremum contour, shown in Figure 5.10. The auxiliary axis, shown in Figure 5.10a, is used to present the lift gradient and rolling moment as functions of the angle along the constrained minimum contour. The magnitudes of the wake-induced lift gradient and rolling moment are shown in Figure 5.10b. As the angle along the contour increases, the lift gradient increases and the rolling moment decreases. When dithering at the constrained extremum on the contour, a larger lift gradient yields larger variations in wake-induced drag, which results in larger variations in the engine thrust required to maintain the follower at its trim airspeed. On the other hand, a smaller wake-induced rolling moment requires smaller aileron and rudder deflections, and less differential thrust, to trim the aircraft laterally. This introduces a trade-off between the amplitude of the thrust variations caused by dithering about the extremum at the constrained minimum drag location, and the magnitude of the rudder and aileron deflections required to counter the wake-induced rolling moment. By moving along the constrained minimum contour, the amplitude of the thrust variations can be reduced at the expense of increase aileron and rudder deflections, and vice versa.

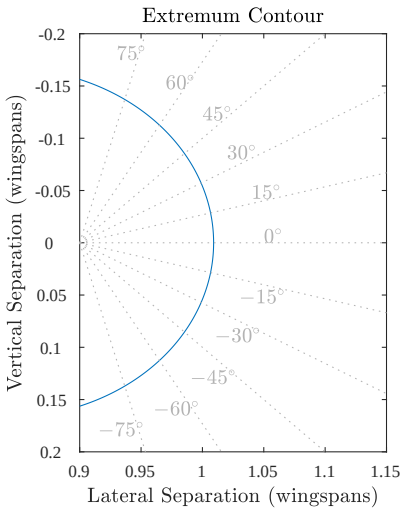

(a) Auxiliary axis.

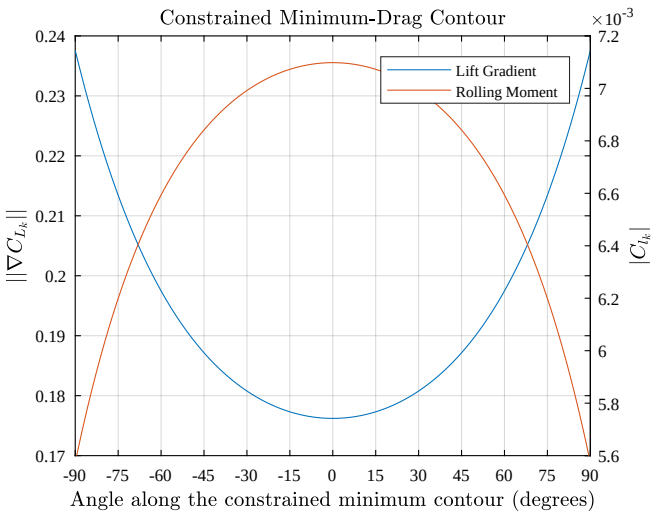

(b) Magnitude of wake-induced lift gradient and rolling moment.

Figure 5.10: Auxiliary angle axis system and the magnitude of the wake-induced lift gradient and rolling moment along the constrained minimum drag contour.

Although not covered by this study, a secondary objective, such as minimising aileron and/or rudder demand or minimising the amplitude of the dither-induced thrust variations, could be used to enable the ESC to guide the follower to a specific position on the constrained minimum drag contour. The extremum-seeking process may be divided into two stages.

The first stage seeks to guide the follower onto the constrained minimum drag contour by minimizing the wake-induced pitch angle deviation objective function. Once the follower detects that it is on the constrained minimum contour, the second stage guides the follower toward a specific position on the contour by minimizing the second objective function.

5.2.3 Freestream Pitch Angle Model

The measured follower pitch angle consists of two components: variations due to wake-induced effects, $\Delta\theta_w$, and variations due to aircraft motion, Θ_z. In order to use only the wake-induced pitch angle as the objective function, the pitch angle variations due to aircraft motion must be removed. Binetti [6, 28] suggests the use of an "observer" based on the isolated aircraft model to extract these variations, since the changes in pitch angle, which are purely due to motion, are the same inside and outside of the leader wake. This section details the design and verification of the suggested model, as shown in Figure 5.11.

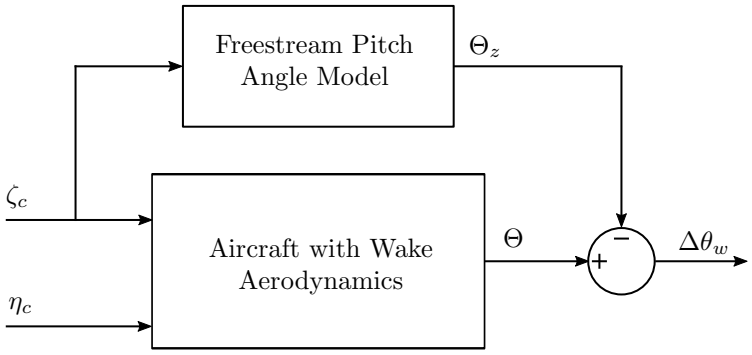

Figure 5.11: Freestream pitch angle model.

In the work of Van Wyk, the freestream pitch angle was calculated through use of a full-order coupled model from elevator command to pitch angle. It will be shown here that a simple transfer function, as proposed by Binetti, is sufficient, since the changes in pitch angle are mainly due to vertical movement. The transfer function from vertical separation command to pitch angle due to aircraft motion is given by,

$$\frac{\Theta_z(s)}{\zeta_{ref}(s)} = \mathbf{C}_\theta(sI - \mathbf{A}_{VS})^{-1}\mathbf{B}_{\zeta_{ref}} \tag{5.2}$$

where $\mathbf{A}_{VS}$ is the state matrix of the closed-loop vertical separation controller state space model, and $\mathbf{B}_{\zeta_{ref}}$ is the first column of the vertical separation controller state space model input matrix $\mathbf{B}_{VS}$ that corresponds to the vertical separation reference ζ_{ref}. The output matrix $\mathbf{C}_\theta$ is given by,

$$\mathbf{C}_\theta = \begin{bmatrix} 0 & 0 & 0 & 1 & 0 & 0 \end{bmatrix} \tag{5.3}$$

The axial contribution is not included as the aircraft is commanded to remain at the same axial separation. In the remainder of the section, the freestream pitch angle model will be validated in freestream as well as in the wake.

Model Validation in Freestream

The first step is to verify that the freestream pitch angle model correctly models the pitch angle response in freestream conditions. Figure 5.12 shows a comparison between the actual and modelled pitch angles for steps in the vertical and lateral directions. For an altitude step, the observer very closely matches the variation in actual pitch angle, sufficiently capturing the dominant dynamics, as shown in 5.12a. From Figure 5.12b it is clear that the effect of lateral movement on the pitch angle is negligible, since the variation is orders of magnitude less than the variation due to vertical movement.

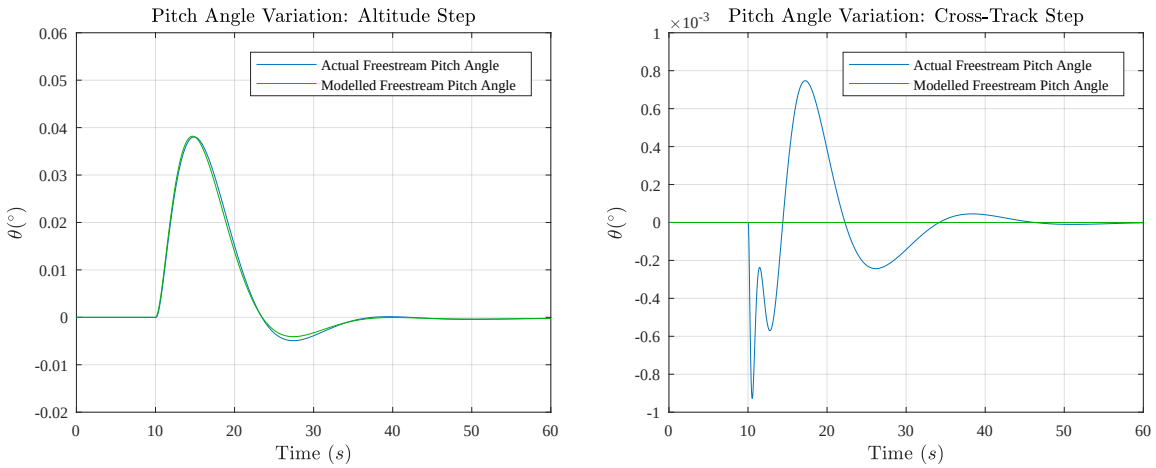

(a) Step of 1m in altitude.

(b) Step of 1m in cross-track.

Figure 5.12: Comparison of actual and modelled pitch angle response due to a vertical and lateral steps in isolated flight.

Figure 5.13 shows a comparison between the actual and modelled pitch angle response due to circular dithering. The dither was chosen to have an amplitude of 1 m and a period of 60 s. From the result it can be seen that the model performs sufficiently well, closely matching the actual pitch angle response. The effect of the lateral dither on the change in pitch angle is seen to be negligible when performing the circular motions required by extremum seeking.

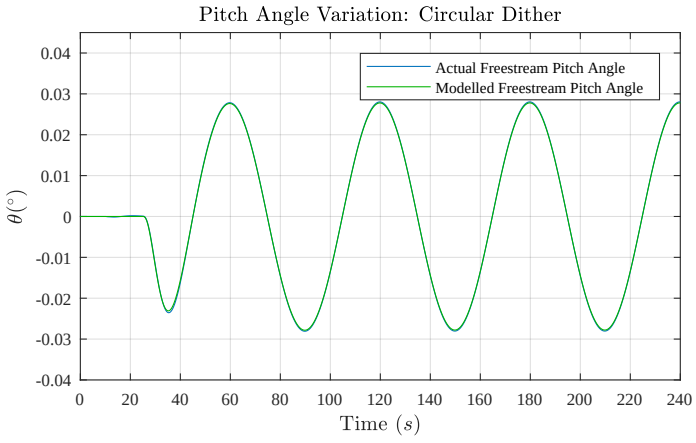

Figure 5.13: Comparison of actual and modelled pitch angle response due to a 1m amplitude circular dither command.

Model Validation in Wake

In this section, the freestream pitch angle model's ability to model the pitch angle response due to aircraft motion only, while flying in the leader's wake, is evaluated. In addition, the accuracy of the wake-induced pitch angle deviation as a proxy for wake-induced lift is evaluated. Figures 5.14 and 5.15 show the results obtained from dithering above the extremum, at separation $\eta = 1.5$ and $\zeta = -0.5$, and below the extremum, at separation $\eta = 1.5$ and $\zeta = 0.5$.

First, the case of dithering above the optimum is considered. Figure 5.14a shows the actual pitch angle, the freestream pitch angle calculated by the model, and the resulting wake-induced pitch angle as calculated by Equation 5.1. When comparing the actual with the freestream model pitch angle, two important differences are identified: the actual pitch angle has a smaller amplitude and slightly lags the freestream pitch angle. This can be attributed to the effect the leader wake has on the follower aircraft dynamics. Freestream dynamics dictate that an increase in altitude is accompanied by an increase in pitch angle. Similarly, if the aircraft decreases its altitude, a decrease in pitch angle occurs. However, flying in the leader wake introduces other dynamic effects. As the follower moves upward, it also moves out of the wake, decreasing the wake-induced lift. This causes the transient pitch angle of the follower to decrease. Conversely, as the follower moves downward, it moves further into the wake, increasing the wake-induced lift which increases the transient pitch angle. The effect of the wake thus causes the amplitude of the actual pitch angle variation to be smaller than the freestream equivalent. Since the wake tends to 'counter' the transient dynamics of the follower, a phase lag is induced in the aircraft movement, resulting in the actual pitch angle lagging the freestream model pitch angle. Considering the amplitude loss and phase lag of the actual follower pitch angle, the wake effects above the extremum effectively lowers the bandwidth of the follower's vertical movement relative to flying in freestream.

Next, the accuracy of the freestream pitch angle model is evaluated by comparing the wake-induced pitch angle, obtained through Equation 5.1, to the wake-induced lift. Since the wake-induced pitch angle has a maximum and the wake-induced lift has a minimum, a proxy to the wake-induced lift is required for comparison. The proxy is defined as,

$$C'_{L_k} = -C_{L_k} \tag{5.4}$$

where the wake-induced lift, C_{L_k}, is measured directly from the wake model in simulation. This, of course, cannot be done in practice, and is done here for evaluation purposes only. When comparing the wake-induced pitch angle to the lift proxy, it is important to note that the magnitude of the two are not the same. This is expected since the two signals are different entities. We are therefore only interested in the relative phase of the two signals. An increase in wake-induced pitch angle should correspond to an increase in the proxy signal. Similarly, a decrease in the wake-induced pitch angle should correspond to a decrease in the proxy signal. From Figure 5.14b it can be seen that the wake-induced pitch angle matches the lift proxy very well except for a slight phase difference, which can be attributed to a lag in dynamics between the pitch angle and experienced lift. The phase delay is very small, however, and is considered to be negligible.

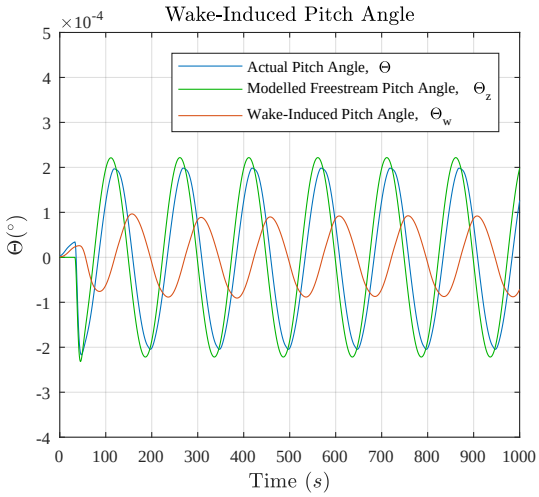

(a) Comparison of actual and calculated freestream pitch angle.

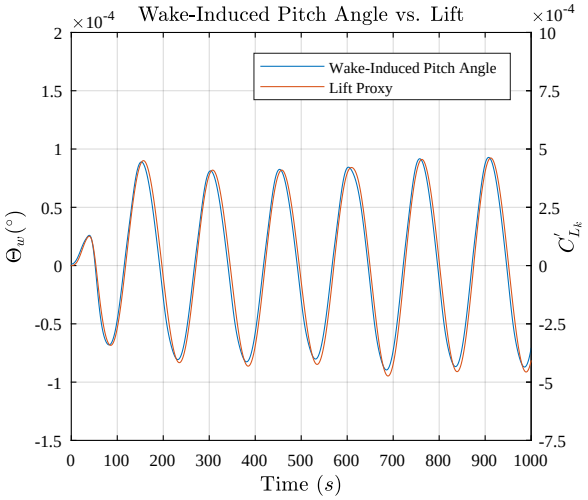

(b) Comparison of wake-induced pitch angle and lift.

Figure 5.14: Operation of the freestream pitch angle model above the leader's wake, with the follower at a separation of $\eta = 1.5$ and $\zeta = 0.5$, and with a dither period of 150 seconds.

Next, the case of dithering below the optimum is considered. Figure 5.15a shows the actual pitch angle, the freestream pitch angle calculated by the model, and the resulting wake-induced pitch angle as calculated by Equation 5.1. From the figure it can be seen that, contrary to the results obtained from dithering above the optimum, dithering below the optimum results in a larger amplitude in actual pitch angle relative to the freestream pitch angle. Once again this can be explained in terms of the effect the leader wake has on the follower aircraft dynamics. When the follower climbs, its pitch angle increases to induce upward movement. However, as the follower moves upward, it also moves further into the wake, increasing the additional wake-induced lift. This causes the transient pitch angle of the follower to also increase. Conversely, when the follower descends, its pitch angle decreases to induce downward movement. The follower moves out of the wake, causing a decrease in wake-induced lift which decreases the transient pitch angle. The effect of the wake thus causes the amplitude of the actual pitch angle variation to be larger than the freestream equivalent. For dithering below the optimum, the wake seems to 'aid' the transient dynamics of the follower, resulting in the actual pitch angle leading the freestream model pitch angle. Considering the amplitude gain and phase lead of the actual follower pitch angle, the wake effects below the optimum effectively increases the bandwidth of the follower's vertical movement relative to flying in freestream. This is a significant result, which will become evident in the extremum seeking simulations presented in section 5.3.2. Figure 5.15b shows a comparison between the wake-induced pitch angle and the lift proxy defined by Equation 5.4. Once again the wake-induced pitch angle matches the lift proxy very well, except for the same negligible phase difference. The slight increase in wake-induced pitch angle amplitude is due to the larger actual pitch angle amplitude in Figure 5.15a. However, for extremum seeking the important things is that the phase difference between the wake-induced pitch angle and the lift proxy signal should be negligible.

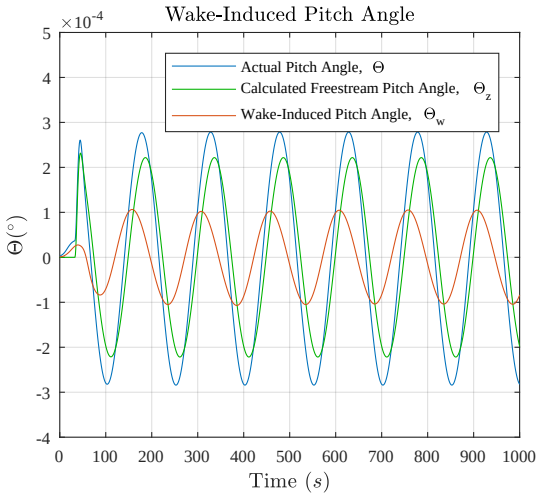

(a) Comparison of actual and calculated freestream pitch angle.

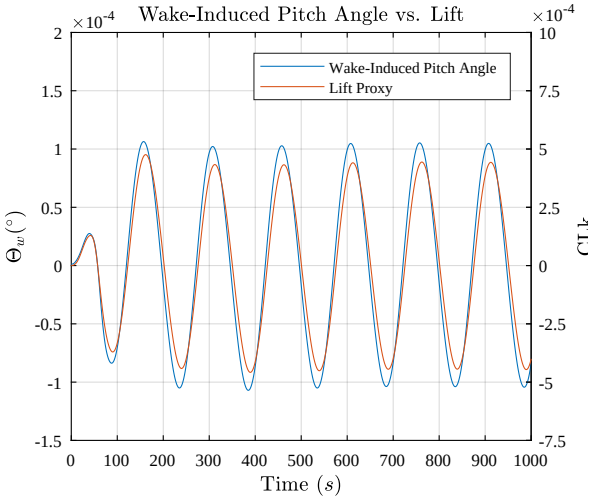

(b) Comparison of wake-induced pitch angle and lift.

Figure 5.15: Operation of the freestream pitch angle model above the leader's wake, with the follower at a separation of $\eta = 1.5$ and $\zeta = -0.5$, and with a dither period of 150 seconds.

5.2.4 Phase Synchronization for Demodulation

For ideal phase demodulation, zero phase lag is required between the demodulating carrier signal and the signal being demodulated. When implementing ESC in a system without dynamics, there typically is not a phase difference between the applied dithering signal and its effects on the objective function. However, in a system with dynamics, such as an aircraft, a phase lag will exist between the applied dithering signal input and objective function output. This introduces a problem when attempting to demodulate the objective function with the original dither signal. If the phase lag is not compensated for, the demodulation and filtering will extract incorrect gradient information, leading to an incorrect update of the control law.

Figure 5.16 shows the scheme proposed for phase synchronization, demodulation and filtering, built on the work of Van Wyk [2]. The wake-induced pitch angle objective $\Delta\theta_w$ is filtered by a band-pass filter BPF_ω with centre frequency equal to the dither frequency ω, which yields only the changes in wake-induced pitch angle due to the dithering motion, $\Delta\theta_{w_\omega}$. The phase shift correction block calculates the phase lag between each dither signal and its resulting aircraft motion. In order to correct for the phase lag at the demodulation step, the calculated phase lag values are used to delay the respective demodulating dithers. The signals after demodulation are then filtered by identical low-pass filters LPF_ω to yield the lateral and vertical components of the objective function estimated gradient, θ_{ω_η} and θ_{ω_ζ} respectively.

This section details the design of a method to detect and correct this phase lag. Firstly, the ideal case with no phase lag present is discussed, illustrating the desired result of the demodulation and filtering stage. Secondly, it is shown how phase lag affects the demodulation result if no compensation occurs. Finally, a phase correction scheme is presented as a solution to compensate for the phase lag.

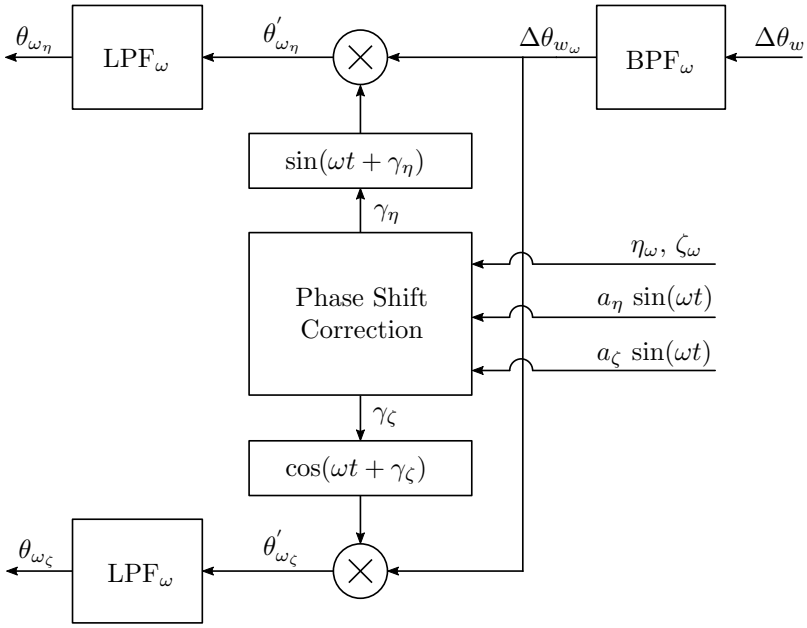

Figure 5.16: Proposed scheme for phase synchronization and demodulation.

Ideal Demodulation and Filtering

The variation in the objective function output due to the dither signal input can be thought of as a modulated signal with two orthogonal components: the variation due to lateral motion $\theta_{w_\eta}(t)$, and the variation due to vertical motion $\theta_{w_\zeta}(t)$. This is described by Equation 5.5, where the modulation carrier frequency is determined by the dither frequency.

$$\theta_w(t) = \theta_{w_\eta}(t)\sin(\omega t) + \theta_{w_\zeta}(t)\cos(\omega t) \tag{5.5}$$

Since the ESC commands the lateral and vertical movement separately, the effect of both directional movements on the objective variation is required to update the control law. The extraction of the orthogonal components is done by the demodulation of Equation 5.5. The lateral component can be reconstructed by demodulation with the unity amplitude lateral dither signal $\sin\omega t$, and passing the result through a low-pass filter to remove high-frequency components. This process is described by Equations 5.6 and 5.7, where $\theta'_{w_\eta}(t)$ represents the lateral component before the low-pass filter is applied.

$$\begin{aligned}
\theta'_{w_\eta}(t) &= \theta_w(t)\sin(\omega t) \\
&= \theta_{w_\eta}(t)\sin^2(\omega t) + \theta_{w_\zeta}(t)\cos(\omega t)\sin(\omega t) \\
&= \theta_{w_\eta}(t)(0.5 - 0.5\cos(2\omega t)) + 0.5\theta_{w_\zeta}(t)\sin(2\omega t) \\
&= 0.5\theta_{w_\eta}(t) - 0.5\theta_{w_\eta}(t)\cos(2\omega t) + 0.5\theta_{w_\zeta}(t)\sin(2\omega t)
\end{aligned} \tag{5.6}$$

$$\theta_{w_\eta}(t) = 2LPF_\omega(\theta'_{w_\eta}(t)) \tag{5.7}$$

Similarly, as shown in Equations 5.8 and 5.9, the vertical component can be reconstructed through demodulation with the unity amplitude vertical dither $\cos\omega t$, and passing the result through a low-pass filter.

$$\begin{aligned}\theta'_{w_\zeta}(t) &= \theta_w(t)\cos(\omega t) \\ &= \theta_{w_\eta}(t)\sin(\omega t)\cos(\omega t) + \theta_{w_\zeta}(t)\cos^2(\omega t) \\ &= 0.5\theta_{w_\eta}(t)\sin(2\omega t) + \theta_{w_\zeta}(t)(0.5 + 0.5\cos(2\omega t)) \\ &= 0.5\theta_{w_\eta}(t)\sin(2\omega t) + 0.5\theta_{w_\zeta}(t) + 0.5\theta_{w_\zeta}(t)\cos(2\omega t)\end{aligned} \tag{5.8}$$

$$\theta_{w_\eta}(t) = 2LPF_\omega(\theta'_{w_\eta}(t)) \tag{5.9}$$

Demodulation and Filtering with Phase Lag

The above process can be applied under the assumption that the phases of the orthogonal lateral and vertical components are synchronized with their respective demodulation signals. For a system such as an aircraft, this assumption no longer holds, as the dynamics introduce phase lag between the dither commands and their resulting aircraft motions. Since the objective variation is dependent on aircraft movement in the wake, the phase lag present in each directional motion will induce phase lag in their respective objective components. This results in a "phase error" between the original dither commands, used for demodulation, and the orthogonal lateral and vertical components. Representing each phase error as a phase shift of the respective objective component, the demodulated output is expressed as,

$$\theta_w(t) = \theta_{w_\eta}(t)\sin(\omega t + \gamma_\eta) + \theta_{w_\zeta}(t)\cos(\omega t + \gamma_\zeta) \tag{5.10}$$

where the phase errors are given by γ_η and γ_ζ. Demodulating with the unity amplitude dither $\sin(\omega t)$ yields,

$$\begin{aligned}\theta'_{w_\eta}(t) &= \theta_{w_\eta}(t)\sin(\omega t + \gamma_\eta)\sin(\omega t) + \theta_{w_\zeta}(t)\cos(\omega t + \gamma_\zeta)\sin(\omega t) \\ &= 0.5\theta_{w_\eta}(t)[\cos(\gamma_\eta) + \cos(2\omega t + \gamma_\eta)] + 0.5\theta_{w_\zeta}(t)[\sin(2\omega + \gamma_\zeta) - \sin(\gamma_\zeta)]\end{aligned} \tag{5.11}$$

Once again, passing the signal though a low-pass filter with a cut-off frequency of ω and a gain of two yields the lateral objective variation,

$$\theta_{w_\eta}(t) = \theta_{w_\eta}(t)\cos(\gamma_\eta) - \theta_{w_\zeta}(t)\sin(\gamma_\zeta) \tag{5.12}$$

Similarly, it can be shown that the vertical objective variation is given by,

$$\theta_{w_\zeta}(t) = \theta_{w_\zeta}(t)\cos(\gamma_\zeta) + \theta_{w_\eta}(t)\sin(\gamma_\eta) \tag{5.13}$$

In Equations 5.12 and 5.13 the first term represents the attenuation of each respective signal, while the second term represents the crosstalk effect of the other dither signal. The attenuation and accompanying crosstalk effects due to phase error are highly undesirable and will result in incorrect updating of the ESC control law. This, in turn, can result in the aircraft being commanded to fly in dangerous zones in the wake.

Proposed Method for Phase Correction

In the work of Van Wyk, phase synchronization was performed between the demodulating dither and band-passed objective output. The phase difference was calculated by identifying zero-crossings in two signals and shifting the demodulating dither by the calculated

amount before demodulation. While this method manages to successfully calculate the phase difference, a conceptual flaw exists in the implementation.

Firstly, considering two dither signals that are separated by phase, the gradient information is captured in the relative phase between the objective function and the respective dithers. By synchronizing the band-pass objective output and dither signal, the gradient information is lost, and the extremum-seeking control law is not updated accurately. Since both demodulating dither signals are synchronized with the same band-passed objective output, the control law is updated equally for both directions of motion. This results in the follower being commanded to only perform the same motions in the vertical and lateral directions. Secondly, relying on the identification of zero-crossings for phase calculation poses a problem when the objective output is contaminated by noise. This noise, introduced by events such as the formation flying through turbulence, might introduce multiple zero-crossings where, for instance, only one is expected.

A different method and implementation for phase synchronization is proposed by this study, utilizing cross-correlation. Similar to the correction of the dither commands, the phase difference may be determined for each direction of motion by calculating the cross-correlation of their respective dither and band-passed separation output recordings. By synchronising the demodulating dithers and their respective aircraft separation outputs, only the phase lag introduced by the aircraft dynamics is removed. The gradient information captured in the relative phase is maintained when demodulating, and the control law is updated correctly. Figure 5.17 shows the scheme used for the lateral phase synchronization, where γ_η is the phase difference between the lateral dither and lateral aircraft movement.

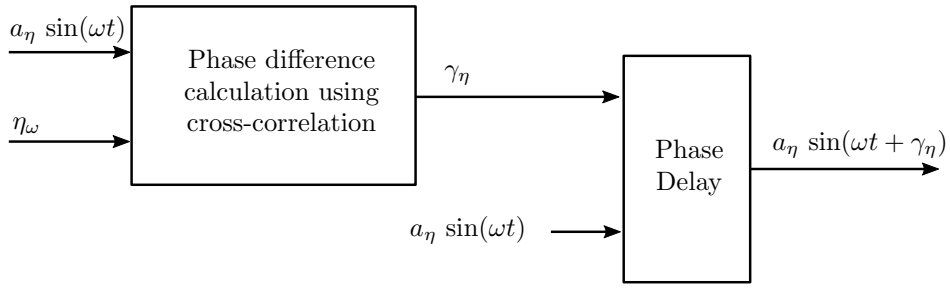

Figure 5.17: Proposed method for phase synchronization.

Calculation of the cross-correlation requires a few dither periods, meaning that before the ESC can start, there will be some setup time required for the necessary calculations. Note that the phase difference is a function of the aircraft's lateral and vertical separation controller transfer functions and the frequency of the lateral and vertical dither signals. For the same controllers and the same dither frequency, the phase differences will therefore be the same. The calculated phase value can thus be used for future applications of the extremum-seeking controller any time during a flight.

Figure 5.18 shows the simulation results of the phase synchronization for a dither period of 100 seconds. After the ESC is initialised, the phase difference is calculated during the following eight dither periods. At $t = 800$ seconds, the dither signal recording used for demodulation is shifted by the calculated phase. In 5.18a, a slight phase shift can be seen in the vertical dither at $t = 400$ seconds, which corresponds to the phase shift in vertical dither command required for circular dithering.

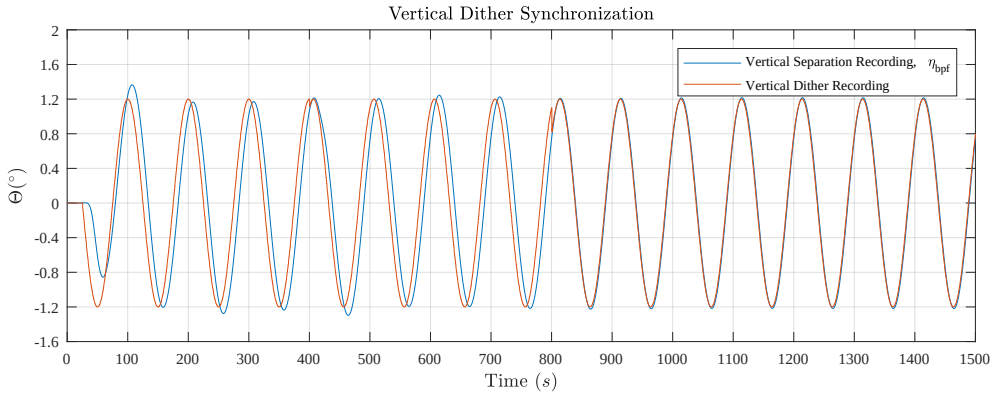

(a) Vertical dither synchronization

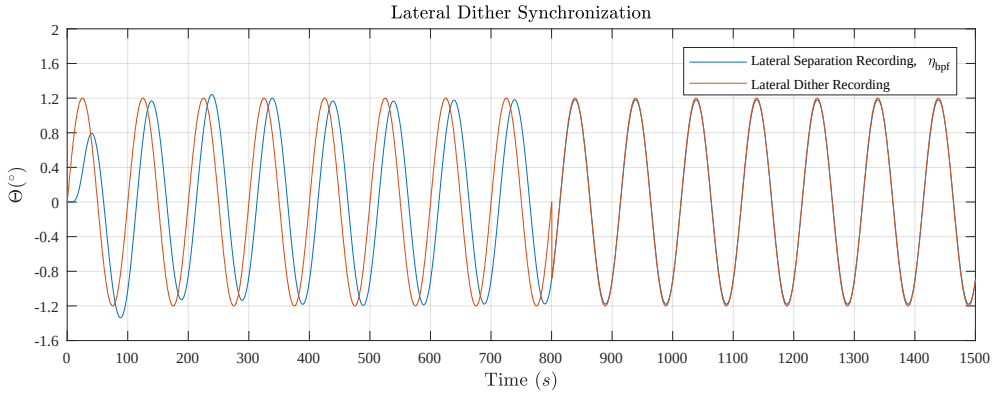

(b) Lateral dither synchronization

Figure 5.18: Phase correction of lateral and vertical demodulation dithers.

5.2.5 Logic Control

The logic controller shown in Figure 5.1 controls the different modes of operation that the follower aircraft transitions through as it approaches the constrained optimum location in the leader's wake. When the follower aircraft is still far away from the constrained optimum, the extremum seeking is inactive and the aircraft approaches the general region where the optimum is expected to be by following a lateral and vertical separation reference trajectory. When the follower aircraft enters the general region of the optimum location, the extremum-seeking is activated using larger dither amplitudes and more aggressive ESC gains to approach the optimum faster. As the follower aircraft nears the constrained optimum, the dither amplitudes are decreased and less aggressive ESC gains are used to approach the optimum more slowly and accurately. When the follower aircraft arrives at the optimum location, the extremum seeking is deactivated and the follower aircraft maintains its location in the wake using the formation-hold controllers. If at a later stage the optimum location changes, then the extremum seeking is activated again to find the new location of the optimum. Finally, if the follower aircraft ventures too deeply into the leader's wake, a mode is activated to guide the aircraft out of the dangerous region. The logic controller decides when to switch from one mode to another, and also sets the ESC gains, K_η and K_ζ, and the lateral and vertical dither amplitudes, a_η and a_ζ, based on the current mode.

Van Wyk proposed and implemented a logic controller that switches between the different modes of operation based on the instantaneous geometric separation between the leader aircraft and the follower aircraft. The regions of operation and the switching boundaries

defined by Van Wyk are shown Figure 5.19. In the blue region, the extremum seeking control is inactive and the formation-hold autopilot is used to guide the aircraft towards the optimum location by following a lateral and vertical separation reference trajectory. When the follower aircraft enters the green region, the extremum-seeking is activated and uses larger dither amplitudes and ESC gains. In the yellow region, the dither amplitudes and ESC gains are decreased to approach the extremum more slowly and accurately. The red region corresponds to the optimum location, and the ESC is deactivated once the follower enters this region. If the follower aircraft moves out of the red region, the extremum-seeking controller is activated again to guide follower back. Finally, the grey region is considered a no-fly zone, as wake-induced rolling moments are large and present danger to the follower aircraft. If the follower aircraft were to end up in the no-fly zone, the large wake-induced rolling moment will roll the follower into the downwash region of the leader.

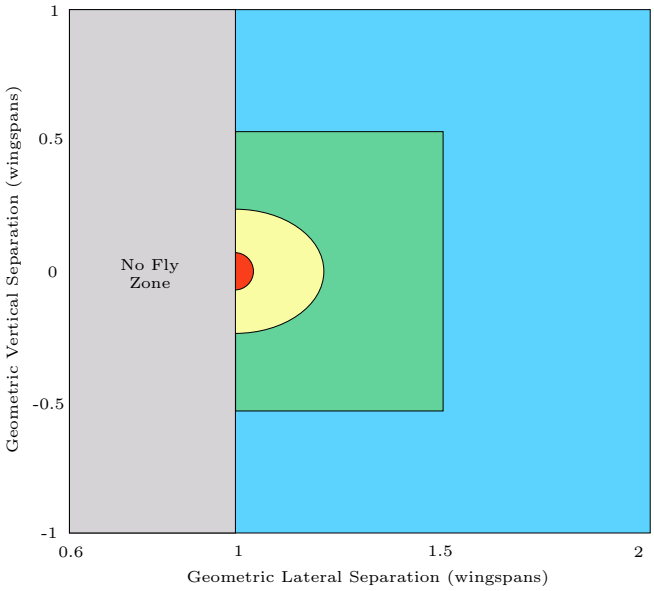

Figure 5.19: Logic control bounds implemented by Van Wyk.

One potential problem that was identified with this logic controller is the fact that the follower aircraft switches between different modes of operation based on the geometric separation between the leader aircraft and the follower aircraft, and not based on the effective separation between the follower aircraft and the trailing vortex. In an ideal scenario with no external wind disturbances to displace the trailing vortex, the geometric separation is equal to the effective separation. This means that the location of the trailing vortex would be well modelled and switching between different modes based on boundaries defined by geometric separation feasible. In a realistic flight scenario, however, the trailing vortex may be displaced by external wind disturbances, and the geometric separation would not be equal to the effective separation. The mode switching boundaries would therefore not be adjusted to compensate for the displacement of the trailing vortex, and the follower aircraft may therefore fly too close to the trailing vortex without knowing it. The problem is better explained by means of an example. If the follower flies at the optimum location and the wake is displaced to the right by a positive static wind, the follower will effectively move deeper into the wake. Ideally the no-fly zone boundary should now also move to the right with the displacement, indicating to the controller that the follower has entered a dangerous part of the wake. However, since the no-fly zone boundary is defined in terms of geometric separation, the boundary

of the no-fly zone as perceived by the follower aircraft will remain at the same static position relative to the leader aircraft, despite the fact that in reality the follower aircraft has already entered the no-fly zone.

We therefore propose a novel new logic controller that takes into account the displacement of the trailing vortex due to external wind disturbances. The new logic controller defines the regions of operation and the switching boundaries as a function of the wake-induced pitch angle deviation, and not as a function of the geometric separation between the leader aircraft and the follower aircraft. This allows the regions of operation and the switching boundaries to move around with the displaced trailing vortex, instead of remaining static relative to the leader aircraft. The proposed switching boundaries and regions of operation are shown in Figure 5.20, while the state machine that governs the logic control is shown in Figure 5.21.

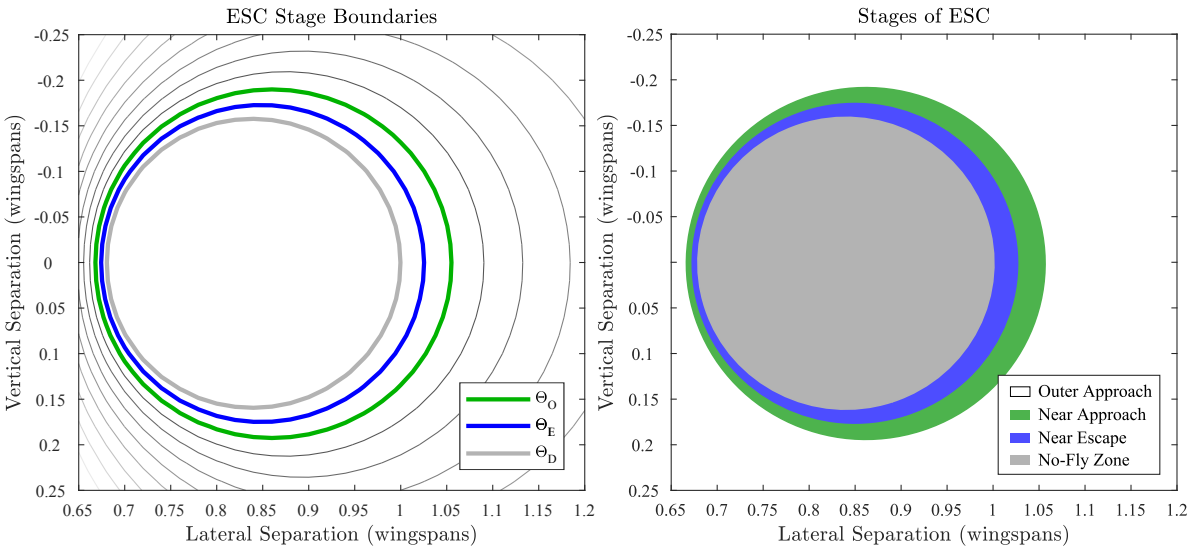

(a) ESC state transition boundaries.

(b) ESC states.

Figure 5.20: States and state transition boundaries for logic controller.

Initially, the follower aircraft approaches the leader aircraft by following a lateral and vertical separation reference trajectory, using the formation-hold autopilot presented in Chapter 4. When the follower aircraft is deemed close enough, the extremum seeking controller is activated and the state machine advances to the first state, namely the *Outer Approach* state, and proceeds to seek the extremum with approach rate C and dither amplitude a. When the follower wake-induced pitch angle decreases to below the first switching boundary, denoted by Θ_O, the state machine transitions to the second state, the *Near Approach* state, and the approach rate and dither amplitudes are halved. In the Near Approach state, the follower aircraft continues to seek the extremum, but more slowly and accurately. When the wake-induced pitch angle decreases to below the second boundary, designated as Θ_E, the follower aircraft is deemed to have reached the constrained extremum, and advances to the final state, namely the *Near Escape* state. In the Near Escape state, the direction of the extremum seeking is reversed to make the follower aircraft move away from the extremum again. As the follower moves away from the extremum, the wake-induced pitch angle will start increasing again. When the wake-induced pitch angle increases to above Θ_E, the state machine will transition back to the Near approach state, and will start approaching the extremum again. This constant oscillation between the Near Approach state and the Near Escape state results

in the follower remaining near the constrained extremum even if it moves around due to the trailing vortex being displaced by external wind disturbances. The no-fly zone is defined as a region of the wake where the wake-induced pitch angle is below a third switching boundary Θ_D. If the wake-induced pitch angle ever decreases below this boundary, the logic controller dictates that the extremum seeking is switched off and the formation-hold controllers are used to immediately guide the follower out of the wake. Once it is deemed safe, the extremum seeking may once again be activated to guide the follower back to the constrained extremum.

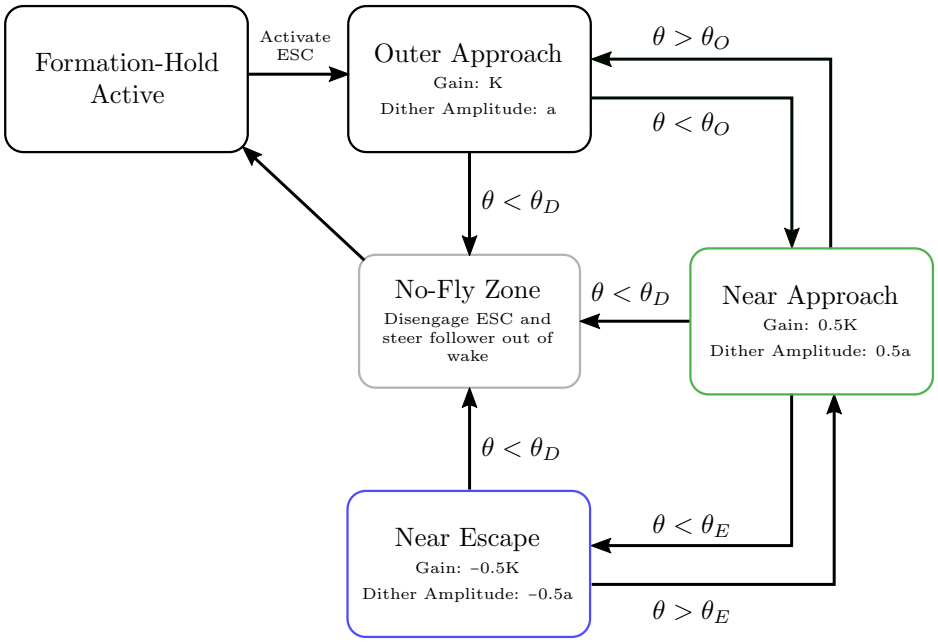

Figure 5.21: Logic controller state machine.

All the components of the extremum-seeking controller have been presented in this section, and the details regarding the design of each component have been discussed. The following section focusses on the application of the extremum-seeking controller to locating a stationary constrained extremum.

5.3 Seeking a Stationary Near-Extremum

The first and basic objective of the extremum-seeking controller is to locate a stationary extremum from any position in the wake. The wake is considered stationary when it is not subjected to any external disturbances, such as wind, that might alter the location of the extremum. While external disturbances will be present in a realistic scenario, this section only considers the operation of the ESC under ideal atmospheric conditions.

Firstly, two different approach methods are presented: (1) approaching the extremum at a rate proportional to the wake gradient, and (2) approaching the extremum at a constant rate. Next, the basic simulation results are presented and discussed for both approach methods. Finally, the effects that different dither and ESC parameters have on the controller performance are investigated.

5.3.1 Approach Methods

In the classic method of extremum-seeking control, the lateral en vertical separation rate is made proportional to the gradient of the objective function. This is the implementation most commonly used in literature [2, 6, 8, 31, 53] and will serve as the first approach method used in this study. The lateral en vertical separation rates are set proportional to the gradient of the wake-induced pitch angle (objective function gradient), further referred to as the *wake gradient*. The vertical separation rate $\frac{d\hat{\zeta}}{dt}$ and lateral separation rate $\frac{d\hat{\eta}}{dt}$ are given by,

$$\textbf{Proportional Rate:} \quad \begin{bmatrix} \frac{d\hat{\zeta}}{dt} \\ \frac{d\hat{\eta}}{dt} \end{bmatrix} = \mathbf{K}\nabla\theta_\omega = \begin{bmatrix} K_\zeta & 0 \\ 0 & K_\eta \end{bmatrix} \begin{bmatrix} \theta_{\omega_\zeta} \\ \theta_{\omega_\eta} \end{bmatrix} \tag{5.14}$$

where $\mathbf{K}$ is the ESC gain matrix with the vertical ESC gain K_ζ and lateral ESC gain K_η respectively. The estimated wake gradient is represented by $\nabla\theta_\omega$ and consists of θ_{ω_ζ} and θ_{ω_η}which are the partial derivatives of $\Delta\theta_w$ with respect to vertical separation and lateral separation respectively.

In this study, we propose a new method of extremum-seeking control where the extremum is approached at a constant rate instead of at a rate that is proportional to the gradient of the objective function. In the constant approach rate method, the wake gradient is determined in the same way as with the proportional method, but the gradient information is only used to dictate the direction of the separation rate command. The magnitude of the approach rate is kept constant, and the separation rate command vector is calculated by normalising the wake-induced pitch angle gradient vector and multiplying the normalised vector with the magnitude of the desired approach rate, as follows,

$$\textbf{Constant Rate:} \quad \begin{bmatrix} \frac{d\hat{\zeta}}{dt} \\ \frac{d\hat{\eta}}{dt} \end{bmatrix} = C\frac{\nabla\theta_\omega}{||\nabla\theta_\omega||} = C\frac{\begin{bmatrix} \theta_{\omega_\zeta} \\ \theta_{\omega_\eta} \end{bmatrix}}{\sqrt{\theta_{\omega_\zeta}^2 + \theta_{\omega_\eta}^2}} \tag{5.15}$$

where C is the desired constant approach rate. The main advantage of using a constant approach rate over a proportional approach rate is that the magnitude of the follower aircraft's approach rate is no longer dependant on the wake gradient. The designer can choose the follower aircraft's desired approach rate, which allows for more predictable aircraft motion and reduces the risk of the follower aircraft overshooting the extremum and flying too deep into the wake. From a psychological perspective, the pilot and passengers on board the follower aircraft would be more comfortable with a constant approach rate than with a varying approach rate.

5.3.2 Basic Simulation Results

A right echelon formation of two aircraft was implemented in simulation. The follower was equipped with the extremum-seeking controller and was tasked with locating a stationary extremum from a given position in the outer wake. First, two simulations were performed using a proportional approach rate: one where the follower approaches the extremum from above, and one where the follower approaches the extremum from below. Next, the simulations were repeated using a constant approach rate. The controller and dither parameters were selected to illustrate the operation of the extremum-seeking controller and the parameters were not specifically optimised to provide the best performance.

It is important to note that dithering can be performed either clockwise or anti-clockwise. The simulation results presented in this section used clockwise dithering, but similar results are obtained when using anti-clockwise dithering. (The simulation results for anti-clockwise dithering can be found in Appendix E).

Proportional Approach Rate

The first set of simulations was performed using a proportional approach rate, the magnitude of which is dependant on the gain of the controller as well as the wake gradient. The follower is commanded to dither clockwise with an amplitude of 0.02 wingspans and a period of 100s.

Figure 5.22 shows the extremum seeking result for a simulation where the follower is initialized *above* the extremum at separations $\eta = 1.5$ and $\zeta = -0.5$. The movement of the aircraft in 2D-space is shown in Figure 5.22a where the objective function is illustrated as a contour in the background. The follower starts by dithering around the initial location, calculating and correcting the dither motion and system phase lag. The controller then guides the aircraft to the extremum using the wake-induced pitch angle information, calculating and updating the correct direction to move in with each time step. This results in the follower moving normal to the objective gradient before eventually oscillating about the extremum.

Figure 5.22b shows the vertical and lateral separations over time. The convergence time is measured from the time instant that the follower aircraft starts moving towards the extremum to the time instant that the follower reaches the extremum, and excludes the setup time that is used to perform the dither phase correction. From the figure, the follower starts to move at roughly $t = 800$ seconds and reaches the constrained extremum at $t = 2500$ seconds, resulting in a convergence time of 1700 seconds.

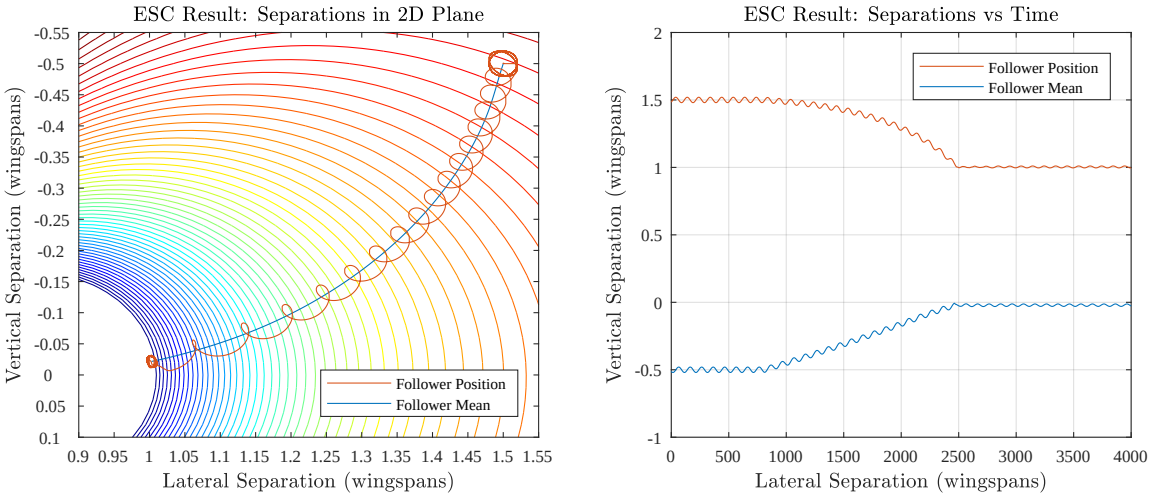

(a) Formation separation in 2D.

(b) Formation separation over time.

Figure 5.22: Formation separation: seeking from above using a proportional approach rate.

Figure 5.23 shows the actuator responses for the extremum seeking scenario presented above. The aileron, elevator and rudder deflections are shown in Figure 5.23a and the common thrust and differential thrust are shown in Figure 5.23b. As the follower aircraft approaches the constrained extremum location, the wake-induced rolling moment disturbance gradually increases.

Because of the complementary filter architecture of the lateral actuators (presented in

Section 4.5.4), the rolling moment is first countered using differential thrust until it saturates, then rudder deflection is added until it saturates, and then finally aileron deflection is added. Figure 5.23b shows that the differential thrust gradually increases to counter the increasing rolling moment disturbance, until the differential thrust saturates at approximately $t = 2000$ seconds. Figure 5.23a shows that the rudder deflection then gradually increases to produce the necessary sideslip angle and additional rolling moment until it too saturates at $t = 2500$ seconds. From that point onwards, the ailerons provide the additional rolling moment to counter the wake-induced rolling moment disturbance. The oscillations observed in the aileron deflections are due to the follower aircraft moving towards and away from the constrained extremum as it switches between the Near Approach and the Near Escape states. From Figure 5.23b, it is seen that thrust demand is reduced considerably as the aircraft moves from its initial position to the constrained extremum. The total thrust savings amount to approximately 23% relative to flying in isolation.

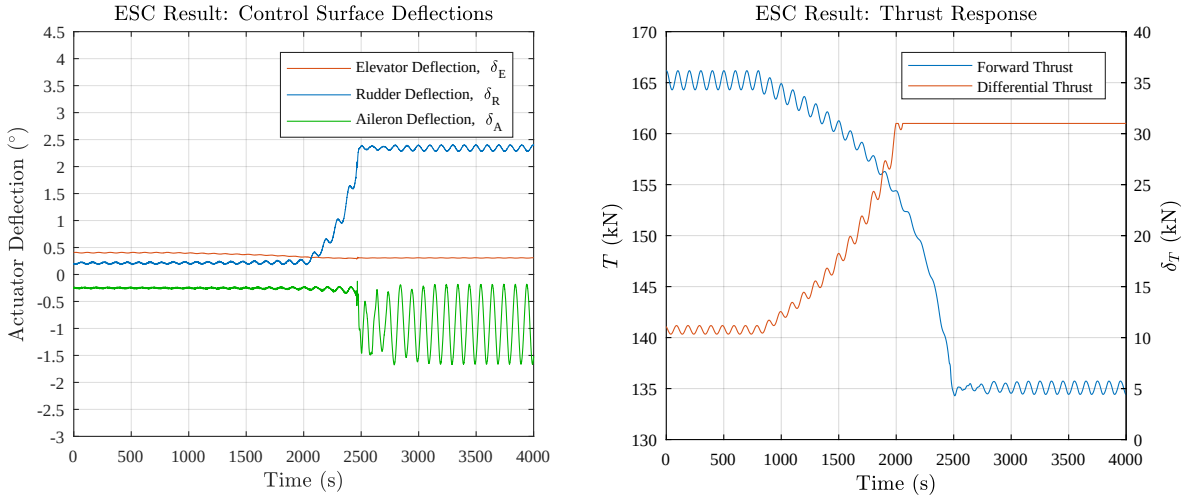

(a) Control surface deflections.

(b) Thrust response.

Figure 5.23: Actuator response: seeking from above at a proportional approach rate.

Figure 5.24 shows the extremum seeking result for a simulation where the follower is initialized *below* the extremum at separations $\eta = 1.5$ and $\zeta = 0.5$. Figure 5.24a again shows the aircraft movement in 2D-space, with the objective function as a contour in the background. The follower is again successfully guided to the constrained extremum, moving normal to the wake gradient and eventually oscillating at the constrained extremum. The vertical and lateral separations are shown in Figure 5.24b. The convergence time for approaching the optimum from below is calculated as roughly 1600 seconds, 100 seconds faster than when approaching from above.

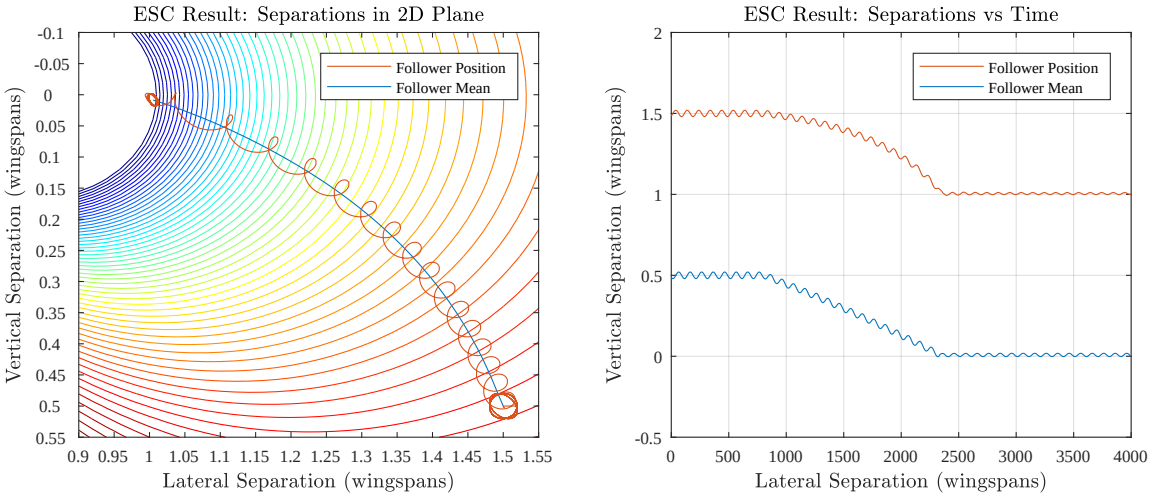

(a) Formation separation in 2D.

(b) Formation separation over time.

Figure 5.24: Formation separation: seeking from below at a proportional approach rate.

Figure 5.25 shows the actuator responses when approaching from below. The effect of the complimentary filter controller is again evident as first differential thrust, then rudder deflection, and finally aileron deflection are cumulatively added to counter the wake-induced rolling moment.

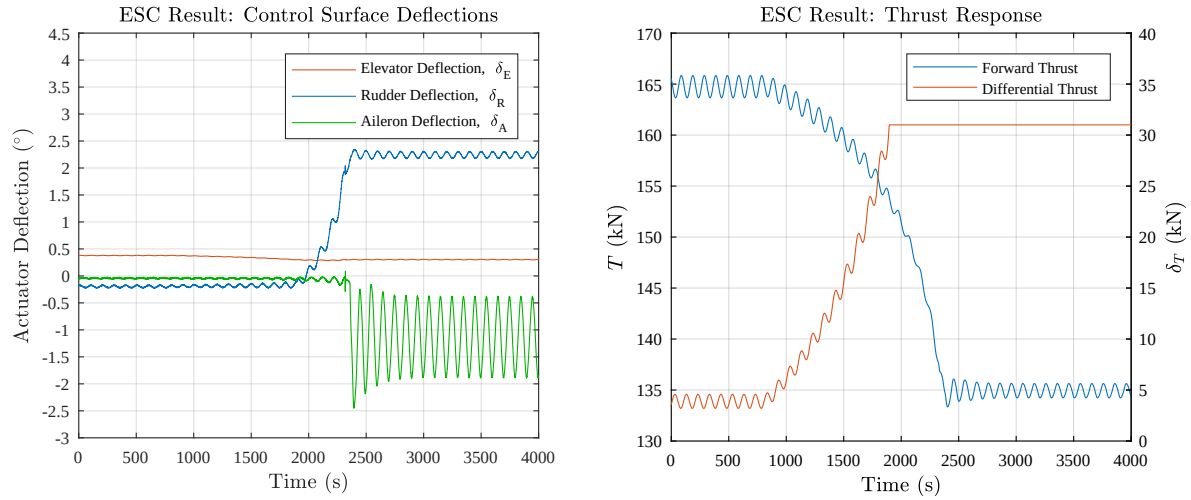

(a) Control surface deflections.

(b) Thrust response.

Figure 5.25: Actuator response: seeking from below using a proportional approach rate.

Constant Approach Rate

The second set of simulations was performed with the same dither parameters but using a constant approach rate. In order to have approximately the same convergence time as that of the proportional approach rate simulations, the constant approach rate C was selected as $0.025\ m/s$.

As seen from the simulation results shown in Figure 5.26, the follower is successfully guided to the extremum using the constant approach rate method. From Figure 5.26a it

is clear that the follower no longer moves faster the closer it flies to the extremum, since the distance the follower moves between consecutive dither oscillations are constant. The actuator signals are shown in Figure 5.27, where a more gradual increase in actuator demand and decrease in thrust is observed.

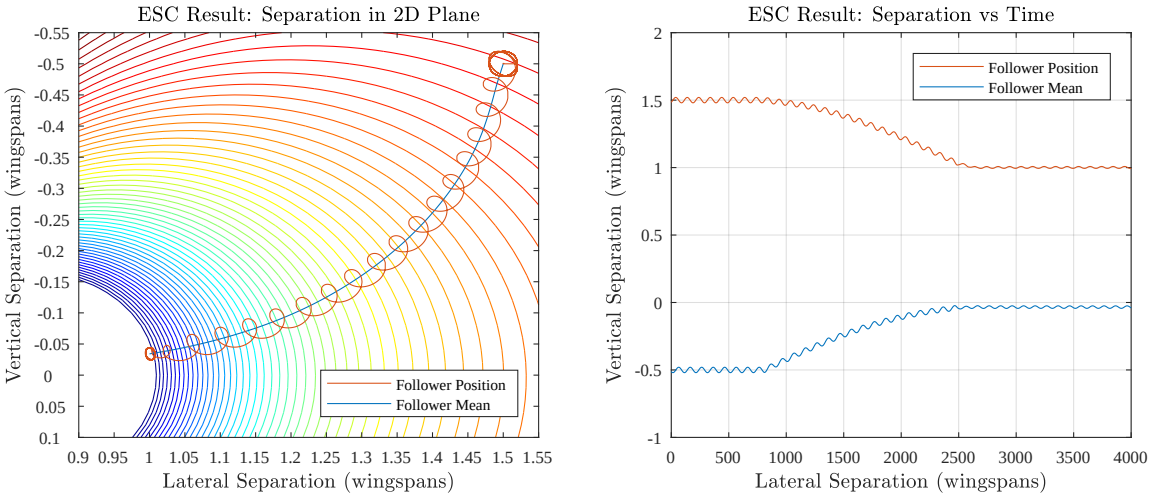

(a) Formation separation in 2D.

(b) Formation separation over time.

Figure 5.26: Formation separation: seeking from above using a constant approach rate.

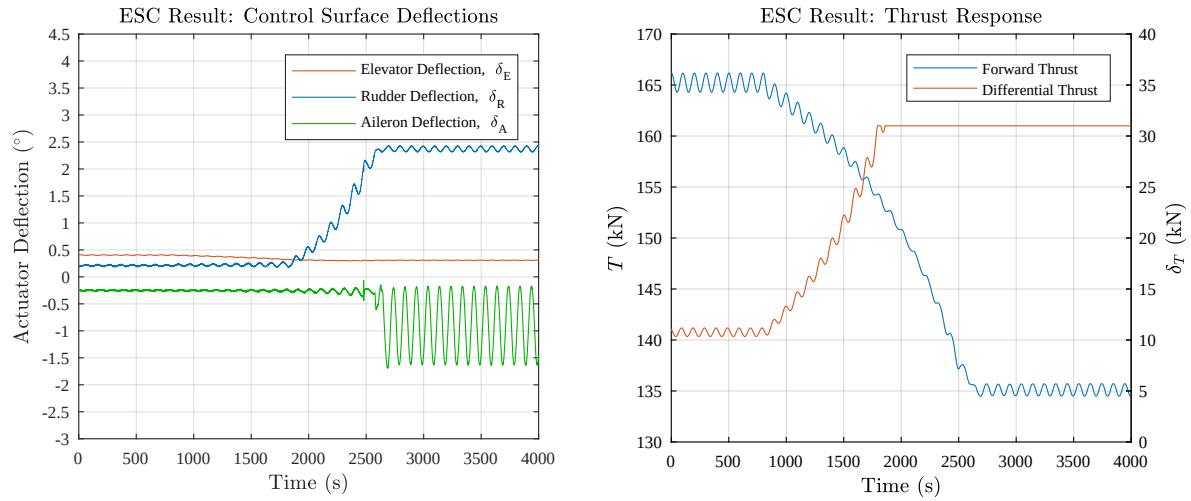

(a) Control surface deflections.

(b) Thrust response.

Figure 5.27: Actuator response: seeking from above using a constant approach rate.

The formation separation and actuator signals when seeking from below, are shown in Figures 5.28 and 5.29. Due to the constant approach rate, the convergence time when seeking from below is equal to the convergence time when seeking from above.

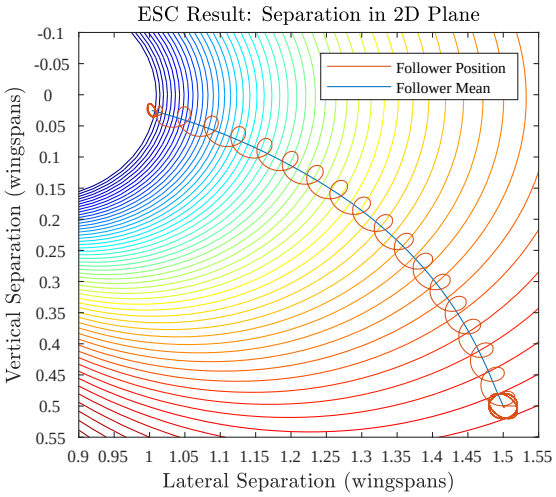

(a) Formation separation in 2D.

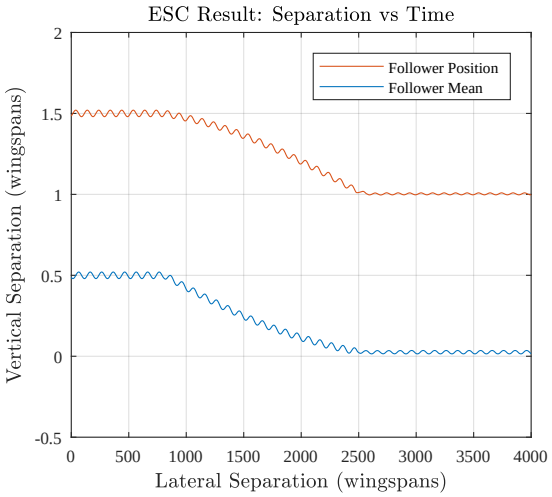

(b) Formation separation over time.

Figure 5.28: Formation separation: seeking from below using a constant approach rate.

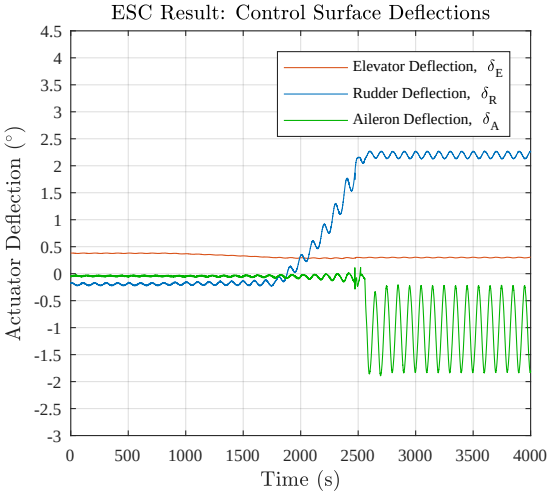

(a) Control surface deflections.

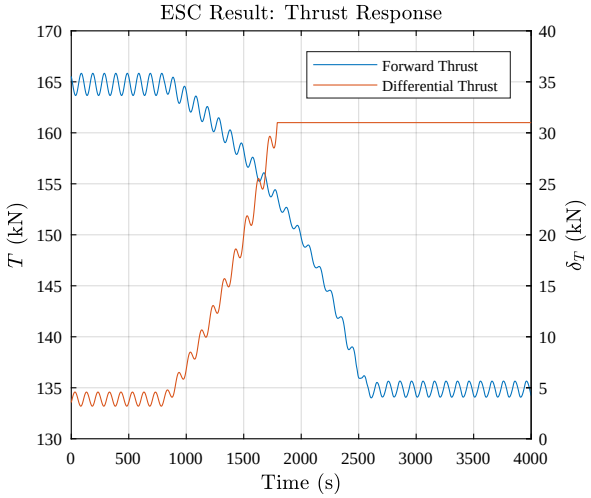

(b) Thrust response.

Figure 5.29: Actuator response: seeking from below using a constant approach rate.

Differential Thrust Demand

From the simulation results shown above, it is observed that the initial differential thrust demand is much less when approaching the extremum from below than when approaching the extremum from above. This is because the wake induces a negative yawing moment when the follower is below the extremum at $\eta = 1.5$ and $\zeta = 0.5$, and induces a positive yawing moment when the follower is above the extremum at $\eta = 1.5$ and $\zeta = -0.5$. Contour maps of the wake-induced yawing moment and wake-induced rolling moment are shown in Figure 5.30.

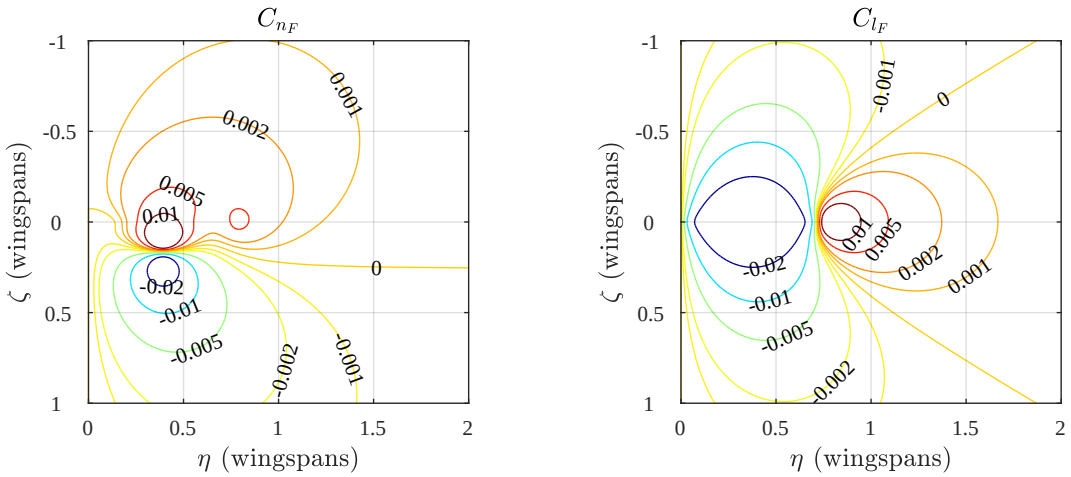

(a) Wake-induced yawing moment.

(b) Wake-induced rolling moment.

Figure 5.30: Contour maps of (a) wake-induced yawing moment and (b) wake-induced rolling moment.

Conventionally, only rudder and aileron deflections would be used to counter the wake-induced yawing and rolling moments respectively. However, with the implementation of the complimentary filter controller, the flight control system can utilise differential thrust as well.

If the follower flies to the right of the leader, as in the simulations above, the follower experiences a positive wake-induced rolling moment that must be countered using a large positive differential thrust. This is evident in the simulation results shown in both Figure 5.23b and 5.27b. The total differential thrust used by the follower aircraft is therefore the sum of the differential thrust required to counter the wake-induced rolling moment and the differential thrust required to counter the wake-induced yawing moment. When approaching the extremum from above, more differential thrust is required because the positive wake-induced rolling moment and the positive wake-induced yawing moment must both be countered with positive differential thrust. When approaching the extremum from below, less differential thrust is required because the positive wake-induced rolling moment must be countered with positive differential thrust, while the negative wake-induced yawing moment must be countered with negative differential thrust. The wake thus appears as to aid the follower in countering the wake-induced rolling moment when the follower is below the extremum. Note that due to the asymmetrical nature of the wake-induced rolling moment around $\zeta = 0$, this effect is not present everywhere below the extremum.

5.3.3 Varying the Controller Parameters

The following section seeks to aid future design of an extremum-seeking controller by investigating the effects different controller parameters have on the system performance. These controller parameters include:

- The dither period T_D (or frequency f_D)
- The lateral and vertical dither amplitudes a_η and a_ζ
- Controller gains, K_η and K_ζ (proportional approach rate)
- The approach rate C (constant approach rate)

The parameters are varied separately and the relative extremum seeking simulation results are evaluated in terms of speed of convergence and domain of attraction. The results are not evaluated in terms steady-state tracking error, since the differences in the steady-state tracking error between simulations are negligible. The goal of this section is to give future designers a better understanding of the effect of each parameter on the system performance, and to hopefully allow for a more informed design process.

The simulations were performed for both proportional and constant approach rates, with the purpose of highlighting some of the differences between the two methods regarding parameter variation.

Dither Period: T_D

The first parameter to be varied is the dither period, while all other parameters are held constant. From literature, it is suggested to choose the dither period sufficiently larger than the time constant of the slowest plant dynamics so that the plant behaves as a static map [8, 32]. The effect of varying the dither period was investigated using three different choices for the dither period, namely 60 seconds, 100 seconds, and 150 seconds. The period of 100 seconds used in the previous section is chosen as the baseline, while the other periods are chosen slightly longer at 150 seconds, and slightly shorter at 60 seconds.

The first set of simulations was performed using a proportional approach rate and the results are shown in Figure 5.31. In Figure 5.31a it can be seen that the aircraft successfully located the extremum for all three dither periods, while flying along the same trajectory in the wake. The dither period has little effect on the convergence time of the controller, as seen in Figure 5.31b. The convergence time was the same for all three choices of dither period. This might seem counter intuitive since one would think that dithering faster must result in faster convergence. It is important to realise that the dither period only determines the amount of information gained on the wake while seeking. Dithering faster thus provides more information which allows for more accurate wake-gradient estimation. The minimum dither period, however, must be selected to be within the bandwidth of the lateral and vertical separation controllers.

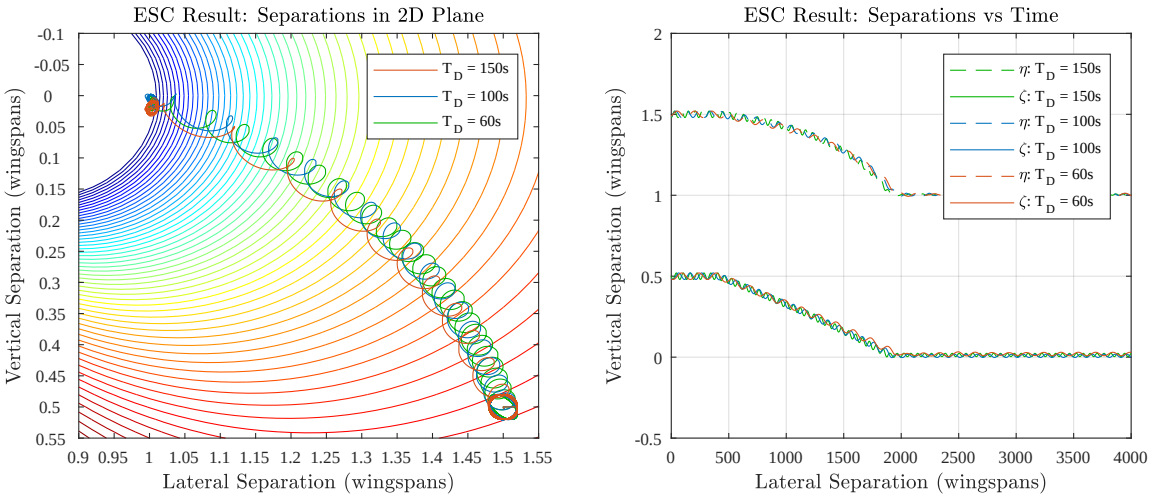

(a) Formation separation in 2D.

(b) Formation separation over time.

Figure 5.31: Results for various dither periods while using a proportional approach rate.

The second set of simulations was performed using a constant approach rate and the results are shown in Figure 5.32. Similar to the results for a proportional approach rate, the dither period is seen to have little effect on the trajectory followed by the follower or the convergence time. This is expected since the convergence rate should only be dependant on the constant approach rate parameter C.

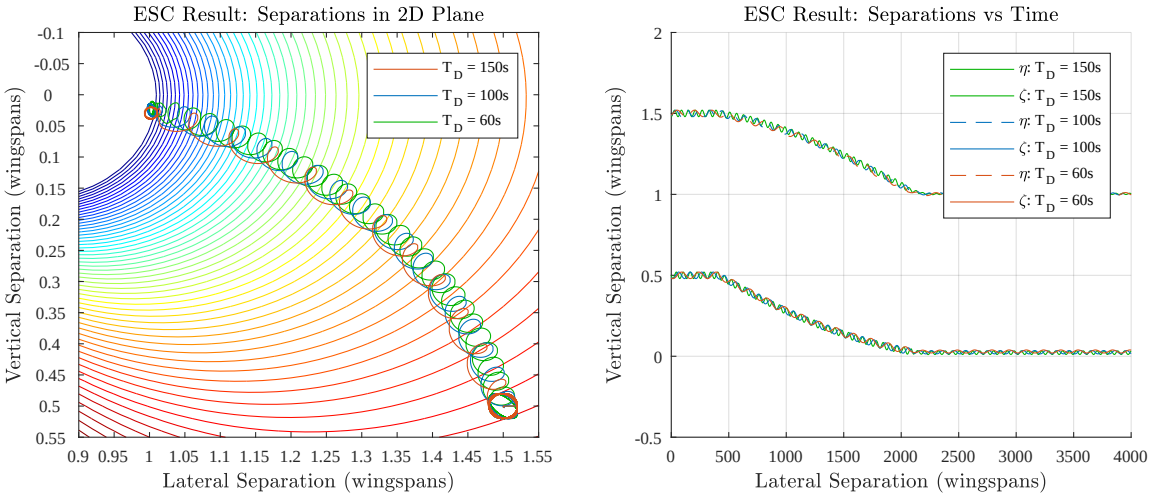

(a) Formation separation in 2D.

(b) Formation separation over time.

Figure 5.32: Results for various dither periods while using a constant approach rate.

However, an improvement in the wake gradient estimation accuracy is not the only benefit to be gained from dithering faster. Since dithering faster increases the information gained per time unit, the designer can increase the approach rate while still ensuring convergence. Increasing the dither frequency can therefore indirectly lead to a reduction in the convergence time by enabling a faster approach rate.

Dither Amplitude: a_D

The second parameter to be varied is the dither amplitude, while all other parameters are held constant. From literature, it is suggested to choose the dither amplitude sufficiently small to ensure a large domain of attraction. Three amplitudes are chosen to sufficiently capture the effect varying the dither amplitude has on the controller performance. An amplitude of 0.02 wingspans is chosen as the baseline, corresponding to the work of Van Wyk [2], and the other amplitudes are chosen slightly smaller at 0.015 wingspans, and slightly larger at 0.03 wingspans.

The first set of simulations was again performed using a proportional approach rate and the results are shown in Figure 5.33. From the result in Figure 5.33a, it can be seen that the aircraft converges to the extremum for all three dither amplitudes. Regarding convergence speed, it can be seen from Figure 5.33b that the controller converges faster for larger dither amplitudes. The larger the dither amplitude is, however, the smaller the domain of attraction will be, since moving faster through the wake with large dither motions increase the risk of overshooting the constrained extremum. The ESC does not obtain as much information on the wake gradient, and may update the vertical and lateral separation rate inaccurately. The follower will therefore converge to the extremum under the requirement that the amplitude is sufficiently small for a given dither period and controller gain.

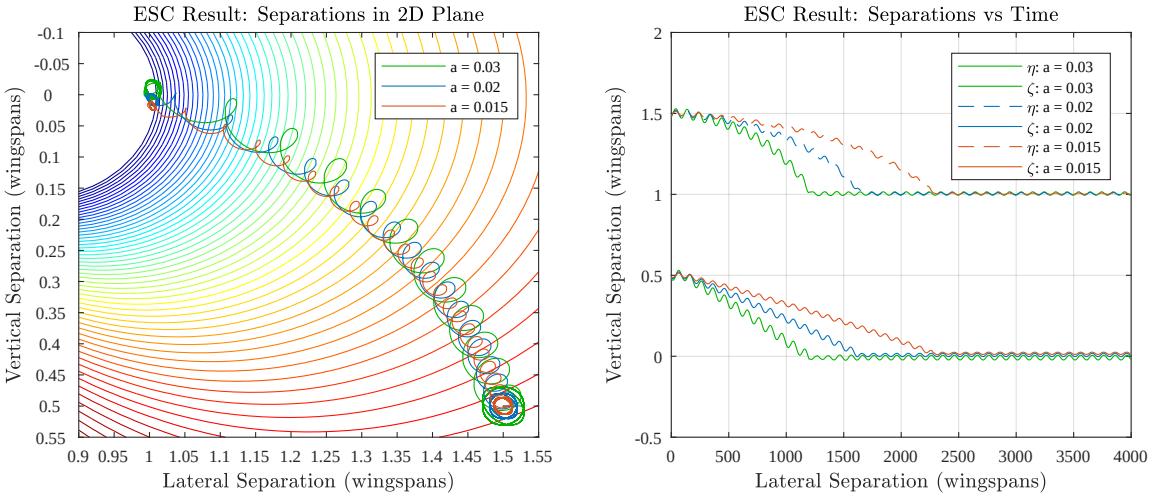

(a) 2D result.

(b) Mean formation separation.

Figure 5.33: Results for various dither amplitudes when using a proportional approach rate.

The second set of simulations was performed using a constant approach rate and the results are shown in Figure 5.34. From the results it can be observed that, contrary to using a proportional approach rate, the dither amplitude has no effect on the convergence time. This also removes the direct dependency of the domain of attraction on dither amplitude, since convergence can be guaranteed under the requirement that the approach rate is sufficiently slow for any realistic dither amplitude.

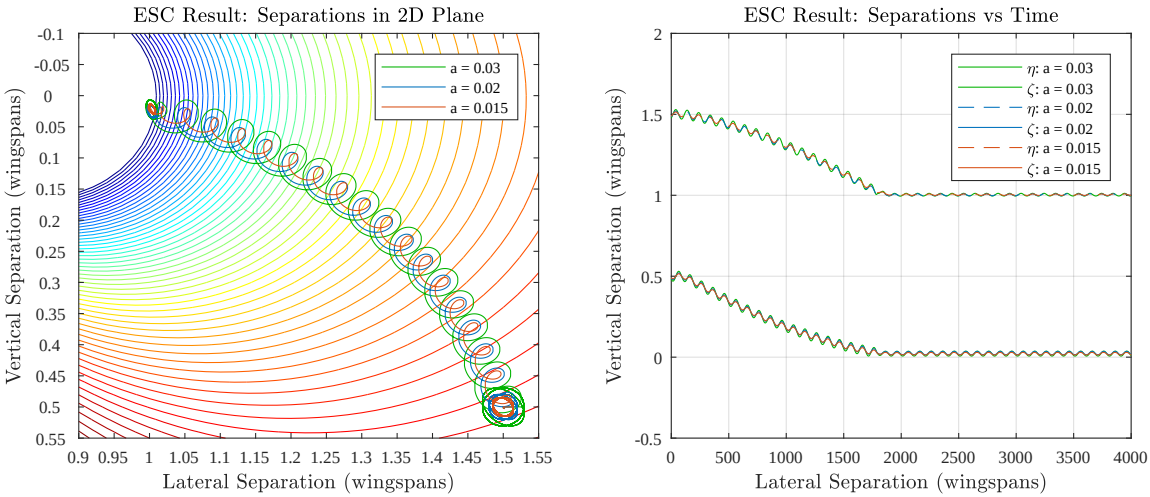

(a) 2D result.

(b) Mean formation separation.

Figure 5.34: Results for various dither amplitudes when using a constant approach rate.

Controller Gains and Constant Approach Rate: K_η, K_ζ, C

The last parameters to be varied are the ESC gains K_η and K_ζ for the proportional approach rate method, and the constant approach rate C for the constant approach rate method. The simulation results for three different controller gains are shown in Figure 5.35a. The results show that larger ESC gains result in faster convergence. The larger the ESC gains are,

however, the smaller the domain of attraction will be, since moving faster through the wake increases the risk of overshooting the constrained extremum. The ESC does not obtain as much information on the wake gradient as when moving slowly through the wake, and may update the vertical and lateral separation rate inaccurately. To ensure convergence, the ESC gains must be sufficiently small for a given dither period and dither amplitude.

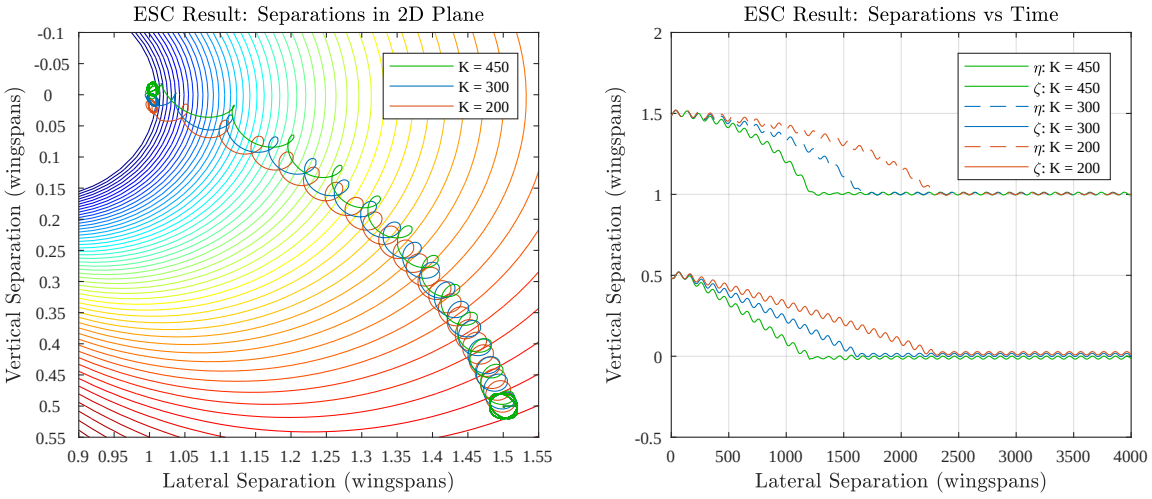

(a) 2D result.

(b) Mean formation separation.

Figure 5.35: Results for various ESC gains when using a proportional approach rate.

The simulation results for three different constant approach rates are shown in Figure 5.36a. As expected, a faster approach rate results in a shorter time for convergence. As mentioned above under the discussion for varying dither amplitude, the domain of attraction can be made infinitely large under the assumption that the approach rate is sufficiently slow for any realistic dither amplitudes and periods, and that the objective function extends over an infinitely large area.

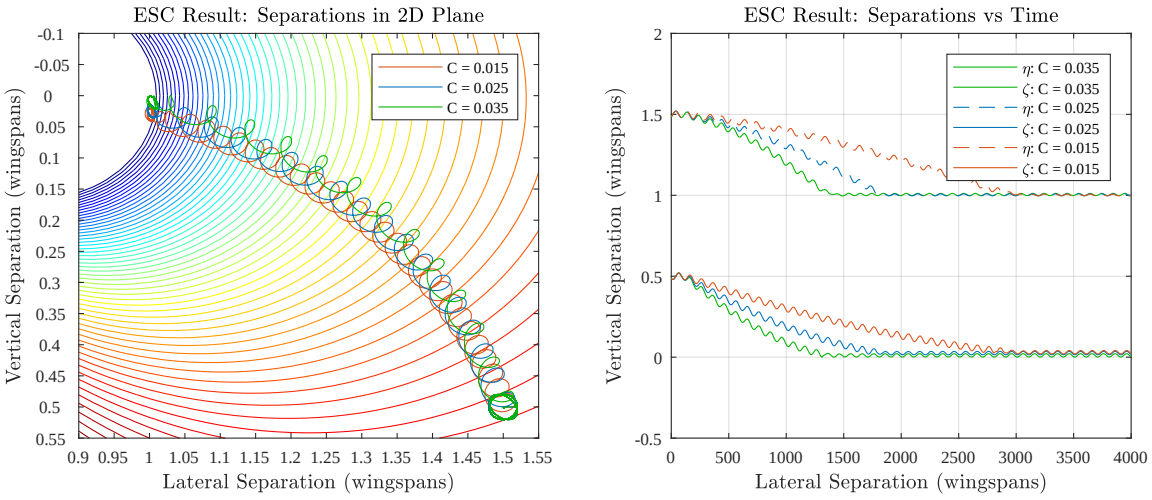

(a) 2D result.

(b) Mean formation separation.

Figure 5.36: Results for various ESC approach rates when using a constant approach rate.

Summary

From the results presented in the previous section, it is clear that the extremum-seeking controller performance is dependant on a combination of the ESC parameters. In summary:

- Speed of Convergence:
  - For a proportional approach rate, the speed of convergence is directly dependant on the control gains and the dither amplitudes. Larger control gains and larger dither amplitudes both result in faster convergence.
  - For a constant approach rate, the speed of convergence is directly dependant on the constant approach rate parameter C. A larger approach rate results in faster convergence.
  - For both approach methods, however, the dither period indirectly influences the speed of convergence. A higher dither frequency increases the information gained per time unit, and allows a higher maximum approach rate to be used. This means that higher ESC gains or a higher constant approach rate may be used. Conversely, a lower dither frequency limits the maximum allowable approach rate, and that smaller ESC gains or a slower constant approach rate must be used.
- Domain of Attraction:
  - For a proportional approach rate, a large domain of attraction can be ensured for any dither period under the requirements that the dither amplitude and control gains are sufficiently small. The domain of attraction can however not be larger than the domain over which the objective function is defined. (The objective function itself must also satisfy all the criteria for convergence.)
  - For a constant approach rate, the domain of attraction is mainly influenced by the approach rate parameter C. Convergence can be ensured for any dither period, given that the approach rate is sufficiently slow and the dither amplitude is sufficiently small.

From this section, it is clear that approaching the extremum at a constant rate has two distinct advantages over approaching at a rate proportional to the wake-gradient. Firstly, by approaching at a constant rate, the follower aircraft no longer moves faster the closer it flies to the constrained extremum. This leads to the second advantage of using a constant rate: choosing the controller parameters is a much simpler task. When using the proportional approach method, the designer has to weigh the effects of different amplitudes and control gains on the system performance, as well as whether the dither period is sufficiently fast for the chosen parameters. If the constant approach method is implemented, the main concern of the designer lies with the choice of approach rate. Although it is still required to select the dither amplitude and period, it is the choice of approach rate that will mainly influence the controller performance. Choosing a higher dither frequency will allow for faster possible approach rates.

5.4 Procedure for Selecting ESC Parameters

The following section presents a procedure for choosing the extremum-seeking controller parameters. In the previous section, an in-depth analysis was performed regarding the effect of each parameter on the ESC performance. These effects, along with the expected flight conditions, govern the choice of extremum-seeking parameters.

The section first presents the effect of static wind on the position of the extremum. It will be shown that the expected static wind plays a key role in selecting the appropriate approach rate. Next, taking into account the expected static wind, a procedure for selecting the controller parameters when using the constant approach rate method is suggested. Similar to the analysis performed in the previous section, the goal of this section is to provide the designer with a conceptual understanding of the factors that influence parameter selection, rather than an optimal solution. Note that the section refers to a *constant* static wind as well as a *changing* static wind. The term *static wind* refers to the low frequency wind disturbances experienced by the formation, and is modelled by the static wind map or field presented in Chapter 3. The formation experiences a *constant* static wind when flying through an area where the magnitude of the static wind velocity is constant (rate of change of the wind velocity is zero). Similarly, the formation experiences a *changing* static wind when flying through an area where the magnitude of the static wind velocity varies (rate of change of the wind velocity is non-zero).

5.4.1 Effect of Static Wind on Extremum Position

In Chapter 3, the effective formation separation was defined as the position of the follower aircraft relative to the wake, which, contrary to geometrical separation, takes into account the changes in the position of the wake due to wind disturbances as well as the time delay between aircraft. This section focusses on the changes in wake position due to static wind, and assumes that the follower maintains a steady axial separation.

Constant Static Wind

Assuming that the formation is subjected to a *constant* static wind, the wake position relative to the follower will be displaced by a fixed distance. Since the static wind consists of a lateral and vertical component, the wake will be displaced both laterally and vertically. Figure 5.37 illustrates the lateral and vertical wake displacement when the formation experiences lateral and vertical static wind components, v_{sw} and w_{sw}. The resulting lateral and vertical displacements are denoted by Δy_{sw} and Δz_{sw} respectively, while the constant axial distance between aircraft is denoted by Δx.

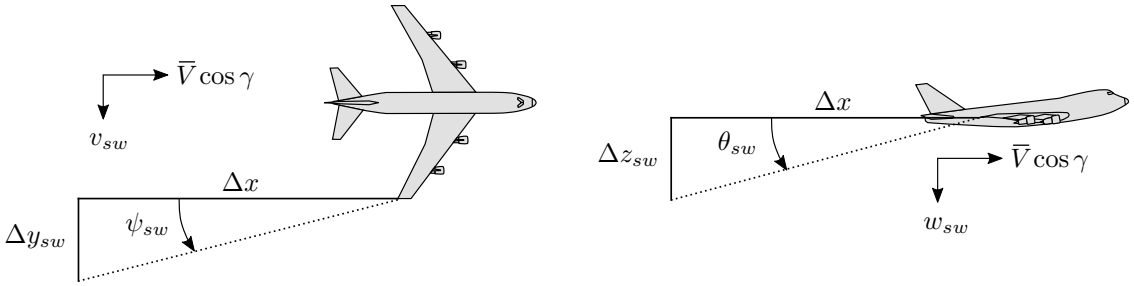

(a) Lateral wake displacement.

(b) Vertical wake displacement.

Figure 5.37: Wake displacement due to static wind.

The wake displacements may be calculated as follows,

$$\Delta y_{sw} = \Delta x \tan\psi_{sw} = \Delta x \frac{v_{sw}}{\overline{V}\cos\gamma} \tag{5.16}$$

$$\Delta z_{sw} = \Delta x \tan\theta_{sw} = \Delta x \frac{w_{sw}}{\overline{V}\cos\gamma} \tag{5.17}$$

where $\overline{V}$ is the airspeed magnitude, γ is the flight path angle, and ψ_{sw} and θ_{sw} are the lateral and vertical angle displacements of the wake. The displacement components in meters may be converted to wingspans by simply dividing by the leader wingspan, or,

$$\Delta\eta_{sw} = \frac{\Delta y_{sw}}{b} \qquad \Delta\zeta_{sw} = \frac{\Delta z_{sw}}{b} \tag{5.18}$$

which is equivalent to using axial separation ξ instead of Δx in Equation 5.17.

Changing Static Wind

If the formation is subjected to a *changing* static wind, the wake will be displaced at a rate proportional to the rate of change of the wind velocity. Assuming that the leader aircraft remains in straight and level flight, the lateral and vertical rates at which the wake is displaced, $\dot{\Delta y}_{sw}$ and $\dot{\Delta z}_{sw}$, may be calculated through,

$$\dot{\Delta y}_{sw} = \frac{\Delta x}{\overline{V}\cos\gamma}\dot{v}_{sw} \tag{5.19}$$

$$\dot{\Delta z}_{sw} = \frac{\Delta x}{\overline{V}\cos\gamma}\dot{w}_{sw} \tag{5.20}$$

where $\dot{v}_{sw}$ and $\dot{w}_{sw}$ are the lateral and vertical components of the rate of change of the static wind's velocity. Once again, the components may be converted to wingspans per second by dividing by the aircraft wingspan.

Static Wind Example

An example of static wind, and the resulting wake displacement, is shown in Figure 5.38. The lateral and vertical static wind components are shown in Figure 5.38a, while the corresponding wake displacements, calculated through Equation 5.18, are shown in Figure 5.38b.

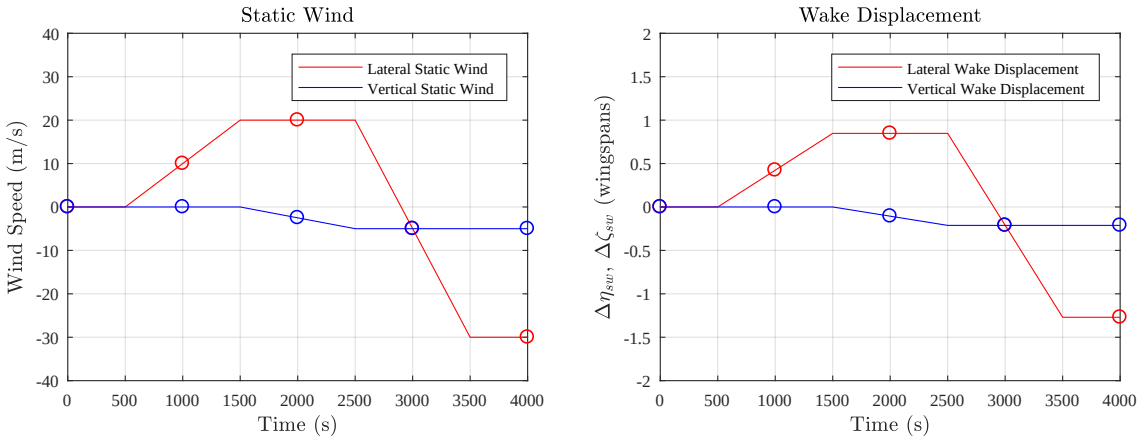

(a) Static wind.

(b) Wake displacement.

Figure 5.38: Example of typical wake displacement due to varying static wind.

Figure 5.39 shows the extremum position at the time steps denoted by the circle markers in Figure 5.38. The black arrowed line displays the direction of movement of the extremum. When the static wind is zero, the extremum is at its undisturbed position directly behind the leader aircraft. Once the lateral static wind is applied, the extremum is displaced from its initial position, and moves around in the XZ-plane of the guidance axis system. If the follower were to maintain a steady geometrical separation at the position of the undisturbed extremum, as depicted by the aircraft silhouette in the figure, the wake-induced effects it experiences will change significantly as the wake is displaced. If the wake moves too far away from the follower, as illustrated at time steps $t = 3000$ and $t = 4000$, wake benefit will significantly decrease. Conversely, if the wake moves to close to the follower, as shown at time step $t = 1000$, the aircraft ends up flying precariously deep in the wake, where it will struggle to maintain station without saturating its control surfaces responsible for countering the wake-induced rolling moment. Finally, when the wake passes far to the right, as depicted at time step $t = 2000$, the follower will no longer be able to counter the disturbance rolling moment and may be rolled into the dangerous downwash region of the leader.

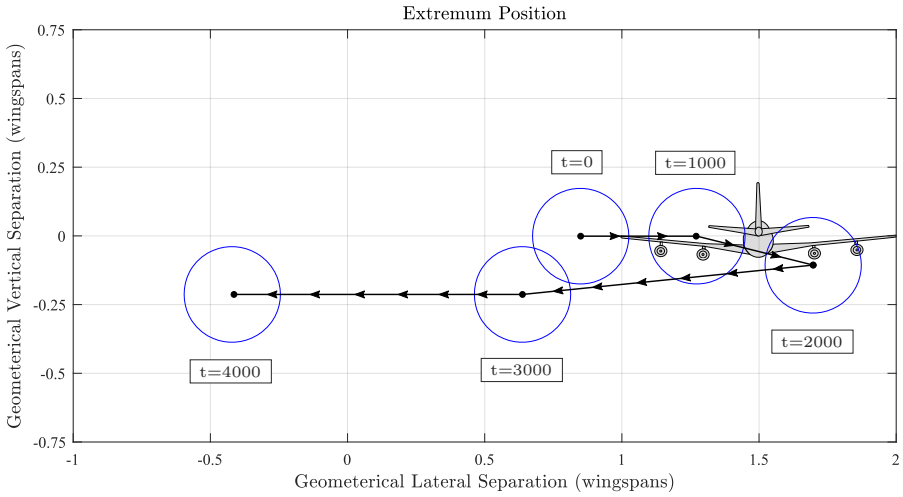

Figure 5.39: Typical wake displacement in 2D.

5.4.2 Suggested Procedure for Selecting the ESC Parameters

Before using the ESC to track a dynamic extremum, the appropriate extremum-seeking controller parameters must be selected. This section presents a systematic procedure for selecting the ESC parameters when using a *constant* approach rate, and requires prior knowledge of the expected rate of change of the static wind. The procedure may be divided into the following steps:

1. **Identify the largest gradient in the static wind velocity along the flight plan.**

   It was shown that the static wind has a significant effect on the position of the wake relative to the follower. In order for the follower to track the dynamic extremum, it is required to know how fast the extremum is moving. This in turn requires knowledge of the rate at which static wind changes. Since the vertical component of static wind is almost negligible relative to the lateral component, the maximum change in static wind is assumed to occur in the lateral plane. The maximum rate of change may be calculated by,

   $$\dot{v}_{\max} = \frac{\Delta v}{\Delta T} \tag{5.21}$$

   where $\dot{v}_{\max}$ is the maximum rate of change in static wind, and Δv is the maximum change in wind velocity over corresponding time period ΔT. The time ΔT depends on the average airspeed of the formation, which determines how fast the formation moves through the static wind map.

2. **Calculate the maximum displacement rate of the trailing vortex.**

   The second step is to calculate the maximum expected rate of change in the extremum position due to the maximum rate of change in static wind identified in the previous step. The maximum extremum displacement rate may be calculated through,

   $$\dot{\Delta y}_{\max} = \frac{\xi b}{\overline{V}\cos\gamma}\dot{v}_{\max} \tag{5.22}$$

   where b is the aircraft wingspan, ξ is the axial separation, $\overline{V}$ is the airspeed magnitude, and γ is the flight path angle. Note that the Equation 5.22 is similar to Equation 5.20.

3. **Calculate the minimum approach rate for the follower aircraft based on the maximum displacement rate of the trailing vortex.**

   The third step is to calculate the minimum approach rate $C_{\min}$ for the extremum-seeking controller. In order to track the dynamic extremum, the approach rate must be selected to be at least equal to the maximum wake displacement rate, expressed mathematically as,

   $$C_{\min} = \dot{\Delta y}_{\max} \tag{5.23}$$

4. **Calculate the maximum dither frequency based on the bandwidth of the lateral and vertical separation controllers.**

   During the fourth step, the maximum dither frequency must be calculated taking into

account the bandwidth of the follower aircraft's lateral and vertical separation controllers. The maximum dither frequency is defined as the highest frequency at which the follower aircraft may dither while still remaining within the bandwidth of the lateral and vertical separation controllers.

5. **Select the dither frequency.**

   The dither frequency must be selected to be lower than the maximum dither frequency calculated in step four, and must also take into account passenger comfort and actuator usage. If the dither frequency is chosen to be too high, the follower aircraft will not be able to track the lateral and vertical dither commands. This will result in inaccurate wake gradient estimation.

6. **Calculate the maximum approach rate based on the selected dither frequency**.

   It was mentioned in Section 5.3.3 that the dither period indirectly affects the convergence time through maximum allowable approach rate. Since dithering faster increases the information gained per time step, faster approach rates can be selected for higher dither frequencies. The maximum approach rate $C_{\max}$ must thus be selected based on the maximum dither frequency.

7. **Select the constant approach rate.**

   The sixth step is to select a suitable approach rate C for the extremum-seeking controller. In order to track the dynamic extremum, the approach rate must be selected to be at least equal to the minimum approach rate $C_{\min}$. However, choosing the approach rate faster will yield a smaller stead-state tracking error, which will be shown in Section 5.5.3. Pilot and passenger comfort must also be taken into account when selecting the approach rate. The final choice of the approach rate is left to the discretion of the designer, with the requirement being,

$$C_{\min} \leq C \leq C_{\max} \tag{5.24}$$

8. **Select the dither amplitude based on the objective function and the selected constant approach rate.**

   The final step is to select the dither amplitude for the extremum-seeking control. The dither amplitude is chosen based on the size of the desired steady state oscillations, which should typically be small. In Section 5.3.3 it was mentioned that the follower will converge to the extremum for any realistic amplitude, given that the approach rate is sufficiently slow. As with the selection of the approach rate, the final choice of the dither amplitude is left to the discretion of the designer

5.5 Seeking a Dynamic Constrained Extremum

In the previous section, it was shown that the extremum-seeking controller is able to successfully locate the constrained optimum location for a *stationary* trailing vortex, using either a proportional or constant approach rate. Since the wake was not displaced by any atmospheric disturbances, the geometric separation between the leader and the follower aircraft were equal to the effective separation between the follower and the trailing vortex, save for the small time delay between the leader and follower aircraft. In a realistic formation flight scenario, however, the wake will constantly be displaced by external disturbances such as wind and turbulence. Because the geometric and effective separations are no longer the same when the trailing vortex is disturbed, the extremum-seeking controller must be able to *locate* the constrained optimum location. In addition, because the trailing vortex may move around due to changes in the wind conditions, the extremum-seeking controller must also be able to *track* the constrained optimum location.

This section therefore aims to address the more practical objective of the extremum-seeking controller, namely that of tracking a *dynamic* extremum. When disturbed by static wind and turbulence, the effective formation separation will constantly change, resulting in large variations in the wake-induced drag benefit experienced by the follower. If the wake moves away from the follower aircraft, the effective separation increases, resulting in a decrease in the wake-induced drag benefit. If the wake moves closer to the follower aircraft, the effective separation decreases, resulting in an increase in the wake-induced rolling moment disturbance, due to the follower flying too deep in the wake.

The section is divided into three parts: (1) seeking an extremum that is moving away from the follower, (2) seeking an extremum that is moving closer to the follower, and (3) investigating the effects of different approach speeds on tracking performance. Since the vertical component of static wind is almost negligible relative to the lateral component, it is assumed that the fastest and largest changes in wake position will occur in the lateral plane. This section thus only considers a change in the lateral position of the wake. It will be shown that for the case where the wake is displaced away from the follower, using the controller as implemented for the stationary case yields satisfactory results. For the case where the wake is displaced towards the follower, however, the extremum-seeking state machine required modification to successfully seek the extremum. Since it was identified in the previous section that there are several advantages to using a constant approach rate rather than a proportional approach rate, only the former method will be considered in this section. The final part of the section investigates the effects of different approach rates on the tracking performance.

5.5.1 Extremum Shifting Away From Follower Aircraft

The first case that is investigated is where the trailing vortex is moving away from the follower aircraft, as shown in Figure 5.40. Firstly, the section presents the problem of not tracking the dynamic extremum and the effect that it has on the thrust demand of the follower. Secondly, it is shown that the dynamic extremum can be tracked using the extremum-seeking controller, and that by doing so, the loss in wake-induced drag benefit is reduced.

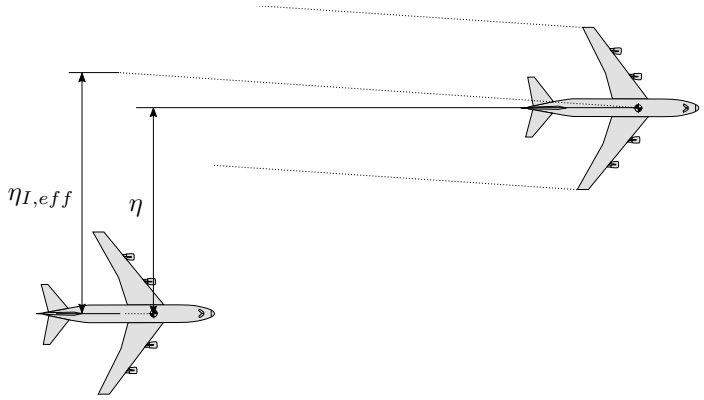

Figure 5.40: Wake moving away from follower (increased effective separation).

Wind Applied in Simulation

For the simulation results presented in this section, a lateral static wind that shifts the extremum *away* from the follower was applied to the formation. The lateral wind speed was changed from 0 to −25 meters per second over a period of 3000 seconds, causing a vortex lateral displacement rate of 0.02 meters per second, or at a rate of 3.33×10^{-4} wingspans per second. This results in a change in effective lateral separation of approximately 1 wingspan over 3000 seconds, while having no effect on the effective vertical separation. The static wind and its corresponding effect on effective separation is shown in Figure 5.41. Note that the magnitude and the rate of change of the simulated wind was selected after consulting the wind data used by the static wind model presented in Chapter 3, and is therefore representative of a real-world scenario.

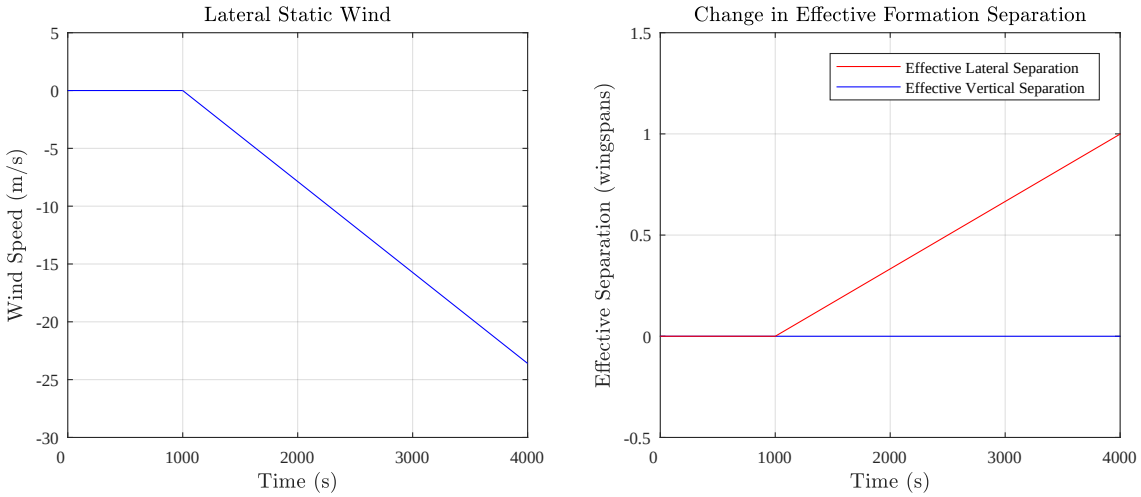

(a) Lateral static wind.

(b) Change in effective separation.

Figure 5.41: Lateral wind applied to formation in order to shift extremum away from follower.

Simulation Results: No ESC Active

Before investigating the dynamic extremum tracking performance, it is first important to consider the effects on the follower aircraft if the extremum is not tracked. Figure 5.42 shows the effective separation and thrust demand in a simulation were the follower is only allowed

to perform station-keeping relative to the leader using the lateral and vertical separation controllers. Without the extremum-seeking controller, the follower aircraft only maintains its geometric separation relative to the leader aircraft at the expected location of the stationary extremum. Once the extremum becomes dynamic and starts to shift away at $t = 1000$ seconds, the follower does not follow the extremum and the effective lateral separation increases. The drag benefit gained from flying in the wake is reduced, and the follower needs to increase its thrust to compensate for the increased drag and to maintain trim.

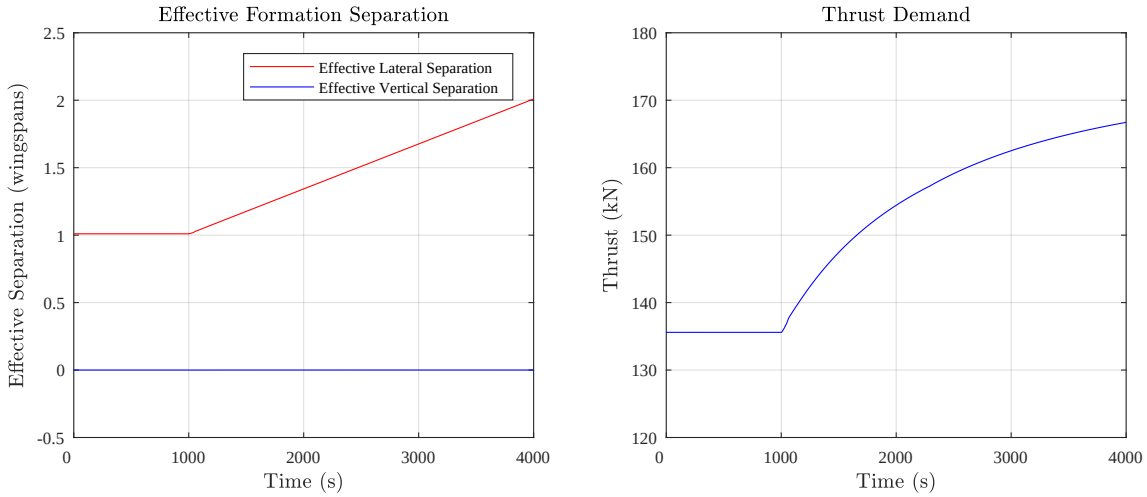

(a) Effective separation over time.

(b) Thrust response.

Figure 5.42: Simulation results where only formation guidance controllers are used to maintain geometrical separation at stationary extremum.

Simulation Results: With ESC active

The next simulations were performed with the extremum-seeking controller switched on and the results are shown in Figure 5.43. Note that in order for the follower to successfully track a dynamic extremum, the constant approach rate would have to be larger than the rate at which the extremum is moving. Since the displacement rate of the extremum is approximately 0.02 meters per second, a constant approach speed C of 0.025 metres per second, or 4.188×10^{-4} wingspans per second, is selected.

The simulation is initialised with the follower aircraft at the location of the constrained optimum, with a stationary trailing vortex and windless conditions. When the wind speed starts increasing at t = 1000 seconds and the extremum starts moving away, the extremum-seeking controller commands the follower aircraft to change its geometric separation in order to maintain the desired effective separation. As the extremum shifts away from the follower, the geometric lateral separation between the leader aircraft and the follower aircraft decreases, as seen in Figure 5.43b, while the geometric vertical separation remains equal to the effective vertical separation. Note, however, that the follower aircraft slightly lags behind the extremum as it moves, which can be observed as a slight increase in effective separation. The distance by which the follower lags the extremum is defined as the tracking error, shown in Figure 5.43c, and exhibits similar behaviour to a Type 1 control system. The follower manages to track a stationary extremum (a step reference) with no error, while it tracks a dynamic extremum moving at a constant rate (a ramp reference) with finite error. The thrust response is shown in Figure 5.43d. Since the follower is able to track the dynamic extremum,

most of the wake-induced drag benefit and the corresponding reduction in thrust demand is retained.

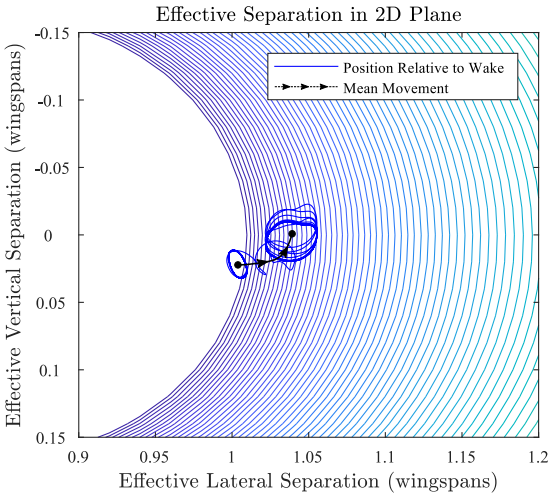

(a) Effective separation in 2D.

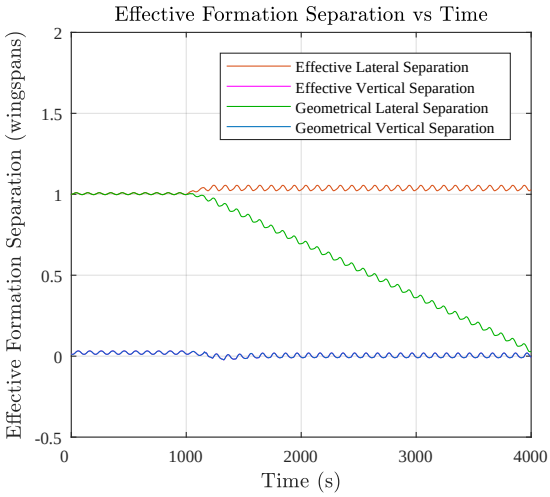

(b) Effective separation over time.

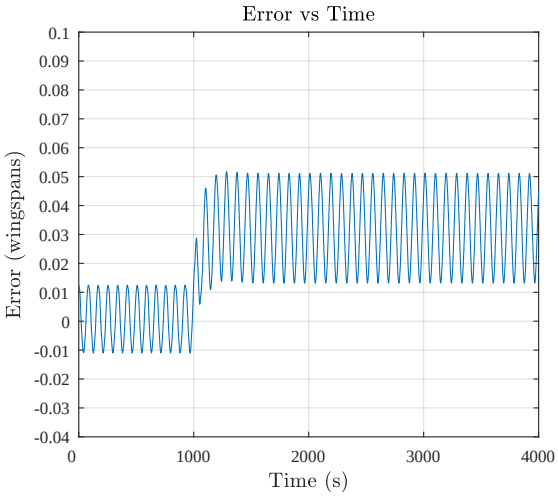

(c) Tracking error.

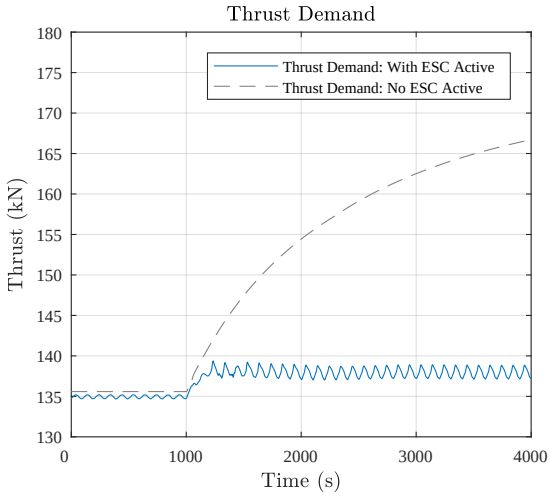

(d) Thrust response.

Figure 5.43: Extremum-seeking results: tracking an extremum that is moving away from a follower aircraft.

5.5.2 Extremum Shifting Closer

The second case that was investigated is where the extremum is moving closer to the follower aircraft, as shown in Figure 5.44. As before, the consequences of not tracking the dynamic extremum is illustrated first. Next, it is shown that the follower is unable to track the dynamic extremum using the current implementation of the extremum-seeking controller when the extremum moves towards the follower aircraft. Finally, a modified logic controller is presented that enables the extremum-seeking controller to successfully track the dynamic extremum, even when the extremum moves towards the follower aircraft, while maintaining a safe but still beneficial effective separation.

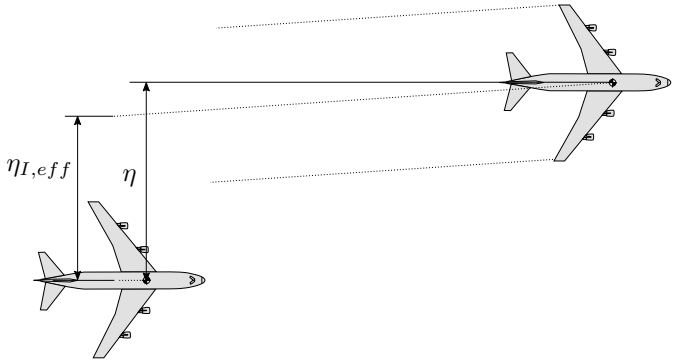

Figure 5.44: Wake moving closer to follower (decreased effective separation).

Wind Applied in Simulation

In this section, a static wind that shifts the extremum *towards* the follower was applied to the formation. The lateral wind speed was changed from 0 to +25 meters per second over a period of 3000 seconds, causing a vortex lateral displacement rate of +0.02 meters per second, or $+3.33 \times 10^{-4}$ wingspans per second. This results in a decrease in the effective lateral separation of approximately 1 wingspan over 3000 seconds, while having no effect on the effective vertical separation. The static wind and its corresponding effect on effective separation is shown in Figure 5.45.

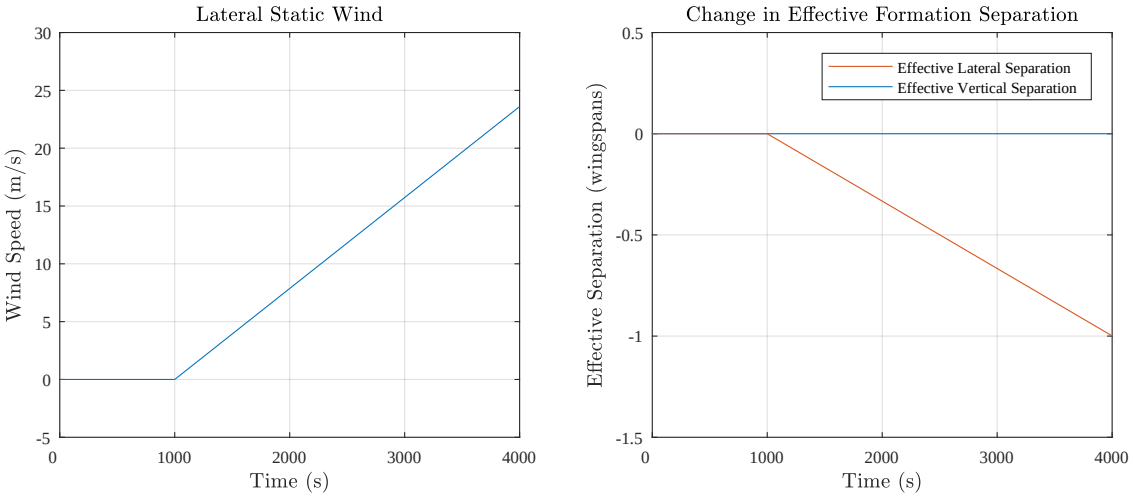

(a) Lateral static wind.

(b) Change in effective lateral separation.

Figure 5.45: Lateral wind applied to formation in order to shift extremum closer to follower.

Simulation Results: No ESC Active

Figure 5.46 shows the effective separation and thrust demand in a simulation were the follower is again only allowed to perform station-keeping relative to the leader using the lateral and vertical separation controllers. When the wake starts to move closer at $t = 1000$ seconds the follower aircraft does not move away, and the effective separation decreases and the follower effectively moves deeper into the wake. Because the follower benefits from additional wake-induced lift deeper in the wake, the wake-induced drag decreases and less thrust is required to maintain trim. However, flying deeper in the wake also increases the wake-induced rolling

moment disturbance and more aileron deflection is required to counter the disturbance, as shown in Figure 5.46c. Once the ailerons saturate, which can more clearly be seen in Figure 5.46d, the follower will no longer be able to counter the rolling moment disturbance, and will not be able to maintain wings level trim so deep into the wake.

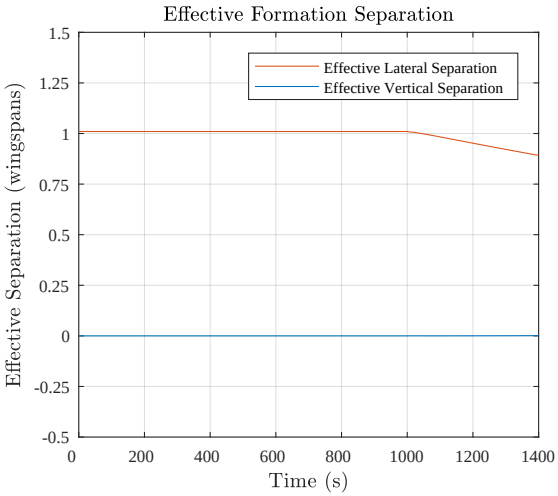

(a) Effective separation over time.

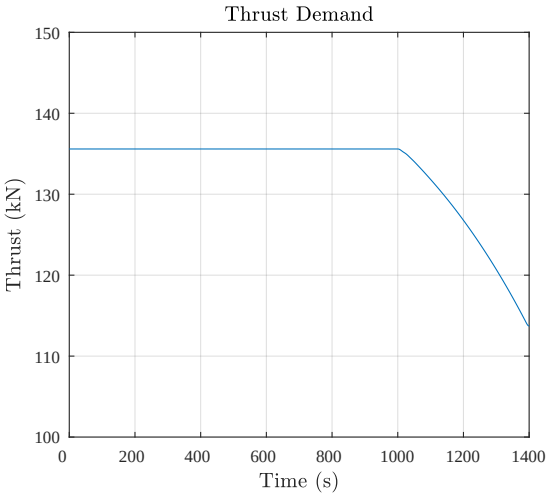

(b) Thrust response.

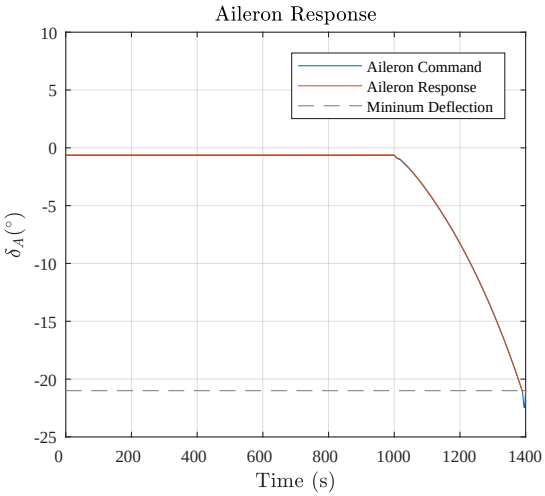

(c) Aileron response.

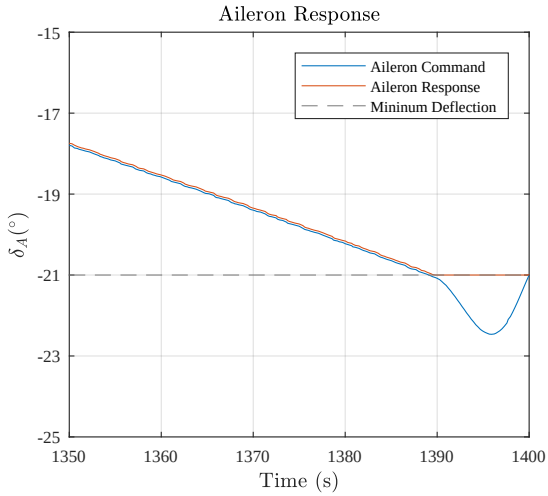

(d) Zoomed view of aileron response.

Figure 5.46: Simulation results where only formation guidance controllers are used to maintain geometrical separation at stationary extremum.

Simulation Results: ESC Active

Figure 5.47 shows the results of a simulation where the extremum-seeking controller is active when trailing vortex moves towards the follower aircraft. Figure 5.47a shows the formation separation in 2D, while Figure 5.47b shows the vertical and lateral separation separately over time. Figure 5.47c shows the thrust response of the follower. From the results it is clear that, although the approach speed is sufficiently fast, the follower aircraft is unable to successfully maintain the desired effective separation. Eventually, the trailing vortex moves too close to the follower aircraft, and the effective lateral separation becomes small enough that the aircraft is overwhelmed by the wake-induced rolling moment disturbance. Both the

vertical geometric and effective separation of the follower aircraft decreases as well. The simulation results are shown up to the point where the follower aircraft is overwhelmed by the wake-induced rolling moment and loses the ability to maintain wings level trim flight.

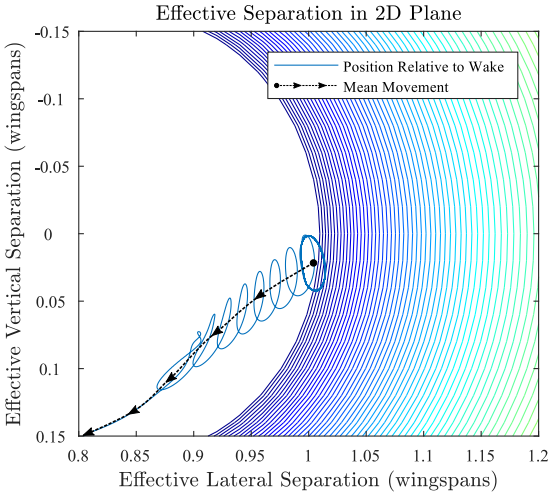

(a) Effective separation in 2D.

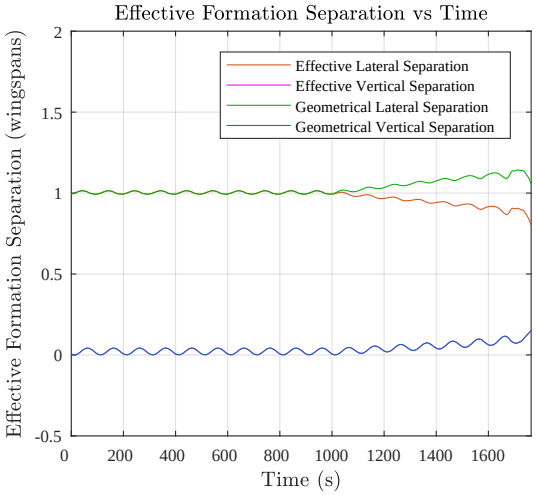

(b) Effective separation over time.

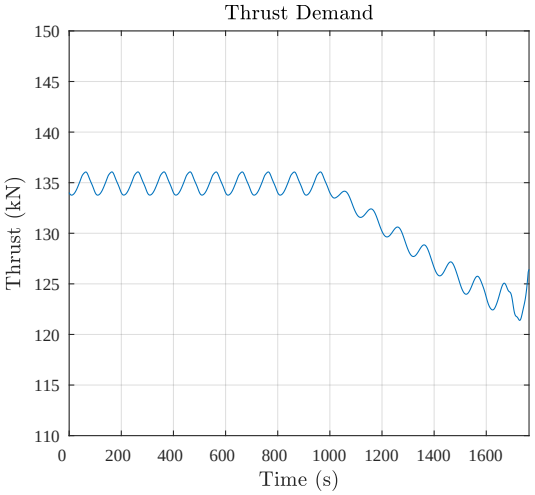

(c) Thrust response.

Figure 5.47: Tracking an extremum that is moving closer to follower aircraft.

The reason that the extremum controller is unable to track constrained extremum when the trailing vortex approaches the follower aircraft is explained as follows:

As presented in Section 5.2.5, the logic controller governs the behaviour of the extremum-seeking controller based on the wake-induced pitch angle. In its current form, once the controller detects that the follower is too deep in the wake, the sign of the motion commands are reversed and the follower is guided out of the wake. This logic yields the desired result when seeking a dynamic extremum that moves away from the follower. It does not, however, enable tracking of a dynamic extremum that is moving closer to the follower. The reason for this is explained with the aid of Figure 5.48.

Since the extremum-seeking controller commands the follower to move along the direction of the wake gradient, the trajectory that the follower will follow is dependant on its position

in the wake. When the follower is outside the constrained extremum contour, the ESC controller is in the *Near Approach* state, and the aircraft is commanded to move in the direction that reduces the wake-induced pitch angle. The commanded trajectory is illustrated by Figure 5.48a, where the initial position of the follower is indicated by the red circle and the trajectory commanded by the ESC controller is indicated by the red dotted line. The figure conceptually illustrates how the follower aircraft would be guided towards the extremum by following the wake gradient inwards. Conversely, when the follower is inside the constrained extremum contour, the ESC controller operates in the *Near Escape* state, and the aircraft is commanded to move in the direction that increase the wake-induced pitch angle. The commanded trajectory is illustrated by Figure 5.48b, where the figure conceptually illustrates how the follower aircraft would be guided away from the extremum by following the wake gradient outwards. Figure 5.48c shows an actual simulation where the extremum-seeking controller was operated only in the *Near Escape* mode. The follower starts on the inside of the constrained extremum contour and follows a path out of the wake along the direction of the wake gradient.

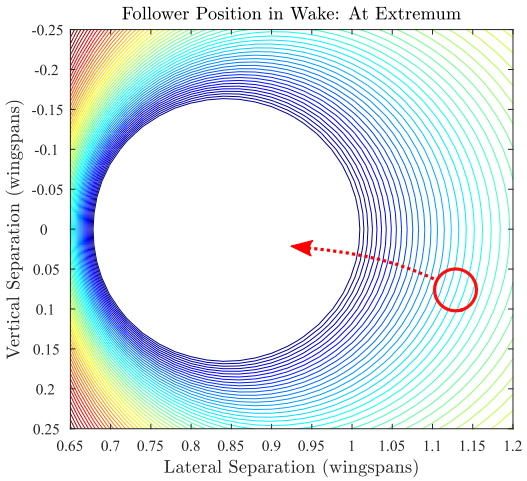

(a) Follower trajectory into wake.

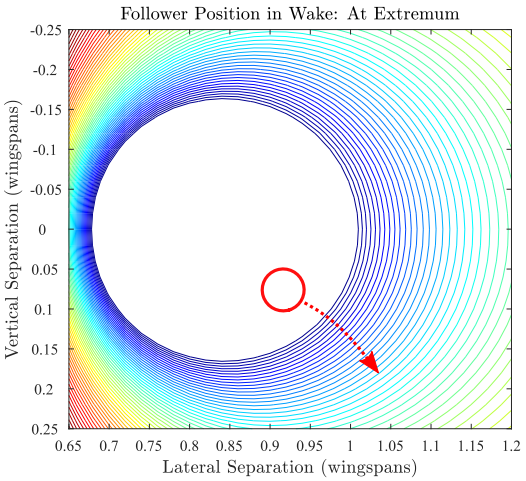

(b) Follower trajectory out of wake.

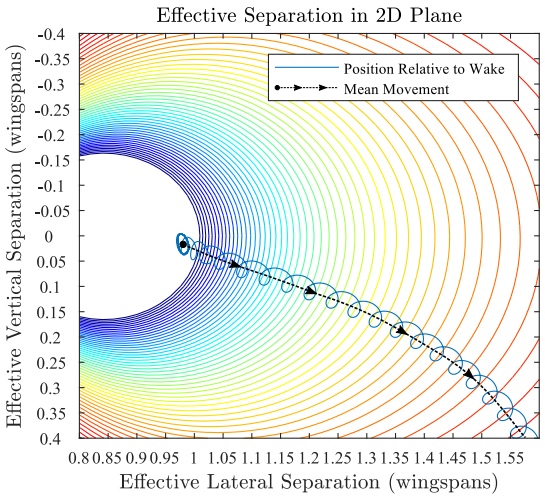

(c) Follower path out of wake verified in simulation.

Figure 5.48: Follower commanded trajectories and actual path out of wake.

It is important to observe that the follower aircraft escapes from the wake by moving both laterally and vertically outwards. This same behaviour is observed when the trailing vortex moves laterally towards the follower aircraft while the extremum-seeking controller tries to track the moving constrained extremum. Consider the scenario where the follower aircraft is operating on the constrained extremum contour. If the trailing vortex starts moving laterally towards the follower aircraft, then the extremum also moves laterally in the same direction and the follower aircraft suddenly finds itself on the inside of constrained extremum contour. The logic controller detects that the wake-induced pitch angle is too low and switches the extremum-seeking controller to the *Near Escape* state, which then tries to follow the constrained extremum by commanding the aircraft to move along the wake gradient in the direction that *increases* the wake-induced pitch angle. However, although the trailing vortex only moved laterally, the aircraft is commanded to move both laterally and vertically due to the direction of the wake gradient (This behaviour is not observed when the vortex moves laterally *away* from the follower aircraft, because the extremum-seeking controller stays in the *Near Approach* state and the follower aircraft is commanded to follow the moving extremum using mainly lateral motion.). Since the follower is not guided in the same direction as in which the extremum is moving, the rate of its lateral motion is too slow to 'escape' the moving extremum. Eventually, the trailing vortex catches up to the follower aircraft and the aircraft is overwhelmed by the wake-induced rolling moment disturbance.

It could be argued that the magnitude of the lateral motion rate can be increased by using a faster constant approach rate. This would prevent the trailing vortex from catching up with the follower aircraft. While this is true, it is important to remember that the follower would still be guided both laterally and vertically out of the wake and away from the constrained extremum. Increasing the approach rate therefore would not improve the extremum-seeking controller's ability to maintain tracking of the constrained extremum when the trailing vortex moves towards the follower aircraft.

The following section proposes a solution to this problem by modifying the state machine for the extremum-seeking control.

Tracking the Dynamic Extremum: A Modified Logic Controller

To enable tracking of an approaching dynamic extremum, the following modification to the state machine for the extremum-seeking controller is proposed. Since the largest variations in static wind occur in the lateral plane, it can safely be assumed that the extremum will mainly shift laterally with respect to the follower. It is therefore argued that the tracking ability can be improved by only seeking in the lateral direction. This prevents the follower from 'climbing' out of the wake, and enables movement in the lateral direction at an increased rate.

The state diagram for the modified logic controller is shown in Figure 5.49, which is similar to the original diagram except for the addition of a fourth logic stage, namely, the *Critical Escape* state. When the follower is lagging too far behind the extremum, detected by comparing the wake-induced pitch angle measurement $\Delta\theta_w$ with a thresh-hold Θ_I and finding that $\Delta\theta_w < \Theta_I$, the extremum-seeking controller commands the follower to update only its lateral separation rate. The vertical separation rate is set to zero while the lateral separation rate is set to C.

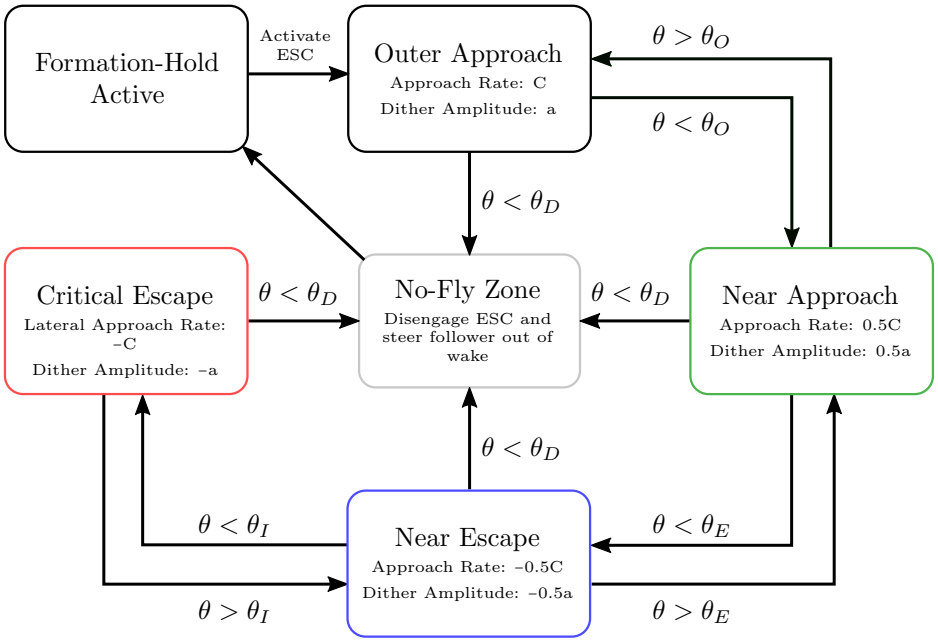

Figure 5.49: Modified logic controller state machine.

The modified logic controller states and state transition boundaries are shown in Figure 5.50. The additional inner boundary Θ_I, seen in Figure 5.50a, introduces the fourth state, shown in Figure 5.50b.

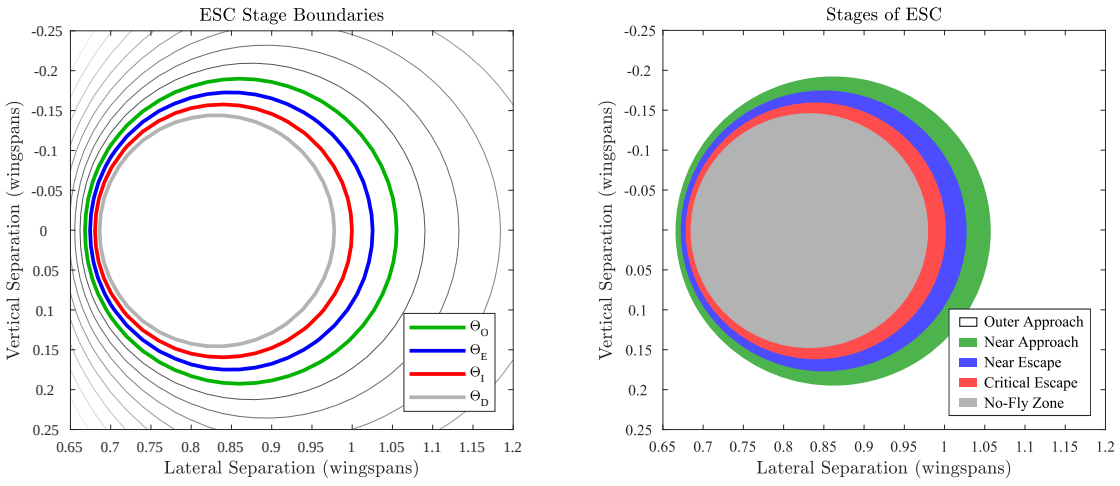

(a) ESC state transition boundaries.

(b) ESC states.

Figure 5.50: States and state transition boundaries for modified logic controller.

The previous simulations were repeated after implementing the modified logic controller, and the results are shown in Figure 5.51. With the modified controller, the follower aircraft managed to successfully track the moving extremum. Comparing the effective separation in Figure 5.51a to the result shown in Figure 5.47, it can be seen that the follower now remains close to the extremum instead of gradually moving deeper into the wake. In order to maintain the desired effective separation, the follower increases its geometrical separation, as seen in Figure 5.51b. Behaviour typical of a Type 1 control system is again observed. The follower

slightly lags behind the moving extremum with a finite tracking error as shown in Figure 5.51c. Since the follower flies slightly deeper in the wake while tracking the extremum, the reduction in drag is increased and the thrust required to maintain the desired axial separation is slightly less.

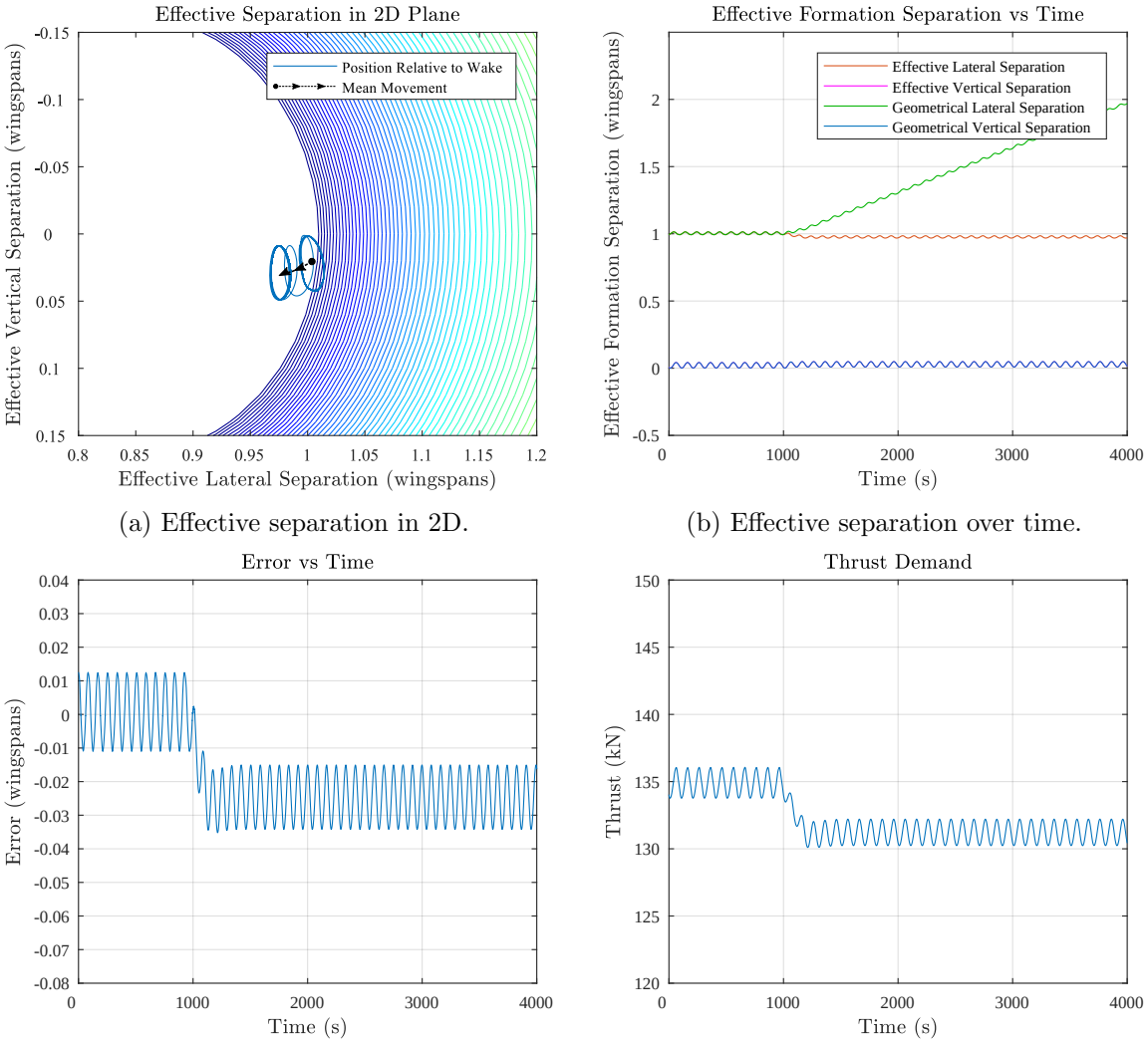

(a) Effective separation in 2D.

(b) Effective separation over time.

(c) Tracking error.

(d) Thrust response.

Figure 5.51: Tracking an extremum that is moving closer to a follower aircraft.

The modified logic controller functions under the assumption that the wind mainly varies in the lateral plane. If the extremum were to move slightly vertically, as it is expected to during a real flight scenario, the follower will first be guided laterally until an acceptable pitch angle is achieved, or, in other words, until the ESC enters the *Near Approach* state or the *Near Escape* state. In these two states, the follower will be guided both laterally and vertically to the extremum.

5.5.3 Effect of Approach Rate on Steady-State Tracking Performance

It has been shown that the extremum-seeking controller enables tracking of a dynamic extremum whether it is moving closer to or away from the follower. This section briefly inves-

tigates and discusses the effects of different approach rates on the tracking performance.

Varying Approach Rates: Tracking the Extremum

The tracking errors for three extremum seeking simulations with a different approach rates, are shown in Figure 5.52. The wake is displaced away from the follower aircraft, which results in a positive tracking error. The three approach rates are chosen fast enough so that the follower still manages to track the dynamic extremum.

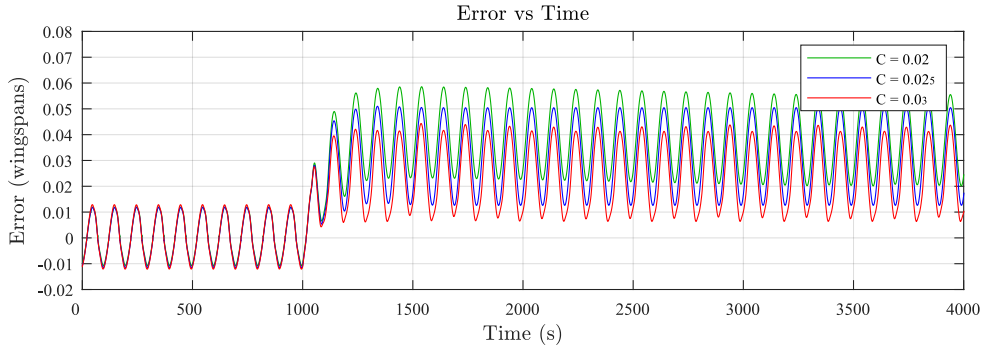

Figure 5.52: Tracking error for various approach speeds.

From the results it can be observed that a faster approach rate yields a smaller tracking error. This corresponds to the behaviour common to Type 1 control systems: larger gains lead to smaller steady-state tracking errors.

Approach Rate Too Slow to Track Extremum

The results for an extremum seeking simulation with an approach rate of $C = 0.015\ m/s$, or 2.5×10^{-1} wingspans per second, are shown in Figure 5.53. Since the approach rate is slower than the rate at which the wind is shifting the extremum, the follower is unable to track the dynamic extremum. The geometrical separation changes too slowly to maintain the desired effective separation, which leads to a tracking error that increases over time.

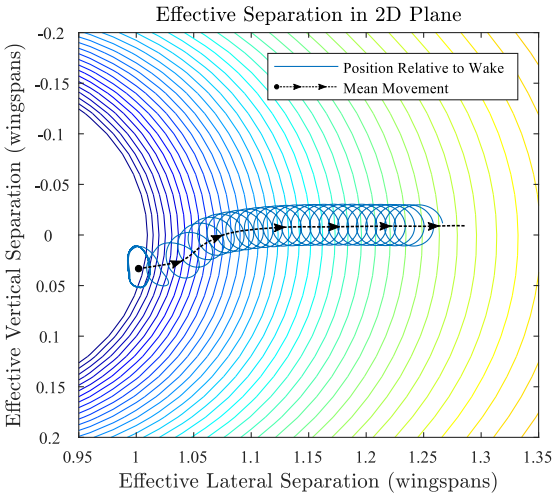

(a) Effective separation in 2D.

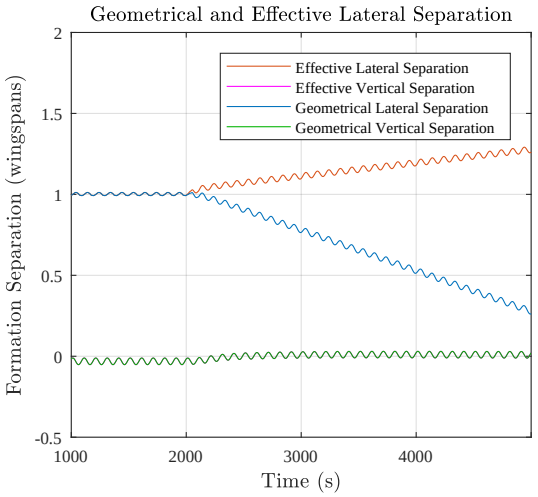

(b) Effective separation over time.

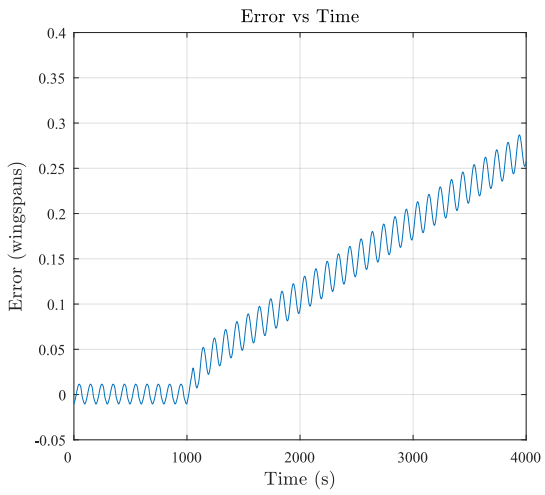

(c) Tracking error.

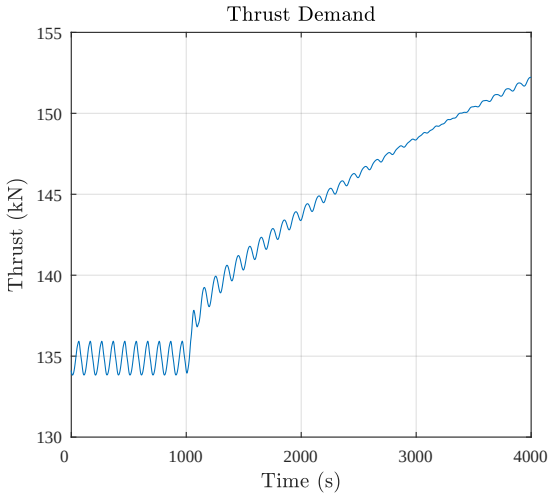

(d) Thrust response.

Figure 5.53: Tracking an extremum that is moving away.

5.6 Summary

This section presented the design, implementation, and verification of an extremum-seeking controller for constrained optimal fuel consumption in formation flight. A general overview of the proposed extremum-seeking controller was presented, and the design and implementation of each component was discussed in detail. In order to ensure that the follower aircraft performs the correct circular motions to explore the wake, the dither signal phase and amplitude were adjusted to compensate for the attenuation and phase lag introduced by the transfer functions of the follower aircraft's lateral and vertical separation controllers. Calculation of both the phase lag, using cross-correlation, and amplitude attenuation was performed on-line.

A novel constrained objective function was proposed, where the extremum is represented by a constrained extremum contour instead of a single point, to allow for tracking of a constrained and dynamic extremum. The wake-induced pitch angle, obtained by subtracting the pitch angle due to general aircraft motion from the measured pitch angle of the follower in the wake, was used as the objective and constrained by defining a minimum allowable

pitch angle for the follower aircraft. A simplified freestream pitch angle model was presented and validated, that uses a simple transfer function instead of a full-order coupled simulation to model the pitch angle response of the follower in freestream.

A phase synchronisation scheme was proposed for phase correction between the demodulating dither signals and the objective function to compensate for the phase lag introduced by the lateral and vertical separation controllers. Similar to the phase correction of the dither signals, the phase synchronisation scheme uses cross-correlation to calculate the phase differences on-line.

An ESC state machine (logic controller) was proposed, that defines the ESC states and the ESC state transition boundaries as functions of the wake-induced pitch angle deviation, and not functions of the geometric separation between the leader aircraft and the follower aircraft. This allows the regions of operation and the switching boundaries to move around with the displaced trailing vortex, instead of remaining static relative to the leader aircraft. This also enables the extremum-seeking control to track a constrained extremum for a dynamic trailing vortex, and not just for a static trailing vortex.

A new extremum-seeking strategy was presented that uses a constant approach rate instead of a approach rate proportional to the wake gradient. It was found that the constant approach rate method holds two distinct advantages over the classical method. Firstly, the follower no longer moves faster the closer it flies to the extremum, and secondly, the process of selecting the controller parameters is significantly simplified. An investigation was performed into the effects of varying the three different ESC parameters, namely dither frequency, dither amplitude, and ESC gains/constant approach rate, on extremum-seeking performance. Simulations were performed using both a proportional approach rate and the novel constant approach rate. A design procedure was proposed for systematically selecting the ESC parameters based on the expected displacement rate of the trailing vortex and the bandwidths of the lateral and vertical separation controllers.

A modified ESC state machine was proposed to enable the extremum-seeking controller to maintain tracking of the constrained extremum when the vortex moves closer towards the follower aircraft. The improved extremum-seeking controller is able to successfully locate and track the constrained extremum, both for a static trailing vortex and for a dynamic trailing vortex that either moves away or towards the follower aircraft due to changes in the wind conditions.

The next chapter presents an analysis on the robustness of the extremum-seeking controller when the formation is subjected to the typical atmospheric disturbances expected during a real formation flight scenario.

Chapter 6

Robustness to Disturbances and Sensor Noise

The aim of this chapter is to investigate the robustness of extremum-seeking control for formation flight in the presence of random wind disturbances such as turbulence and gusts, and in the presence of realistic sensor noise. In the previous chapter, the use of extremum-seeking control in the tracking of a dynamic extremum was investigated and discussed. It was shown that a constrained extremum could successfully be tracked even when it is moving under the influence of changing wind conditions. However, the wind disturbances simulated in the previous chapter only included a static wind component, and did not include turbulence or gusts. The turbulence and gusts represent random external disturbances that affect the flight control of the leader aircraft, the formation flight control of the follower aircraft, and also randomly disturb the leader aircraft's wake. Another practical concern is the robustness of the extremum-seeking controller to sensor noise in the pitch angle measurements. The follower aircraft relies on its own pitch angle measurements to determine the wake gradient and also to decide when to switch between states in the ESC state machine. It is therefore important to verify the correct operation of the extremum-seeking controller in the presence of sensor noise.

The robustness of the extremum-seeking controller will be verified and evaluated using simulation scenarios where the formation is subjected to typical wind disturbances encountered in a real flight scenario. The results are presented in the form of two realistic flight scenarios, with each highlighting important aspects of controller robustness and performance. The first scenario presents the results for a simulation where the formation is subjected to moderate static wind and various levels of turbulence. In the second scenario, the static wind level is increased, requiring changes to the extremum-seeking approach rate. Finally, the robustness of the controller is investigated in the presence of sensor noise on the pitch angle measurement of the follower aircraft.

6.1 Realistic Flight Scenario: CPT - DXB

The first flight scenario is illustrated in Figure 6.1. The formation is initialized at Cape Town International Airport (CPT) and flies at a constant heading towards Dubai International Airport (DXB). The flight trajectory followed by the formation is shown in Figure 6.1a and the corresponding static wind obtained from the global wind data model is shown in Figure 6.1b.

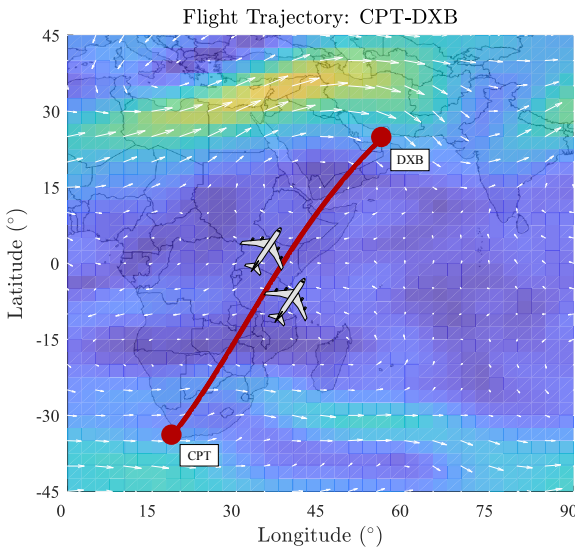

(a) Flight trajectory.

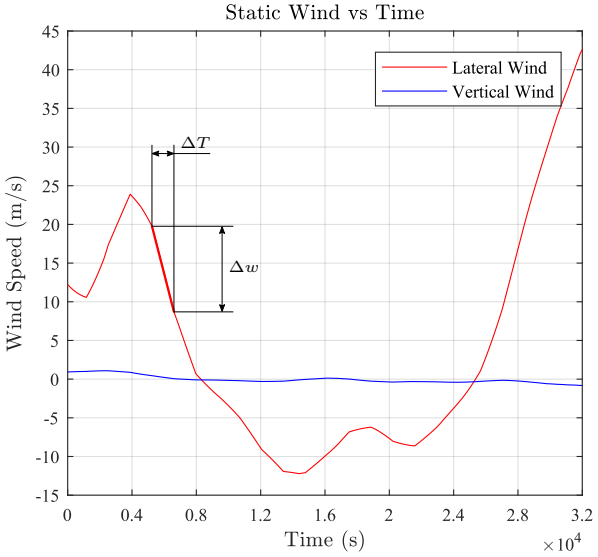

(b) Static wind.

Figure 6.1: Flight trajectory and expected static winds for CPT to DXB.

To select the controller parameters, the procedure presented in Section 5.4 is followed. The first step is to identify the largest gradient in the expected static wind. Considering Figure 6.1b, the largest gradient is denoted by the thick red line where Δv_{sw} is the difference in wind magnitude over the time ΔT. The magnitude of the gradient may be calculated using Equation 5.23 as follows,

$$\dot{v}_{sw} = \frac{\Delta v_{sw}}{\Delta T} \approx -0.008\, m/s^2 \tag{6.1}$$

The second step is to calculate the maximum expected displacement rate of the trailing vortex due to the static wind. Using Equation 5.23 yields,

$$\dot{\Delta y}_{CPT-DXB} = \left| \frac{\xi b}{\overline{V}} \dot{v}_{sw} \right| \approx 0.0202\ m/s \tag{6.2}$$

where ξ is the axial separation, b is the wingspans, and $\overline{V}$ is the airspeed magnitude. Next, the approach speed, C, is selected to be at least equal to the maximum expected displacement rate, $\dot{\Delta y}_{CPT-DXB}$. The dither parameters and approach rate are selected as follows:

- $C = 0.025\ ms^{-1}$ $(C > \dot{\Delta y}_{CPT-DXB})$
- $T_D = 100s$
- $a_D = 0.02b$

where the dither amplitudes and period is chosen to ensure small steady state oscillations within the bandwidth of the aircraft controllers. It is important to understand that there are an infinite number of feasible choices for the dither parameters. The values chosen here are equal to the baseline values used in Section 5.3.3.

The following sections present the simulation results for various levels of disturbances. In Section 6.1.1, simulations are performed with a time-varying static wind, but with no turbulence. In Section 6.1.2, simulations are performed with different levels of turbulence in addition to the time-varying static wind.

6.1.1 Robustness in Moderate Static Wind

The simulation results for a formation flight subjected to only a slowly-varying moderate static wind (but no turbulence) is shown in Figure 6.2. The simulation results show that the extremum-seeking controller successfully controls the follower aircraft to follow the moving constrained extremum and retains most of the wake-induced benefit, which is observed as a significant reduction in the forward thrust required to trim the aircraft.

The slowly-varying static wind is shown in Figure 6.2a, the geometric and effective lateral and vertical separations of the follower aircraft are shown in 6.2b, the control surface deflections are shown in Figure 6.2c, and the forward and differential thrusts are shown in Figure 6.2d using two separate y-axes. The follower aircraft is initialised at a position below the extremum at a geometric lateral separation of $\eta = 2$ and a geometric vertical separation of $\zeta = 1$. The static wind profile has been calculated for the specific flight plan. At the start of the simulation, the static wind has a positive wind speed, which displaces the wake towards the right behind the leader aircraft and therefore closer to the follower aircraft. The effective lateral separation ($\eta_{\text{eff}} = 1.5$) is therefore initially less than the geometric lateral separation ($\eta = 2$). At $t = 2000$ seconds, the extremum-seeking control is activated, and the ESC state machine starts in the *Outer Approach* mode. The extremum-seeking control then guides the follower aircraft towards the extremum, which is observed in the effective lateral separation being regulated towards ($\eta_{\text{eff}} = 1$). At $t = 4000$ seconds, the follower aircraft reaches the extremum, which is still being displaced towards the right behind the leader aircraft. The follower aircraft then tracks the moving extremum by changing its geometrical separation to maintain the desired effective separation. The effective lateral separation remains constant at $\eta_{\text{eff}} = 1$, while the shape of the geometric lateral separation follows the shape of the lateral wind speed. Both the geometric and effective vertical separations are controlled to zero, as there is minimal static wind disturbance in the vertical direction. At $t = 8000$ seconds, the wind speed becomes negative and wake starts being displaced towards the left behind the leader aircraft. The follower aircraft keeps on tracking the constrained extremum and the geometric lateral separation decreases to below $\eta = 1$. The follower aircraft receives a significant wake-induced drag benefit by flying at the constrained extremum, and an average reduction of 23% is observed in the forward thrust. The extremum-seeking controller ensures that this reduction in thrust is maintained throughout the flight even when the leader and follower aircraft and the leader generated wake are subjected to a slowly-varying static wind. The differential thrust saturates to counter the bulk of the wake-induced rolling moment at the constrained extremum. The rudder and aileron deflections exhibit variations due to the dithering motion of the aircraft. However, the control surfaces operate well within their physical limits, with the aileron deflection only exhibiting large variations to counter the large rolling moment when the follower aircraft operates at the constrained extremum location.

At $t = 27000$ seconds, the wakes is displaced rapidly towards the right again, towards the follower aircraft, which then attempts to track the constrained optimum using the *Near Escape* mode. As discussed in Chapter 5, the follower cannot move fast enough to track the extremum moving towards it, due to the fact that the aircraft is commanded to move both laterally and vertically to follow the wake gradient away from the extremum. The follower begins to lag behind the extremum, as seen from the change in both the lateral and the vertical effective separations. The follower aircraft eventually detects that the trailing vortex is too

close, and switches to the *Critical Escape* mode, where it seeks the constrained extremum using only lateral motion. By doing so, the follower aircraft is able to successfully keep on tracking the moving extremum, but with a constant steady-state tracking error. However, it is observed that the magnitude of the thrust variations increases slightly. This is due to the follower aircraft operating slightly deeper into the wake where the magnitude of the lift gradient is larger. The follower therefore experiences larger variations in the wake-induced drag benefit as it dithers, which leads to larger variations in the forward thrust to maintain trim.

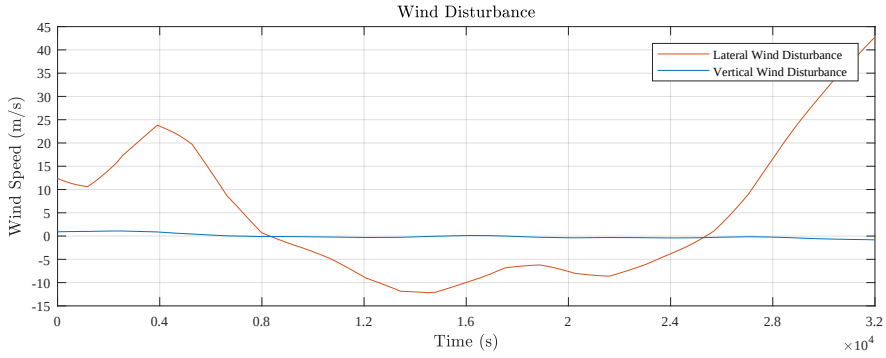

(a) Static wind.

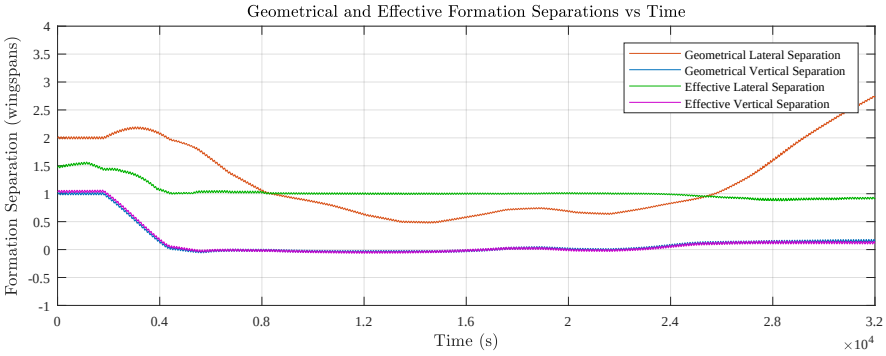

(b) Geometrical and effective formation separations.

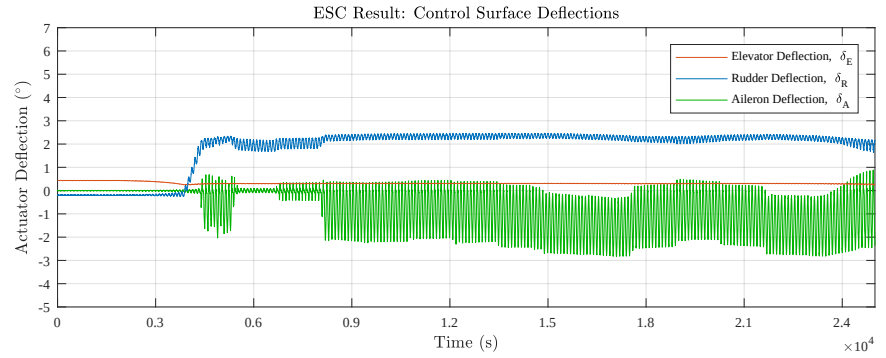

(c) Control surface deflections.

Figure 6.2: Simulation results for the flight from CPT to DXB under moderate static wind.

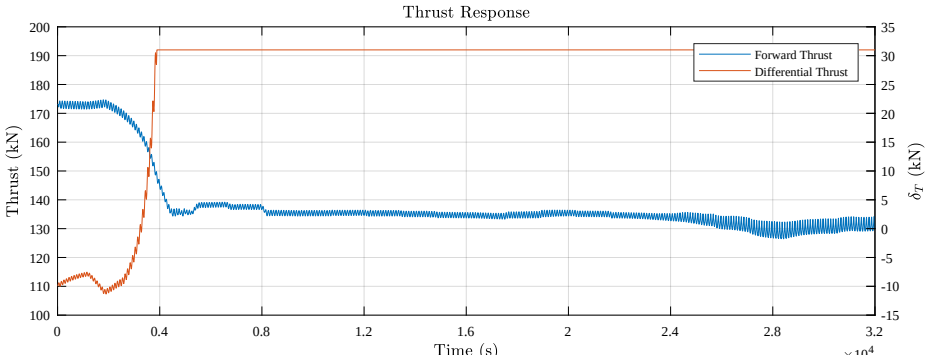

(d) Thrust response.

Figure 6.2: Simulation results for the flight from CPT to DXB under moderate static wind (cont.).

6.1.2 Robustness in Turbulent Conditions

This section investigates the robustness of the extremum-seeking controller when seeking under turbulent conditions. Different levels of turbulence were applied in simulation using the von Kármán turbulence model discussed in Chapter 3. In order to simulate a realistic flight scenario, the formation is subjected to the turbulence in addition to the moderate static wind shown in Section 6.1.1.

In light turbulence, the extremum-seeking control successfully enables the follower to locate and track the dynamic extremum. The simulation results show similar controller performance to what was obtained when seeking in only moderate static wind. Similar simulations were attempted in moderate turbulence, but the controller was unable to safely guide the follower towards the extremum. Finally, since previous studies found the case of severe turbulence too intense for even conventional formation flight, the extremum-seeking was not tested in such conditions.

Extremum Seeking under Light Turbulence

The simulation results for a formation flight subjected to both a slowly-varying static wind and light turbulence is shown in Figure 6.3. The wind disturbance is shown in Figure6.3a, and is the superposition of the moderate static wind profile calculated for the specific flight plan and light turbulence generated with the von Karman turbulence model. The geometric and effective lateral and vertical separations of the follower aircraft are shown in Figure 6.3b, the control surface deflections are shown in Figure 6.3c, and the forward and differential thrusts are shown in Figure 6.3d using two separate y-axes.

The simulation results show that the extremum-seeking controller successfully controls the follower aircraft to follow the moving constrained extremum even in the presence of light turbulence. (The effective lateral separation is regulated to zero, while the geometric lateral separation follows the same profile as the static wind disturbance. Both the geometric and effective vertical separations are controlled to zero, as there is minimal static wind disturbance in the vertical direction.) The follower aircraft therefore retains most of the wake-induced benefit, which is observed as a significant reduction in the forward thrust required to trim the aircraft. (The thrust reduction is similar to what obtained in the simulation with only the slowly varying static wind and without turbulence.) The differential thrust saturates to counter the bulk of the wake-induced rolling moment at the constrained extremum. The rudder and aileron deflections exhibit larger amplitude variations due to the light turbulence.

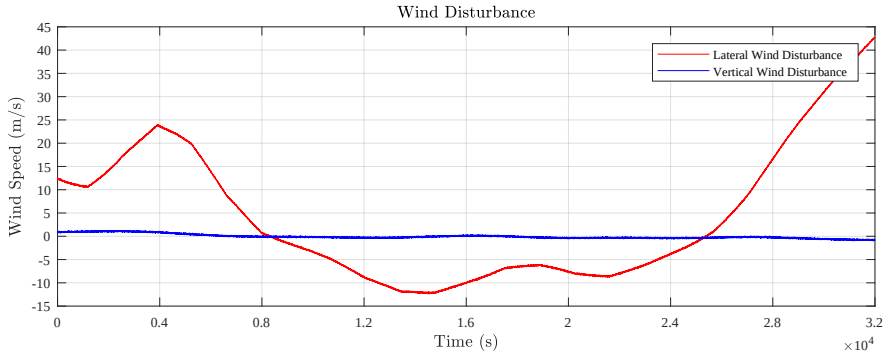

(a) Static wind.

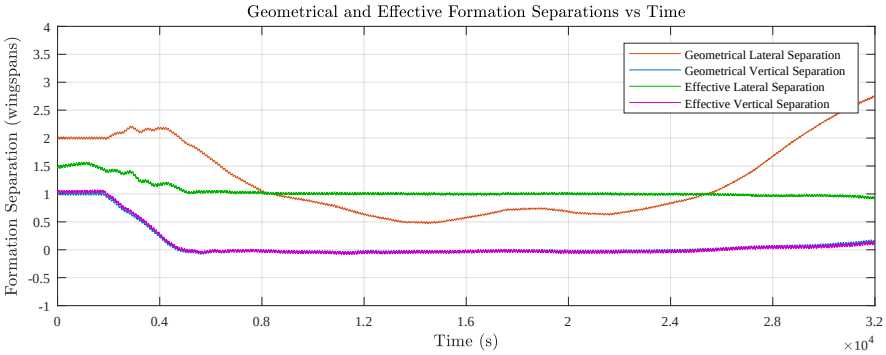

(b) Geometrical and effective formation separations.

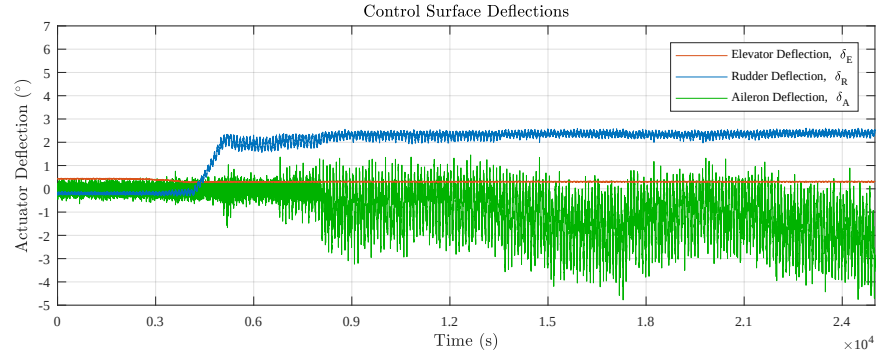

(c) Control surface deflections.

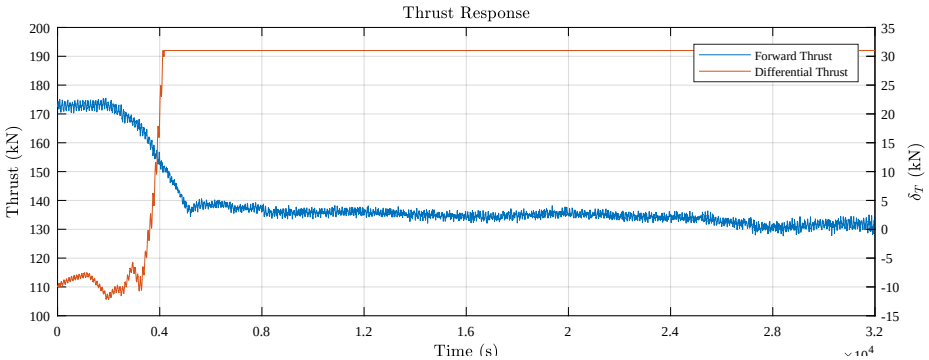

(d) Thrust response.

Figure 6.3: Simulation results for the flight from CPT to DXB under moderate static wind and light turbulence.

Extremum Seeking under Moderate Turbulence

The simulation results for a formation flight subjected to both a slowly-varying static wind and moderate turbulence is shown in Figure 6.4. The wind disturbances are shown in Figure 6.4a, and the geometric and effective lateral and vertical separations of the follower aircraft are shown in Figure 6.4b. The random component of the wind speed exhibits a much greater variance in moderate turbulence than was seen in light turbulence, and therefore induces larger variations in the lateral and vertical formation separations.

The simulation results show that, although the follower aircraft does not become unstable, the extremum-seeking controller is not able to locate or track the constrained extremum in moderate turbulence. For the extremum-seeking controller to function properly, it must be able to detect the dither signal frequency in the objective function output. The high level of noise introduced by moderate turbulence distorts the pitch angle of the follower by amplitudes that are greater than the dither amplitude, and the dither signal frequency thus 'disappears' in the process noise [2]. This results in the extremum-seeking controller being unable to extract the correct gradient information, and the follower thus 'drifts' around in the wake. Since it is possible for the follower aircraft to drift too deep into the wake, where it might be overwhelmed by the wake-induced rolling moment disturbance, it is recommended that the follower should disengage and exit the formation when moderate turbulence is encountered during the flight. Only once all aircraft in the formation have cleared the moderate turbulence, should the formation be re-engaged.

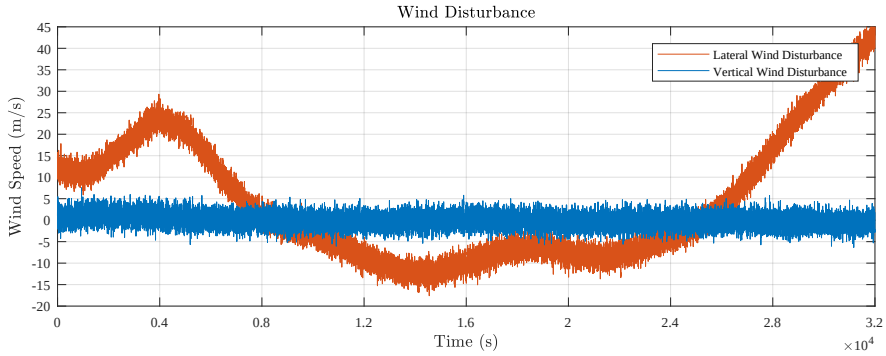

(a) Static wind.

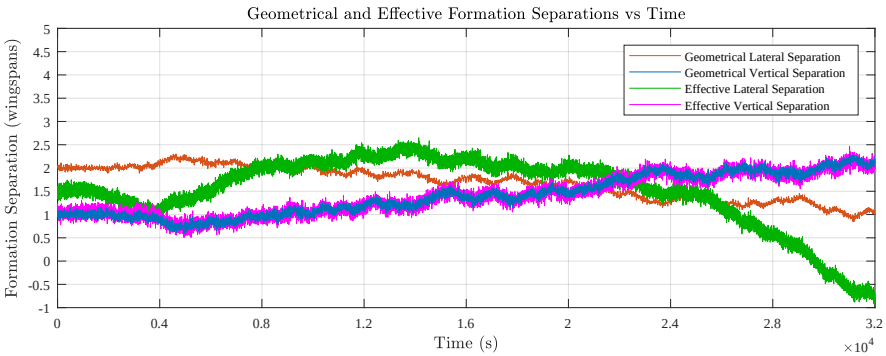

(b) Geometrical and effective formation separations.

Figure 6.4: Simulation results for the flight from CPT to DXB under moderate static wind and moderate turbulence.

Extremum-Seeking under Varying Turbulence

For the final turbulence robustness test, the formation is subjected to varying levels of turbulence during the same flight. The aim of the simulation is to demonstrate the robustness of the extremum-seeking controller when the formation transitions from light turbulence to moderate turbulence, and back again. Since the extremum-seeking controller is unable to locate and track the extremum in moderate turbulence, the formation is only subjected to a patch of moderate turbulence for a short period of time. Once the moderate turbulence has passed, the simulation continues in light turbulence.

The simulation results for a formation flight subjected to both a slowly-varying static wind and abruptly varying turbulence levels are shown in Figure 6.6, where the different turbulence levels are applied at the times shown in Figure 6.5. The simulated wind disturbance is shown in Figure 6.6a, the geometric and effective lateral and vertical separations of the follower aircraft are shown in Figure 6.6b, the control surface deflections are shown in Figure 6.6c, and the forward and differential thrusts are shown in Figure 6.6d.

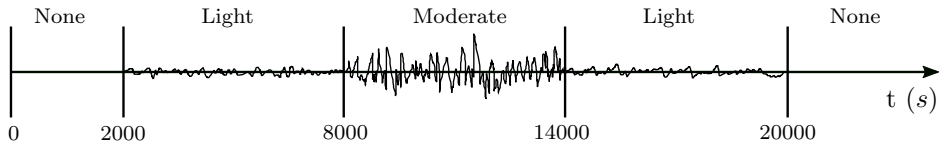

Figure 6.5: Order of applied turbulence.

The formation begins the flight in calm air with no turbulence present. At $t = 2000$ seconds, light turbulence is encountered but does not hinder the performance of the extremum-seeking controller. The follower is successfully guided to the extremum, as is evident from the effective formation separation responses settling at roughly $\eta = 1$ and $\zeta = 0$ at $t = 5000$ seconds. At $t = 8000$ seconds, the formation encounters moderate turbulence and the extremum-seeking controller is unable to effectively guide the follower to track the dynamic extremum. This results in the follower 'drifting' away from the extremum, as seen by the gradual deviation in both lateral and vertical effective separation during the patch of moderate turbulence. However, at $t = 14000$ seconds, when the moderate turbulence has passed and the formation again experiences only light turbulence, the extremum-seeking controller successfully manages to guide the follower back to the extremum. This process of the follower losing and reacquiring the extremum is clearly evident in the actuator responses as well. During the moderate turbulence patch, the variations in aileron, rudder, and forward thrust demand increase greatly, with the ailerons even saturating near the start of the patch. As the follower drifts away from the extremum, the wake-induced rolling moment slowly decreases, and less aileron and rudder demand is required for trim. Near the end of the moderate turbulence patch, the follower moves sufficiently far away to cause a reduction in differential thrust as well. Conversely, as the wake-induced drag increases, additional forward thrust is required to maintain the desired axial separation. Once the formation has passed through the moderate turbulence patch, the follower is guided back into the wake, and the forward thrust decreases again.

Two important conclusions may be drawn from the simulation results. Firstly, when passing from light to moderate turbulence, the follower does not become unstable, but rather simply drifts away from the extremum. Secondly, given that the follower does not drift too deep into the wake where it might become unstable, it is able to reacquire the extremum once the formation has passed through the moderate turbulence field and back into light turbulence.

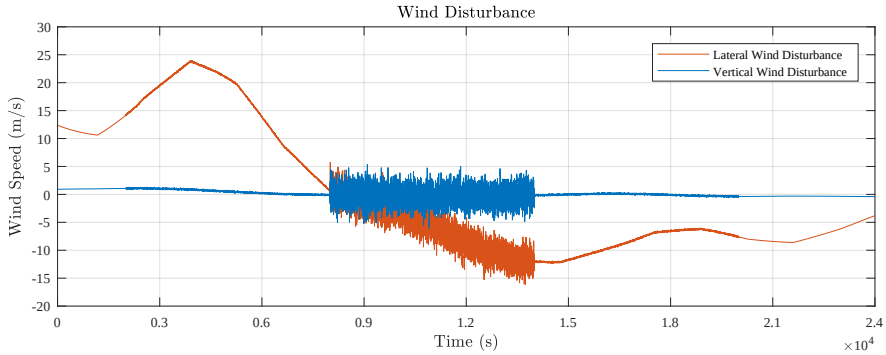

(a) Static wind.

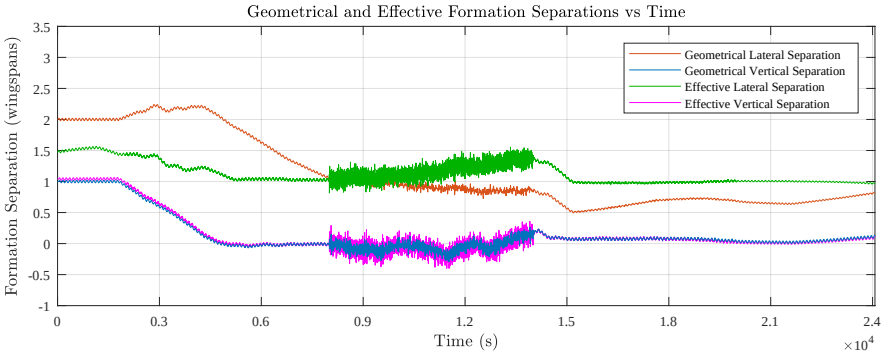

(b) Geometrical and effective formation separations.

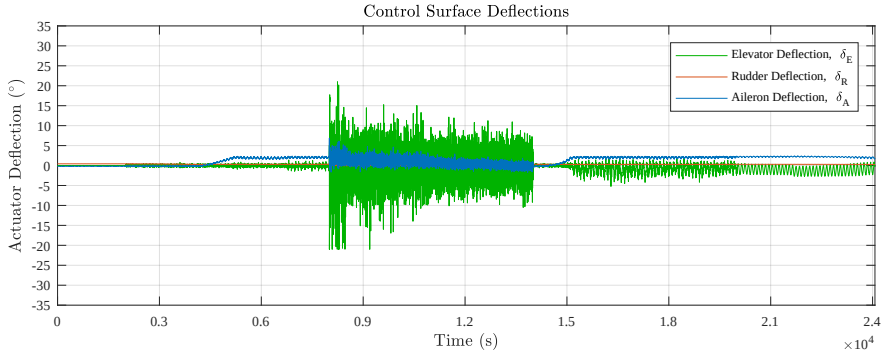

(c) Control surface deflections.

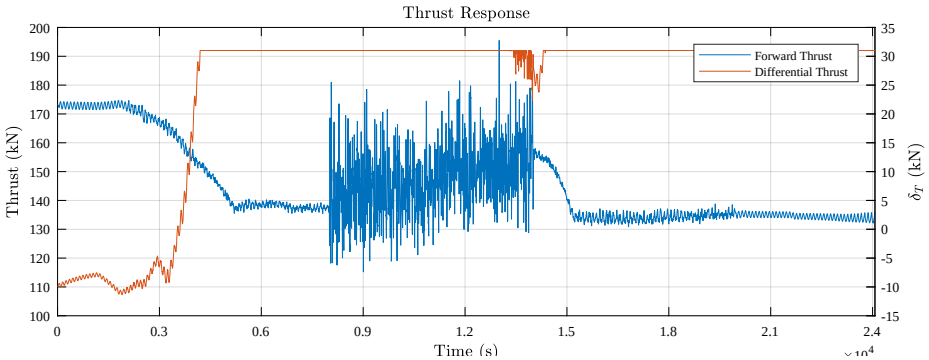

(d) Thrust response.

Figure 6.6: Simulation results for the flight from CPT to DXB under moderate static wind and varying turbulence.

6.2 Realistic Flight Scenario: DXB - MUN

The second flight scenario is illustrated in Figure 6.7. The formation is now initialized at Dubai International Airport (DXB) and flies at a constant heading towards Munich International Airport (MUN). The flight trajectory followed by the formation is shown in Figure 6.7a and the corresponding static wind that in Figure 6.7b.

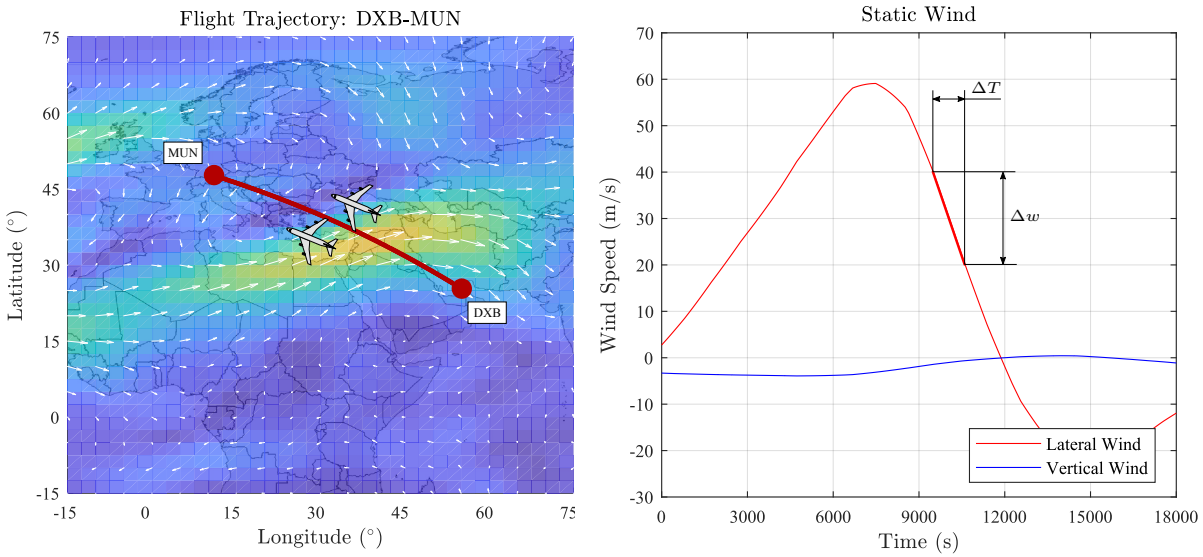

(a) Flight trajectory.

(b) Static wind.

Figure 6.7: Flight data DXB-MUN

The aim of this flight scenario is to demonstrate the robustness of the extremum-seeking controller in strong static winds. As seen in Figure 6.7a, flying from Dubai to Munich, the formation crosses through a jet stream with a maximum crosswind of roughly 60 m/s. The largest gradient in the expected static wind is again denoted by the thick red line in Figure 6.7b, and may be calculated as follows,

$$\dot{v}_{sw} = \frac{\Delta v_{sw}}{\Delta T} \approx -0.008\, m/s^2 \tag{6.3}$$

where Δv_{sw} is the difference in wind magnitude over the time ΔT. Next, the maximum expected displacement rate of the extremum may be calculated as,

$$\dot{\Delta y}_{DXB-MUN} = \left| \frac{\xi b}{\overline{V}} \dot{v}_{sw} \right| \approx 0.045\ m/s \tag{6.4}$$

where ξ is the axial separation, b is the wingspans, and $\overline{V}$ is the airspeed magnitude. The approach speed, C, is then selected to be slightly larger than the maximum expected displacement rate, $\dot{\Delta y}_{DXB-MUN}$. The dither parameters are selected to be the same as those that were used for the flight from CPT to DXB. The selected parameters and approach rate are summarised as follows:

- $C = 0.055\ ms^{-1}$ $(C > \dot{\Delta y}_{DXB-MUN})$
- $T_D = 100s$

- $a_D = 0.02b$

The simulation results are shown in Figure 6.8. The static wind is shown in Figure 6.8a, the geometrical and effective formation separations in Figure 6.8b, the control surface deflections in Figure 6.8c, and finally, the thrust response in Figure 6.8d. The follower is initialised below the extremum at a geometrical lateral separation of $\eta = 2$ and a geometric vertical separation of $\zeta = 1$.

During the first 7000 seconds of the simulation, the static wind is accelerating in the positive direction, which constantly shifts the extremum closer to the follower aircraft. Before the extremum-seeking is activated, the lateral effective separation is seen to decrease as the wake shifts closer. At $t = 2000$ seconds, the extremum-seeking controller is activated, and successfully guides the follower to the extremum. As the extremum moves in the positive direction, the follower slightly lags to the inside, effectively flying deeper in the wake. This is evident in the effective lateral separation being slightly smaller than $\eta = 1$. The oscillations in the aileron and rudder deflections are thus quite large, since the wake-induced rolling moment is larger deeper in the wake. At approximately $t = 7500$ seconds, the magnitude of the static wind begins to decrease, which results in the extremum being shifted in the negative direction and away from the follower. The follower now lags the extremum on the outside, which is evident from the effective lateral separation being slightly larger than $\eta = 1$. The forward thrust demand slightly increases as the follower experiences a smaller wake-induced drag benefit further from the extremum. Since the wake-induced rolling moment decreases, the aileron demand also decreases.

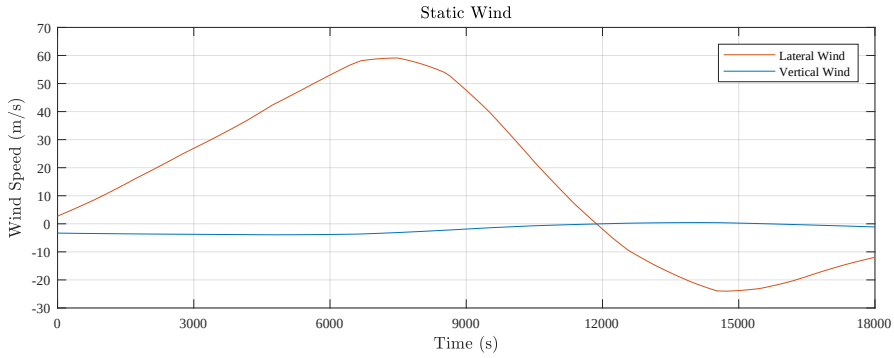

(a) Static wind.

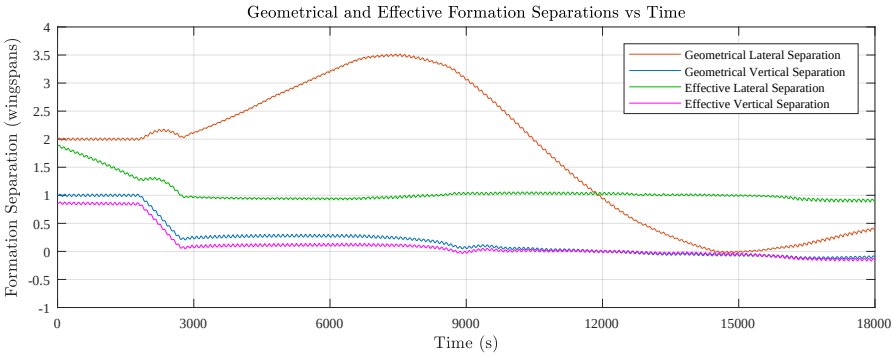

(b) Geometrical and effective formation separations.

Figure 6.8: Simulation results for the flight from DXB to MUN under moderate static wind and light turbulence.

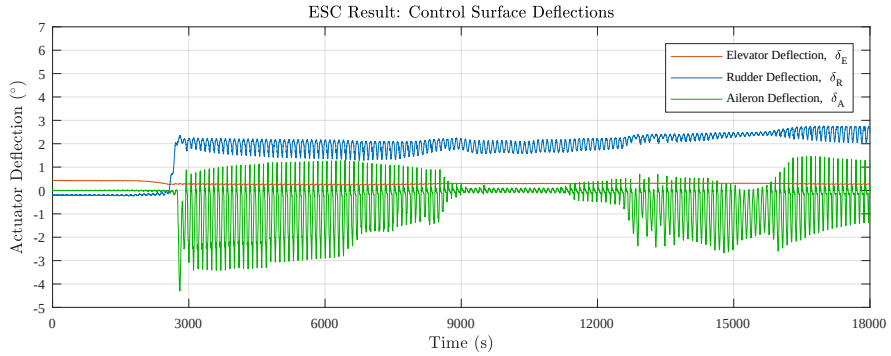

(c) Control surface deflections.

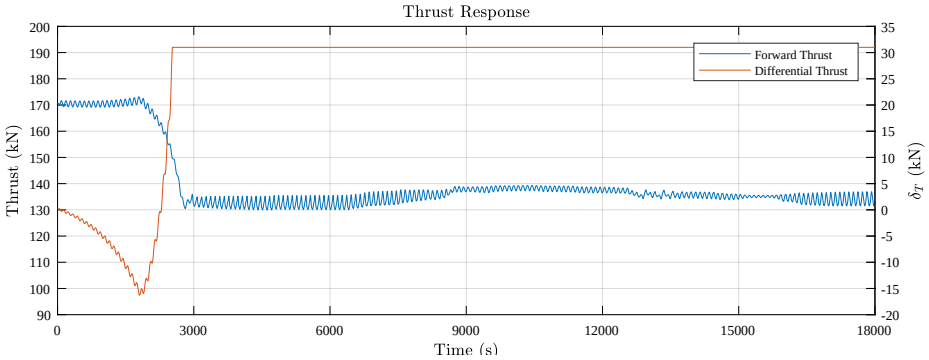

(d) Thrust response.

Figure 6.8: Simulation results for the flight from DXB to CPT under moderate static wind and light turbulence (cont.).

These simulation results demonstrate that, by selecting appropriate controller and dither parameters, the extremum-seeking controller is able to successfully locate and track a dynamic extremum displaced by strong, quickly varying static winds. However, it is still possible that in some cases the expected displacement rate of the vortex may exceed the maximum approach rate of the aircraft. In these cases, it is recommended that the follower aircraft should disengage from the formation and re-engage when the displacement rate of the vortex is lower than the maximum approach rate again.

6.3 Robustness in the Presence of Sensor Noise

In this section, the robustness of the extremum-seeking controller to sensor noise in the pitch angle measurements is verified and evaluated in simulation. The follower aircraft relies on its own pitch angle measurements to determine the wake gradient and also to decide when to switch between states in the ESC state machine. It is therefore important to verify the correct operation of the extremum-seeking controller in the presence of realistic sensor noise.

Published sensor noise figures for a Boeing 747 were unavailable for this study, and representative noise figures were therefore obtained from a previous study performed by Malan [54]. Malan obtained datasheets that specify the sensor ranges and sensor resolutions of the air data sensors and the inertial sensors typically used on a commercial airliner, and postulated the sensor noise figures based on the sensor resolutions. For this study, only the pitch angle measurement noise is required, and the relevant noise figure postulated by Malan was therefore used. The pitch angle sensor noise is therefore modelled as zero mean,

band-limited Gaussian noise with $3\sigma = 0.067°$.

The simulation results for a formation flight from Cape Town to Dubai in light turbulence, and with representative sensor noise added to the pitch angle measurement, are shown in 6.9. The geometric and effective lateral and vertical separations of the follower aircraft are shown in Figure 6.9a, and the follower pitch angle measurements is shown in Figure 6.9b. From the results it can be seen that the presence of sensor noise on the pitch angle measurement does not adversely affect the controller performance, and the formation separation responses are similar to those obtained when simulating without sensor noise. The extremum-seeking controller therefore has no trouble locating and tracking the extremum in the presence of both light turbulence and pitch angle sensor noise.

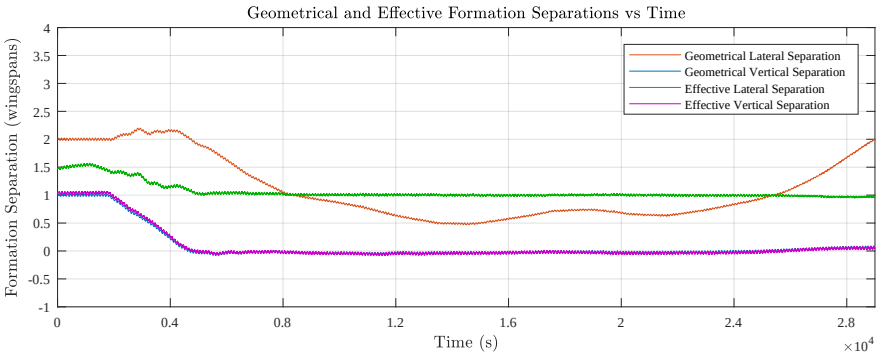

(a) Geometrical and effective formation separations.

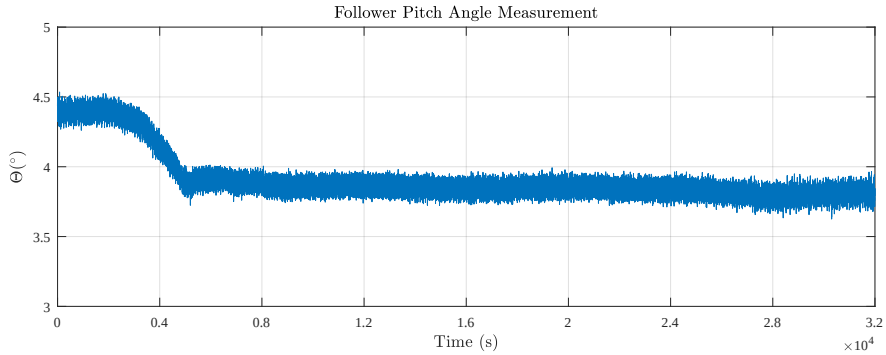

(b) Follower pitch angle measurement.

Figure 6.9: Simulation results for the flight from CPT to DXB under moderate static wind and light turbulence.

6.4 Summary

In this chapter, the robustness of the extremum-seeking controller in presence of random wind disturbances, such as turbulence and gusts, and in the presence of realistic sensor noise was analysed. The robustness of the extremum-seeking controller was verified and evaluated using simulation scenarios where the formation is subjected to typical wind disturbances encountered in a real flight scenario. The results were presented in the form of two realistic flight scenarios. The first scenario presented the results for a simulation where the formation is subjected to moderate static wind and various levels of turbulence. It was shown that the extremum-seeking controller is able to locate and track the constrained extremum in the presence of moderate static winds and light turbulence. During moderate turbulence, the

extremum-seeking controller is not able to track the constrained extremum, and the follower aircraft drifts around in the wake. However, if the formation clears the moderate turbulence and transitions into light turbulence, the extremum-seeking controller is able to locate and the constrained extremum once again. In the second scenario, the static wind level was increased, which required changes to the extremum-seeking approach rate to enable successful tracking of the constrained extremum. Finally, the robustness of the extremum-seeking controller was analysed in the presence of pitch angle sensor noise. It was shown that typical sensor noise levels on the pitch angle measurement of the follower aircraft do not adversely affect the performance of the controller.

Chapter 7

Conclusions and Recommendations

This chapter provides the final conclusions on the implementation of an extremum-seeking controller as a means of increasing fuel efficiency during formation flight of commercial airliners. An overview of the achieved research objectives is given, along with a several recommendations and possible future work.

7.1 Summary

This thesis presented the design, implementation, and verification of a constrained extremum-seeking controller for the formation flight of passenger airliners that controls the follower aircraft to locate and track the constrained optimal location in the leader aircraft's wake, to minimise the follower aircraft's fuel consumption while maintaining a minimum safe separation distance from the leader aircraft's trailing vortex. A literature study was performed on aircraft dynamics and modelling, and on the conventional fly-by-wire flight control architectures used on modern commercial airliners. A Boeing 747 aircraft model was created using a six-degrees-of-freedom equations of motion model, and a simulation model of the aircraft dynamics was developed in Matlab Simulink. Conventional fly-by-wire flight controllers were designed using the linearised aircraft model, and were verified in simulation using the full non-linear simulation model. Once the isolated aircraft model had been implemented, a formation flight model was developed that includes the aerodynamic effects caused by a leading aircraft's wake. The existing conventional flight control system was modified to include formation guidance controllers that control the axial, lateral, and vertical separation between the leader and the follower aircraft, as well as a complementary filter system developed by Van Wyk [2]. The extended formation flight controllers were verified in a two-aircraft formation flight simulation.

Next, a literature review was performed on extremum seeking and the application thereof to formation flight. A new extremum-seeking controller was proposed and the different components of the system were designed in detail. A novel constrained objective function and extremum-seeking state machine were proposed that prevent the extremum-seeking controller from guiding the follower aircraft too close to the vortex core. The states and the state transition boundaries of the state machine were defined as functions of the objective function, which allow them to move around with the displaced trailing vortex, instead of remaining static relative to the leader aircraft. This enables the extremum-seeking controller to track a constrained extremum for a dynamic trailing vortex, and not just for a static trailing vortex. Simulation experiments were performed to investigate the effects of varying the extremum-seeking controller parameters on the seeking performance, and based on the results a systematic procedure for selecting the parameters were proposed. It was shown that by

approaching the constrained extremum at a constant approach rate, rather than the classical proportional approach rate, the effect of the non-linear wake on the seeking performance may be mitigated. The extremum-seeking controller was verified in simulation on the Boeing 747 formation flight model, in which the formation was subjected to realistic atmospheric disturbances and sensor noise. The simulation results show that the extremum-seeking controller is able to successfully guide the follower to the constrained extremum, even in the presence of varying static wind and light turbulence, and that thrust reductions of up to 25% may be achieved.

The following sections provide more detailed summaries of the design, implementation, and verification of the constrained extremum-seeking controller.

7.1.1 Design of the Extremum-Seeking Controller

The design of the extremum-seeking controller was presented, and each of the following controller components were discussed in detail: (1) the dither signals used to induce circular aircraft motions, (2) the objective function to be optimised by the controller, (3) the freestream pitch angle model used to obtain the objective function, (4) the phase synchronization and demodulation for gradient estimation, and (5), the logic controller that governs the decision making process of the extremum-seeking controller.

Firstly, it was decided to separate the lateral and vertical dither motions by phase, since separation by frequency requires very accurate filtering. The dither signal commands required correction in amplitude and phase, since the dynamics of the aircraft induce attenuation and phase lag from dither commands to motion outputs. The phase lag was identified through the cross-correlation of each dither input and its resulting aircraft motion respectively, and was corrected with simple phase shifts of the commands.

Next, the wake-induced pitch angle was discussed as an objective function for the controller. Ideally, lift or drag would be used as an objective since it corresponds directly to the wake benefit. However, both characteristics are difficult to measure. The wake-induced pitch angle is also a function of formation separation, with a minimum location corresponding to that of maximum reduction in drag. Since pitch angle is simple to measure without the need of additional sensors, the wake-induced pitch angle was selected as the extremum-seeking objective. In order to only allow flight in the acceptable outer region, the objective function was constrained with a minimum allowable pitch angle, which results in the extremum being a contour rather than a point. Anywhere along the constrained extremum contour the follower aircraft would experience the same reduction in drag, but not the same wake-induced rolling moment. The rolling moment was, however, found to be acceptable for most of the contour.

Thirdly, the design and validation of the freestream pitch angle model was presented. The measured pitch angle of the follower comprises two components: changes in pitch angle induced by the wake, and variations due to general aircraft motion and dithering. This 'freestream' pitch angle was calculated using a simple linear transfer function, and subtracted from the measured pitch angle to produce the wake-induced pitch angle. The model was found to be representative of the pitch angle dynamics of the full non-linear aircraft model. Additionally, it was found that when dithering below the extremum, the wake aids the transient dynamics of the follower aircraft, as opposed to the countering characteristic observed when dithering above. A follower aircraft dithering below the extremum will thus exhibit a higher effective bandwidth in its vertical motion.

Next, the phase synchronisation, demodulation, and filtering step was presented. For accurate demodulation, the effect of the aircraft dynamics must be removed and the demodulating dither signal and resulting aircraft motions are required to be of equal magnitude and phase. A process similar to the dither signal correction was followed to modify the demod-

ulating dither signal. A second order Butterworth band-pass filter was designed to remove any DC component in the wake-induced pitch angle before demodulation, while two low-pass filters were designed to extract the gradient information after demodulation.

Finally, an extremum-seeking state machine was designed to govern the approach of the follower to the near-extremum. Extremum-seeking control is typically used for the seeking of global extrema, and has not been applied to constrained objectives. The ESC states and the ESC state transition boundaries were defined as functions of the wake-induced pitch angle deviation, and not as a function of the geometric separation between the leader aircraft and the follower aircraft. This allows the regions of operation and the switching boundaries to move around with the displaced trailing vortex, instead of remaining static relative to the leader aircraft. This also enables the extremum-seeking control to track a constrained extremum for a dynamic trailing vortex, and not just for a static trailing vortex In order for the follower to maintain a formation separation at the near-extremum, the logic controller inverses the sign of the extremum-seeking controller gains whenever the wake-induced follower pitch angle increases or decreases beyond the desired level corresponding to the constrained extremum.

7.1.2 Basic Simulation and Analysis of the Extremum-Seeking Controller

The extremum-seeking controller was integrated into a Boeing 747 right echelon formation flight simulation model in Matlab Simulink. The aircraft were modelled using data provided by [41], and followed the modelling procedure presented by [38]. A wake-interaction model developed at the University of Cape Town was used to simulate the aerodynamic forces and moments experienced by a follower Boeing 747 due to flying in the wake of a leader. Conventional fly-by-wire controllers were designed according to the general architecture used by the Airbus company, and the follower aircraft was augmented with specially designed extended formation flight controllers to allow for station-keeping within the leader wake. The extended formation flight controllers stem from the work done by previous internal studies. Basic simulations were performed during which the extremum-seeking controller was tasked with locating a static near-extremum. Two approach methods were investigated: the classic proportional approach method where the follower is guided towards the extremum at a rate proportional to the objective gradient, and a novel, constant approach rate method, during which the gradient estimates are only used to determine the direction of movement in the wake. Both methods successfully guided and regulated the follower at the static near-extremum, following the objective gradient with sufficient accuracy. It was also found that seeking from below requires less differential thrust demand due to the asymmetric nature of the wake-induced yawing moment around the zero vertical separation axis.

An investigation was conducted into the effect of the various controller parameters on seeking performance. For the classic proportional approach rate method, it was found that convergence speed and domain of attraction significantly depend on the selected dither amplitude and control gains. Larger values result in faster convergence while sufficiently small values ensure a large domain of attraction. For the constant approach rate method, the approach rate parameter C has the most significant effect on performance. Both the speed of convergence and domain of attraction are directly dependant on it, while being less affected by the choice of dither amplitude. For both methods, the selected dither period indirectly influences the speed of convergence, since dithering faster increases the information gained per time step allowing for larger control gains and approach rates. From this investigation it was found that the novel constant approach rate method holds two distinct advantages over the classical method. Firstly, approaching at a constant rate reduces the non-linear effects that the wake has on extremum-seeking control, and secondly, the selection of controller

parameters are much simpler because of the singular dependence on the approach rate.

7.1.3 Tracking a Dynamic Vortex in Realistic Atmospheric Disturbances

For the rest of the study, focus shifted to addressing the more practical purpose of extremum-seeking control: tracking a dynamic extremum during realistic flight conditions. The effect of static wind on the extremum position was presented, illustrating the need for tracking. A simple procedure was suggested for the selection of the extremum-seeking controller parameters, using the constant approach rate method and taking into account the expected static wind. The approach rate C must be chosen sufficiently fast as to allow the follower to keep up with the moving extremum. Failing to do so will either lead to reduced wake benefit or flight dangerously deep in the wake. The process of seeking a dynamic extremum was divided into two parts: (1) seeking an extremum that is displaced further from the follower aircraft, effectively moving the follower out of the wake, and (2), an extremum that is displaced closer, resulting in the follower moving deeper into the wake. For the former case, the extremum-seeking controller enabled the follower to successfully track the dynamic constrained extremum. A constant mean reduction in thrust was achieved and the follower remained close to the desired location in the wake. For the latter case, however, the state machine of the extremum-seeking controller required an additional state to enable successful tracking of the dynamic constrained extremum. It was found that the constant approach rate method exhibits typical Type 1 control system behaviour, since a constant steady state error exists when tracking what is essentially ramp references. Faster approach rates reduce the tracking error.

During the final phase of the study, the formation was subjected to realistic flight conditions with the aim of analysing robustness. Two practical scenarios with different flight conditions were simulated. It was found that, as long as the approach rate is selected sufficiently fast, the extremum-seeking controller will enable the follower to track the dynamic leader wake even when exposed to quickly varying static winds. During light turbulence, extremum-seeking performance was similar to the performance achieved during non-turbulent conditions. The follower successfully managed to locate and track the dynamic extremum during the entire simulated flight. During moderate turbulence, however, the extremum-seeking controller was unable to track the extremum, which results in the follower drifting around in the wake. The high level of noise introduced by moderate turbulence distorts the pitch angle of the follower by amplitudes that are greater than the dither amplitude, and the dither signal frequency disappears in the process noise. Since the follower might drift into dangerous regions of the wake, it is strongly suggested to refrain from using extremum-seeking control during moderate turbulence. However, if the follower moves from moderate to light turbulence before becoming unstable, the extremum-seeking controller is able to 'reacquire' the near-extremum. Finally, since the follower pitch angle plays such a crucial role in both the extremum-seeking logic and objective function, seeking robustness in the presence of realistic pitch angle measurement noise was investigated. It was found that the controller still effectively extracted the correct gradient information and successfully guided the follower to the near-extremum. It is thus concluded that the designed extremum-seeking controller is fairly robust to measurement noise, static winds and light turbulence.

In conclusion, all research objectives were successfully addressed. An extremum-seeking controller was designed capable of locating and tracking a dynamic near-extremum in a realistic formation flight scenario. A novel constant approach method was presented that provides advantages over the classic proportional method. The effects of controller parameters on seeking performance were investigated, and a general procedure for selecting parameters was suggested. The robustness of the controller was analysed by subjecting the formation to

realistic atmospheric disturbances and sensor noise.

7.2 Limitations and Recommendations

This section outlines some of the important simplifications and limitations of the current study.

- Although the engine distribution was modelled with high fidelity, a simple first order model was used to simulate the engine dynamics. This simplification was deemed sufficient since the aircraft in formation remain close to their specified trim conditions during flight. The higher order engine model developed by van Wyk [2] should be included for a more complete model. In addition, this study relates fuel consumption to thrust demand, and although there is a direct correlation, the model developed by van Wyk more accurately estimates fuel flow. Furthermore, the aileron, rudder, and elevator actuators were modelled with only rate limits and saturation. The accuracy of simulation results may be improved by uses higher fidelity actuator models.

- Formation flight was limited to the outer region due to the danger of approaching the more beneficial inner region [5]. Additionally, the assumptions made by Bizinos, such as uniform wing load distribution, significantly amplified results near the wingtip-vortices, producing inaccurate results [10]. As stated in the work of van Wyk, the development of a more representative wake model remains the most significant priority for the future of formation flight research, which may lead to more accurate simulation analyses.

- The extremum-seeking dither signals were limited to separation by phase, due to the lack of accurate filters. Designing specialised filters, or utilizing a Kalman filter, will allow for accurate separation by frequency. Since frequency components can more easily be identified in the objective output than phased separated components, aircraft dynamics will have a less significant effect on controller performance and choice of dither period. If faster dither periods can be selected, without fear of the effect of phase lag, the speed of convergence might be increased.

- The static wind model developed in this study linearly interpolates between discrete points provided by the global wind dataset. This results in the static wind consisting of linear ramp segments, which does not model the non-linear transients expected between points. It suggested to test alternative interpolate methods, to better represent realistic static winds.

7.3 Future Work

Through this study, several contributions were made to further the advancement of optimal formation flight research. There are, however, some interesting areas of study that have not been addressed, which could be explored in future work. All of the mentioned topics have been considered in this thesis, but have been disregarded due to limitations on time and scope.

- **Application of Extremum-seeking Control to Multi-aircraft Formations**

  Although this study has only addressed a formation of two aircraft, the concept of extremum-seeking may easily be applied to larger formations of multiple aircraft. Utilizing the circular wake displacement of a dithering follower aircraft, a second follower

downstream might be able to perform extremum-seeking without physically dithering. Since the wake is already moving relative to the second follower, oscillations in pitch angle will occur purely due to the change in wake. The extremum-seeking controller could use this information to extract the gradient of the objective and guide the second follower in the wake of the first. Additionally, the application of extremum-seeking control to different formation topologies might be investigated.

- **Improvement of Gradient Estimation through Kalman Filtering**

  Several studies have investigated the is use of a Kalman filter during the gradient estimation step instead of the classic demodulation [32, 23, 7]. It is argued that by having more accurate gradient estimation, the rate of convergence may be increased, and that the controller should be more robust to system noise. The tracking performance for an extremum-seeking controller utilising the classic wake estimation method, as well as the suggested Kalman filter scheme, should be investigated and compared for the realistic flight scenarios as presented in this thesis.

- **Strategies for Safe Formation Engagement and Disengagement**

  Another interesting and important topic for future work is that of safe formation engagement and disengagement strategies. Given certain constraints, i.e. maximum control surface deflections or minimum formation separations, non-linear programming methods may be used to find optimal solutions for engagement and disengagement. Scenarios that require immediate disengagement, such as engine failure, might have different constraints and specifications.

Bibliography

[1] S. A. Ning, "Aircraft drag reduction through extended formation flight", Stanford University, August 2011.

[2] F. van Wyk, "Optimal control for minimum thrust demand in extended formation flight", Masters Thesis, Department of Electric & Electronic Engineering. Stellenbosch University, 2015.

[3] R. J. Ray, B. R. Cobleigh, M. J. Vachon, and C. John, "Flight test techniques used to evaluate performance benefits during formation flight", tech. rep., NASA Dryden Flight Research Centre, Edwards, California, August 2002.

[4] E. F. Trollip, "Ride comfort in commercial aircraft during formation flight using conventional flight control", Masters Thesis, Department of Electric & Electronic Engineering. Stellenbosch University, 2015.

[5] D. Büchner, "Automatic control of commercial airliners in formation flight", Masters Thesis, Department of Electric & Electronic Engineering. Stellenbosch University, 2015.

[6] P. Binetti, M. Krstić, K. B. Ariyur, and F. Bernelli, "Formation flight optimization using extremum seeking feedback", *Journal of Guidance, Control, and Dynamics*, vol. 26, no. 1, pp. 132–142, 2003.

[7] M. Brodecki, K. Subbarao, and Q.-P. Chu, "Formation flight control system for in-flight sweet spot estimation", *51st AIAA Aerospace Sciences Meeting including the New Horizons Forum and Aerospace Exposition*, pp. 15 458–15 472, January 2013.

[8] K. B. Ariyur and M. Krstić, *Real-Time Optimization by Extremum-Seeking Control*. John Wiley & Sons, Inc., 2003.

[9] Y Tan, W. Moase, C. Manzie, D. Nešić, and I. Mareels, "Extremum seeking from 1922 to 2010", in *Proc. of the 29th Chinese Control Conference*, (Beijing, China), July 2010, pp. 14–26.

[10] N. Bizinos, "Passenger comfort during formation flight within atmospheric turbulence", Masters Thesis, Department of Mechanical Engineering, University of Cape Town, 2012.

[11] S. A. Ning, T. C. Flanzer, and I. M. Kroo, "Aerodynamics performance of extended formation flight", in *48th AIAA Aerospace Sciences Meeting Including the New Horzions Forum and Aerospace Exposition*, (Orlando, Florida), 2010.

[12] C. Breitsamter, "Wake vortex characteristics of transport aircraft", *Progress in Aerospace Sciences*, vol. 47, pp. 89–134, 2011.

[13] Z. Bangash, R. Sanchez, and A. Ahmed, "Aerodynamics of formation flight", *Journal of Aircraft*, vol. 43, pp. 907–912, July–August 2006.

[14] D. Hummel, "The use of aircraft wakes to achieve power reduction in formation flight", in *Proceedings of the AGARD Fluid Dynamics Panel Symposium*, 1996, 1777–1794.

[15] W. Okolo, A. Dogan, and W. Blake, "Determination of sweet spot for trailing aircraft in formation flight", in *Proc. of AIAA Atmospheric Flight Mechanics Conference*, (Portland, Oregan), August 2011.

[16] M. S. Hemati, J. D. Eldredge, and J. L. Speyer, "Wake sensing for aircraft in formation flight", *Journal of Guidance, Control, and Dynamics*, vol. 37, no. 2, pp. 513–524, March–April 2014.

[17] S. Bradley, E. Mursch-Radlgruber, and S. von Hünerbein, "Sodar measurements of wing vortex strength and position", *Journal of Atmospheric and Oceanic Technology*, vol. 24, no. 2, pp. 141–155, February 2007.

[18] F. Barbaresco, P. Brovelli, P. Currier, O. Garrouste, P. Klein M. Juge, Y. Ricci, and J. Schneider, "Radar sensors for wind and wake vortex monitoring on airport", *7th European Conference on Radar in meteorology and Hydrology*, May 2012.

[19] R. J. Rodenhiser, W. W. Durgin, and H. Johari, "Ultrasonic method for aircraft wake vortex detection", *Journal of Aircraft*, vol. 44, no. 3, pp. 726–732, May–June 2007.

[20] D. Hinton, J. Charnock, D. Bagwell, and D. Grisby, "Nasa aircraft vortex spacing system development status", *AIAA Paper 99-0753*, 1999.

[21] D. Fischenberg, "A method to validate wake vortex encounter models from flight test data", *27th International Congress of the Aeronautical Sciences*, 2010.

[22] D. Vicroy, P. M. Vijgen, H. M. Reimer, J. L. Gallegos, and P. R. Spalart, "Recent nasa wake-vortex flight tests, flow-physics database and wake-development analysis", *AIAA Paper 1998-5592*, 1998.

[23] D. F. Chichka, J. L. Speyer, and C. G. Park, "Peak-seeking control with application to formation flight", December 1999, pp. 2463–2470.

[24] S.-J. Liu and M. Krstić, *Stochastic Averaging and Stochastic Extremum Seeking*. Springer-Verlag London, 2012, pp. 11–20.

[25] H.-H. Wang and M. Krstić, "Extremum seeking for limit cycle minimization", *IEEE Transactions on Automatic Control*, vol. 45, no. 12, pp. 2432–2437, December 2000.

[26] H.-H. Wang and M. Krstić, "Stability of extremum seeking feedback for general nonlinear dynamic systems", *Automatica*, vol. 36, pp. 595–601, 2000.

[27] B. Calli, W. Caarls, P. Jonker, and M. Wisse, "Comparison of extremum seeking control algorithms for robotic applications", *International Conference on Intelligent Robots and Systems*, 1998.

[28] P. Binetti, M. Krstić, K. B. Ariyur, and F. Bernelli, "Control of formation flight via extremum seeking", in *Proceedings of the American Control Conference*, May 2002, pp. 2848–2853.

[29] Y Tan, D. Nešić, I. Mareels, and A. Astolfi, "On global extremum seeking in the presence of local extrema", *Automatica*, vol. 45, pp. 245–251, 2009.

[30] Y Tan, D. Nešić, and I. Mareels, "On non-local stability properties of extremum seeking control", *Automatica*, vol. 42, pp. 889–903, 2006.

[31] K. B. Ariyur and M. Krstić, "Analysis and design of multivariable extremum seeking", in *Proceedings of the American Control Conference*, (Anchorage), May 2002, pp. 2903–2908.

[32] G. Gelbert, J. P. Moeck, C. O. Paschereit, and R. King, "Advanced algorithms for gradient estimation in one- and two-parameter extremum seeking controllers", *Journal of Process Control*, vol. 22, pp. 700–709, 2012.

[33] D. Hummel, "Aerodynamic aspects of formation flight in birds", *J. theor. Biol.*, vol. 104, pp. 321–347, 1983.

[34] D. Hummel, "Formation flight as an energy-saving mechanism", *Israel Journal of Zoology*, vol. 41, no. 3, pp. 261–278, 1995.

[35] D. F. Chichka, J. L. Speyer, C. Fanti, and C. G. Park, "Peak-seeking control for drag reduction in formation flight", *Journal of Guidance, Control, and Dynamics*, vol. 29, no. 5, pp. 1221–1230, September-October 2006.

[36] F. Xie, Z. Zhang, R. Fierro, and M. Motter, "Autopilot-based nonlinear uav formation controller with extremum-seeking", in *Proceedings of the 44th IEEE Conference on Decision & Control*, December 2005, 4933–4983.

[37] J. Engelbrecht and I. Peddle, "Advanced automation 833 - introductory course to aircraft dynamics", University of Stellenbosch, April 2016.

[38] I. Peddle, "Autonomous flight of a model aircraft", University of Stellenbosch, April 2005.

[39] I. Peddle, "Acceleration based manoeuvre flight control system for unmanned aerial vehicles", University of Stellenbosch, April 2008.

[40] J. H. Blakelock, *Automatic Control of Aircraft and Missiles*. John Wiley & Sons, Inc., 1991.

[41] R. K. Heffley and W. F. Jewell, "Aircraft handling qualities data", NASA, December 1972.

[42] C. R. Hanke and D. R. Nordwall, "The simulation of a jumbo jet transport aircraft volume ii: Modeling data", The Boeing Company, September 1970.

[43] C. E. Hanson, J. Ryan, M. J. Allen, and S. R. Jacobson, "An overview of flight test results for a formation flight autopilot", tech. rep., NASA Dryden Flight Research Centre, Edwards, California, August 2002.

[44] E. Kalnay, M. Kanamitsu, R. Kistler, W. Collins, D. Deaven, L. Gandin, M. Iredell, S. Saha, G. White, and J. Woollen, "The ncep/ncar 40-year reanalysis project", *Bulletin of the American meteorological Society*, vol. 77, no. 3, 1996.

[45] N. W. Service. (2017). Turbulence, [Online]. Available: `www.weather.gov`.

[46] F Hoblit, *Gust Loads on Aircraft: Concepts and Applications*. AIAA Education Series, 1988.

[47] *U.S. Military Specification MIL-F-8785C*. 19 December 1980.

[48] MathWorks, "Von kármán wind turbulence model (continuous)", 2017.

[49] J. Burnham, "Atmospheric gusts - a review of the results of some recent r.a.e. research", Aerodynamic Dept.,R.A.E.,Bedford, Technical Report, 1970.

[50] T. L. Coleman and R. Steiner, "Atmospheric turbulence measurements obtained from airplane operations at altitudes between 20,000 and 75,000 feet for several areas in the northern hemisphere", Langley Research Center, NASA, Technical Note, 1960.

[51] C Favre, "Fly-by-wire for commercial aircraft: The airbus experience", *International Journal of Control*, vol. 59, no. 1, pp. 139–157, 1994.

[52] B. L. Stevens and F. L. Lewis, *Aircraft Control and Simulation*. Wiley-Interscience, 1992.

[53] M. Krstić, "Performance improvement and limitations in extremum seeking control", *Systems & Control Letters*, vol. 39, pp. 313–326, 2000.

[54] P. Malan, "Upset detection for passenger airliners using classification of anemometric and inertial sensor data", Masters Thesis, Department of Electric & Electronic Engineering, Stellenbosch University, 2016.

Appendix A

Conventional Boeing 747 Aircraft Model Parameters

The following presents the modelling parameters used to model the Boeing 747 aircraft simulated in this thesis. Similar data may be found in the appendices of the theses compiled by van Wyk [2] and Trollip [4].

A.1 Actuator Model

The ailerons, rudder, and elevator responses were modelled as simple first order transients with non-linearities captured through rate limiting and saturation. Parameters typical of an Airbus A330 were used, as provided by the Airbus company, and are summarised in Table A.1.

Table A.1: Aircraft actuator characteristics.

Actuator	Time Constant (s)	Rate Limits ($^\circ/s$)	Saturation Levels ($^\circ$)
Aileron (δ_A)	0.07	40	$-21, +21$
Rudder (δ_R)	0.025	30	$-32, +32$
Elevator (δ_E)	0.07	30	$-30, +15$

A.2 Inertial and Geometric Attributes

The inertial and geometric parameters were obtained from Heffley and Jewel [41], and are listed in Table A.2.

Table A.2: Boeing 747 aircraft physical parameters.

Symbol	Unit	Value
Inertial Data		
m	kg	288770
CG	m	$\begin{bmatrix} 31.75 & 0 & 0.84 \end{bmatrix}$
$\begin{bmatrix} I_{xx} & 0 & I_{xz} \\ 0 & I_{yy} & 0 \\ I_{zx} & 0 & I_{zz} \end{bmatrix}$	kg·m^2	$\begin{bmatrix} 24675878 & 0 & -2115075 \\ 0 & 44877559 & 0 \\ -2115075 & 0 & 67384129 \end{bmatrix}$
Wing Data		
b	m	59.7
S	m^2	510.96
$\bar{c}$	m	8.32
$\mathcal{R}$	m	6.95
Tailplane Data		
l_T	m	29.6
S_T	m^2	141
z_T	m	–5.1
b_h	m	22.4
a_1	rad	pi
Tailfin Data		
l_T	m	29.6
S_T	m^2	141
z_T	m	–5.1
a_1	rad	pi

A.3 Conventional Aerodynamic Model

The conventional aerodynamic model, as obtained from Heffley and Jewel [41], is linearised about a specific trim condition. This *linearisation point* is described by Condition 9 by Heffley and Jewel, and corresponds to a clean aircraft in straight and level flight at an altitude of 40000 ft. The model parameters are listed in Table A.3 while the non-dimensional aerodynamic coefficients at the linearisation point are summarised in Table A.4. The stability and control derivatives are summarised in Table A.5.

Table A.3: Aerodynamic model variables at linearisation point, LP.

Description	Symbol	Unit	Value
Mach Number	M_{LP}	-	0.8
Angle of Attack	α_{LP}	$^\circ$	4.6
Sideslip	β_{LP}	$^\circ$	0
Angular Velocities	P_{LP}, Q_{LP}, R_{LP}	$^\circ/s$	0
Control Surfaces	$\delta_{A_{LP}}, \delta_{R_{LP}}, \delta_{E_{LP}}$	$^\circ$	0

Table A.4: Non-dimensioal aerodynamic coefficients at linearisation point, LP.

Description	Symbol	Value
Lift Coefficient	$C_{L_{LP}}$	0.66
Drag Coefficient	$C_{D_{LP}}$	0.0415
Pitching Moment Coefficient	$C_{m_{LP}}$	0

Table A.5: Aerodynamic stability and control derivatives at linearisation point, LP.

Drag Force		Lift Force		Pitching Moment	
C_{D_α}	0.425	C_{L_α}	4.92	C_{m_α}	–1.033
C_{D_M}	0.0275	$C_{L_{\dot\alpha}}$	5.91	$C_{m_{\dot\alpha}}$	–6.41
C_{D_β}	0.0287	$C_{L_{\delta_E}}$	0.367	$C_{m_{\delta_E}}$	–1.45
$C_{D_{\delta_R}}$	0.0183	C_{L_M}	0.205	C_{m_Q}	–24
-	-	C_{L_Q}	6	C_{m_M}	0.166
-	-	-	-	$C_{m_{\delta_R}}$	0.0802
-	-	-	-	C_{m_β}	–0.1146
Side Force		**Rolling Moment**		**Yawing Moment**	
C_{Y_β}	0.425	C_{l_β}	–0.277	C_{n_β}	0.195
C_{Y_P}	0	C_{l_P}	–0.334	C_{n_P}	–0.0415
C_{Y_R}	0	C_{l_R}	0.3	C_{n_R}	–0.327
$C_{Y_{\delta_R}}$	0.1157	$C_{l_{\delta_R}}$	0.007	$C_{n_{\delta_R}}$	–0.1256
$C_{Y_{\delta_A}}$	0	$C_{l_{\delta_A}}$	0.137	$C_{n_{\delta_A}}$	0.195

The full aerodynamic coefficients in the stability axis are expanded about the linearisation point, and the result is shown in Equations A.2a to A.2f. The stability and control derivatives on the right hand side of the equations are of the form,

$$C_{A_B} \equiv n\frac{\partial C_A}{\partial B} \tag{A.1}$$

where C_A is the aerodynamic coefficient affected by the state or control variable B, and n is the appropriate normalising coefficient of B. For the incidence and control deflection angles, n is equal to 1, for the pitch rate Q it is $\bar{c}/2\overline{V}$, and for the roll and yaw rates it is $b/2\overline{V}$.

$$\begin{aligned} C_{L_S} = {} & C_{L_{LP}} + C_{L_\alpha}(\alpha - \alpha_{LP}) + \frac{\bar{c}}{2\overline{V}_{LP}} C_{L_{\dot{\alpha}}}\dot{\alpha} + C_{L_M}(M - M_{LP}) \\ & + \frac{\bar{c}}{2\overline{V}_{LP}} C_{L_Q} Q + C_{L_{\delta_E}}\delta_E \end{aligned} \tag{A.2a}$$

$$C_{D_S} = C_{D_{LP}} + C_{D_\alpha}(\alpha - \alpha_{LP}) + C_{D_M}(M - M_{LP}) + C_{D_\beta}|\beta| + C_{R_{\delta_R}}\delta_R \tag{A.2b}$$

$$C_{Y_S} = C_{Y_\beta}\beta + \frac{b}{2\overline{V}_{LP}} C_{Y_P} P + \frac{b}{2\overline{V}_{LP}} C_{Y_R} R + C_{Y_{\delta_A}}\delta_A + C_{Y_{\delta_R}}\delta_R \tag{A.2c}$$

$$C_{l_S} = C_{l_\beta}\beta + \frac{b}{2\overline{V}_{LP}} C_{l_P} P + \frac{b}{2\overline{V}_{LP}} C_{l_R} R + C_{l_{\delta_A}}\delta_A + C_{l_{\delta_R}}\delta_R \tag{A.2d}$$

$$\begin{aligned} C_{m_S} = {} & C_{m_\alpha}(\alpha - \alpha_{LP}) + \frac{\bar{c}}{2\overline{V}_{LP}} C_{m_{\dot{\alpha}}}\dot{\alpha} + C_{m_M}(M - M_{LP}) + \frac{\bar{c}}{2\overline{V}_{LP}} C_{m_Q} Q \\ & + C_{m_{\delta_E}}\delta_E + C_{m_{\delta_R}}\delta_R + C_{m_\beta}\beta \end{aligned} \tag{A.2e}$$

$$C_{n_S} = C_{n_\beta}\beta + \frac{b}{2\overline{V}_{LP}} C_{n_P} P + \frac{b}{2\overline{V}_{LP}} C_{n_R} R + C_{n_{\delta_A}}\delta_A + C_{n_{\delta_R}}\delta_R \tag{A.2f}$$

where M is the Mach number defined as $\overline{V}/V_S$, and the subscript LP denotes the trim variables at the linearisation point defined by Heffley and Jewel [41]. In order to obtain the aerodynamic forces and moments in the body axis system, a rotation is performed about the Y_B axis through the angle of attack α to achieve,

$$C_X = -C_{D_S}\cos\alpha + C_{L_S}\sin\alpha \tag{A.3a}$$

$$C_Y = C_{Y_S} \tag{A.3b}$$

$$C_Z = -C_{D_S}\sin\alpha - C_{L_S}\cos\alpha \tag{A.3c}$$

$$C_l = C_{l_S}\cos\alpha - C_{n_S}\sin\alpha \tag{A.3d}$$

$$C_m = C_{m_S} \tag{A.3e}$$

$$C_n = C_{l_S}\sin\alpha + C_{n_S}\cos\alpha \tag{A.3f}$$

The aerodynamic forces and moments that act upon the aircraft in the body axis system are given by,

$$X^A = qSC_X \tag{A.4a}$$
$$Y^A = qSC_Y \tag{A.4b}$$
$$Z^A = qSC_Z \tag{A.4c}$$
$$L^A = qSbC_l \tag{A.4d}$$
$$M^A = qS\bar{c}C_m \tag{A.4e}$$
$$N^A = qSbC_n \tag{A.4f}$$

where S is the area of the wing, b is the wingspan, $\bar{c}$ is the mean aerodynamic chord, q is the dynamic pressure, and $C_{()}$ are the non-dimensional aerodynamic coefficients. The dynamic pressure q is defined as,

$$q = \frac{1}{2}\rho\overline{V}^2 \tag{A.5}$$

where ρ is the air density, and $\overline{V}$ is the airspeed magnitude.

A.4 Thrust Distribution Model Dimensions

The dimensions for the thrust distribution model are shown in Figure 3.7, while the values are summarised in Table A.6.

Table A.6: Dimension values for thrust distribution model.

Dimension	Unit	Value
$\begin{bmatrix} a_{ix} & a_{iy} & a_{iz} \end{bmatrix}$	m	$\begin{bmatrix} 27.08 & 12.07 & 2.8 \end{bmatrix}$
$\begin{bmatrix} a_{ox} & a_{oy} & a_{oz} \end{bmatrix}$	m	$\begin{bmatrix} 35.71 & 21.15 & 2.23 \end{bmatrix}$
ψ_e	°	2
θ_e	°	2.5

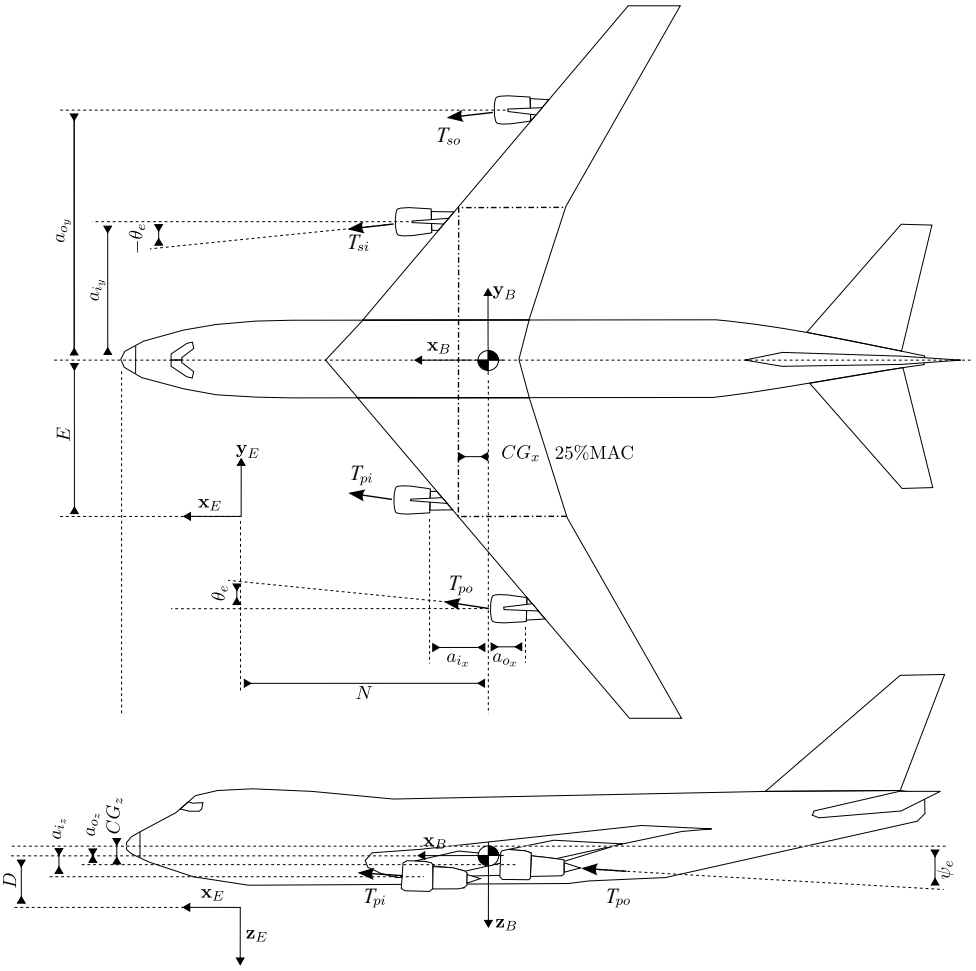

Figure A.1: Dimensions for thrust distribution model (reproduced from [2]).

Appendix B

Wake Interaction Model

The wake interaction model for the Boeing 747 aircraft was first developed by Bizinos [10] at the University of Cape Town. Under a collaboration agreement, the model was shared with the University of Stellenbosch, and was implemented in the work of Büchner [5], Trollip [4], and van Wyk [2]. The coefficients that describe the aerodynamics of the follower when flying in the wake of the leader, were modelled as the sum of the conventional aerodynamic coefficients and the purely formation induced aerodynamics. The full follower aerodynamic coefficients are given as,

$$C_{L_{S_k}} = C_{L_S} + C_{L_F} < \eta, \zeta > \tag{B.1a}$$

$$C_{D_{S_k}} = C_{D_S} + C_{D_F} < \eta, \zeta > \tag{B.1b}$$

$$C_{Y_{S_k}} = C_{Y_S} + C_{Y_F} < \eta, \zeta > \tag{B.1c}$$

$$C_{l_{S_k}} = C_{l_S} + C_{l_F} < \eta, \zeta > \tag{B.1d}$$

$$C_{m_{S_k}} = C_{m_S} + C_{m_F} < \eta, \zeta > \tag{B.1e}$$

$$C_{n_{S_k}} = C_{n_S} + C_{n_F} < \eta, \zeta > \tag{B.1f}$$

were the terms of the form $\boldsymbol{C_{()_S}}$ represent the conventional coefficients, and the terms $\boldsymbol{C_{()_F}}$ the additional formation coefficients. The formation coefficients may be calculated through,

$$C_{L_F} < \eta, \zeta > = \frac{-c_{l_\alpha} C_{L_j}}{2\pi^2 \mathcal{AR}} \sigma_{jk} \tag{B.2a}$$

$$C_{D_F} < \eta, \zeta > = \frac{2C_{L_k} C_{L_j}}{\pi^3 \mathcal{AR}} \sigma_{jk} \tag{B.2b}$$

$$C_{Y_F} < \eta, \zeta > = \frac{2C_{l_j} S_t}{\pi \mathcal{AR} \zeta_t S} \sigma_{jk_f} \tag{B.2c}$$

$$C_{l_F} < \eta, \zeta > = \frac{c_{l_\alpha} C_{L_j}}{2\pi^2 \mathcal{AR}} \tau_{jk} \tag{B.2d}$$

$$C_{m_F} < \eta, \zeta > = C_{L_F}(h - h_0) - V_{tail} \frac{-2C_{L_j}}{\pi^3 \mathcal{AR} \eta_h} \left(1 - \frac{d\epsilon}{d\alpha}\right) \sigma_{jk\omega h} \tag{B.2e}$$

$$C_{n_F} < \eta, \zeta > = \frac{2C_{L_k} C_{L_j}}{\pi^3 \mathcal{AR}} \tau_{jk} - V_t \frac{2C_{L_j}}{\pi \mathcal{AR} \zeta_t} \sigma_{jk_f} \tag{B.2f}$$

were the influence parameters are derived as,

$$\sigma_{jk} = \ln\left|\frac{\left((\eta-\frac{\pi}{4})^2+\zeta^2+\mu^2\right)\left((\eta+\frac{\pi}{4})^2+\zeta^2+\mu^2\right)}{(\eta^2+\zeta^2+\mu^2)^2}\right| \tag{B.3a}$$

$$\begin{aligned}\sigma_{jk_f} = &\ln\left|\frac{(\eta-\frac{\pi}{8})^2+(\zeta+\zeta_v)^2+\mu^2}{(\eta-\frac{\pi}{8})^2+(\zeta+\zeta_v-\zeta_t\frac{\pi}{8})^2+\mu^2}\right| \\ &-\ln\left|\frac{(\eta+\frac{\pi}{8})^2+(\zeta+\zeta_v)^2+\mu^2}{(\eta+\frac{\pi}{8})^2+(\zeta+\zeta_v-\zeta_t\frac{\pi}{8})^2+\mu^2}\right|\end{aligned} \tag{B.3b}$$

$$\begin{aligned}\tau_{jk} = &-2\sqrt{\zeta^2+\mu^2}\left[\tan^{-1}\left(\frac{\eta-\frac{\pi}{4}}{\sqrt{\zeta^2+\mu^2}}\right)+\tan^{-1}\left(\frac{\eta+\frac{\pi}{4}}{\sqrt{\zeta^2+\mu^2}}\right)-2\tan^{-1}\left(\frac{\eta}{\sqrt{\zeta^2+\mu^2}}\right)\right] \\ &-\eta\ln\sigma_{jk}-\frac{\pi}{8}\ln\left|\frac{(\eta+\frac{\pi}{4})^2+\zeta^2+\mu^2}{(\eta-\frac{\pi}{4})^2+\zeta^2+\mu^2}\right|\end{aligned} \tag{B.3c}$$

$$\sigma_{jkw_h} = \ln\left|\frac{\left(\zeta^2+(\eta-\frac{\pi}{8}-\frac{\pi}{8}\eta_h)^2+\mu^2\right)\left(\zeta^2+(\eta+\frac{\pi}{8}+\frac{\pi}{8}\eta_h)^2+\mu^2\right)}{\left(\zeta^2+(\eta-\frac{\pi}{8}+\frac{\pi}{8}\eta_h)^2+\mu^2\right)\left(\zeta^2+(\eta+\frac{\pi}{8}-\frac{\pi}{8}\eta_h)^2+\mu^2\right)}\right| \tag{B.3d}$$

The formation flight induced aerodynamic coefficients are illustrated in Figure B.1 as functions of lateral separation at $\xi = -10$ and $\zeta = 0$, and in Figure B.2 as functions of lateral and vertical separation at $\xi = -10$.

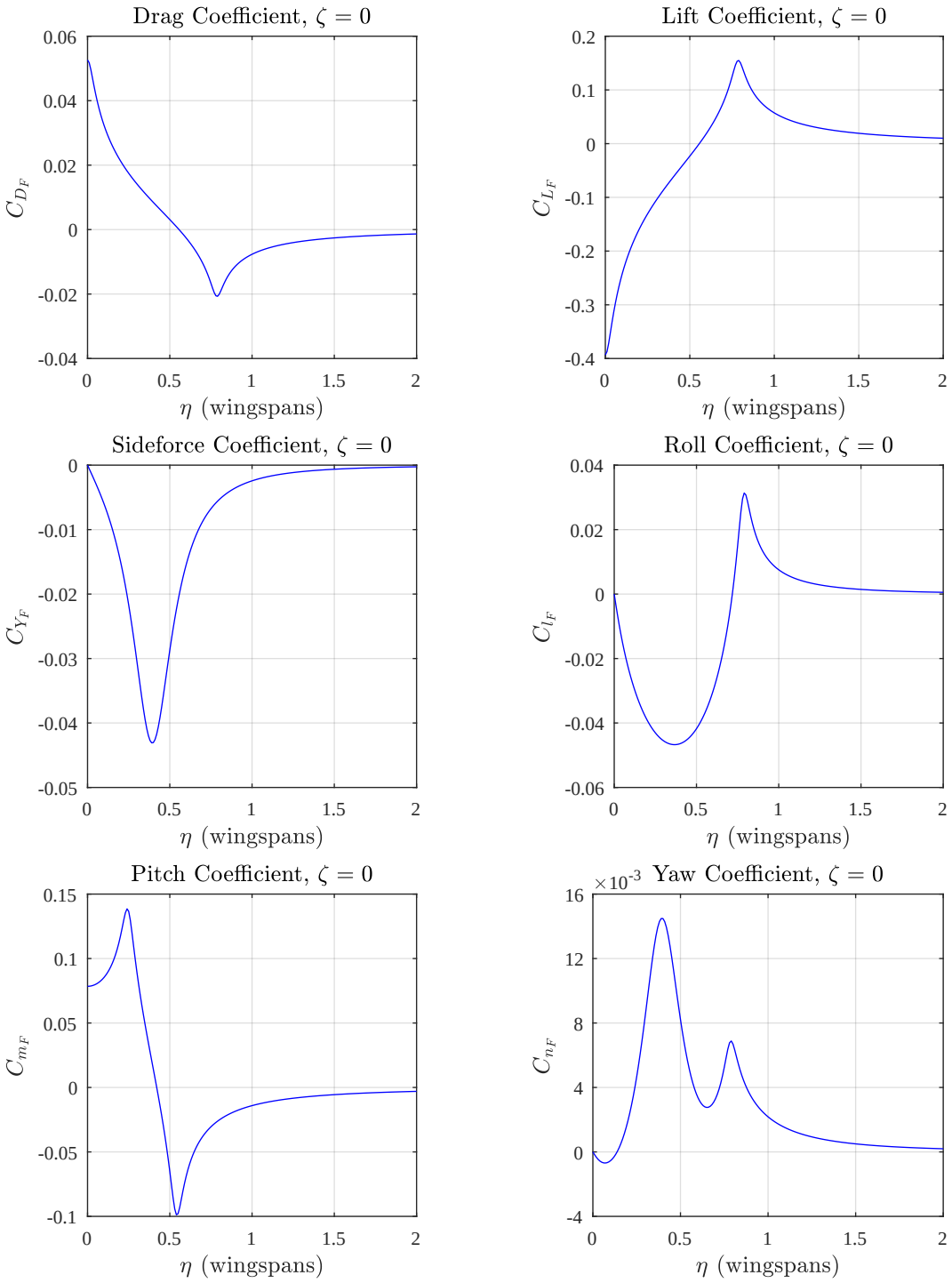

Figure B.1: Formation flight induced aerodynamic coefficients as functions of lateral separation at $\xi = -10$ and $\zeta = 0$.

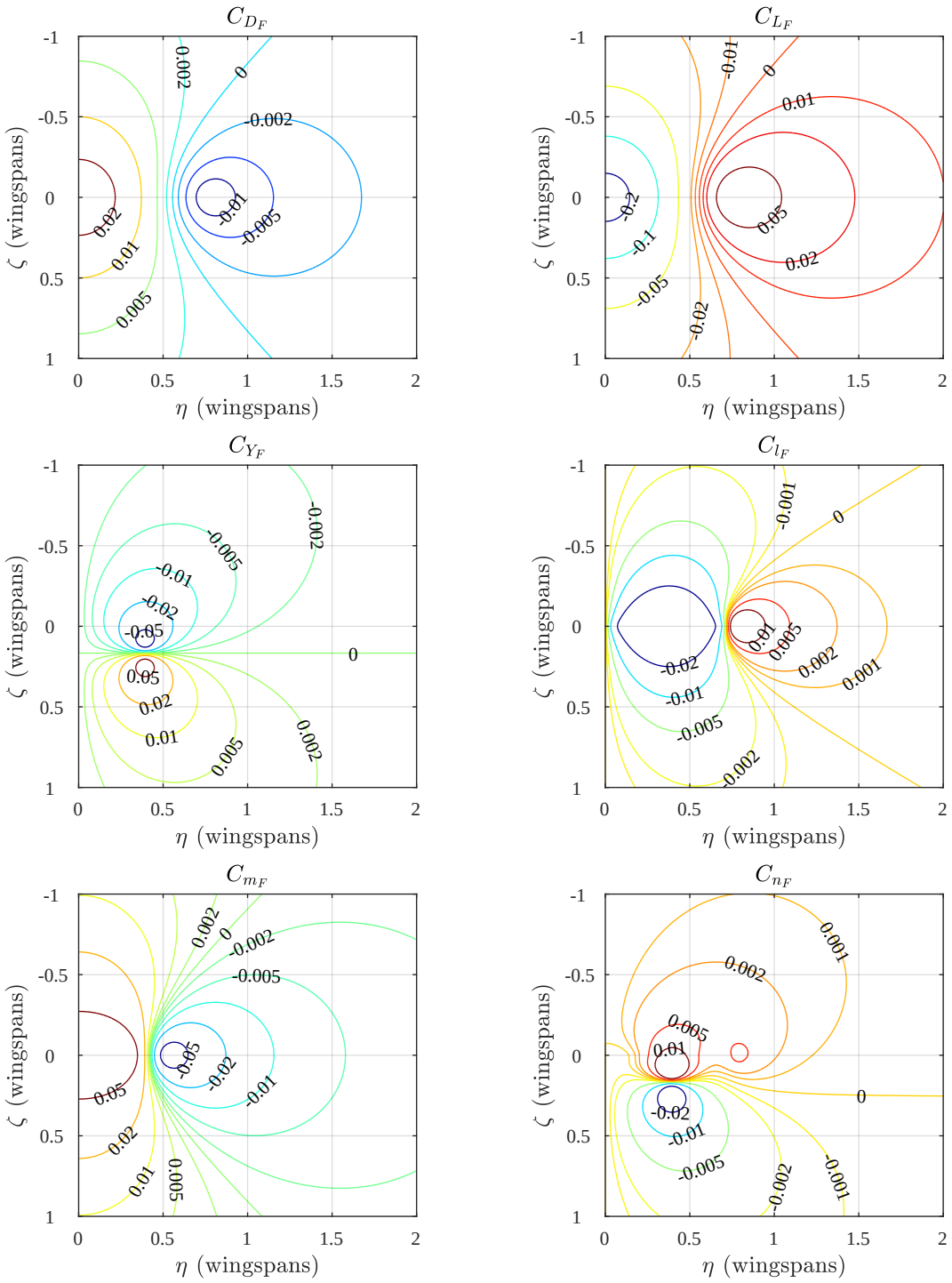

Figure B.2: Formation flight induced aerodynamic coefficients as functions of lateral separation and vertical separation.

Appendix C

DQ Controller Elevator Feed-Forward Constant

This appendix details the derivation of the elevator feed-forward constant N included in the closed-loop model of the DQ controller dynamics. The normal acceleration state for the full-order closed-loop DQ model consists of of a state output matrix $\mathbf{C}_{a_z}$ and an elevator control feed-forward term D_{a_z},

$$a_z = \mathbf{C}_{a_z}\mathbf{x}_{long} + D_{a_z}\delta_e \tag{C.1}$$

The full-order DQ law is given by,

$$\delta_e = -\mathbf{K}_{DQ}\mathbf{x}_{DQ} - K_I x_{I_{DQ}} + K_{FF}a_{z_c} \tag{C.2}$$

where,

$$\mathbf{x}_{DQ} = \begin{bmatrix} \bar{v} \\ a_z \\ q \\ \theta \end{bmatrix} = \mathbf{C}_{DQ}\mathbf{x}_{long} + \mathbf{D}_{DQ}\delta_e \tag{C.3}$$

By substituting Equation C.3 into Equation C.2 and gathering terms, the elevator command may be reduced to,

$$\delta_e[1 + \mathbf{K}_{DQ}\mathbf{D}_{DQ}] = -\mathbf{K}_{DQ}\mathbf{C}_{DQ}\mathbf{x}_{long} - K_I x_{I_{DQ}} + K_{FF}a_{z_c} \tag{C.4}$$

$$\delta_e = -N\mathbf{K}_{DQ}\mathbf{C}_{DQ}\mathbf{x}_{long} - NK_I x_{I_{DQ}} + NK_{FF}a_{z_c} \tag{C.5}$$

where N is the control-loop constant,

$$N = \frac{1}{1 + \mathbf{K}_{DQ}\mathbf{D}_{DQ}} \tag{C.6}$$

Appendix D

A Note on Vector Notation

The vector notation used to describe the formation guidance axis systems and separation variables, were based on the work done by Peddle [39]. This appendix recalls a simple explanation of the basic vector notation as presented by Peddle.

An axis system A is defined by three basis unit vectors $\boldsymbol{i^A}$, $\boldsymbol{j^A}$ and $\boldsymbol{k^A}$ that originate from an origin vector o^A and span three dimensional space. The basis vectors are chosen to be orthogonal, and are denoted by boldface, italic symbols. Consider axis systems A and B, and the vector $\boldsymbol{R}$, which may be written as a linear combination of the basis vectors of either axis system. Equation D.1 illustrates the vector $\boldsymbol{R}$ coordinated in the A axis system.

$$\boldsymbol{R} = X^A\boldsymbol{i^A} + Y^A\boldsymbol{j^A} + Z^A\boldsymbol{k^A} \tag{D.1}$$

By convention, the coordinate variables are denoted with the superscript of the respective axis system, which proves convenient when the same vector is coordinated into multiple axis system since the same coordinate symbol may be used. The full vector notation of equation D.2 can become cumbersome, and as a result, the basis vectors of A may be dropped when coordinating $\boldsymbol{R}$ into A. Equation D.2 illustrates the notation where only the coordinates are written in matrix form. A boldface, non-italic symbol is used to show that only the coordinates of the vector, in the subscripted axis system, are begin referred to and not the vector itself. $\mathbf{R_A}$ is thus now referred to as a *coordinate vector*.

$$\mathbf{R_A} = \begin{bmatrix} X^A \\ Y^A \\ Z^A \end{bmatrix} \tag{D.2}$$

Coordinating R into an axis system does not change the vector, and it is perfectly legal to write,

$$\boldsymbol{R} = X^A\boldsymbol{i^A} + Y^A\boldsymbol{j^A} + Z^A\boldsymbol{k^A} = X^B\boldsymbol{i^B} + Y^B\boldsymbol{j^B} + Z^B\boldsymbol{k^B} \tag{D.3}$$

However, unless the two axis systems coincide, when referring to the coordinate vectors the following is true,

$$\mathbf{R_A} \neq \mathbf{R_B} \tag{D.4}$$

In the work of Peddle, additional information is provided with regards to how the vector notation is applied when performing operations such as dot product, cross product and time derivatives. Since this appendix only covers the very basics of the notation, the reader is encouraged to study the work of Peddle for more insight.

Appendix E

Extended Extremum Seeking Results

This appendix details additional extremum-seeking results in which a static near-extremum is approached by dithering in the opposite direction as presented and discussed in Chapter 7. When approaching from above, dithering is performed in a counter clockwise direction, while a clockwise dither is performed when seeking from below. For both cases, it is shown that the extremum-seeking controller manages to locate the near-extremum with performance similar to the results presented in Chapter 7. It can thus be concluded that the dither direction has little impact on seeking operation.

E.1 Proportional Approach Rate

E.1.1 Approaching Extremum from Above

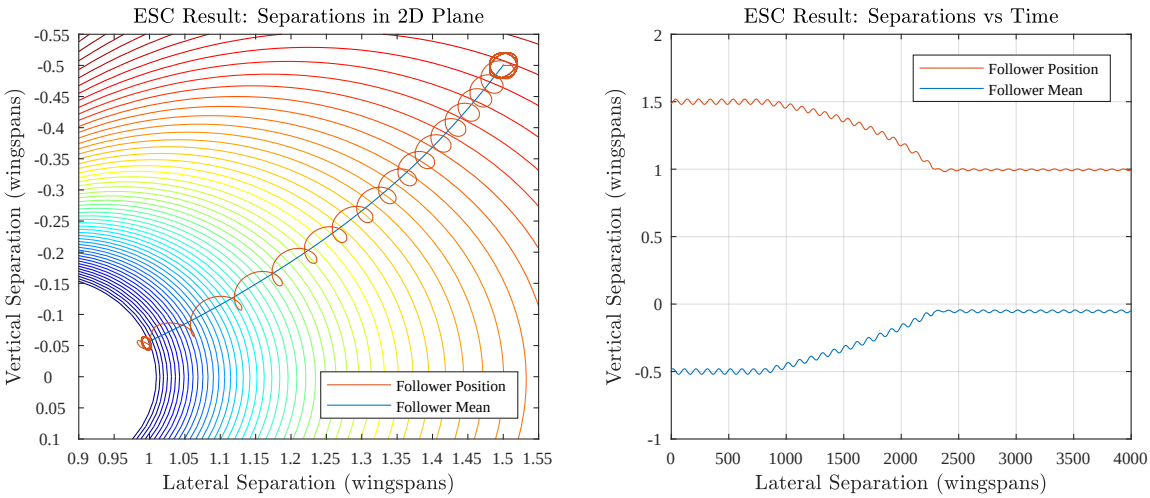

(a) 2D result.

(b) Formation separation.

Figure E.1: Extremum-seeking from $\eta = 1.5$ and $\zeta = 0.5$ with dither period 150s and amplitude 0.02b at a proportional approach rate.

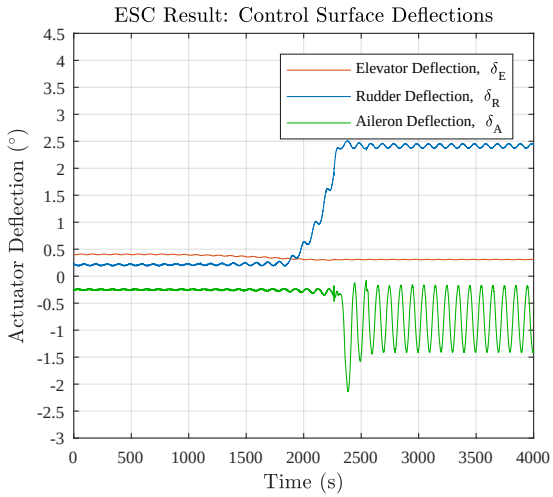

(a) Control surface deflections.

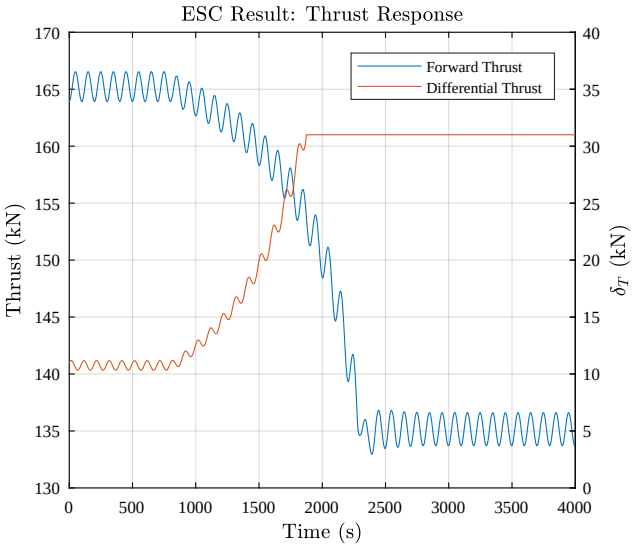

(b) Thrust response.

Figure E.2: Actuator responses when extremum-seeking from $\eta = 1.5$ and $\zeta = 0.5$ with dither period 150s and amplitude 0.02b at a proportional approach rate.

E.1.2 Approaching Extremum from Below

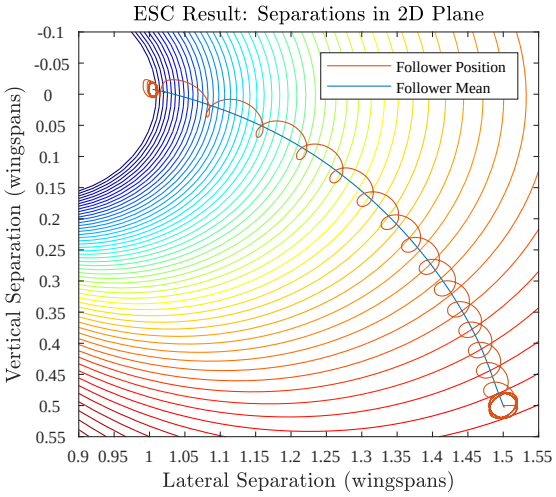

(a) 2D result.

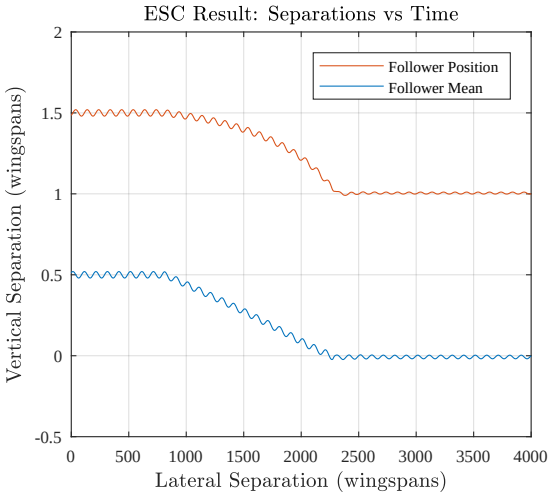

(b) Formation separation.

Figure E.3: Extremum-seeking from $\eta = 1.5$ and $\zeta = -0.5$ with dither period 150s and amplitude 0.02b at a proportional approach rate.

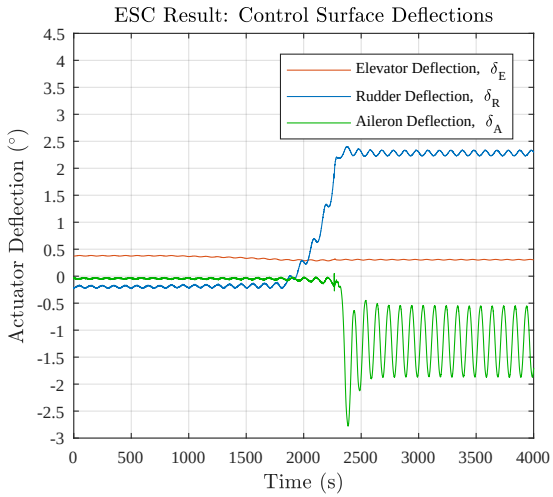

(a) Control surface deflections.

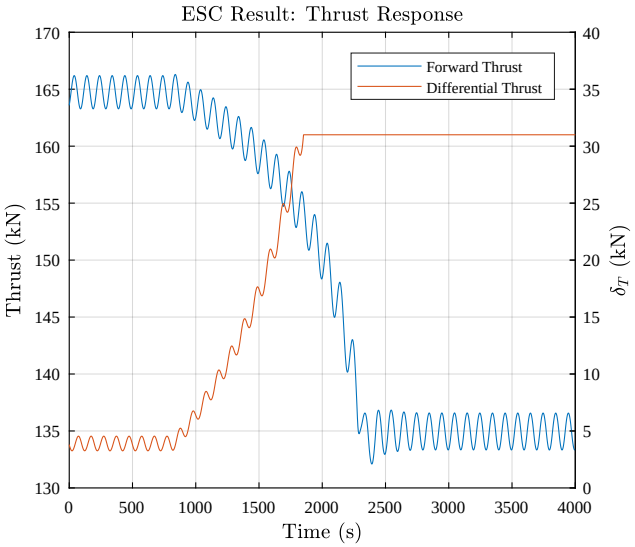

(b) Thrust response.

Figure E.4: Actuator responses when extremum-seeking from $\eta = 1.5$ and $\zeta = -0.5$ with dither period 150s and amplitude 0.02b at a proportional approach rate.

E.2 Constant Approach Rate

E.2.1 Approaching Extremum from Above

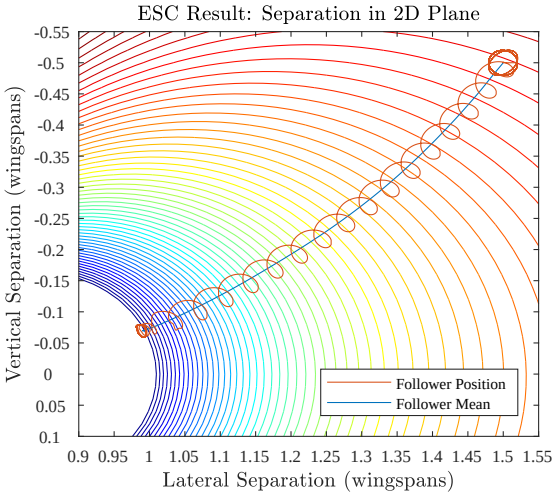

(a) 2D result.

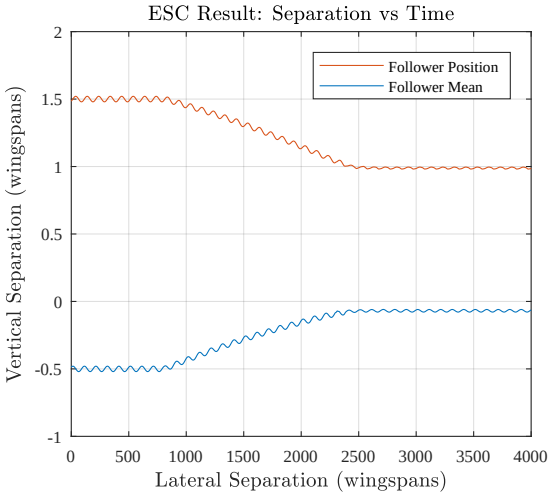

(b) Formation separation.

Figure E.5: Extremum-seeking from $\eta = 1.5$ and $\zeta = 0.5$ with dither period 150s and amplitude 0.02b at a constant approach rate.

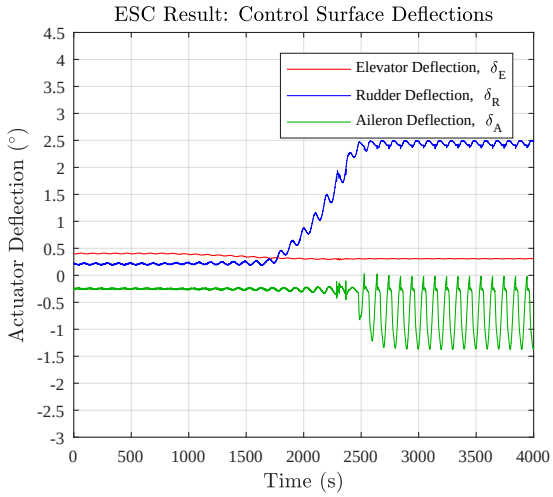

(a) Control surface deflections.

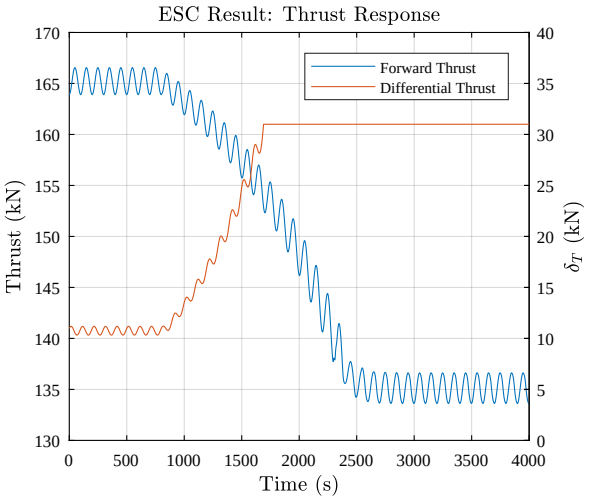

(b) Thrust response.

Figure E.6: Actuator responses when extremum-seeking from $\eta = 1.5$ and $\zeta = 0.5$ with dither period 150s and amplitude 0.02b at a constant approach rate.

E.2.2 Approaching Extremum from Below

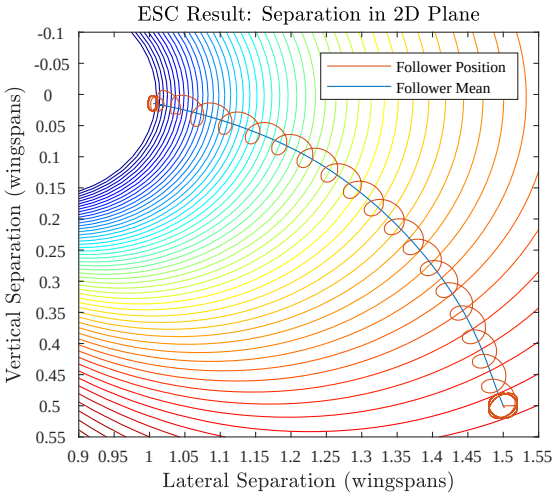

(a) 2D result.

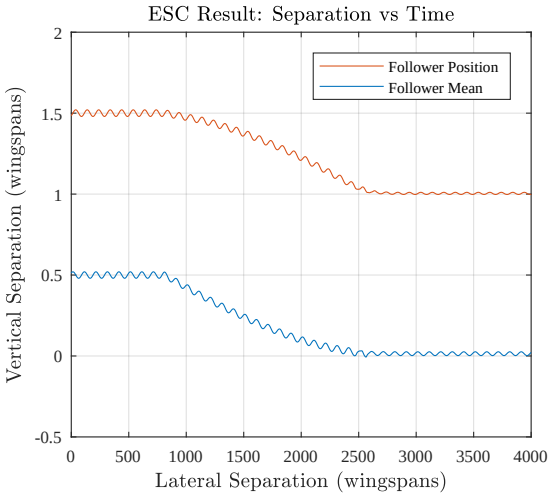

(b) Formation separation.

Figure E.7: Extremum-seeking from $\eta = 1.5$ and $\zeta = -0.5$ with dither period 150s and amplitude 0.02b at a constant approach rate.

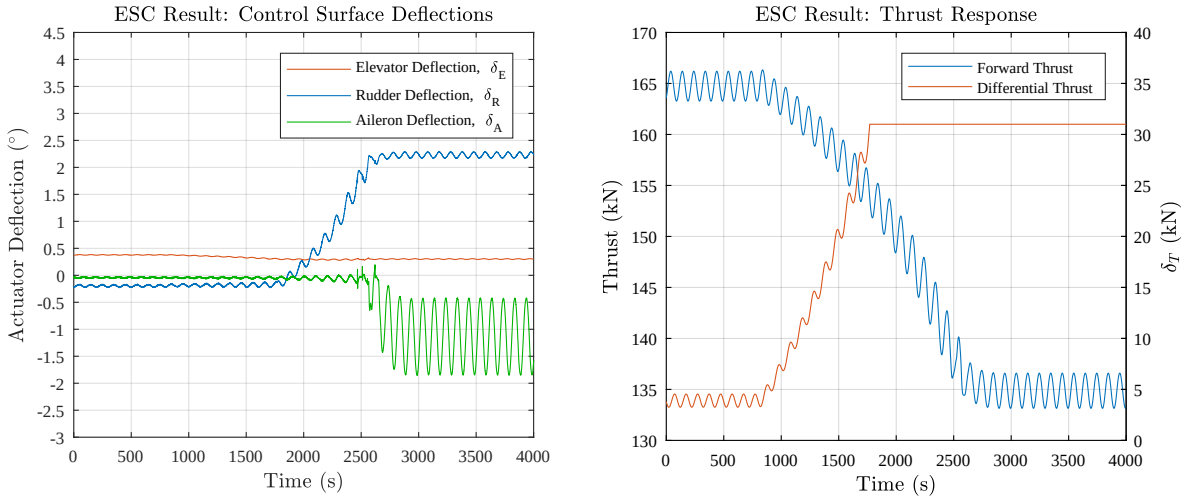

(a) Control surface deflections.

(b) Thrust response.

Figure E.8: Actuator responses when extremum-seeking from $\eta = 1.5$ and $\zeta = -0.5$ with dither period 150s and amplitude 0.02b at a constant approach rate.